Aus dem Institut für Schlaganfall-und Demenzforschung (ISD)
Klinikum der Ludwig-Maximilians-Universität München

Dissertation

zum Erwerb des Doktorgrades der Medizin

an der Medizinischen Fakultät der

Ludwig-Maximilians-Universität München

Scalable Three-dimensional intact human organs labeling and clearing by Tissue Clearing Technologies

vorgelegt von

Hongcheng Mai

aus

Zhongshan, Guangdong, China

Jahr

2023

Mit Genehmigung der Medizinischen Fakultät der

Ludwig-Maximilians-Universität zu München

Erster Gutachter: Prof. Dr. med. Michael Ewers

Zweiter Gutachter: Prof. Dr. med. Jochen Herms

Dritter Gutachter: Prof. Dr. med. Thomas Knösel

Mitbetreuung durch den
promovierten Mitarbeiter: ______________________

Dekan: Prof. Dr. med. Thomas Gudermann

Tag der mündlichen Prüfung: 08.02.2023

Affidavit

LMU

LUDWIG-
MAXIMILIANS-
UNIVERSITÄT
MÜNCHEN

Promotionsbüro
Medizinische Fakultät

MMRS

Affidavit

Mai,Hongcheng

Surname, first name

Street

Zip code, town, country

I hereby declare, that the submitted thesis entitled:

Scalable Three-dimensional intact human organs labeling and clearing by Tissue Clearing Technologies

……….

is my own work. I have only used the sources indicated and have not made unauthorised use of services of a third party. Where the work of others has been quoted or reproduced, the source is always given.

I further declare that the dissertation presented here has not been submitted in the same or similar form to any other institution for the purpose of obtaining an academic degree.

Munich, 08.02.2023 Mai,Hongcheng

place, date Signature doctoral candidate

Table of content

List of abbreviations

3D	Three-dimensional
MRI	Magnetic Resonance Imaging
CT	Computed Tomography
SNR	Signal-to-noise ratio
GFP	Green fluorescent protein
LSFM	Light-sheet fluorescence microscopy
RI	Refractive index
THF	Tetrahydrofuran
FPs	Fluorescence proteins
DBE	Dibenzyl ether
ECi	Ethyl cinnamate
DCM	Dichloromethane
TDE	2,2'-thiodiethanol
CUBIC	Clear, unobstructed brain imaging cocktails and computational anslysis
SDS	Sodium dodecyl sulphate
CLARITY	Crosslinked to a three-dimensional network of hydrophilic polymers
EDTA	Ethylenediaminetetraacetic acid
PI	Propidium iodide
NA	Numerical aperture
SHANEL	Small-micelle-mediated human organ efficient clearing and labeling
3DISCO	3D imaging of solvent-tissue cleared organs
CNS	Central nervous system
uDISCO	ultimate dimension imaging of solvent-tissue cleared organs

vDISCO	variable domain of heavy chain antibodies dimension imaging of solvent-tissue cleared organs
a-uDISCO	alkaline pH-based uDISCO
fDISCO	DISCO with superior fluorescence-preserving capability
DBE	Dibenzyl ether
iDISCO	immunolabeling enabled three-dimensional imaging of solvent-cleared organs
SeeDB	See Deep Brain
FRUIT	a cocktail of fructose and urea
ScaleS	a sorbitol-based optical clearing method that provides stable tissue preservation
ClearT2	detergent- and solvent-free clearing method
PACT	passive tissue clearing and immunolabeling protocol for intact thick organs
FxClear	Free-hydrogel Electrophoretic Tissue Clearing Method
BABB	benzyl-alcohol and benzyl-benzoate
SBB	Sudan Black B
H2O2	Hydrogen peroxide
CMC	Critical micelle concentration
CMT	Critical micelle temperature
CHAPS	3-((3-cholamidopropyl) dimethylammonio)-1-propanesulfonate
CHAPSO	3-([3-Cholamidopropyl]dimethylammonio)-2-hydroxy-1-propansulfonat
DAPI	4′ ,6-diamidino-2-phenylindole
DRAQ5	1,5-bis([2-(di-methylamino)ethyl]amino)-4,8 dihydroxyanthracene-9,10-dione
FITC	Fluorescein isothiocyanate
AD	Alzheimer's disease
JPEG	Joint Photographic Experts Group

HDF5	Hierarchical Data Format 5
LZW	Lempel–Ziv–Welch

List of publications

1. **MAI, H.**, RONG, Z., ZHAO, S., CAI, R., STEINKE, H., BECHMANN, I. & ERTURK, A. 2022. Scalable tissue labeling and clearing of intact human organs. Nat Protoc. (doi.org/10.1038/s41596-022-00712-8)(**Cumulative dissertation Publication I**)
2. ZHAO, S., TODOROV, M. I., CAI, R., MASKARI, R. A., STEINKE, H., KEMTER, E., **MAI, H.**, RONG, Z., WARMER, M., STANIC, K., SCHOPPE, O., PAETZOLD, J. C., GESIERICH, B., WONG, M. N., HUBER, T. B., DUERING, M., BRUNS, O. T., MENZE, B., LIPFERT, J., PUELLES, V. G., WOLF, E., BECHMANN, I. & ERTURK, A. 2020. Cellular and Molecular Probing of Intact Human Organs. Cell, 180, 796-812 e19. (doi.org/10.1016/j.cell.2020.01.030) **(Cumulative dissertation Publication II)**
3. PAN, C., SCHOPPE, O., PARRA-DAMAS, A., CAI, R., TODOROV, M. I., GONDI, G., VON NEUBECK, B., BOGURCU-SEIDEL, N., SEIDEL, S., SLEIMAN, K., VELTKAMP, C., FORSTERA, B., **MAI, H.**, RONG, Z., TROMPAK, O., GHASEMIGHARAGOZ, A., REIMER, M. A., CUESTA, A. M., CORONEL, J., JEREMIAS, I., SAUR, D., ACKER-PALMER, A., ACKER, T., GARVALOV, B. K., MENZE, B., ZEIDLER, R. & ERTURK, A. 2019. Deep Learning Reveals Cancer Metastasis and Therapeutic Antibody Targeting in the Entire Body. Cell, 179, 1661-1676 e19.
4. SCHOPPE, O., PAN, C., CORONEL, J., **MAI, H.**, RONG, Z., TODOROV, M. I., MUSKES, A., NAVARRO, F., LI, H., ERTURK, A. & MENZE, B. H. 2020. Deep learning-enabled multi-organ segmentation in whole-body mouse scans. Nat Commun, 11, 5626.

Your contribution to the publications

1.1 Contribution to paper I

DOI https://doi.org/10.1038/s41596-022-00712-8

Scalable tissue labeling and clearing of intact human organs

Hongcheng Mai, Zhouyi Rong, Shan Zhao, Ruiyao Cai, Hanno Steinke, Ingo Bechmann & Ali Ertürk

Contribution to the publication

As the first author of this publication, I was deeply involved in designing the study, performed most of the publication related experiments, and wrote the manuscript with Zhouyi Rong, Shan Zhao, and corresponding author Ali Ertuerk. First, I summarized the pipeline of SHANEL protocols (Fig. 1 and Extended Data Fig. 7) and summarized the challenges in human deep tissue clearing, immunolabelling and visualization (Table 1). The most challenging step is to use blood vessels to perfuse solutions in already dissected intact human organ, and I have performed the experiments illustrating the perfusion of human kidney in the manuscript (Fig. 2). Before starting the labeling, I have performed experiments to screen several SHANEL protocol compatible chemical dyes and antibodies (summarized in Table 3) as well as the time guidelines for treating different human organs based on my experimental results (Table 4). Moreover, I labeled and cleared the human organs and established a protocol on how to embed organs and image them with light sheet fluorescent microscopy (LSFM). This protocol overcomes the limitation of commercial imaging systems that cannot accommodate large cleared human organs (Fig. 3). Then, I provided an example of how to image a human pancreas with LSFM (Fig. 4). Later, after the imaging steps, I summarized the main steps for data handling, including image stitching, renaming, and compression. Also, the steps for 3D reconstruction and visualization of the image data using Arivis Fusion and Imari's Data Loading and Visualization (Extended Data Fig. 5 and Extended Data Fig. 6). Finally, I performed the experiments using SHANEL protocols on the different human organs and human tissue from the manuscript. The intact human organs were labeled through perfusion (a procedure we named active labeling) with dextran vascular labeling dye (Fig. 5). The human tissues were incubated (named passive labeling) with chemical probes and antibodies for labeling blood vessels, cell nuclei, and microglia in brain, lung, pulvinar, and skull. (Fig. 6 and

Fig. 7). In this publication, we showed the different applications and summarized detailed steps to mark and clear intact human organs.

1.2 Contribution to paper II

DOI https://doi.org/10.1016/j.cell.2020.01.030

Cellular and Molecular Probing of Intact Human Organs

Shan Zhao, Mihail Ivilinov Todorov, Ruiyao Cai, Rami Al-Maskari, Hanno Steinke, Elisabeth Kemter, Hongcheng Mai, Zhouyi Rong, Martin Warmer, Karen Stanic Aguilera, Oliver Schoppe, Johannes Christian Paetzold, Benno Gesierich, Milagros N. Wong, Tobias B. Huber, Marco Duering, Oliver Thomas Bruns, Bjoern Menze, Jan Lipfert, Victor G. Puelles Rodriguez, Eckhard Wolf, Ingo Bechmann, Ali Ertürk

Contribution to the publication

As co-author of this publication, I contributed to parts of the experimental work and revised the manuscript. While developing the SHANEL method, I performed 2D epifluorescence microscopy to test compatible nanobodies as a prototype experiment for labeling EGFP samples from transgenic mice. Later, I performed the high-resolution 3D LSFM to screen individual SHANEL methods compatible with chemical labels (PI, lectin) in human tissues. In addition, I tested the compatible nano-booster for the INS-EGFP transgenic pig pancreas (Fig. 2 D-F). To efficiently process large amounts of data, I helped to develop a Deep Learning-based quantification method by generating ground truth data derived from 3D cell reconstruction of human brain samples (Fig. 7 D-E).

2. Introduction

2.1 Chapter 1.1 Holistic mapping of human organisms

The study of human organ anatomy is fundamental in medicine for several applications, from diagnosing diseases to generating treatments. So the organs of the human body must be mapped with a resolution of a single cell(Schiller et al., 2019). A comprehensive atlas of human organs is essential for clinical physicians to determine the course of treatment, obtain reference images of the various human structures from a large volume, and serve as a preoperative tool(Reardon, 2016, Rozenblatt-Rosen et al., 2021). However, Intricate three-dimensional anatomical complexity has remained a challenge for mapping intact human organs (Reardon, 2016). This limitation is primarily due to the lack of scalable and unbiased cellular-level technologies capable of mapping human organs.

2.1.1 Chapter 1.1.1 Imaging technology for intact human organs and cleared human tissue

Several advanced technologies attempt to map high-resolution structural data on human organs. The standard method for reconstructing many human organs provides valuable digital anatomical images of human organs but is time-consuming and omits some valuable information. For example, the sectioning histology is very labor intensive for large human organs, and reconstructing information from adjacent sections into a 3D view of the tissue is extremely time consuming and difficult. Magnetic resonance imaging (MRI) is one of the most popular and sensitive methods used for visualizing vital organs in clinical studies(Sijens et al., 2010). Although MRI can provide longitudinal images of human organs, including the brain(Tuch et al., 2001) and kidney(Nikken and Krestin, 2007), its maximum resolution still does not reach a cellular resolution. Even the advancement of higher-resolution MRI with high Tesla values has limitations(Schmidt et al., 2010). First, various human tissues and regions require the development of new MRI scanning techniques and imaging protocols to visualize the regions of interest. Second, visualization depends on subject compliance and technician skills in sequence planning, execution, and post-processing. Third, detecting tissue edema, fibrosis, and inflammation in internal structures may be less accurate. The optional method is computed tomography

(CT), which usually targets the human organ vasculature and is required to segment important human organ regions and structures(Walsh et al., 2021). In addition to the limited resolution, CT Imaging has a high cost (Fu et al., 2019). Furthermore, CT carries a potential risk of radiation exposure for clinicians. Because CT and MRI have limited image resolution and cannot accurately reflect the exact condition of detail of human organs, such as capillary vessels, more extensive imaging technology is required to develop for human organ mapping(Kaller and An, 2022).

Overall, we are still searching for a method that can bridge the gap between large-scale intact imaging and high-resolution histological imaging for intact human organs, for examples, the human brain, kidney, and pancreas. One promising approach is using the newly developed method "tissue clearing," that enables high-resolution in situ labeling of macroscopic structures and renders anatomical specimens transparent by minimizing light absorption and scattering in cleared tissues(Tian et al., 2021). Although simple tissue clearing method was invented over a century ago(Richardson and Lichtman, 2015), it has only recently gained broader interest in the neuroscience community when combined with fluorescent markers (fluorescent proteins and chemical probes) and antibody deep tissue labeling methods(Ueda et al., 2020). The most critical element in the recent success of tissue clearing methods is the development of LSFM, which extends the technique to larger fields of view(Costantini et al., 2019). The main advantage of LSFM is that it accurately preserves the macroscopic 3D spatial relationships of the cleared tissues.

Microscopies for cleared tissue imaging

The development of fluorescence light microscopy has led to many tissue clearing methods applicable in various fields (**Table 1**). Researchers must select the most appropriate microscopy for their optically transparent samples(Chen et al., 2015, Ku et al., 2016). Tissue after transparent allows deep 3D imaging using confocal (Decroix et al., 2015, Ariel, 2017), two-photon, or LSFM. Two-photon imaging is traditionally used for deep imaging in living animals and thick fluorescent tissues(Denk et al., 1990). Recently cellular 3D imaging can be accomplished with objectives optimized two-photon microscopy by imaging cleared samples at depths of up to 5 mm in high resolution and contrast (Ragan et al., 2012). However, two-photon microscopy is not suitable for large-volume sample imaging. In addition, the main drawbacks of this two-photon microscopy applied to cleared human tissues are the slow scanning speed and the unavoidable light bleaching. These drawbacks restrict two-photon microscopy for further development of cleared human tissue. Compared with two-photon microscopy, LSFM has advantage of illuminating the whole layer of interest in the sample with single panel of light, when sparing the rest of the region from laser illumination, significantly reducing the damage from light bleaching and increasing scanning speed(Jonkman et al., 2020, Reynaud et al., 2008). LSFM enables volumetric imaging of much larger human tissues that need only account for the relationship between tissue size and imaging chamber size.

Because of the renewed interest in LSFM development and optimization, it is now possible to study large volumes of intact human tissue at cellular resolution(Santi, 2011). With LSFM, large human sample volumes can be scanned quickly, alleviating imaging bottlenecks during high-throughput tissue sample preparation (Power and Huisken, 2017). The organic solvent-based method reduces the volume of tissue samples by approximately 30%, allowing human organs to fit into the imaging chamber of LSFM. With LSFM, images can be captured at tens-to-thousands of frames per second with the camera, allowing for detailed analysis and optically clear 3D observations by reducing fading and phototoxicity (Voie et al., 1993). In particular, LSFM uses a thin slice of illumination plane to illuminated a fluorescent sample, such as the whole embryos, as well as objects as small as organelles, which benefit most from selective illumination when analyzing complex, dynamic 3D fluorophore distributions (Tomer et al., 2011, Verveer et al., 2007). Because LSFM uses a high speed camera for signal detection, it enables acquisition in a short time, which has made powerful acquisition and minimal laser toxicity of LSFM an extremely versatile microscopy for 3D imaging of samples at up to five biologically relevant scales (Ueda et al., 2020).

Table 1 Summarized characteristics of microscopies for tissue clearing samples

Microscopy type:	Resolution Z	Imaging depth
Wide-field	Usually less than 1µm	Bad
Laser-Scanning Confocal	Good can reach 700 nm	Good (less than 100um)
Multi-point Confocal	Good but slightly less than LSFM	Typically less than 50µm
Light Sheet Fluorescence Microscopy	Good depends on the thickness of the light sheet	Best (can reach several mm)
Lattice Light with super resolution microscopy	Best with super resolution	Generally less than 20µm

Volume imaging by adapting LSFM systems in conjunction with the tissue clearing method could be a powerful platform for imaging transparent human organs. Indeed, in **Publication I**, we demonstrated that the SHANEL method combined with LSFM for volumetric imaging enables in-depth analysis of the functional anatomy of large volumes of human tissue and even intact organs.

2.1.2 Chapter 1.1.2 Optical Tissue clearing

Tissue clearing methods render biological specimens transparent by matching the refractive indices of various cellular compartments. Reduced light scattering enhances imaging light to penetrate deeper into the tissue. When combined with fluorescent labeling of cells and molecules, the entire transparent organs or even whole organisms can be imaged via LSFM at subcellular resolution. Organic solvent-based tissue clearing methods, particularly the 3D imaging of solvent-tissue cleared organs (3DISCO), first introduced by Dr. Ertürk, are a straightforward and reproducible technique to clear dissected mice organs(Erturk et al., 2012) and achieve the most satisfied level of optical transparency among all reported methods. To study the entire central nervous system (CNS) and beyond, our group developed the ultimate uDISCO(Pan et al., 2016) and a whole mouse immunolabeling method known as vDISCO(Cai et al., 2019), which can render not limited to dissected mouse organs but also entire adult rodent bodies transparent.

Organic solvent-based tissue clearing

The advantages of organic solvent-based methods in the tissue clearing field often result in rapid, complete transparency of an intact mouse organ. Most tissue clearing organic solvent-based methods have evolved from the method of 3DISCO, which was the first to render an adult mouse organ optically transparent in 1–2 days, depending on the organ size. Methods based on DISCO include a major step of dehydration which would remove water and lipid—the main light scatterer components in biological tissues (RI of aqueous is 1.33 and the RI of lipid and other soft tissues is 1.44–1.56) and an immersion step in an organic solvent is to meet the mean RI of biological tissue and reach a homogenous RI in the tissue. The RI for organic solvents based tissue clearing method is ~1.56(**Figure 1**)(Masselink et al., 2019, Buenrostro et al., 2013). 3DISCO and its variants have been improved in response to the problem that solvent chemicals preserve fluorescent proteins for only a few days. For instance, Pan et al. developed the another organic solvent based tissue clearing method called-uDISCO which extended the applicant of whole mouse tissue clearing and visulization, with the features of maintained mouse endogenous FPs for up to 6 months, and reduced the tissue size to around thirty percentage of their previous tissue size, allowing whole-body visulization at cellular resolution using LSFM. a-uDISCO(Li et al., 2018) improves fluorescence intensity and stability by adjusting pH conditions. Based on uDISCO, its successors, fDISCO, and sDISCO(Matryba et al., 2021), have been used extensively in imaging studies of rodent neural circuits, inflammation, and stem cells, as well as human biopsy specimens. fDISCO(Qi et al., 2019) was developed by controlling the temperature and pH settings in the protocol. fDISCO makes it possible to preserve FPs and fluorescent chemical tracers for several months and rescan the cleared samples for multiple times. By stabilizing DBE with antioxidants, sDISCO further preserves fluorescent signals for longer time. With applying sDISCO, FP fluorescence could be maintained for over one year. In addition to DISCO-based methods relying on the FPs, immunological deep labeling approaches were applied to study rodent embryos, whole mouse bodies, human embryos, and human cancer biopsy samples. Labeling large human tissues in depth with selected chemical dyes and specific antibodies remains challenging because antibody permeabilization decreases with the sample size. To resolve this issue, Renier et al. developed iDISCO(Renier et al., 2014), which combines different chemicals in the pretreatment solutions that allow permeabilization of whole mouse embryos and adult organs. This technique enabled the identification of distinct neuronal regions of whole mouse brains through successful immunolabeling and volumetric imaging. For whole mouse immunolabeling, Cai et al. recently developed vDISCO(Cai et al., 2019), an immunolabeling technology in which nanobodies are perfused into the entire mouse body at high pressure to solve the low ratio signal intensity of endogenous fluorescent protein. This technique amplified fluorescent signals enabled visualization of cellular even subcellualr details and quantification of intact mouse body through bone and muscle with single cells resolution, as well as the detection of neurodegeneration in whole mouse body neuronal projections.

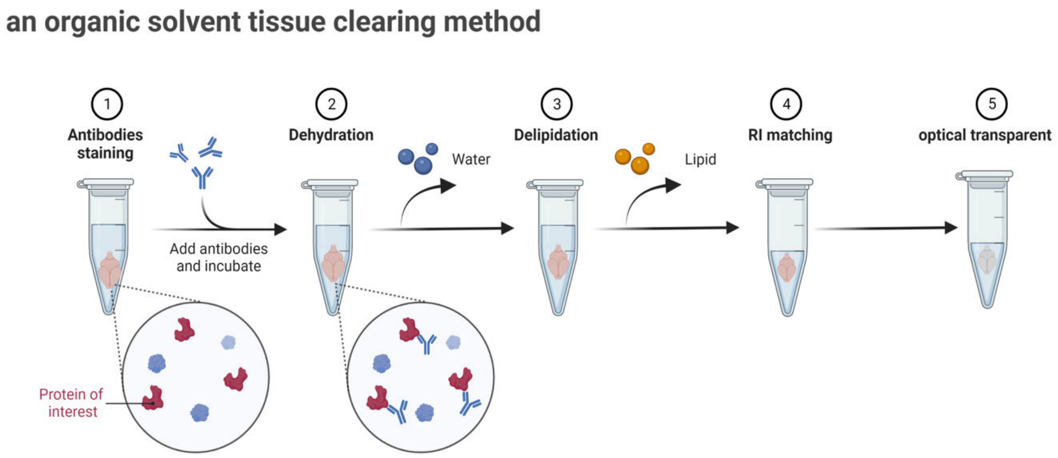

Figure 1. The organic solvent tissue clearing methods and the main feature steps. Organic solvent tissue clearing methods are based on major step of fully dehydration of the tissue and lipid extraction. Then immersion of RI matching organic solvents.

Hydrophilic-based tissue clearing

Researchers have developed hydrophilic-based tissue clearing reagents, that have several advantages over solvent-based tissue clearing reagents, including non-toxic, biosafety, and protein function preservation. Tissue clearing processes use high concentrations water dissolvable hydrophilic reagents as RI matching media (**Figure 2**). Because hydrophilic reagents contain hydrogen bonds whihc can react with tissue components including proteins and water molecules, these bonds can help maintain the tissue's 3D structure and preserve the signal of the FPs.

The method of hydrophilic-based tissue clearing divides into two main categories: simple immersion and delipidation. In simple tissue clearing regents immersion, samples are immersed with the appropriate hydrophilic RI solutions by stepwise conversion to fructose(Calve et al., 2015), 2,20-thiodiethanol (TDE)(Aoyagi et al., 2015), and formamide(Xie et al., 2019). Because direct hydrophilic immersion is performed without detergent permeabilization or dehydration steps, biological samples are neither stretched nor shrunk, thus preserving morphology. For instance, the See Deep Brain (SeeDB) tissue clearing protocol(Ke et al., 2013) using fructose immersion as the RI adaptation component. Ke et al. (2013) discovered that SeeDB was unsuitable for whole organ tissue clearing and was limited to clearing mouse brains several millimeters in size. The updated SeeDB2(Ke et al., 2016) protocol, with a hydrophilic solution with a higher RI, enabled imaging of neural circuits in mouse brains in super-resolution. In 2015, the SeeDB-derived FRUIT tissue clearing method was improved by adding urea to SeeDB and clearing the whole brain of adult rabbits. Later, other RI-matching hydrophilic solutions were used in the formamide-based ClearT2(Kuwajima et al., 2013) tissue clearing method and ScaleS(Hama et al., 2015), which was created by combining urea and sorbitol in the procedures.

By simple immersion, the chemical has the advantage of being simple to use, but after tissue clearing, it does not achieve optimal optical transparency. Therefore, Ueda and his colleagues developed more powerful hydrophilic tissue cleaning agents. They selected amino alcohols that delipidate and decolorize rodent tissue using computational analysis. They discovered more than 1,600 amino alcoholic chemicals in the hydrophilic-based tissue clearing method, named CUBIC. CUBIC(Susaki et al., 2014) is used for various applications, including whole-brain imaging of genes expressed, drug administration, and whole-brain imaging of cancer metastases. By combining the most advanced delipidation (CUBIC-L) and RI-adapting reagents (CUBIC-R)(Matsumoto et al., 2019), the improved tissue clearing method provides higher performance in terms of biosafety and protein antigens preservation.

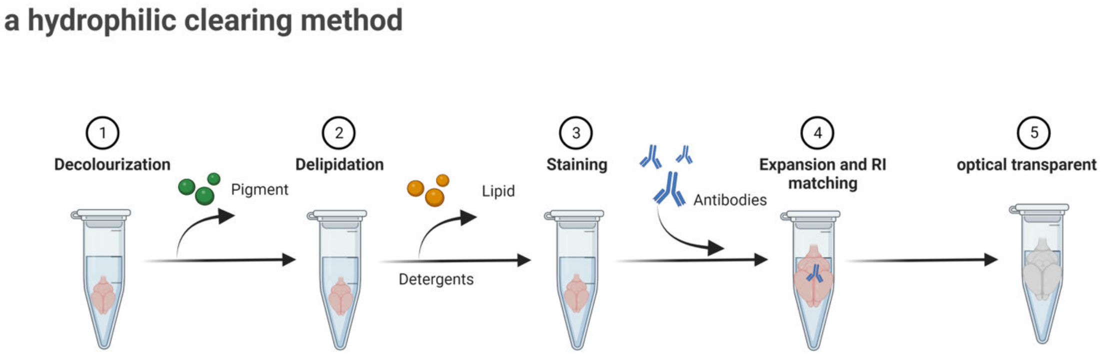

Figure 2. The main features of hydrophilic tissue clearing methods. Hydrophilic tissue clearing methods are relied on water-soluble regents in each step and are generally included decolorization and delipidation steps, and then match the RI in the final step. Some hydrophilic tissue-clearing methods enlarge the tissue size.

Hydrogel embedding tissue clearing

Despite the hydrophilic-based tissue clearing method was used to clear small human tissue samples, the high concentration of detergents in the hydrophilic-based method for clearing tissue would remove some proteins in the tissue. Hydrogel-based methods attempt to solve these problems by embedding the tissue in the hydrogel (**Figure 3**). After embedding in the hydrogel, lipids are removed passively by incubation in detergents for weeks (8% SDS) or rapidly (days) by electrophoresis. The hydrogel is generally composed of a polymer matrix and can protect the biomolecules of the samples under harsh treatment conditions and preserve endogenous fluorescence with good optical transparency. The first reported method for embedding hydrogels is CLARITY(Chung et al., 2013), which is relied on electrophoretic lipid extraction and increases the speed of lipid extraction to overcome fluorescence attenuation more than an organic solvent-based method. However, CLARITY meets the drawbacks of the heating process (electrophoretic CLARITY is performed at 42 °C) that can damage the antigens and cause an expansion for the sample after clearing. Other problems of active CLARITY are the chemicals' toxicity and the long preparation times characterized by loss of epitopes/proteins, resulting in incorrect structural representation. An improved CLARITY method has overcome some limitations of previous protocols, specifically, mouse heart clearing. In addition, it allows visualization of cardiac fibroblasts in uninjured and injured mouse hearts. This technique enabled very high heart tissue transparency, even in ischemic areas(Brenna et al., 2022). The following hydrogel-embedded method, the PACT(Yang et al., 2014), accelerates tissue clearing efficiency by diffusing SDS into the samples with moderate tissue expansion and improved the analyzing of high resolution structural details. PACT not only improves the protection of biomolecules from degradation by using hydrogels but also efficiently preserves endogenous fluorescence. However, the PACT method has a significant drawback: a long preparation time and toxic chemicals for the hydrogel and the lipid removal reagent. Therefore, an updated hydrogel embedding tissue clearing method, the FxClear protocol(Choi et al., 2019), a hydrogel method without active electrophoretic, was developed to remove lipids rapidly and preserve tissue immunoreactivity. The FxClear protocol improved image resolution and fluorescence protein preservation by removing acrylamide from the mouse brain. Nevertheless, using acrylamide removal-based techniques is sometimes more difficult for muscle tissue. Later, a new method, Myoclear(Williams et al., 2019), was developed targeting staining neuromuscular junctions and muscle shapes between healthy and diseased mice.

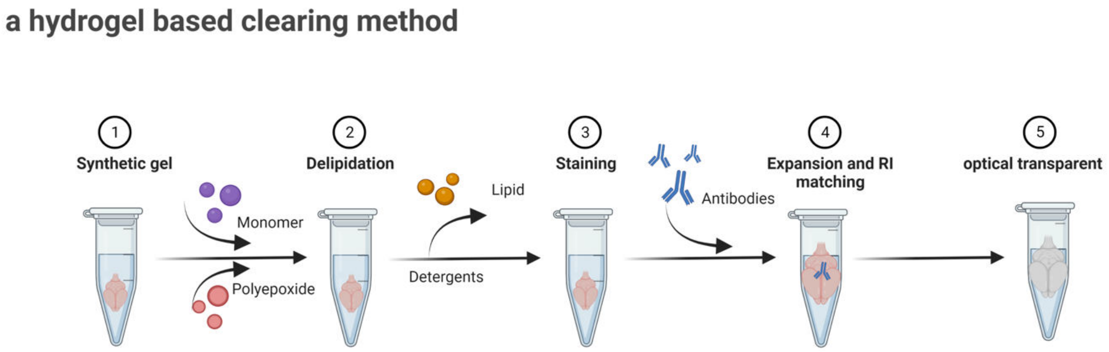

Figure 3. The hydrogel-based tissue clearing methods and their main features. Hydrogel-based tissue clearing methods use monomers and polyepoxide to produce a synthetic gel. Hydrogel-based methods are generally associated with delipidation, staining, expanded tissue size, and RI matching.

2.1.3 Chapter 1.1.3 Application of optical tissue clearing methods for particular human organs

Here is a brief review of different tissue clearing methods for clearing human tissue and the molecular probes used to label human tissue.

Eye

The major challenge of optically clearing the entire human eye is that various protocols cannot eliminate pigment accumulation in the retina. Hohberger et al. used a protocol with a hydrophilic-based clearing method called SeeDB(Hohberger et al., 2017), which makes the sclera and adjacent optic nerve transparent. Further studies on optical clearing of the entire human eye were performed by **Publication II**(Zhao et al., 2020), which is a solvent-based protocol for clearing human organ tissue. The anatomical structures of the human eye cell nucleus were displayed in TO-PRO-3, and LSFM imaged the autofluorescence signals of the intact optic transparent eye structure.

Skin

Histological sections have been the standard method for studying human skin for several decades. However, this approach provides only 2D information because human skin is a complex tissue. Although the multiple layers of human skin cause inhomogeneous light scattering, optical tissue clearing can be used to examine human skin biopsies. Fernandez et al(Fernandez and Marull-Tufeu, 2019) investigated different solvent-based protocols (3DISCO, ethanol-BABB, ethanol-DBE) to clear human skin biopsies and applied the solvent-based 3DISCO tissue clearing method and rhodamine B staining to imaging the entire epidermis under the confocal microscope. Later, Abadie et al(Abadie et al., 2018). Although both 3DISCO and ethanol-DBE were equally rapid in achieving optical transparency of human skin, they were less effective than the ethanol-BABB method, which involved dehydration with ethanol followed by incubation in BABB and provided detailed 3D visualization of skin compartments and appendages.

Bones

Because the bone's refractive index (RI) is approximately 1.60, this would limit the selection of tissue clearing methods, mainly the organic solvent-based tissue clearing methods. Furthermore, the hard tissue of the bone itself would make it challenging to identify the cells and vessels using antibodies or chemical probes. Several methods have recently been developed to clear bone tissue, but without satisfactory results(Tainaka et al., 2018). For example, tissue clearing methods based on hydrophilic reagents, such as CUBIC-R, efficiently clear soft human tissues but not the hard tissues of human organs, especially bone tissues(Greenbaum et al., 2017). Specifically, the bone RI is higher than any hydrophilic-based tissue clearing reagent. Even in the solvent-based tissue clarification methods, uDISCO achieved only partial success in clarifying hard tissues, and the applicant is limited to mouse bones, and its tissue-clearing effect on human bone tissues is not known. Although numerous human tissues have been previously imaged, They are only a few decalcification methods regarding the different types of human bones. Therefore, a focus of our publication was the decalcification step instead of the direct reagent for RI matching with bone tissue. In **Publication I**, we demonstrate the advantages of labeling human bone with chemical probes, and the clearing of the tissue should consist of two main steps: 1) removal of minerals from the bone by decalcification with EDTA and 2) subsequent incubation of the decalcified bone with a validated chemical probe for vascular and nuclear labeling.

Heart

The human heart is one of the body's most vital organs for maintaining blood circulation. The human heart has complex multicellular structures that serve as rigid tissues, making it increasingly difficult to study its 3D anatomy(Litvinukova et al., 2020). Even MRI allows visualization of the 3D structure of human heart tissue, but its limited resolution means it is not the best technique for studying human heart structure(Zerhouni et al., 1988). In contrast, tissue clearing technology provides access to a full 3D cellular resolution of human cardiac tissue that reflects the structure of human cardiac muscle under physiological or pathological conditions(Kolesova et al., 2021). Recently, a variant of the hydrogel-based tissue-clearing method was used to provide 3D imaging of 300 μm-thick myocardial slices free of acrylamide(Perbellini et al., 2017). This method provides 3D information on the collagen content and distribution of cardiac tissue. Because of the limited thickness of the myocardial slices used in this method, the minimum distance required to study the vascular network connecting complex vascular networks with multiple regions cannot be achieved. Therefore, a more advanced tissue sampling method should focus on creating a complete vascular network for the human heart. In **Publication I**, we developed a stepwise tissue sampling protocol to illustrate a 3D vascular network of the entire human heart over long distances (related to **Publication I**).

The vascular network of the human heart, vasa vasorum, a specialized nutrient microvessel implicated in the coronary artery vessel wall, has been suggested for further study of its biology and pathology. Although scientists have tried to study the vasa vasorum in the coronary artery in recent decades, the lack of suitable imaging tools impedes progress. As we described in the **publication I,** we revealed changes of vasa vasorum after atherosclerosis using advanced tissue clearing technology. This technology shortens the timeline of exploring vasa vasorum and provides a high-resolution pattern of adjusting changing vessels in a coronary artery. Here we identified the vasa vasorum of the right coronary artery through an optic transparent post-modern human heart. Vasa vasorum revealed a sparse capillary plexus in the right coronary arteries vessel wall region free of atherosclerosis. Compared with the non-atherosclerotic injury region, we found abundant nutrient vessels surrounding the plaque region. Further analyzing the optic slices from the transparent human heart demonstrated that the rich adventitia vasa vasorum penetrated through the tunica media border and showed capillaries extended to the opposite or uninjured regions. This novel method from our **publication I** enable researchers to investigate crucial questions regarding the response pathology pattern and the role of the vasa vasorum in the pathogenesis of coronary atherosclerosis.

Pancreas

Knowledge of pancreatic anatomy may aid in evaluating pancreatic pathology and promote the development of interventions for pancreatic diseases(Dolensek et al., 2015). Compared with the conventional two-dimensional method of anatomy examination, the application of tissue clearing techniques may provide new insights into the three-dimensional structure and function of the human pancreas(Fowler et al., 2018). Several recently developed tissue clearing methods were applied to human pancreatic tissue to achieve this goal. A hydrogel-based method, PACT, was tested for clearing the human pancreas and found to balance clearing time and morphological preservation in 1–2 mm thick human pancreas sections(Butterworth et al., 2018). Another organic solvent-based method was used to obtain 5-mm thick sections of the human pancreas. To visualize blood vessels in normal pancreatic tissue, this method used the AF properties of collagen and elastin and labeled cytokeratin 19. (Noe et al., 2018). The following method adjusted the RI of the clear solution to 1.52 to better visualize and identify the microenvironment of the human pancreas. This method allowed better light penetration for optical imaging of the microenvironment of islets, and applied to visualize neurovascular networks in 350-μm thick tissue of human pancreas from human patients. In addition, pancreatic ductal adenocarcinoma is associated with marked lymphangiogenesis and the remodeling of lymphatic vessels. Another method enabled to clear 350-μm thick human pancreatic cancer tissue and study 3D remodeling of lymphatic vessels by deep tissue staining. Another advanced tissue clearing method focused on clear thicker human pancreatic cells. This method allowed the imaging of thick pancreatic tissue sections (1 mm) with multifluorescent channels in two to three days, as well as the analysis of several hundred islets(Fowler et al., 2018). However, most of the existing methods for tissue clearing cannot elucidate the entire human pancreas, diminishing the importance of whole-organ imaging for assessing pancreatic anatomy. Using LSFM, we solved this whole-organ imaging problem and volume imaging of the intact human pancreas with the SHANEL method to visualize the entire ductal system in three dimensions (related to **Publications I** and **II**).

Urinary tract

Tissue-clearing protocols have attempted to resolve light scattering in the urinary system and are consistent with enhanced antibody penetration into human kidney tissue. Although most of these approaches have been limited to human embryo size and rodent kidney tissue, one study overcame light scattering in mouse kidney tissue and displayed images of whole glomeruli across the renal cortex(Puelles et al., 2021). Another study, using the passive CLARITY technique, examined metanephric kidney development and an 11-week-old fixed human fetal kidney embedded in an acrylamide hydrogel matrix to achieve optical transparency(Isaacson et al., 2018a). In the following procedures to examine ureteric bud epithelium branching morphogenesis, fetal kidneys were stained with anti-E-cadherin antibodies. Subsequently, this laboratory published another study in which the acrylamide-based hydrogel matrix technologies were applied to investigate the morphological changes in the urogenital tract of the human fetus from the bisexual stage (<9 weeks of fetal age) to gender differentiated stage organs (>13 weeks of fetal age). This laboratory demonstrated that the development of the human genitourinary tract is more complex after labeling the urethral plate, epidermis, urothelium, and dorsal aspect of the vestibular groove in 3D by using LSFM(Isaacson et al., 2018b). However, the major limitation of their laboratory studies, also shared by all previous reports, is that their tissue clearing methods could not be applied to the size of adult intact human kidneys(Isaacson et al., 2018a).

Recently, advanced LSFM with a larger chamber and a longer working distance of the objective has been developed for imaging large human renal tissue. The first step is identifying the optimal labeling method for human kidney structure. For instance, antibodies could be used to label the blood vessel structure of the human kidney, but most labeling experience to date has been with rodent kidneys. Even for labeling mouse kidneys with antibodies of limited size, the advanced CLARITY protocol requires 7–28 days and the iDISCO protocol(Saritas et al., 2019) requires 8–18 days. Furthermore, many of these studies are limited to antibody staining of the surface of renal tissue and do not achieve homogeneous labeling. Optional labeling of human kidney tissue with chemical probes has allowed for homogeneous and in-depth staining of thick human kidney samples. For instance, DNA dyes and large-molecule dye injections can ensure that cells and blood vessels can be distinguished by using different excitation wavelengths in LSFM. Therefore, in our **Publication I**, we took advantage of chemical probes compatible with the organic solvent-based method for tissue clearing and labeling the entire kidney of vessels and cell nuclei. Furthermore, the advantage of the SHANEL pipeline in labeling human kidneys than previous publications is the ability to quantify larger structures, such as human glomeruli, highlighted in **Publications I** and **II**.

Brain

Current tissue clearing protocols for 3D imaging of brain tissue are generally applied to optimally small-volume human brain tissue, resulting in limited new brain structural anatomy finding(Parra-Damas and Saura, 2020). Because the human brain is a complex organ with various organizational forms, a tissue clearing method is necessary to study the macroscopic organization of each brain region and visualize its neural network. The neurons of the various brain regions are distributed differently and form a complex network(Fang et al., 2022). Although some technologies have been developed recently, imaging all of the neurons of representative brain regions or the entire brain is an enormous challenge(Scardigli et al., 2021).

In studies of cleared brain anatomy, little progress has been made in staining human neurons with chemical probes or tissues with antibodies. In contrast, in studies of cerebral vessels(Kostrikov et al., 2021), several options are available in combination with deep tissue staining methods, and providing new anatomy was not achieved in previous studies. At present, we know little about the exact structure of the vasculature aside from its macro distribution in the cerebral cortex(Harrison et al., 2018). Because most tissue clearing techniques combined with LSFM technologies only permit unbiased scanning of human brain tissue in a small area, our understanding of blood vessels in the brain parenchyma has evolved with limited progression. Therefore, given the increasing interest in the role of the vasculature in various human brain diseases, it is time to develop a new method of characterizing the vessels of the human cerebral cortex comprehensively. Compared with other published studies, the SHANEL method provided advanced 3D visualization of cerebral cortical vessels in human postmortem brain tissue stored in formalin for several years. We present human cerebral cortex tissue blocks from aged patients immunized against vascular amyloid deposition stained with fluorescent Congo red. Endothelium vasculature was labeled with Lycopersicon esculentum agglutinin (tomato lectin) (related to **Publication I** and **II**).

In short, with the widespread application of these unbiased human tissue and imaging technologies, more studies will be conducted leading to unexpected discoveries.

2.2 Chapter 1.2 Practical considerations for human tissue clearing and imaging

2.2.1 Chapter 1.2.1 Properties of cleared human tissues

Autofluorescence (AF) and Decolorization

Compared to rodent organs, one of the main characteristics of human organs after tissue clearing is their high AF. Even AF signal provides sufficient information about human tissue morphology, especially ductal or vascular structure, and can be used for atlas alignment(Sartori et al., 1988), but it would reduce the target protein signal-to-background ratio(Weiss et al., 2021). Because of the similarity between the AF units and standard fluorescent probes, even if human tissue perfectly matches RI and is completely optically transparent, strong AF under LSFM can still influence the sufficiency of image quality for analysis. AF occurs in human cells and tissues with a broad spectrum between 450 nm and 650 nm, which is included in the commonly available selection of fluorophores used in deep tissue staining(Beisker et al., 1987). A previous study has demonstrated that AF derives from two major sources: endogenous sources of human structure, such as collagen, red blood cells, lipofuscin, and melanin(Schnell et al., 1999, Monnier et al., 1984), and exogenous influences from chemical interactions during tissue fixation or clearing. Human tissue is more complex than rodent tissue and, in particular, contains more lipofuscin, triglycerides, and lipoproteins(Moreno-Garcia et al., 2018). Furthermore, tissue clearing in human organs requires special chemical treatment procedures that significantly improve AF following tissue clearing.

So far, with several methods and advanced techniques, it is complicated to separate and eliminate AF from human tissue after tissue clearing (**Table 2**)(Weiss et al., 2021). The best way to reduce AF is to remove the blood in human organs by sufficient perfusion, but this is not easy to achieve in human tissue collection from surgical or clinical biopsies. Another practical way would be to select a chemical that effectively removes heme and pigment from human organs. In our publications, we selected amino alcohol as a decolorizing agent to remove heme and effectively reduce AF. Other agents used in heme removal to reduce AF include m-xylylenediamine and N-butyldiethanolamine (Tainaka et al., 2014).

Recent reports have described various methods to overcome AF issues by incubating with some dyes to block tissue illumination(Zhang et al., 2018). Dyes for blocking AF reported in histological studies can also be used in the areas of tissue clearing (Table 2). Sudan black B (SBB) is the most common and efficient dye for eliminating AF(Erben et al., 2016). Although SBB is an effective AF quencher in tissue sections, the pigmentation or extra color brought by SBB would affect the optical transparency of the cleared human tissue and block the penetration of the laser of microscopy. Besides SBB, copper (II) sulfate pentahydrate is known as blue vitriol and reportedly has the function of eliminating AF. Therefore, our newly updated protocol selected different copper(II)sulfate concentrations and tested their ability to eliminate AF. Specifically, after labeling antibodies or chemical probes, the step of copper sulfate (II) incubation should be before clearing the tissue (related to **Publication I**).

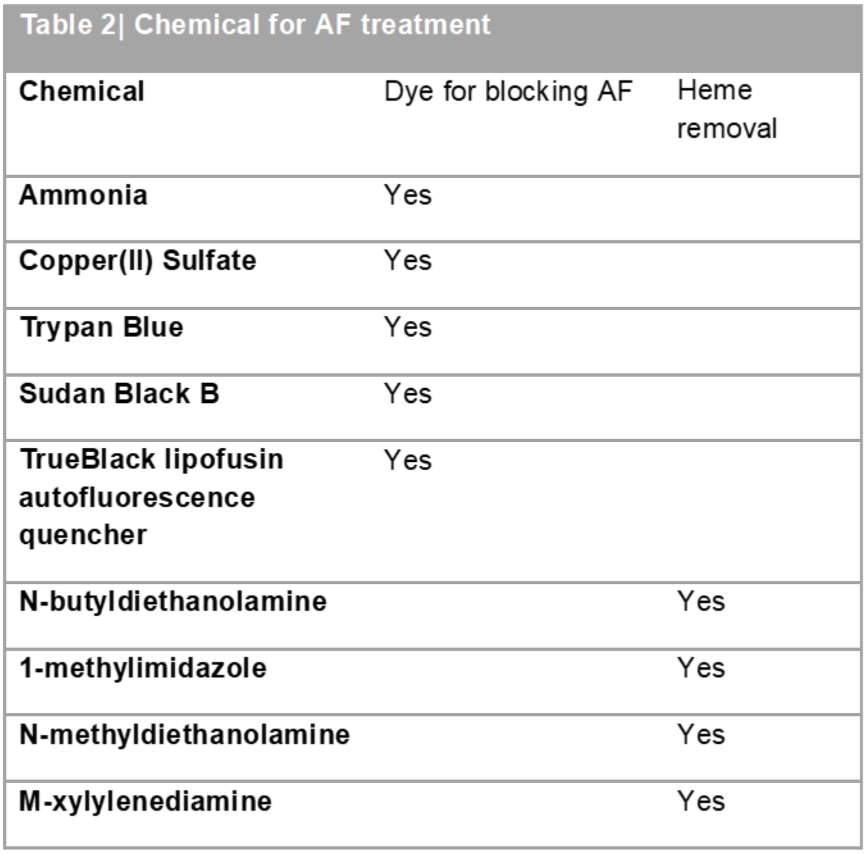

Table 2| Chemical for AF treatment

Chemical	Dye for blocking AF	Heme removal
Ammonia	Yes	
Copper(II) Sulfate	Yes	
Trypan Blue	Yes	
Sudan Black B	Yes	
TrueBlack lipofusin autofluorescence quencher	Yes	
N-butyldiethanolamine		Yes
1-methylimidazole		Yes
N-methyldiethanolamine		Yes
M-xylylenediamine		Yes

Most AF typically emit from 450 nm and 650 nm. One non-dyes blocking way to reduce AF in imaging is to use NIR fluorescence illumination(Jun et al., 2017). The NIR fluorescence of the human sample is very specific to the structures and has lower absorption by hemoglobin and collagens. Because the NIR fluorescence probe penetrates tissue better and has lower absorption of photons by tissue, it is the best choice for deep staining of human tissue and application in tissue elucidation.

Pigment removal

Another practical consideration for human tissue clearing is the pigments from blood or melanin-rich regions. Although one of the significant blood pigments, the heme, can be resolved with some tissue clearing protocols, other strategies and optimizations for removing other human tissue pigments remain missing (Weiss et al., 2021). One of the significant dark color pigments in human skin and eyes is melanin, a UV-protective substance derived from tyrosine(Rzepka et al., 2016). Melanin is insoluble in almost all lipid- and water-based solvents, so its removal can be difficult with existing tissue clearing methods(Chung et al., 2016). Although melanin is resistant to most tissue clearing methods(Konno and Okazaki, 2018), a method of melanin removal incorporating peroxidase into the pretreatment steps has proven effective. For instance, the organic solvent-based method, iDISCO incorporates the H2O2 steps and achieves adequate melanin removal. Recently, some methods for Hydrophilic-based tissue clearing have been developed, such as adapting the CUBIC protocol for pigmented crustaceans and developing an eye pigment-specific protocol(Gurdita et al., 2021). Other chemical treatments, such as acetate buffer or NaBH4, may be helpful for pigment suppression in human tissue staining but require further investigation in human tissue clearing methods.

2.2.2 Chapter 1.2.2 Detergents selection

Characterization of detergents: an overview

Detergents are necessary for dilution and to improve the penetration of chemical probes or antibodies for deep human tissue staining. The classic molecular structure of detergents contains hydrophilic and hydrophobic domains that are well suited for breaking cell membranes(Sadaf et al., 2021). A hydrophobic, nonpolar hydrocarbon moiety (tail) attached to a hydrophilic, polar head group represents the simple structure of detergents (**Figure 4A**). In addition, micelles have hydrophobic cores that can bind to proteins with hydrophobic regions (**Figure 4B**). Based on the structure of detergents, we can observe differences between detergent molecules and phospholipid molecules leading to spherical micelles (**Figure 4C**). During the deep tissue staining experiment, amphiphilic molecules are dissolved in water at the right concentration and temperature. They self-arrange into spherical micelles in a form where the hydrophilic head groups remain outside the water, and their hydrophobic tails remain inside the water. Because detergent molecules and phospholipid bilayers have similar amphiphilic phospholipids found in human cell membranes(**Figure 4D**), the detergent can penetrate and dissolve the membrane.

Another critical feature of detergents is the phase separation at a specific temperature and solubility for micelles at a particular concentration. The aggregation number is a measure of detergent molecules in a micelle which can reflect the detergent ability in penetrate and solubilize membrane proteins. Micelles are observed at a critical micelle concentration (CMC), which is minimum detectable number of detergents in a micelle(Nguyen et al., 2018). At detergent concentrations below the CMC, detergents are present as monomers. At detergent concentrations above the CMC, detergents are presented as micelles and not dissolved in water.

Similarly, the critical micelle temperature (CMT) is the lowest temperature at which micelles form (Chae et al., 2010). When determining the CMC, it is also important to consider the lipophilicity of the head group. In addition, CMCs are generally high when lipophilicity or lipophobicity is low. Therefore, selecting an appropriate detergent should consider the CMC and CMT in deep human tissue staining processes.

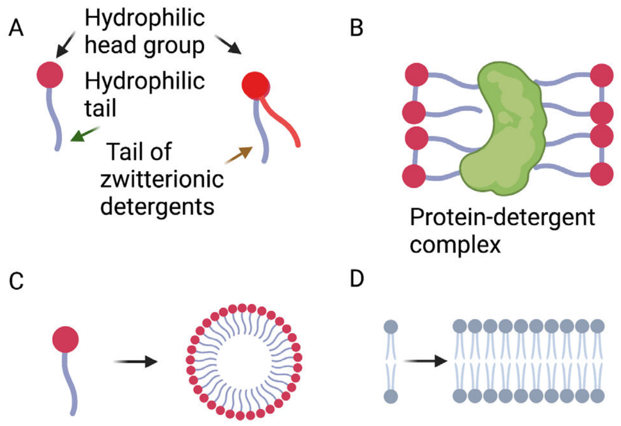

Figure 4. Typical monomer structure of detergents. A: a diagram of detergent molecules. B: Detergents can surround and solubilize hydrophobic proteins. C: Detergents contain a large hydrophilic head group and a long hydrophobic tail in aqueous environment, whereby they can form undissolved spherical micelles. D: Cell membrance phospholipids have matched hydrophobic tails, which make them easy to make phospholipid bilayers in aqueous solutions.

There are different kinds of detergents applicated in tissue clearing research, so we highlighted the most commonly used ones. Detergents have similar hydrophobic domains, but their charged head groups are different. Common detergents divide into three categories based on their charged head groups properties (**Table 3**): ionic (anionic or cationic), nonionic, and zwitterionic. Here are some common laboratory detergents and essential information on their selection and application.

Table 3. Classification of detergents used in human tissue clearing.

Type	**Chemicals**
Ionic	Sodium dodecyl sulfate (SDS), deoxycholate, cholate, sarkosyl
Nonionic	Triton X-100, digitonin, tween 20, tween 80
Zwitterionic	CHAPS
Chaotropic	Urea

The ionic detergent

Ionic detergents usually have a higher CMC and are more potent for penetration. Basically, they contain a anionic or cationic charged head comparing to other detergents. Because ionic detergents contain charged head groups and cannot be removed in the tissue, even using ion exchange chromatography. Furthermore, some of their properties may change as the ionic strength of a buffer varies (e.g., the CMC can decrease drastically if the NaCl concentration quickly reaches 500 mM).

The anionic detergent of SDS is a widely used detergent in the tissue clearing field, especially in the CLARITY-based tissue clearing methods. Proteins are bound to SDS in a ratio of about one SDS molecular pair to two amino acids. (weight to protein ratio 1.4:1)(Han et al., 2021). For this reason, SDS negatively charges all proteins in a tissue sample, regardless tissue protein isoelectric point. As soon as the negatively charged SDS molecules bind, size-based protein separation is possible (Chung et al., 2013). Since SDS disrupts both active proteins and protein-protein interactions, it cannot be used when active proteins are needed. Furthermore, SDS can be affected at low temperatures, and the presence of potassium salts exacerbates this effect.

Nonionic detergent

Unlike ionic detergents, nonionic detergents have hydrophilic head groups that are not charged. They are mild detergents since they break lipid related bonds but not protein-protein interactions. Therefore, many membrane proteins can be kept in their native and

and non denature. However, different nonionic detergents would have hetergenity influence to the protein itself, so it is advisable to perform a preliminary study to select the ideal detergents for human tissue clearing.

The Triton family

The Triton X-100, Triton X-114, and Nonidet P-40 (NP -40) are the nonionic detergents that belong to the Triton family. In addition, their polyethylene glycol (PEG) based head groups vary in size, and the average number of monomers per micelle varies (9.6, 8.0, and 9.0, respectively) (Tao et al., 2010). These detergents have low CMC values, so they are not easily removed from tissues. The nonionic detergent Triton X-100 is derived from polyoxyethylene and is widely used for many tissue clearing experiments.

The Tween family

The nonionic detergents Tween-20 and Tween-80 contain a fatty acid ester moiety and long polyoxyethylene chains (Yang et al., 2019). Because they have a more low CMC compared to the Triton family and are generally work as more gentle detergents that do not interfere with antigen activity. If you compare the difference between Tween 20 and Tween 80, Tween 20 contains lauric acid, while Tween 80 contains oleic acid (Ouadah et al., 2019). In immunoblotting and ELISA, Tweens are routinely used as detergents to minimize non-specific binding of antibodies and permeabilize cell membranes (Greenwood et al., 2019). However, they are not normally used as detergents in deep tissue staining penetration buffers.

The zwitterionic detergent

Zwitterionic detergents contain hydrophilic head groups with equal numbers of positive and negative charges(Luche et al., 2003). Therefore, they do not have a charge. The detergents penetration ability of these products is more potent than those in nonionic detergents. Zwitterionic detergents are commonly known as CHAPS (3-(4-oxopropyl) ammonio)-1-propanesulfonate(Banerjee et al., 2013). CHAPS is an efficient detergent due to the high CMC (6 mM at room temperature). In isoelectric focusing and 2D electrophoresis, it is commonly used at 2%–4% concentration, but in our **Publication I** and **II**, we applied 10% concentration for better penetration in the human organs. CHAPSO differs from CHAPS in which it contains one more polar head group, allowing it to solubilize hydrophobic molecules(Liscia et al., 1982). Therefore, CHAPSO may be a new candidate to be used in integral membrane proteins-rich human organs.

Selection of detergents for deep tissue staining

A detergent with a high CMC should be selected for deep tissue staining. A good detergent must lyse the cell membrane and be suitable for subsequent application(s). Some considerations for detergent selection before experimental design, for example, some detergent would affect the solubilized protein in native and denatured forms(Rabilloud, 2009, Na et al., 2022). It is impossible to recommend an ideal detergent for every application, and even results may vary within the same application. Therefore, preliminary experiments are often required to find the best detergent after selecting the target tissue or protein for staining. A combination of detergents may be optional for better penetration. The working solution must be prepared fresh to avoid hydrolysis and oxidation of detergents.

2.2.3 Chapter 1.2.3 Compatible probes and antibodies selection

Chemical probes selection

LSFM measures the structure of human tissue or organs based on the 3D distribution of fluorophores within a given viewing volume. Therefore, using specific fluorophores to stain and label human samples is crucial for human tissue clearing. In mouse tissue clearing, gene transfection with fluorescent proteins was widely used to visualize cellular structures in tissues, but it has limited applicability and cannot be transferred to human tissues(Marx, 2016). Compared with current genetic methods, using toxin tracers in rodent tissues is still not viable for labeling post-modern human tissues(Susaki and Ueda, 2016, Lerner et al., 2016). Due to the shortcomings of commonly used methods for labeling human tissues with antibodies that have a short penetration distance, it was necessary to develop a new strategy for labeling human tissues. Therefore, using chemical probes represents a uniquely reliable and primary approach for deep labeling of human tissue. Hundreds of dyes with smaller molecular sizes than antibodies have been developed to visualize various fluorophore-labeled targets(Lai et al., 2017). The spectral properties of conventional fluorescence microscopy can also be used in LSFM.

Selecting an appropriate chemical probe for human tissue clearing is crucial. An ideal fluorescent chemical probe can be used for human tissue labeling and will survive after the chemical treatment steps of tissue clearing. Before beginning human tissue labeling, it is crucial to study the physicochemical processes that occur during tissue clearing and their impact on choosing the most appropriate chemical probes. Here, I highlighted the characteristics of chemical probes in the field of tissue clearing, especially the chemical probes compatible with organic solvent-based steps of tissue clearing.

Several steps in the tissue clearing procedure influence the choice of chemical probes. The commonly used tissue fixation method is a formaldehyde-based crosslinking method, which can increase the nonspecific binding of amine probes(Tainaka et al., 2014). Organic solvent-based tissue methods alter the physicochemical properties of the tissue mainly through delipidation and dehydration steps, which involve multiple chemical buffers and may alter the efficacy of the chemical probes(Treweek et al., 2015). The delipidation steps remove the lipids in the cell membranes of human tissues, making the lipid dyes incompatible with most types of human tissues if the chemical probes do not contain cross-linkable groups(Liu et al., 2017). During dehydration, the chemical solution for tissue clearing can also dissolve the chemical probes by competing for the affinity of the binding site with human tissue. Furthermore, the change of pH in the organic buffer decreases the stability of the binding of the chemical probes with the human tissue and leads to a low noise signal in the cleared human tissue. Because of the dilapidation and dehydration steps in human tissue clearing, the RNA is also not well preserved in the organic tissue clearing method, so selecting RNA staining probes is not recommended(Evers et al., 2011).

Another criticism of using chemical probes is the high AF of human tissue after tissue clearing owing to the high content of lipofuscin in the aged tissue, hemoglobin in the red blood cells, and pigments in human tissue. Despite the chemical solution with hydrogen peroxide, the hemoglobin-related AF background can be reduced during the preprocessing of the tissue preparation(Treweek et al., 2015). However, the remnants of lipofuscin still absorb the laser spectrum of about 450-550 nm wavelength and reduce the noise signal in imaging procedures. To solve the problem of AF background, the wavelengths of chemical probes should ideally be in the near far red.

Therefore, an ideal chemical probe for human tissue labeling should be specific to the target structure or cellular components, have a near far red-shifted fluorescence spectrum, a high signal-to-noise ratio, and be suitable in various tissue clearing methods(Umezawa et al., 2014, Yuan et al., 2013). Furthermore, this selected chemical probe is commercially available and compatible with other multiple-staining chemical probes or antibodies. To this end, we sought different chemical probes and tested them for compatibility with SHANEL protocols. First, we looked for chemical probes suitable for the cell's most common structure, the nucleus. The nucleus contains a lot of DNA, so we chose nucleic acid probes to label common DNA molecules as DNA is packaged in chromatin. The mechanism of the nucleic acid probes for DNA binding is based on the DNA structure, which contains the base pairs, the phosphoribosyl backbone of the nucleic acids. In addition, the structure of the DNA furrow. When the chemical probe targets the DNA in the nucleus, it forms π-π-stacking interactions or electrostatic interactions with the phosphate ester backbone, which is unique and highly specific(Shi and Ma, 2012). As a result of the formation of homo- or heterodimers between the chemical probes and DNA, the probes can further increase their binding affinity and produce essentially irreversible bis-intercalation(Miao et al., 2022). Since there is not a single nucleic acid probe that is easily compatible with all types of tissue clearing methods, it is recommended to search and test the working capability of the nucleic acid probe before formal experiments. Even though the nucleic acid probes of DAPI and Hoechst are widely used in many fluorescent labeling methods, they are still not suitable for labeling large amounts of human tissue because their emission wave length is short and can be a problem in cleared human tissue imaging in which AF is more evident(Kolesova et al., 2021), and the image depth also would be limit by the short-wavelength from DAPI and Hoechst(Sovenyhazy et al., 2003). Also, previous publications have indicated that organic solvent-based tissue clearing methods are incompatible with DAPI, Hoechst dyes, and DRAQ5(Renier et al., 2014). One of the reasons may be that a non-aqueous environment can reduce the binding affinity of these chemical probes to DNA. In this **Publication I** and **II**, we used propidium iodide (PI), a membrane-impermeable DNA binding dye with 668 Da that shows bright red when bound to RNA or DNA. Because PI is a fluorescent dye that intercalates with DNA and can be used for cell nuclease staining, we used PI to label the nuclei of human tissues. After the cell nuclei have been stained with PI, the cell distribution can be viewed with an LSFM. Similar to PI, To-pro-3 is a DNA intercalator that is impermeable to the cell membrane. Alternatively, nuclei of all cell types can be sorted with nuclear staining using To-pro-3(Russo et al., 2009). To-pro-3 is a near far-red fluorescent dye that binds to nuclear and chromosomal counterstain. Since To-pro-3 is a carbocyanine dye with an excitation wavelength of 642 nm and emission wavelength of 661 nm, it exhibits far-red fluorescence(Hoffman et al., 2010), sufficient to separate the background channel and the target signal channel. These two DNA-binding chemical probes (PI and To-pro-3) are effective nucleic acid staining agents that are compatible with other multiple labeling and antibody labeling chemical probes for fluorescent immunostaining of fixed human tissue. Therefore, we selected the PI and To-pro-3 for most of our cell nuclear staining in human organs.

Beyond cell nucleus staining, most initial applications of tissue clearing originate from the CNS. Because the CNS is remarkably rich in lipids than other tissues, it is easier to achieve homogeneous transparency after tissue clearing(Parra-Damas and Saura, 2020). Tissue clearing field structural chemical probes are also primarily generated in the CNS area. For instance, this Nissl stain is commonly used to identify the neuronal structure and highlight the essential structural features of neurons in the CNS tissue. The primary application of Nissl staining is in the histological brain sections, which capture the texture of the neuronal tissue by aligning the density Nissl body(Heilingoetter and Jensen, 2016). The Nissl body is a specific structure that shows the endoplasmic reticula structure within neurons; when the Nissl body disappears, it can be used as a marker for the injured neuron when it disappears. Several cationic probes, including cresyl violet, methylene blue, and neural trace, can stain Nissl bodies, which contain much of the ribosomes(Lanciego and Wouterlood, 2011). However, not all chemical probes have the same binding affinity to the Nissl body when combined with the organic-solvent-based tissue clearing method. How the organic solvent solution affects the interaction between the chemical probe and the Nissl body is poorly understood. After searching different publication, one of the fluorescent Nissl stains called NeuroTrace has been developed with a range of fluorescent spectra and have good staining quality when applied in the tissue clearing method(Shan et al., 2022). Similar to conventional Nissl stains, NeuroTrace dyes is now widely applied in tissue clearing as they have comparable signal of noise in deep tissue staining. By using SHANEL technology combined with NeuroTrace for 3D Nissl staining of human brain slice and volumetric imaging, we stained and imaged the neural cells in slices of adult human brain (related to **Publication I** and **II**).

Detailed histologic studies of pathologic neurons in big volumes of human brain tissues are lacking. One of the pathological changes in neurodegenerative diseases of amyloid deposits(Jakob-Roetne and Jacobsen, 2009). Amyloid deposits accumulate insoluble, misfolded proteins that form fibrils and are correlated with disease progression and microglial activation in specific brain regions(Querfurth and LaFerla, 2010). The progressive formation of amyloid plaques and vascular deposits of the amyloid beta peptide is a pathological hallmark of AD(Ross and Poirier, 2004). Large-volume imaging and quantification of amyloid plaques could give more disease-related structural changes in the onset and development of neurodegenerative diseases(Gupta and Goyal, 2016). Because of the spatial distribution of amyloid deposits in the whole human brain, it is time-consuming to section different small portions of human brain tissue using conventional histological techniques.

Furthermore, the unbiased examination method for brain tissue is being developed in the field of tissue clearing, so the next step is to find a compatible chemical probe for staining amyloid deposits is the goal in human brain tissue clearing field(Zhang et al., 2015, Cui et al., 2011, Cui et al., 2014). In our **Publication I** and **II**, we tested two chemical probes for staining amyloid plaques, Methoxy-X04(Jahrling et al., 2015) and Congo Red(Liebmann et al., 2016), for 3D imaging and quantification in human brain slices. Although staining with Congo red might slightly affect the optical transparency of human tissue after clearing, the signal-to-noise ratio of staining amyloid plaques is still bright and strong enough to detect human amyloid plaques, so these dyes are not limited in their application in the field of human tissue clearing. In addition to only staining amyloid plaques in human brain tissue, we have also showed cell nuclei staining with chemical probes to detect cells surrounding the amyoid plaques.

Not only nucleic acids, neuronal cell bodies, and disease-associated protein aggregates, but also mapping vascular structures using chemical probes remains an essential contribution to the human organs tissue clearing field. Recently, some fluorescent dyes have been reported to be suitable for artery-specific labeling(Shen et al., 2012), but only when used in conjunction with the hydrophilic-based tissue clearing method. One possible way is to label the global vascular network targeting carbohydrates(Roth, 2011) widely expressed in the endothelium and peristyle. Because these two cell types are most abundant in the brain vasculature, we chose lectin(Mazzetti et al., 2004, Porter et al., 1990), which targets the carbohydrates for staining the human brain vasculature in our SHANEL protocol. In an organic solvent-based tissue clearing protocol by SHANEL, we confirmed the compatible use of lectin staining for the target ligands that were not denatured in the multiple treatments (related to **Publication I** and **II**).

In our SHANEL protocol, we test several compatible chemical probes and give a chemical probe selection guidline for scientists who consider using SHANEL techniques.

Antibody compatibility

The antibodies used in the human tissue clearing protocol must be compatible with the chemical treatment condition in the various steps. This point is crucial when considering selecting the organic-solvent-based tissue clearing method. This is because the antigens in human tissue and the antibodies used in the protocol are also affected by the pH, different charges, and dehydration in the tissue-clearing treatment steps(Molbay et al., 2021).

Determining available antibodies compatible with tissue clearing chemicals is similar to the conventional immunochemical staining method(Park et al., 2018). The principle of the immunochemical staining method is to bind an antibody to the protein of interest and then precipitate the antibody-protein complex with the secondary antibodies by fluorophore conjugation(Magliaro et al., 2016). Due to antibody incompatibilities, which always occur in the multiple chemical treatments of deep tissue staining, we need to perform the antibody validation step and test the compatibility of antibodies in preliminary studies(Susaki et al., 2020). For instance, an antibody validation step was performed to test the compatibility of antibody binding to antigen when the pretreatment step with methanol is included in the iDISCO + method(Renier et al., 2014). It is optimal to cut the human tissue with an original thickness of approximately 1.5 mm and use this human tissue section to test antibody compatibility. After comparing the antibody concentrations, the amounts of antibodies were optimized, and their compatibility was ensured in preliminary tests. We summarize the tested antibodies that were compatible with the SHANEL protocol table(related to **Publication I**).

2.2.4 Chapter 1.2.4 How to image human organs and data handle

Sample mounting

Whole organ or whole human specimens imaging is essential to preserve 3D integrity. Accordingly, to keep the 3D integrity imaging, managing the LSFM-associated sample mounting has become an important practical issue(Richardson et al., 2021). The LSFM sample chamber-based instruments differ from the conventional mounting methods in slide scanning(Weiss et al., 2021). Mounting the different tissue clearing methods for human samples meets the challenge with sample holders' size not fitting to the whole cleared human tissue and might not be compatible with different refract index chemical buffers. Therefore, these challenges must be addressed before starting the tissue clearing method design and developing a practical mounting method. In order to ensure stable samples for long-term and accurate positional scans, embedding methods must provide complete spatial control over the samples. Furthermore, mounting methods should minimize the illumination path and allow light detection through the tissue (related to **Publication I**).

Image compression

LSFM is a powerful method for imaging transparent human organs with high spatial and temporal resolution (Voie et al., 1993). However, this volume scanning of a human organ typically generates terabytes of complex image data containing information from 3D and serveral color channels. Handling image data, especially data processing, can become a challenge at the next stage of biological questioning and discovery requiring efficient data processing solutions for data management prior to analysis(Amat et al., 2015). Therefore, data management must be included the processes of correcting technical errors, reconstructing complex geometries, preparing them for visualization, and file size compression (Ellenberg et al., 2018) (related to **Publication I**).

Here we compare various image compression formats. We focused on widely used formats that provide lossless compression because researchers typically wanted to store an unaltered version of their data and make it comparable for use with various analysis or visualization software. The JPEG 2000 image format is one of the most widely used in reducing the image size. Although the JPEG 2000 image format includes a process of 3D compression, few applications have implemented it(Amat et al., 2015, Conrath et al., 2007). Furthermore, it is difficult to efficiently process all of the encoding and decoding steps of the JPEG 2000 image format, making it difficult to meet the requirements of modern, high-quality multicore workstations. In contrast, HDF5 is another iamge format for reducing image data size(Gibbs et al., 2021). HDF5 provides lossless data compression and the ability to store data in blocks for quickly access to regions of interest. However, HDF5's interface does not parallelize writes, which has a negative impact on performance. Because tiff files are widely used in various visualization programs, we showed in our SHANEL protocol how LZW tiff compression could be used to reduce data size. LZW-Tiff compression compresses image data layer by layer but is still efficient in finding arbitrary regions of interest in large multidimensional cleared human tissue image sets (related to **Publication I**).

Data visualization

Following the processing steps of stitching and volume fusion for cleared human organs image sets, appropriate rendering tools are a powerful option for visualization(Richardson et al., 2021). These rendering tools allow users to understand the detailed characterization of biological structures, complex geometries and complex morphogenetic cascades of multiple human organs. The easiest step for rendering large volumes is to find Fiji's open-source plugin(Schindelin et al., 2012). For instance, the Fiji ClearVolume plugin can visualize large datasets during acquisition(Royer et al., 2015). Other open-source plugins from Fiji for rendering or creating animations using the 3Dscript plugin: the TeraFly extension(Bria et al., 2016) for Vaa3D(Peng et al., 2010). BigVolumeViewer, another Fiji plugin, is an enhanced version of BigDataViewer that enables volume rendering regardless of dataset size(Pietzsch et al., 2015). Alternatively, UCSF Chimera is another open source option(Pettersen et al., 2004, Goddard et al., 2005), as it supports the rendering of 3D images and has already been used to visualize LSFM data. In addition to free open-source software, the commercial software solutions are widely available, offering an user friendly interface and commercial graphical operating software integration. Commercial software would be more suitable for rendering large human organs on a stable platform.

To date, there is much software available for visualizing image stacks. The continued development of software frameworks such as open-source image processing in parallel with adapting advances in microscope technology has resulted in comprehensive data processing solutions. Many software modules for image data acquisition are open source, but image stacks visualized with commercial software are more accessible (Kermany et al., 2018, Prahst et al., 2020). Examples of this software are Imaris (Bitplane), Amira (FEI), Zen (Zeiss), Leica Application Suite (Leica Microsystems), Huygens (SVI) and Arivis Vision4D (Arivis). Regarding the large volume of human organs, Arivis Vision4D (Arivis) is the friendliest and most widely used software. Therefore, we selected Arivis Vision4D for volume stitching in our SHANEL protocols (related to **Publication I**).

2.2.5 Chapter 1.2.5 Prospective of human tissue clearing

Although we have shown some successful applications of human tissue clearing methods for various tissues and organs, and the effectiveness of human tissue clearing methods has been greatly improved in recent years, there is still room for improvement of human tissue clearing methods in practice. One of the general practical problems with imaging cleared human tissue is that it can be scanned with relatively low image resolution based on the working distance of the light sheet microscope and the image depth, which makes it challenging to analyze various cellular processes in 3D. Therefore, large-area and fast-LSFM innovations are necessary to allow new imaging applications. In addition, we still need to improve a thorough comprehend of the biophysical and biochemical principles of human tissue underlying tissue clearing processes and as well as appropriate solutions for labeling, imaging, and data analysis. Particularly, we would require faster and homogeneous antibodies, DNA and RNA labeling methods for large human tissue, more accurate, and more user-friendly algorithms for images stitching, human organ atlas generation, and structure mapping. In addiction, a standard 3D atlas of human organs should be combined with single-cell RNA sequencing and proteomics to gain more spatial and omics knowledge about a whole human organ. Finally, developing a machine learning-based algorithm for higer speed and more accurate diagnosis and clarification of 3D human tissue histopathology using tissue clearing methods would be crucial for significantly improving clinical applicants.

3. Summary (in Englisch)

Clearing human tissues is a complex, multi-step process that most laboratories are not well-equipped to reproduce or troubleshoot without proper guidance. Specifically, it involves a sequence of tissue processing steps, optical clearing, imaging with specialized microscopes, and data analysis – all of which need to be optimized separately. Therefore, I set out to create a detailed protocol for human tissue clearing that includes the critical steps of the methods for a laboratory working with a specific human sample to demonstrate reproducibility. My **Publication I** provides a comprehensive, detailed step-by-step protocol for human organ tissue clearing. Specifically, I describe the SHANEL protocol for intact human organ tissue clearing. It is a scalable tissue clearing protocol combined with labeling chemical probes or antibodies for various human organs or tissues. I have shown the results of representative cleared human organs, such as the pancreas, kidney, brain, spleen, heart, and lung. In addition, I have extended the application to include human hard tissue with bone. The protocol is compatible with labeling cell nuclei, amyloid plaques, and vessels for different kinds of human organ labeling. This method is also suitable for staining antibodies in human tissues or biopsies, which increases its adaptability in biomedical research. After the human organs or tissues are labeled, **Publication I** provides the detailed steps of imaging the transparent human organs or tissues using LSFM and later efficiently processing the whole raw images dataset with easy-to-use software and visualization in 3D. Because imaging whole human organs generates terabytes of image data, the pipeline described in **Publication II**, which takes advantage of deep learning algo-rithms, can quickly and accurately analyze large datasets of 3D whole organ images. It provides information on using deep learning approaches to achieve accuracy and speed in quantifying human brain cells. After showing the whole pipeline of intact human organ labeling in **Publication I**, and **Publication II**, I investigated mammalian organs' complex structure and identified the spatial distribution of key targets by labeling them with chemical probes or antibodies. For example, we use high-performance LSFM to record a complete map of the islets in a transgenic pig pancreas and reconstruct the images in 3D. Overall, these two publications provide steps to map intact human organs with cellular resolution, and machine-learning-assisted automated analysis, paving the way for future mapping of intact organs and providing opportunities to expand our knowledge of human organ anatomy.

4. Zusammenfassung (deutsch)

Das Clearing menschlicher Organe ist ein komplexer Prozess mit vielen Schritten, den die meisten Labore nicht ohne detaillierte Anleitung reproduzieren oder optimieren können. Die Schritte zum Permeabilisieren und Verarbeiten der Gewebeproben sind besonders schwierig zu optimieren, da die Optimierungsschritte oft anders ablaufen als bei herkömmlichen Immunfärbungen.

Daher habe ich ein detailliertes Protokoll für das Clearing menschlicher Gewebe erarbeitet, das die kritischen Schritte der Methode darlegt, und für Labore aufarbeitet, die schon mit menschlichen Gewebeproben arbeiten, aber noch kein Clearing durchführen. Meine **Publikation I** stellt ein umfangreiches, detailliertes Schritt-für-Schritt-Protokoll für das Clearing menschlicher Gewebeproben mittels des SHANEL-Protokolls dar. SHANEL ist ein vielseitiges Protokoll zum Clearing menschlicher Gewebeproben, das auch die gleichzeitige Anfärbung mittels chemischer Farbstoffe oder Antikörpern ermöglicht. In der **Publikation I** zeige ich die Anwendung für verschiedene repräsentative menschliche Organe, unter anderem für die Bauchspeicheldrüse, Niere, Hirn, Milz, Herz, und Lunge. Das Protokoll erlaubt das Anfärben von Zellkernen, Amyloid-Plaques, und Blutgefäßen mittels chemischer Marker, und erlaubt zusätzlich das Anfärben spezifischer Ziele mittels fluoreszenter Antikörper. SHANEL kann sowohl auf menschliche Gewebeproben als auch auf Biopsien angewandt werden, was die Nützlichkeit für Biomedizinische Forschung erhöht. **Publikation I** stellt auch detaillierte Anleitung für die nachfolgenden Schritte bereit, in denen die angefärbten und transparenten menschlichen Gewebeproben mit einem Lichtblattmikroskop aufgenommen werden können, und die so erzeugten Datenmengen mit einfach zu benutzender Software verarbeitet und in 3D visualisiert werden können.

Dieses Bildgebende Verfahren erzeugt eine sehr detaillierte digitale Repräsentation der Gewebeprobe, die dann mehrere Terabyte pro Probe umfasst. Um diese Datenmengen einfach verarbeiten zu können, präsentiere ich in **Publikation II** eine Pipeline mit Deep-Learning-Algorithmen, die diese großen Datenmengen schnell und akkurat verarbeiten kann. In der **Publikation II** zeigen wir dies durch die Quantifizierung von Zellen im durchsichtigen Menschenhirn. Außerdem erforschen wir in dieser Publikation die komplexe Organstruktur verschiedener Säugetierorgane und identifizieren die räumliche Verteilung wichtiger Ziele mittels chemischer Farbstoffe und spezifischer Antikörper. Beispielsweise benutzen wir SHANEL und Lichtblattmikroskopie, um die Verteilung von Langerhans'schen Inseln in der gesamten Bauchspeicheldrüse von transgenen Schweinen aufzunehmen, und daraus eine vollständige 3D-Ansicht zu generieren.

Insgesamt stellen diese beiden Publikationen einen Fortschritt in der Erforschung intakter menschlicher Organe mit zellulärer Auflösung dar. Durch die Kombination von Clearing und neuartigen Maschinenlern-Analysetechniken und die sorgfältige Dokumentation machen wir das Clearing menschlicher Gewebeproben auch für andere Labore zugänglich und schaffen die Möglichkeit, unser Wissen über menschliche Anatomie zu erweitern.

4. Paper I

nature protocols

PROTOCOL

https://doi.org/10.1038/s41596-022-00712-8

Check for updates

Scalable tissue labeling and clearing of intact human organs

Hongcheng Mai[1,2,3,6], Zhouyi Rong[1,2,3,6], Shan Zhao[1,2,3,6], Ruiyao Cai[1,2], Hanno Steinke[4], Ingo Bechmann[4] and Ali Ertürk[1,2,5]✉

Advances in tissue labeling and clearing methods include improvement of tissue transparency, better preservation of fluorescence signal, compatibility with immunostaining and large sample volumes. However, as existing methods share the common limitation that they can only be applied to human tissue slices, rendering intact human organs transparent remains a challenge. Here, we describe experimental details of the small-micelle-mediated human organ efficient clearing and labeling (SHANEL) pipeline, which can be applied for cellular mapping of intact human organs. We have successfully cleared multiple human organs, including kidney, pancreas, heart, lung, spleen and brain, as well as hard tissue like skull. We also describe an advanced volumetric imaging system using a commercial light-sheet fluorescence microscope that can accommodate most human organs and a pipeline for whole-organ imaging and visualization. The complete experimental process of labeling and clearing whole human organs takes months and the analysis process takes several weeks, depending on the organ types and sizes.

Introduction

Three-dimensional (3D) mapping of the human organs at cellular resolution and generating reference maps of organs across ages or diseases represent the common objectives of diverse consortia including Human Biomolecular Atlas Program (HuBMAP)[1,2], Human Cell Atlas[3], Human Tumour Atlas[4] and LungMap[5]. Traditional histological techniques of slicing, staining, imaging and 3D reconstruction of the cellular details of biological tissue pieces are challenging to scale up to large human organs. For example, mapping one intact adult human brain using such traditional methods took years of tedious work, and the lengthy process resulted in mechanical distortion and accidental loss of sections of tissue[6]. While improvements are constantly being made in the instruments and methods for iterative image analysis of multimodal imaging of human organs using PET/MRI, these modalities are still limited by low resolution and the inability to probe cellular and molecular parameters.

In recent years, extensive biomedical research in neuroscience[7–12], development[13] and cancer[14,15] has substantially benefited from the optical tissue labeling and clearing methods that bypass the major problems of histology. Especially, clearing and imaging of whole adult mouse bodies has opened a holistic examination window into physiological and pathological systems in an unbiased way[9,14]. However, human organs obviously are much larger in size and, owing to the effects of aging, contain more complex tissue components, which limit the post-staining methods that can be applied to human organs compared with organs from months-to-year-old rodents. Therefore, achieving whole human organ transparency has been challenging, despite numerous trials on slices[11,16–19]. Hence, we developed a full pipeline for whole human organ labeling, clearing, imaging and 3D map reconstruction at cellular level, which implemented a new tissue labeling and clearing technology termed SHANEL and an advanced volumetric imaging system using a commercial light-sheet fluorescence microscope (LSFM)[20]. This pipeline can easily be adopted in laboratories, within routinely available reagents and equipment (Fig. 1).

---

[1]Institute for Tissue Engineering and Regenerative Medicine (iTERM), Helmholtz Center, Neuherberg, Munich, Germany. [2]Institute for Stroke and Dementia Research, University Hospital, Ludwig-Maximilians University Munich, Munich, Germany. [3]Munich Medical Research School (MMRS), Ludwig-Maximilians University Munich, Munich, Germany. [4]Institute of Anatomy, University of Leipzig, Leipzig, Germany. [5]Munich Cluster for Systems Neurology (SyNergy), Munich, Germany. [6]These authors contributed equally: Hongcheng Mai, Zhouyi Rong, Shan Zhao.
✉e-mail: erturk@helmholtz-muenchen.de

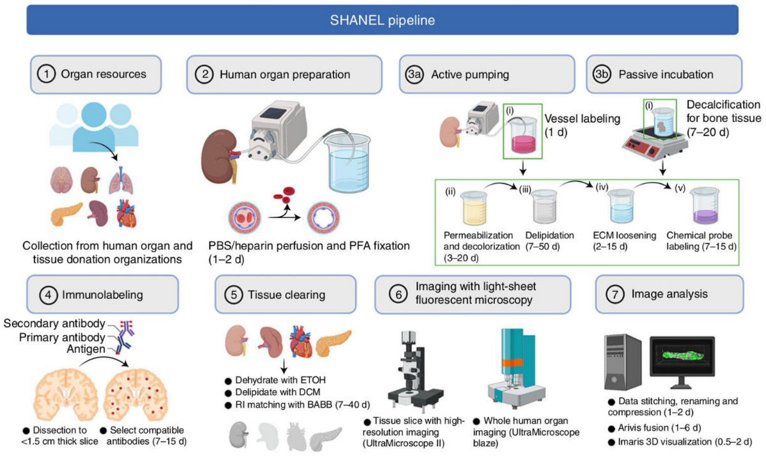

Fig. 1 | Overview of SHANEL pipeline. SHANEL is composed of seven parts. After human organs and tissue are collected (Part 1), they are prepared for blood removal and fixation (Part 2). The next step is performed by active pumping (Part 3a) or passive incubation (Part 3b), based on whether the organs are intact or not. Samples are then subjected to permeabilization, delipidation, ECM loosening and labeling with chemical probes. If antibodies compatible with the SHANEL protocol are used, the organ of interest should be dissected into slices less than 1.5 cm thick for immunolabeling (Part 4). Samples are then dehydrated, delipidated and matched for RI, until they become transparent (Part 5). Imaging of whole human organs is performed in an UltraMicroscope Blaze LSFM, and images of tissue slices are captured with an UltraMicroscope II LSFM at high resolution (Part 6). The data are stitched, volume fused, and rendered in a 3D visualization (Part 7).

Development of the SHANEL protocol

Clearing, labeling and imaging of human organs is difficult to implement in practice owing to several challenges. In Table 1, we delineate the key challenges encountered during the time-consuming endeavor of human organ processing and the ways in which these problems could be addressed.

Perfusion and fixation of intact organs

To preserve human organs rapidly and uniformly in a life-like state, we introduced an active perfusion system to deliver 0.01 M phosphate-buffered saline (PBS)/heparin and 4% paraformaldehyde (PFA) solutions into whole organs through the vascular network before the organs are harvested if major blood vessels are available (Fig. 2 and Extended Data Fig. 1a). The advantages of this step include washing out as much remaining blood as possible, preventing clot formation by maintaining circulation of the vascular system and achieving faster tissue fixation than through passive immersion. The organs are dissected carefully to preserve intact anatomical shapes and connect the main arteries with exogenous tubes for later experiments. Alternatively, human samples could be passively fixed in 4% PFA or 10% formalin buffer to covalently crosslink proteins. It is worth mentioning that human organ and tissue donation organizations such as the International Institute for the Advancement of Medicine are reliable resources that provide transplantable organs with intact vascular systems and detailed donor information.

Organ clearing strategy

Among the hydrophilic reagent-based[21–24], hydrogel-embedding[19,25–27] and hydrophobic reagent-based[9,10,13,14] tissue clearing methods, we chose to work with hydrophobic reagents in the SHANEL pipeline. An important advantage of hydrophobic tissue clearing is sample shrinkage, enabling us to accommodate and image large organs using an LSFM. Ethanol is employed to remove the water inside of human tissue, by increasing ethanol concentration in a stepwise manner. Dichloromethane (DCM) is used to extract the remaining lipids and ethanol, after which the tissue is mostly composed of fixed proteins. In the end, the relatively homogeneous human tissue is rendered transparent by

Table 1 | Challenges of labeling, clearing and imaging human organs

Problem	Solution
Uncontrollable variables from human organ resources related to the premortem state and postmortem delay	Selecting reliable human organ and tissue donation organizations
Extremely complicated chemical compositions in terms of lipidome complexity, myelin density, lipofuscin accumulation and nonsoluble, nonenzymatic collagen changes	An efficient detergent permeabilization is necessary to render the human tissue accessible to reagents traveling end-to-end through it
Residual blood clots due to delay in postmortem dissection	Setting up an active perfusion system to deliver 0.01 M PBS/heparin before 4% PFA fixation to reduce the blood remaining in the vessels as much as possible
Strong autofluorescence at visible wavelengths (400–700 nm) from lipofuscin	Chemical treatment (e.g., $CuSO_4$, Sudan Black B, $NaBH_4$) or photobleaching has been reported to reduce autofluorescence. We found that $CuSO_4$ was very efficient in reducing autofluorescence while being compatible with labeling
Advanced transgenic or virus tracing techniques for fluorescent labeling not being applicable to human organs	Selecting chemical probes or antibodies with high binding specificities and affinities for labeling human organs
Increased costs of reagents and dyes due to the size of human organs	Using a cheaper NMDEA and CHAPS mixture to achieve permeabilization and decolorization
Volume of large-sized human organs exceeds the limit of volumetric imaging	Developing fully automated light-sheet microscopes with larger chamber size to cover the range from entire mice to most human organs
Massive imaging datasets are generated and need to be stored and analyzed	Using LZW TIFF compression and large-capacity drive (for example, high-capacity Network-attached storage connected to a network that is accessible by both computers dedicated to microscope imaging and data analysis)

immersing it in BABB solution (benzyl benzoate:benzyl alcohol 2:1, v/v). BABB solution has a refractive index (RI) of 1.56, which is the same as that of the cross-linked proteins.

Imaging system

In general, organs cleared with hydrophobic reagents will shrink ~30% in volume[10,20]. However, commercially available microscopes such as the LaVision UltraMicroscope II system (chamber size of 72 × 74 × 35 mm, sample traveling range of 10 × 10 × 10 mm in *X*, *Y*, *Z*) or ZEISS Lightsheet 7 (sample size of 10 × 10 × 20 mm) cannot hold large cleared human organs such as an intact eye (size of 30 × 30 × 30 mm). To overcome this limitation, together with Miltenyi Biotec we developed a prototype UltraMicroscope (chamber size of 250 × 90 × 70 mm) (Fig. 3). This microscope is now commercialized by Miltenyi Biotec as UltraMicroscope Blaze (chamber size of 129 × 51 × 64 mm, sample travel range of 50 × 24 × 23 mm)—a fully automated light-sheet microscope for imaging large cleared samples covering the range from an entire mouse to most human organs.

Permeabilization and decolorization reagents

Efforts to label and clear human brain tissue by screening thousands of delipidation and decoloring chemicals[28] or chemicals that increase tissue permeability[17,19] have already shown the difficulties related to incomplete tissue transparency, time-consuming procedures and limited antibody penetration. Given that aged human tissue is composed of dense and intricate hydrophobic and hydrophilic molecules, we hypothesized that efficient detergent permeabilization is necessary to render the human tissue accessible to reagents traveling end-to-end through it. Detergents are amphiphilic, possessing both hydrophilic and hydrophobic properties, and form micelles in solution that can interact with molecules of the tissue. Traditional detergents such as ionic sodium dodecyl sulfate (SDS) or non-ionic Triton X-100 (4-(1,1,3,3-tetramethylbutyl) phenyl-polyethylene glycol), carrying typical 'head-to-tail' chemical structures, are inefficient at permeabilizing sturdy human tissues because the micelle sizes of these detergents are too big to enter deep inside the tissue. We identified CHAPS (3-[(3-cholamidopropyl) dimethylammonio]-1-propanesulfonate) as a powerful candidate to completely and quickly permeabilize intact human organs, as it forms much smaller micelles with molecular weight of 6,150 Da. CHAPS renders the cellular and extracellular matrix of aged tissue within intact human organs more permeable, thus improving the accessibility of reagents. To remove

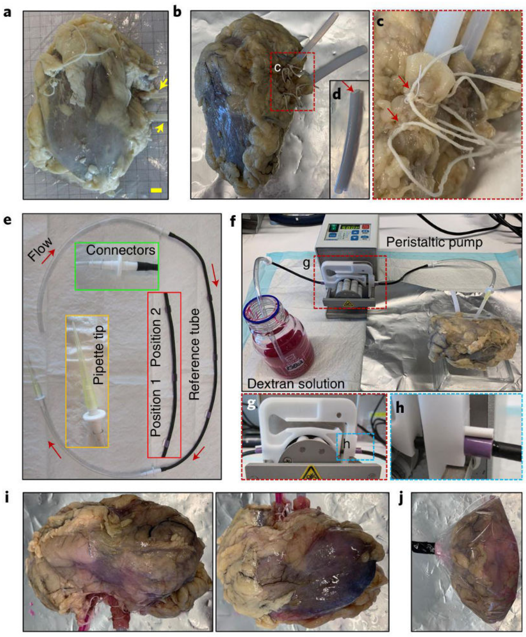

Fig. 2 | Blood vessel labeling with dextran solution by active perfusion. **a**, Photo of dissected human kidney with inserted tubing (yellow arrows). Scale bar, 1 cm. **b**,**c**, The original tubing was replaced with a PTFE (chemical-resistant, anti-adhesive, biocompatible) tube (**b**) and tightly fixed by double rope-fastening (**c**; red rectangle in **b**). **d**, The inserted nozzle of the PTFE tube was cut at an angle to ensure smooth insertion into the organ. **e**, A set of connecting tubing containing a black pump reference tube in the middle, two colorless PVC tubes at both ends, three tube connectors and a pipette tip. Switch between position 1 and position 2 to avoid breakage of the reference tubing. The red arrows indicate the flow circulation direction. **f**, Blood vessel labeling with dextran solution using a pump perfusion system. **g**, Rotation of the wheel enables solution flow into the kidney. **h**, The correct way to fasten the black pump reference tube to the cassette is shown. **i**, Photos of human kidney after dextran labeling. **j**, The dextran-labeled human kidney was sealed in a plastic bag.

the red color of remaining blood clots, we screened diverse heme-eluting chemical analogs that are compatible with CHAPS. Analogs bearing ethanolamine structures have been shown to improve decolorization effects in the presence of CHAPS[20]. Potential candidates such as *N*-butyldiethanolamine[28] and *N*,*N*,*N*′,*N*′-tetrakis (2-hydroxypropyl) ethylenediamine (Quadrol)[24] have been proven to be efficient in decolorizing tissues, but they are at least twice as expensive as *N*-methyldiethanolamine (NMDEA) (the price of NMDEA is ~30€/L). Considering that intact human organs require large amounts of decolorization chemical agents, we decided to use a NMDEA and CHAPS mixture to achieve cost-efficient permeabilization and decolorization. Still, the volume of the reagents consumed in a single step of handling an intact human brain is ~5–6 L, and the total cost of CHAPS/NMDEA solution is ~1,800€ (ref. [20]).

Labeling

Small molecular dyes (<1–2 kDa) or large antibodies (~150 kDa) provide fluorescence contrast of sufficient signal-to-background ratio to identify specific structures of human tissue. DNA or RNA chemical probes show high binding specificities and affinities to the nucleic acid of cells across a wide range of fluorescence spectra (e.g., DAPI, Hoechst in the blue–green range; JO-PRO-1, propidium iodide (PI) in green–red range; TO-PRO3, short-wavelength infrared (SIR) in the infrared range)[29]. However, primary or secondary antibodies conjugated to chemical fluorochromes cannot penetrate and label more than 1 cm deep into adult human organs due to the probes' big sizes. Hence, we introduced chemical pretreatments to loosen the cellular and extracellular matrix. First, a solvent mixture of DCM:methanol (2:1, v/v) was used to extract the hydrophobic lipids inside the tissue,

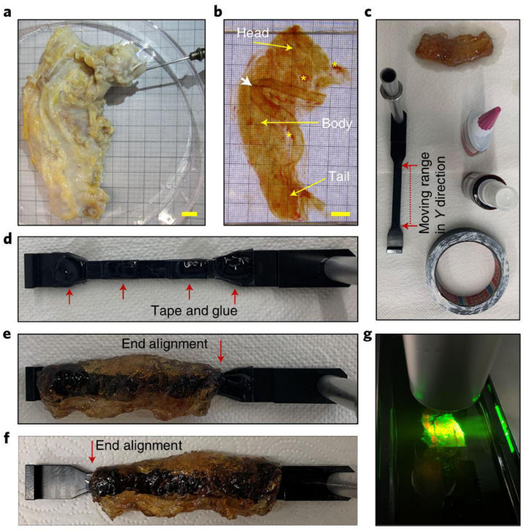

Fig. 3 | Organ mounting and imaging with light-sheet microscopy. a, Photo of human pancreas before clearing. Scale bar, 1 cm. **b**, Photo of transparent human pancreas after PI cell nuclei labeling and clearing, showing mesenteric artery (white arrow) and lymph nodes (yellow asterisks). Scale bar, 1 cm. **c**, The mounting of an organ on a sample holder requires glue and black tape. The red arrows show the boundaries of the moving range of the holder in the *Y* direction. **d**, The sample holder was wrapped with four sections of tape, and a drop of glue was placed on top of each section. **e**, An example of sample positioning with alignment to one end of the holder to cover one sample edge. **f**, Another example of sample positioning with alignment to the other end to cover the other sample edge. **g**, The mounted human pancreas was illuminated by light-sheet microscopy.

which would prevent the free movement of hydrophilic labeling reagents dissolved in buffer[30]. Second, the tissue was subjected to acetic acid for partial hydrolysis of intertwined collagen by cleavage of the noncovalent intra- and intermolecular bonds[31]. This process maintains the collagen chains intact, but the cross-links are cleaved. Third, guanidine hydrochloride buffer was employed to extract the proteoglycans of the tissue in dissociative conditions[32]. After these chemical extraction steps, the tissue matrix became accessible to both small-molecule dyes and large antibodies at a depth range of several centimeters. Cell nuclei in intact human pancreas were perfused and labeled with PI (Fig. 4). Vasculature in multiple human organs was labeled with dextran solution (Fig. 5). SHANEL is also compatible with passive incubation of dye and antibodies to stain PFA-fixed human tissue up to several centimeters size range (Fig. 6). As we have previously demonstrated, 1.5 cm cubic human brain pieces were successfully labeled with primary and secondary antibodies to reveal microglia (e.g., Iba1) and dopaminergic cells (e.g., tyrosine hydroxylase)[20]. Antibodies conjugated with large protein dyes (e.g., phycoerythrin) also fully labeled more than 1 cm cubic human kidney and lung pieces to reveal cytoplasmic (e.g., catalase), extracellular (e.g., collagen IV) and membranous (e.g., cytokeratin 19) structures of tissue (Extended Data Fig. 2 and Table 2).

Image analysis

With the prototype or commercial UltraMicroscope Blaze, it is possible to scan the intact human eye, kidney, thyroid and pancreas by mosaic imaging. The scanning time depends on the size of the sample, the percent overlap between images of the mosaic, the number of scanning channels and the size of the *Z* step (Extended Data Fig. 3). Consequently, terabytes of large data can be generated from a single organ. Software such as Fiji, Arivis, Imaris and Photoshop can be used to handle the large datasets for 3D reconstruction and movie generation with a standard lab workstation (e.g., >256 gigabytes of RAM and terabytes of storage space) (Extended Data Figs. 4–6). However, quantitative analysis of such large datasets can be difficult and imprecise using such software, which in general relies on simple strategies such as filter-based normalization, thresholding or watershed algorithms. Recently, deep learning approaches[14,20,33] have shown superior performance in quantification of

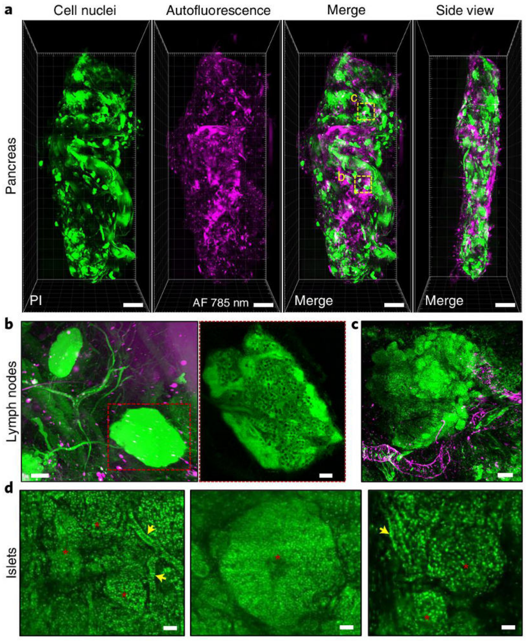

Fig. 4 | 3D reconstruction of human pancreas. **a**, 3D reconstruction of human pancreas imaged by light-sheet fluorescence microscopy showing the PI-labeled cell nuclei (green) and autofluorescence at 785 nm (magenta). Scale bar, 1 cm. **b**, Zoomed 3D reconstruction showing the blood vessels and lymph nodes (red rectangle). Scale bars, 1 mm and 200 µm, respectively. **c**, Higher magnification of the endocrine portion region in the human pancreas is zoomed in using a 12× light-sheet microscopy objective and reconstructed in 3D by Imaris software. Scale bar, 200 µm. **d**, Various pancreas islets can be easily identified in the 3D-reconstructed endocrine portion region on the basis of their specific shapes (red asterisks). Intralobular ducts (yellow arrows) can be located near the islets. Scale bars, 50 µm, 50 µm and 30 µm, respectively.

large-scale data in terms of processing accuracy and speed. It is anticipated that 3D human organ mapping could be greatly advanced with a full exploitation of tissue clearing and imaging combined with deep learning technologies.

Applications of SHANEL

Mammalian skeletal bones protect delicate internal organs, contain most of our body's calcium supply and are especially difficult to label and clear. Expanding deep tissue labeling, clearing and imaging of bones using SHANEL would greatly benefit investigations of the 3D geometric features of bone volume and cells. In addition to soft tissues such as bone marrow, bones contain hard mineral-dense regions that are deposited with calcium-bearing hydroxyapatite crystals embedded in a collagen matrix. The calcium content considerably increases the optical scattering of bone[34]. EDTA has been demonstrated as an effective decalcification reagent in previous studies[35,36]. Similarly, Tainaka et al. developed a carbonated hydroxyapatite-based screening system to identify potent decalcification chemicals compatible with tissue clearing and found EDTA combined with imidazole showed superior effects[28]. Hence, we conducted decalcification of bones using 20% EDTA at 37 °C before SHANEL tissue labeling and clearing, as shown with examples of human skull pieces and pulvinar soft tissue inside the joint cartilage surface surrounded by bones (Fig. 7). As human bones are much thicker and harder than mouse ones, a much longer decalcification time—in the range of weeks to months—is needed to achieve the desired softness. Alternatively, reagents composed of strong, mild or weak acids (e.g., nitric acid, formic acid, hydrochloric acid, chromic acid, etc.) can be used for faster decalcification. For example, 5% nitric acid is an option for rapid decalcification yielding acceptable tissue integrity and antigenicity[37,38].

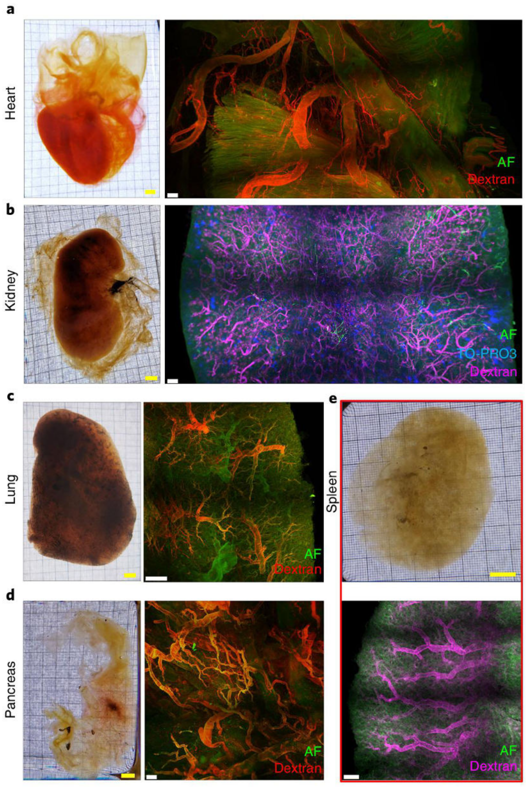

Fig. 5 | SHANEL of human organs with perfusion of dextran vessel labeling dye. a, Human heart after performing the SHANEL protocol. 3D reconstruction shows blood vessels of the coronary artery (red) and myocardium that can be imaged in autofluorescence at 488 nm (AF, green). Scale bars, 1 cm and 2 mm, respectively. **b**, Human kidney after SHANEL. The structure of glomeruli can be seen in dextran-labeled tissue. TO-PRO3-labeled cell nuclei are shown in blue. Scale bars, 1 cm and 2 mm, respectively. **c**, One lobe of human lung was cleared and stained with dextran. Bronchus can be seen in AF. Scale bars, 1 cm and 2 mm, respectively. **d**, Image of human pancreas. Ductal structures are shown with AF, and vasculature is labeled with dextran after SHANEL. Scale bars, 1 cm and 2 mm, respectively. **e**, Human spleen after SHANEL. The fine structure of the splenic artery is marked with dextran, and the other blood vessel structures are visualized with AF in Imaris. Scale bars, 1 cm and 2 mm, respectively.

SHANEL tissue clearing technology has been successfully applied to organs from other mammalian species such as pig brain and pancreas, and is compatible with vDISCO immunostaining[20]. This enables imaging large mammalian organs in which fluorescent proteins such as GFP, YFP, mCherry and tdTomato are expressed. Since transgenic zebrafish, rat, mouse, pig and macaque with fluorescent protein expression in specific organs have been developed, SHANEL could readily be adopted to clear and image organs from diverse organisms. To combine vDISCO immunostaining with SHANEL organ clearing, we recommend that the organs are first actively perfused or passively incubated with the mixture of CHAPS and NMDEA to permeabilize and decolorize tissue. Afterwards, vDISCO immunostaining process is used via perfusion/incubation with the chosen nanobody in a solution of 1.5 vol% goat serum, 0.5 vol% Triton X-100, 0.5 mM of methyl-β-cyclodextrin, 0.2 wt/vol% *trans*-1-acetyl-4-hydroxy-L-proline and 0.05 wt/vol% sodium azide in PBS. Finally, the organs are ready to be cleared by SHANEL reagents. We anticipate that, after CHAPS and NMDEA treatment, nanobody/antibody immunolabeling and SHANEL tissue clearing could be applied to diverse mammalian species to investigate broad biological questions. In cases where antibody-based tissue labeling fails owing to inability of large antibodies to cross through whole organs, nanobodies that are ten times smaller than conventional antibodies could provide a more viable alternative.

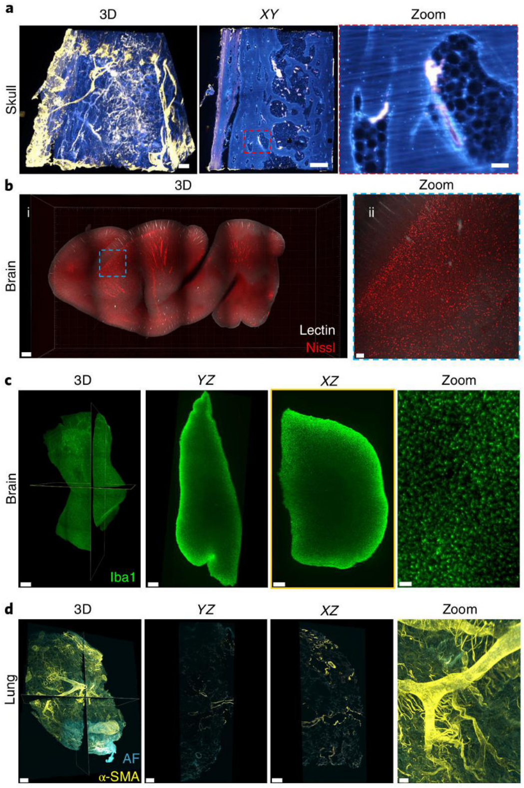

Fig. 6 | SHANEL of human tissues by passive incubation. a, Skull labeled with lectin (blood vessels, yellow) and PI (nuclei, blue); details of blood vessels and cell nuclei can be seen in *XY* view. Scale bars, 1 mm, 1 mm and 100 μm, respectively. **b**, Brain slice labeled with lectin (blood vessels) and Neurotrace Nissl stain. Scale bars, 2 mm and 300 μm, respectively. **c**, Human brain tissue labeled with Iba1 antibody. Penetration of antibody can be verified in the *YZ* and *XZ* view cross-sections, details of microglia can be seen in the magnified *XY* view. Scale bars, 1,000 μm, 700 μm, 500 μm and 40 μm, respectively. **d**, Lung tissue is labeled with α-SMA antibody, and AF shows morphometry of the bronchial tree and acinar structure. *YZ* and *XZ* views, and magnified *XY* view are also shown. Scale bars, 700 μm, 500 μm, 500 μm and 150 μm, respectively.

Although the SHANEL tissue labeling and clearing method was developed for intact human organs, it also works for small tissue pieces, for example, on human biopsies[20]. In general, biopsy samples are small in size and suitable for the application of the passive SHANEL labeling and clearing method.

Comparison with other methods

In the last years, a diverse array of methods for labeling and clearing of human organ pieces has been developed, including CLARITY[17,39], OPTIClear[16], MASH[18], CUBIC[28], SWITCH[40], SHIELD[11] and ELAST[19]. CLARITY and OPTIClear take months to clear fixed human brain tissue pieces (<5 mm thickness). MASH explored the small-molecule fluorescent dye labeling and clearing of human brain cortex (<5 mm thickness) by modifying the iDISCO protocol. Other methods are applicable to 3D imaging of human myocardial tissue[41], lymph node and lung pieces (<1 cm^3) (ref. [42]). SWITCH allowed multiple rounds of antibody labeling in 100-μm-thick human brain sections. On the basis of the SWITCH method, SHIELD used a tissue transformation strategy to stabilize a 2-mm-thick human brain slice via intramolecular epoxide linkages to prevent degradation. ELAST enabled human

Table 2 | Dyes and antibodies compatible with SHANEL protocol

	Supplier	Cat. no.	Dilution	RRID
Hoechst	Invitrogen	H3570	1:1,000	—
PI	Invitrogen	P3566	1:1,000	—
TO-PRO-3	Invitrogen	T3605	1:1,000	—
Neurotrace Nissl	Invitrogen	N21483	1:1,000	—
DRAQ5	Thermo Fisher	62251	1:1,000	—
Methoxy-X04	Tocris	4920	100 μM	—
Dextran	Sigma	52194	5 mg/ml	—
Congo Red	Sigma	C6277	10 μM	—
Lycopersicon esculentum (tomato) lectin	Vector	DL1174	1:200	—
Lycopersicon esculentum (tomato) lectin	Vector	DL1178	1:200	—
Antibodies				
Tyrosine hydroxylase	abcam	ab112	1:200	AB_297840
Ionized calcium binding adapter protein 1 (Iba1)	Wako	019-19741	1:500	AB_839504
Neuropeptide Y	abcam	ab30914	1:200	AB_1566510
Myelin basic protein	Atlas	AMAb91064	1:200	AB_2665784
Laminin	Sigma	L9393	1:200	AB_477163
Alpha-smooth muscle actin	Sigma	C6198	1:500	AB_1840528
CD8	abcam	ab237709	1:200	—
Angiotensin-converting enzyme 2 (ACE2)	Invitrogen	PA5-20039	1:200	AB_11154831
Conjugated antibodies				
Atto647N-conjugated anti-GFP nanobooster	Chromotek	gba647n-100	1:1,000	AB_2629215
Collagen IV	Miltenyi	130-122-866	1:100	AB_2857566
Catalase	Miltenyi	130-123-367	1:100	AB_2857591
Cytokeratin 19	Miltenyi	130-125-272	1:100	AB_2857769
Antibodies tested on mouse tissue				
Peripheral-type benzodiazepine receptor	abcam	ab109497	1:500	AB_10862345
Cleaved caspase 9	CST	9509	1:500	AB_2073476
Caspase 9	abcam	ab184786	1:500	—
Gama-H2AX	Invitrogen	14-9865-82	1:500	AB_2573048

brain tissue (<5 mm thickness) antibody labeling and clearing by mechanically stretching tissue–hydrogel hybrids.

For the first time, SHANEL technology achieved the labeling and clearing of intact adult mammalian organs as large as several cubic centimeters, including human brain, pig brain, pig pancreas, human kidney, human thyroid[20], human heart, human pancreas, human lung and spleen (Fig. 5). The key step of the SHANEL technology relies on the permeabilization and decolorization by CHAPS/NMDEA solution. The whole process can be conducted by passive incubation or active perfusion, depending on the availability of major vessels for external connection to commercialized pumps. Active perfusion permits scaling up the process to multiple organs, with general lab equipment available in most molecular biology labs, and no special expertise or training required to implement. It is preferred to perform active perfusion for large adult organs, in order to speed up the process to a reasonable period (e.g., 1.5 months for human kidney, 4 months for human brain). The timeline for each step varies case by case depending on the specific organ. Even a pair of kidneys from the same donor could be different in size, hardness, amount of blood clots and pigments accumulation. It is important to ensure that each step—permeabilization and decolorization, delipidation, cellular and extracellular matrix loosening and labeling, dehydration and RI matching—has been fully completed.

Overview of the protocol

SHANEL provides a flexible platform to achieve whole or partial organ labeling, clearing, and imaging at a cellular level in diverse human and animal organs (Fig.1, Extended Data Fig. 7). The pipeline includes the following main stages: (i) preparation of fixed organs by perfusion or passive

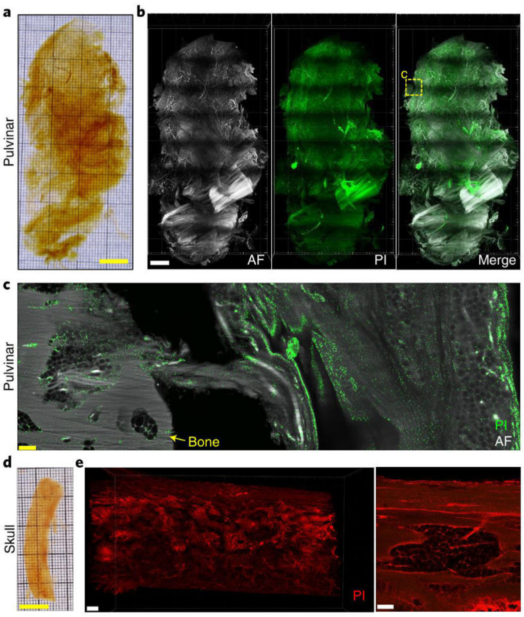

Fig. 7 | Passive incubation, clearing and 3D reconstruction of human pulvinar and skull. a, Photo of transparent human pulvinar after PI cell nuclei labeling and clearing by passive incubation. Scale bar, 1 cm. **b**, 3D reconstruction of human pulvinar imaged by light-sheet fluorescence microscopy showing autofluorescence (AF) at 488 nm (gray) and PI-labeled cell nuclei (green). Scale bar, 1 cm. **c**, *XY* section view of pulvinar showing the connection between bone tissue and the pulvinar fibrofatty tissue. Scale bar, 150 µm. **d**, Human skull bone after PI cell nuclei labeling and clearing. Scale bar, 1 cm. **e**, The human skull bone imaged by light-sheet microscopy (left) and confocal microscopy (right). Scale bars, 500 µm and 200 µm, respectively.

incubation, depending on the donor (Steps 1–5); (ii) sample pretreatment, including optional steps such as decalcification and blood vessel labeling (Steps 6–10); (iii) labeling with chemical probes or antibodies (Steps 11–18); and (iv) tissue clearing and imaging with light-sheet microscopy (Steps 19–39).

Expertise needed to implement the protocol

We would recommend researchers with a biological, medical or human anatomy background or with previous experience in handling commercial light-sheet microscopes to implement this protocol. Experience using Fiji, Imaris and Arivis software, will aid in mastering the image analysis pipeline more quickly.

Limitations of the current SHANEL pipeline

Like most of the tissue clearing methods, the SHANEL tissue labeling and clearing protocol includes a delipidation step, which is not compatible with labeling using fluorescent lipophilic dyes, such as DiI. One possibility to overcome this limitation is using modified DiI analogs, such as CM-DiI, SP-DiI or FM 1-43FX, that could be covalently attached to tissue proteins during aldehyde fixation. These dyes would adhere to the cellular membranes and proteins, even after lipid clearing[43].

Another issue that we have to take into consideration is the fact that blood clots and lipofuscin cause strong autofluorescence in human samples. The accumulation of lipofuscin is associated with the process of aging[44], and its presence complicates the analyses of specific fluorescence labels. It has been reported that chemical treatment[45–47] (e.g., $CuSO_4$, Sudan Black B and $NaBH_4$) or photobleaching[19] can reduce or eliminate autofluorescence, without adversely affecting the targeted labels. We found that $CuSO_4$ was very effective in reducing the lipofusin autofluorescence while being compatible with labeling. However, owing to the natural blue color of $CuSO_4$ solution, the sample could turn light blue after treatment depending on the concentration of $CuSO_4$ solution and would partially absorb the laser light energy used during imaging. Therefore, there is a compromise of fluorescence signal-to-background ratio when using $CuSO_4$ to decrease the autofluorescence signal. In the future, it would be valuable to identify a colorless chemical for effective removal of autofluorescence in the SHANEL protocol.

Furthermore, the validation of new antibodies, nanobodies or dyes before their application within large organs is an additional necessary step. Human organs have to be pretreated with diverse chemicals to loosen the extracellular matrix (ECM) to allow the antibody or nanobody to travel inside. These chemicals could potentially affect the binding of the antibody or nanobody to its target antigen epitopes. Nevertheless, positive staining after performing the SHANEL protocol indicates that the antibody target is well preserved, and specificity is confirmed by comparing the staining pattern with previous results obtained using traditional immunostaining techniques (e.g., in tissue slices). A well-accepted way of quickly selecting an antibody that is sensitive, specific and compatible with SHANEL is to choose an antibody listed in the top-cited ranks in a searchable antibody database[48] (https://www.citeab.com/). Even commercially available antibodies/nanobodies that have been subjected to rigorous in-house validation for other applications need to be tested for compatibility with SHANEL. To test these antibodies, human organs firstly go through all pretreatment steps of CHAPS/NMDEA, delipidation and ECM loosening in SHANEL, then are subjected to a traditional slicing technique (e.g., cryostat) to generate lots of thin sections (e.g., 10–50 μm). We use these sections to test the product lot, and optimize the working concentration and staining conditions. An antibody that provides a good signal in tissue sections has a good chance of being compatible with SHANEL in intact organs. For a list of labeling reagents confirmed in our lab, see Table 2.

Although the SHANEL tissue labeling and clearing technology can turn human organs as large as the intact brain transparent, current LSFMs are limited in the size of organs they can accommodate. Owing to imaging chamber size limitations, the LaVision light-sheet microscopy can image a maximum sample size of 4 × 12 × 1.7 cm, in *X*, *Y*, *Z*, respectively. For volumetric imaging of whole organs with long-working-distance objectives, in particular, the current commercial light-sheet microscopes have poor resolution in *Z* (available resolution 5 μm), which inevitably leads to non-isotropic volumetric images. To reduce the influence of non-isotropic volumetric images in light-sheet microscopy, recently developed light-sheet microscopes such as MesoSPIM are integrated with a moving-waist beam that increases resolution, especially in the *Z* dimension[49].

Finally, The SHANEL method does not include a step to eliminate the signal from antibody staining, and we have not tried multiple rounds of antibody relabeling. In the future, we hope to optimize SHANEL for multiple-round antibody labeling.

Materials

Human organ materials

! CAUTION Procedures involving human organs or tissues must conform to relevant institutional and national regulations. Informed consent must be obtained from each donor. Human organs were taken from different human body donors. All donors gave their informed and written consent to explore their cadavers for research and educational purposes, when still alive and well. The signed consents are kept at the Anatomy Institute, University of Leipzig, Germany. Institutional approval was obtained in accordance with the Saxonian Death and Funeral Act of 1994. The signed body donor consents are available on request.

- Human kidney, pancreas, pulvinar and human brain with skull dissected from an 88-year-old female donor
- Human heart, lung, spleen and pancreas for vessel labeling from a 79-year-old female donor
- Brain slices for immunolabeling from an 86-year-old female donor and lung and kidney tissue for immunolabeling from a 97-year-old female donor

Reagents

- 0.01 M PBS (diluted from 0.1 M PBS stock solution, which contains 1.37 M sodium chloride, 0.027 M potassium chloride, 0.08 M disodium hydrogen phosphate and 0.02 M potassium dihydrogen phosphate, pH 7.4, Apotheke Klinikum der Universität Munchen, cat. no. P32799)
- Deionized water (diH2O; in-house purification system)

- 4% PFA in 1× PBS solution, 4 wt/vol%, pH 7.4 (Morphisto, cat. no. 11762.01000) **! CAUTION** Toxic reagent; use only in a well-ventilated fume hood. **▲CRITICAL** Store at 4 °C.
- Heparin (Braun, cat. no. 2047217, 25000 IE/5ml)
- Tetramethylrhodamine isothiocyanate–dextran (mw 500000, Sigma-Aldrich, cat. no. 52194)
- *p*-Maleimidophenyl isocyanate (PMPI; Thermo Fisher, cat. no. 28100) **! CAUTION** Eye and skin irritation; wear suitable protective clothing (gloves, lab coat and safety glasses).
- Dithiothreitol (DTT; Sigma-Aldrich, cat. no. 43815) **! CAUTION** Eye, skin and respiratory irritation; wear suitable protective clothing (gloves, lab coat and safety glasses).
- PI (Thermo Fisher, cat. no. P1304MP)
- CHAPS (Carl Roth, cat. no.1479.4) **! CAUTION** Light powder; avoid contact and inhalation of dust. **▲CRITICAL** Store at 4 °C.
- NMDEA (Sigma-Aldrich, cat. no. 471828) **! CAUTION** Eye irritation; wear suitable protective clothing (gloves, lab coat and safety glasses).
- Guanidine hydrochloride (Carl Roth, cat. no. 6069.3) **! CAUTION** Skin and eye irritation; wear suitable protective clothing (gloves, lab coat and safety glasses).
- Acetic acid (Carl Roth, cat. no. T179.1) **! CAUTION** Flammable and corrosive; keep bottle in a storage cabinet with extreme fire resistance. Skin and eye damage; wear suitable protective clothing (gloves, lab coat and safety glasses).
- Sodium acetate (Sigma-Aldrich, cat. no. S2889) **▲CRITICAL** Store separated from strong acids and strong oxidants.
- Triton X-100 (PanReac Applichem, cat. no. A4975,1000) **! CAUTION** Corrosive, irritant and environmental hazard. Skin and eye damage; wear suitable protective clothing (gloves, lab coat and safety glasses).
- 2-Hydroxypropyl-β-cyclodextrin (HPCD; PanReac Applichem, cat. no. A0367,0100)
- DMSO (Carl Roth, cat. no. A994.2) **! CAUTION** Skin and eye irritation; wear suitable protective clothing (gloves, lab coat and safety glasses).
- NaOH (Carl Roth, cat. no. 6771.1) **! CAUTION** Corrosive hazard. Skin and eye damage; wear suitable protective clothing (gloves, lab coat and safety glasses).
- Ethanol (Merck, cat. no. 10098535000) **! CAUTION** Flammable; keep bottle in a storage cabinet with extreme fire resistance.
- Methanol (Carl Roth, cat. no. 4627.6) **! CAUTION** Flammable; keep bottle in a storage cabinet with extreme fire resistance. Acute toxic and health hazard; handle with care. Wear suitable protective clothing (gloves, lab coat and safety glasses).
- DCM (Carl Roth, cat. no. KK47.1) **! CAUTION** Health hazard. Volatile; use only in a well-ventilated fume hood.
- BABB (benzyl benzoate:benzyl alcohol 2:1, Sigma-Aldrich, cat. no. W213802, cat. no. 24122) **! CAUTION** Irritant and environmental hazard; recycle hazard waste.
- Sodium azide (Sigma-Aldrich, cat. no. 71290) **! CAUTION** Acute toxic and environmental hazard; recycle hazardous waste according to institutional regulations.
- Goat serum (GIBCO, cat. no. 16210072)
- Copper sulfate ($CuSO_4$; Carl Roth, cat. no. CP86.1)
- Ammonium chloride (Carl Roth, cat. no. P726.1)

Equipment

- Surgery scissors (FST, cat. no. 14958-11)
- Big metal tweezers (FST, cat. no. 11000-20)
- Fine metal tweezers (FST, cat. no. 11252-40)
- Peristaltic pump (ISMATEC, REGLO Digital MS-4/8 ISM 834)
- Polytetrafluoroethylene (PTFE) tubing (VWR, cat. no. 228-0735)
- Reference tubing for the ISMATEC peristaltic pump (ISMATEC, cat. no. SC0026)
- PVC tubing (Omnilab, cat. no. 5437920)
- Tubing connector (Omnilab, cat. no. 5434482)
- Glass chamber (Omnilab, cat. no. 5163279)
- Glass chamber (LABICAT, cat. nos. 40070360, 40070180)
- Shaking rocker (IKA, 2D digital)
- Shaker (IKA, model KS 260 basic)
- 5 ml tubes (Eppendorf, cat. no. 0030 119.401) **▲CRITICAL** Using these tubes is highly recommended owing to their resistance to clearing solutions.

- 15 ml tubes (Thermo Fisher Scientific, cat. no. 339651) ▲**CRITICAL** Using these tubes is highly recommended owing to their resistance to clearing solutions.
- 50 ml tubes (Thermo Fisher Scientific, cat. no. 339653) ▲**CRITICAL** Using these tubes is highly recommended owing to their resistance to clearing solutions.
- 1 L glass beakers (any; we used the ones from DURAN)
- 1 L glass bottles (any; we used the ones from DURAN)
- 2 L glass bottles (any; we used the ones from DURAN)
- 500 ml glass bottles (any; we used the ones from DURAN)
- PTFE covered magnetic stirring bars (any)
- Hot magnetic stirrer (IKA, model RCT basic B-5000, cat no. 0003810000)
- Aluminum foil (any)
- Plastic wrap (any)
- Disposable underpads (Medimex, cat. no. E1911804, or any)
- Syringes of 1 ml, 5 ml, 10 ml, 50 ml (any)
- Tapes, black and transparent ones (any)
- Parafilm (Bemis, cat. no. PM-992)
- pH meter (WTW, model pH7110)
- Shaking rocker (IKA, model 2D digital)
- Incubator (Memmert, model UN160, although any incubator that reaches and maintains 37 °C and has a shaker inside is suitable)
- Fume hood

Imaging systems

- Computer (coupled with a custom light-sheet microscope) and equipped with the following characteristics. Processors: Intel Core i7-7800X CPU @ 3.50 GHz; graphic card: NVIDIA Quadro K420; random access memory: 32 GB; solid state drive: Samsung SSD 860 PRO 1 TB; hard disk drive: Seagate Enterprise Capacity SATA 12 TB (ST12000NM0007); operating system: Windows 10 Pro, 64 bit
- Miltenyi Biotec UltraMicroscope II light-sheet microscope coupled with:
  - SuperK EXTREME/FIANIUM supercontinuum white light laser (NKT Photonics, model SuperK EXTREME EXW-12)
  - Andor sCMOS camera Neo 5.5 (Andor, mod. no DC-152Q-C00-FI)
  - Filter sets: excitation (ex) 470/40 nm, emmission (em) 535/50 nm; ex 545/25 nm, em 605/70 nm; ex 560/30 nm, em 609/54 nm; ex 580/25 nm, em 625/30 nm; ex 640/40 nm, em 690/50 nm
  - Olympus MVX10 zoom body (zoom range 0.63–6.3×)
  - Olympus revolving zoom body unit (U-TVCAC)
  - 1× air objective (Olympus MV PLAPO ×1/0.25 NA, working distance (WD) 65 mm)
  - 2× immersion objective (Olympus MVPLAPO2XC/0.5 NA, WD 6 mm)
  - 4× immersion objective (Olympus XLFLUOR ×4 corrected/0.28 NA, WD 10 mm)
  - 12× immersion objective (LaVision MI PLAN 12×/0.53 NA, WD 10 mm)
  - 20× immersion objective (Zeiss ×20 Clr Plan-Neofluar/0.1 NA, WD 5.6 mm)
- Miltenyi Biotec prototype UltraMicroscope light-sheet microscope for large samples coupled with:
  - LASOS Multi Color System Series for the laser box (LASOS, model MCS5 F2-01)
  - Andor sCMOS camera Zyla 5.5 (Andor, mod. no ZYLA-4.2P-CL10)
  - Filter sets: ex 488 nm, em 525/50 nm; ex 561 nm, em 595/40 nm; ex 640 nm, em 680/30 nm; ex 785 nm, em 845/55 nm
  - Olympus revolving zoom body that can switch between 1× and 2× with an autofocus-Cube AFC-UM2-UBG
  - 1.1× objective (LaVision MI PLAN ×1.1/0.1 NA, WD 17 mm)
- Zeiss LSM 880 inverted laser-scanning confocal microscope coupled with: 25× water-immersion objective (Leica, ×25/0.95 NA, WD 2.5 mm) mounted with a custom mounting thread ▲**CRITICAL** Check the compatibility of the microscope and objectives of different brands with the vendors.

Computer and data processing and analysis tools

- Computer (HP Z840 workstation; Windows 10 Pro, 64 bit; CPU: Intel Xeon E5-2640 v3; installed memory: 256 GB; GPU: NVIDIA Quadro M5000)

- Fiji (ImageJ2, https://fiji.sc/) and the Stitch Sequence of Grids of Images plugin[50] for stitching original mosaic tiffs from light-sheet microscope
- Total Commander (v. 8.52a x64, https://www.ghisler.com/) for renaming the files of stitched tiffs
- ImageMagick (v. 7.0.5-4, https://imagemagick.org/script/index.php) for Lempel–Ziv–Welch (LZW) TIFF compression
- Vision4D (v.3.0.1 ×64, Arivis) for stitching different organ parts from multiple scans
- Arivis converter (v.2.12.6, Arivis)
- Imaris (Bitplane) for visualization of 3D images
- Photoshop CS6 (v. 13.0, Adobe)
- The source code of the 'Stitching.py' Fiji macro for stitching sequences of images is available at http://discotechnologies.org/ or Zenodo (https://doi.org/10.5281/zenodo.5383535)

Reagent setup

Dextran blood vessel labeling solution

Tetramethylrhodamine isothiocyanate–dextran is a commonly used dye to trace blood vessels in vivo. To chemically fix dextran inside the blood vessels, we used PMPI and DTT to crosslink the hydroxyl group of dextran to the surrounding sulfhydryl-containing proteins. The working solution of dextran contains 5 mg/ml tetramethylrhodamine isothiocyabate–dextran, 0.4 mM PMPI and 1 mM DTT in PBS. As shown in the table below, each reagent is prepared separately as follows: (1) dissolve 8.6 mg PMPI in 2 ml DMSO; (2) dissolve 15.4 mg DTT in 5 ml PBS; (3) dissolve 0.5 g dextran in 93 ml PBS. Mix all solutions together before the perfusion.

	PMPI	DTT	Dextran	PBS
MW (g/mol)	214.2	154.2	500,000	-
Stock concentration (mM)	20	20	-	-
Stock solution	DMSO	PBS	-	-
Weight (mg)	8.6	15.4	500	
Volume of solution (ml)	2	5	-	93

▲CRITICAL Prepare fresh solutions before starting the experiment. **!CAUTION** Prepare the solutions in a hood and wear a mask.

EDTA solution

Prepare EDTA decalcification solution by dissolving 20% (w/v) EDTA in diH_2O, adjusting the pH to 8.0–8.5 using NaOH or HCl. In a 2 L bottle with a stirring bar, dissolve NaOH continuously to keep 1.5 L diH_2O alkaline, then slowly add 400 g EDTA powder. Replenish diH_2O, adding more NaOH or HCl until reaching 2 L with a pH of 8.0–8.5. **!CAUTION** If EDTA precipitation is observed during storage, add more NaOH until the solution becomes transparent with a pH of 8.0–8.5. EDTA solution can be stored at 4 °C for several months.

CHAPS/NMDEA solution

CHAPS/NMDEA mixture is composed of 10% (wt/v) CHAPS and 25% (wt/v) NMDEA in diH_2O. In a 2 L bottle, mix 200 g of CHAPS and 500 g of NMDEA in diH_2O with a stirrer at room temperature (22–25 °C) and set the final volume to 2 L. The reagent can be stored at 4 °C for several months. **!CAUTION** CHAPS is a light powder; it is suggested to wear a mask to avoid inhalation during the process.

Acetic acid solution

Acetic acid solution is 0.5 M in diH_2O. In a 1 L bottle, mix 30 mL acetic acid in diH_2O at room temperature and adjust the final volume to 1 L. The reagent can be stored at room temperature for several months. **!CAUTION** Prepare the solution in a hood and wear a mask owing to the smell of acetic acid.

Guanidine solution

Guanidine solution is a mixture of 4 M guanidine hydrochloride, 0.05 M sodium acetate and 2% (wt/vol) Triton X-100 in PBS, pH 6.0. In a 2 L bottle, mix 764.2 g guanidine hydrochloride, 8.2 g sodium acetate and 40 g Triton X-100 in PBS with a stirrer at room temperature and set the final volume to 2 L. Adjust the pH to 6.0 with 4 M NaOH solution and 30% hydrochloric acid solution. The reagent can be stored at room temperature for several months.

Dehydration and rehydration solutions
Prepare a series of dehydration solutions by mixing ethanol with diH_2O to obtain 50%, 70% and 100% (v/v) ethanol solutions. Prepare the solutions fresh before using.

Delipidation solutions
The delipidation solution could be a DCM/methanol mixture or pure DCM solution. For tissue pretreatment before labeling, prepare a mixture of two volumes of DCM and one volume of methanol. For tissue clearing after labeling, use pure DCM. **! CAUTION** DCM is a health hazard and highly volatile. It should be handled in a fume hood, wearing safety goggles and double-layer nitrile gloves to avoid inhalation and contact with skin/eyes. **▲ CRITICAL** Prepare fresh solution before use.

Sodium azide stock solution
The concentration of sodium azide stock solution is 0.05% (wt/v) dissolved in 1× PBS. This solution can be stored at 4 °C for several months. **! CAUTION** Avoid contact with skin and eyes.

Blocking buffer for antibody staining
The blocking buffer contains 0.2% (v/v) Triton X-100, 10% (v/v) DMSO and 10% (v/v) goat serum in 1× PBS. In a 500 ml bottle, mix 1 ml Triton X-100, 50 ml DMSO and 50 ml goat serum in PBS with a stirrer at room temperature. **▲ CRITICAL** Prepare fresh solution before use. The pretreated tissue samples can be stored in blocking buffer at 4 °C for several weeks before antibody staining if adding 0.01% (w/v) sodium azide.

Antibody incubation buffer
The antibody incubation buffer is composed of 3% (v/v) goat serum, 3% (v/v) DMSO, 0.2% (v/v) Tween-20 and 10 mg/L heparin in 1× PBS. If antibody solubility in water is poor, prepare an alternative antibody incubation buffer composed of 10% (w/v) HPCD, 3% (v/v) goat serum and 10 mg/L heparin in 1× PBS. **▲ CRITICAL** Prepare solution fresh before use.

Antibody washing buffer
Prepare the antibody washing buffer by combining 0.2% (v/v) Tween-20 and 10 mg/L heparin in 1× PBS. This solution can be stored at 4 °C for several months.

$CuSO_4$ solution
The $CuSO_4$ solution can be used to eliminate tissue autofluorescence. Dissolve 1.6 g $CuSO_4$ and 2.67 g ammonium chloride in diH_2O, adjust pH to 5.0 with NaOH or HCl and set the final volume to 1 L.

RI matching solution (BABB)
BABB is the RI matching solution. Prepare by mixing benzyl alcohol and benzyl benzoate in a ratio of 1:2 by volume. BABB solution should be prepared in a glass container in a fume hood and stored with a tight bottle cap at room temperature for several months in a laboratory cabinet. **! CAUTION** Benzyl benzoate is harmful if swallowed, and causes skin and eye irritation. Benzyl alcohol is harmful if swallowed and inhaled. Handle wearing safety goggles, nitrile gloves (preferably double layer) and a lab coat.

Equipment setup

Pump system
To set up an active perfusion system, connect an Ismatec peristaltic pump to a set of tubing: one black pump reference tube, two colorless PVC tubes, three tube connectors and a pipette tip as shown in Fig. 2 and Extended Data Fig. 1. This pump allows connecting up to four channels.

Procedure

Perfusion, fixation and washing of human organs ● Timing 1–2 d

1 Select plastic tubes matching the diameter of the opened arteries and veins of the human organs, and use these tubes to stitch in the opened arteries and veins.
! CAUTION Identify and mitigate any risk factors for infectious disease transmission before human organ handling.

2 At room temperature, using a gravitation irrigator system, set up the irrigator height as 0.5 m to perfuse the human organs. Mark the start level of PBS/heparin (2.5 U heparin per milliliter) solution of the irrigator and perfuse via the plastic tubes with PBS/heparin solution for 3–5 h until the blood is flushed out, which is signaled by the specimens becoming brighter. It takes 50 L of PBS/heparin solution to flush the blood out from a heart–lung block and 20 L from smaller organs such as kidney, spleen or brain.

3 Swap the PBS/heparin solution with 4% PFA solution and continue to perfuse for 15 minutes. Control the perfusion speed by setting up the irrigator height to 0.5 m. Twenty liters are needed per lung–heart block and 10 L for organs such as kidney, spleen or brain.
! CAUTION If there is no noticeable flow from the human organs, lift the irrigator to increase the perfusion speed (maximal 1.2 m height). A fume hood is necessary when working with formalin solution, which is toxic and has a strong, pungent odor.

4 Post-fix the human organs with ten times the volume of 4% PFA solution used in Step 3 for 7 d.
! CAUTION The duration of fixation can affect sample integrity. Optimal fixation conditions should be assessed for each organ and tissue to prevent underfixation or overfixation.

5 Wash the PFA-fixed human organ(s) to prepare them for subsequent experiments. If perfusion is applicable, under a fume hood, set up the pump perfusion system with connecting tubing on a layer of disposable pads. Put the PFA-fixed human organs in an appropriate glass container, and actively perfuse with enough PBS by covering the surface of the organ at room temperature. Wash three times with PBS solution for 2 h each. Set the speed of the pump to 45–46 rpm (160–170 mmHg), and the flow rate to 12.5 ml/min. If perfusion is not applicable, under a fume hood, put a layer of disposable pads on the shaker. Put the PFA-fixed human organs in an appropriate glass container or falcon tubes, then passively incubate with enough PBS to cover the sample at room temperature for 4 h each time and at least three buffer changes. The speed of shaker is 50 rpm.
! CAUTION Stretch the parafilm tight to seal the connection point for protection if needed.
■ PAUSE POINT The fixed human organs can be stored at 4 °C in PBS with 0.01% (wt/vol) sodium azide for several months.

Organ pretreatment according to the experimental needs ● Timing 1–14 d

6 In this step, we describe two methods that are suitable for different kinds of human organs. If the organ vasculature is well preserved, we can perfuse it with dextran blood vessel labeling solution (option A). EDTA decalcification is needed in case there is bone tissue to be labeled and cleared (option B).

A **Blood vessel labeling with dextran by perfusion** ● Timing 1 d

(i) Set up the pump perfusion system with connecting tubing on a layer of disposable pads (Fig. 2). Put the fixed human organ in an empty, clean glass container, then perfuse it with fresh dextran blood vessel labeling solution (see ‘Reagent setup’). Ensure that the solution is flowing out from each tube inserted in the organ, which means the blood vessel is fully filled with dextran solution. Set the speed of the pump to 45–46 rpm (160–170 mmHg), and the flow rate to 12.5 ml/min. The leaking solution can be collected in a container and reused for another round of perfusion labeling.
▲ CRITICAL STEP Ensure that the organ turns red after dextran injection.

(ii) After completing vessel labeling, wash the surface of the organ with running water to get rid of the unspecific contaminations from the leaking solution.
! CAUTION If there is extra dye solution coming out from the organ, wipe the organ dry with paper to keep the whole organ surface clean from dye solution.

(iii) Put the labeled organ in a plastic bag, and seal with tape.

(iv) Put the plastic bag with labeled organ in a container, and place it in a 37 °C incubator overnight.

(v) The next day, take the organ out and cover it with enough PBS at room temperature and place on the shaker to wash. Wash three times with PBS solution for 2 h each.
? TROUBLESHOOTING

B **Decalcification with EDTA** ● Timing 7–20 d

(i) Incubate human organs with bone tissue in 20% (wt/vol) EDTA (pH ~8.0) with 0.01% (wt/vol) sodium azide solution at 37 °C. Refresh the solution every 3–5 d until the bone part becomes soft and pliable (test by bending the bone), then wash with PBS three times for 2 h each time.
! CAUTION If the container is not sealed well, the solution will evaporate, leading to formation of EDTA crystals.

Permeabilization and decolorization with CHAPS/NMDEA ● Timing 3–20 d

7 If perfusion is applicable, continue using the same pump perfusion system with enough CHAPS/NMDEA solution to cover the organ for days to 1 month at room temperature for decolorization. A successful decolorization is achieved when the solution turns green or dark green. Refresh the solution two to three times until it does not change color anymore. Place the glass chamber in a fume hood, and cover with plastic wrap and aluminum foil to avoid the evaporation of water and exposure to light (Extended Data Fig. 1c,d).

? TROUBLESHOOTING

8 If the sample is not suitable for perfusion, continue with passive incubation on the shaker. Incubate the organs with enough CHAPS/NMDEA solution to cover the organs for days at 37 °C, refreshing the solution when it turns green or dark green, until the solution does not change color anymore. This should take two to three solution changes.

! CAUTION The reference tubing should be displaced back and forth between position 1 and position 2 (Fig. 2e) every 2 d to avoid the tubing attachment becoming loose after continuous long-term abrasion. Check the tubing quality carefully from time to time, as the perfusion solution can occasionally leak from cracks in tubing if there is accumulation of abrasion from continuous running of the pump, especially in the evening when the system is unsupervised. The disposable pads are useful for cleaning up any leaking accidents.

Delipidation ● Timing 7–50 d

9 Perform the incubations outlined below at room temperature under the fume hood. If perfusion is applicable, continue with same pump perfusion system, if not, continue with passive incubation on the shaker.

- PBS wash twice for 6 h each time
- Dehydrate with 50% EtOH/H_2O solution for 1–7 d
- Dehydrate with 70% EtOH/H_2O solution for 1–7 d
- Dehydrate with 100% EtOH solution for 1–7 d
- Dehydrate with 100% EtOH solution for 1–7 d, until the organ does not shrink anymore
- Delipidate with DCM/MeOH (2:1, v/v) solution for 1–7 d, refresh the solution two to three times
- Rehydrate with 100% EtOH solution for 1–7 d
- Rehydrate with 70% EtOH/H_2O solution for 1–7 d
- Rehydrate with 50% EtOH/H_2O solution for 1–7 d
- Rehydrate with diH_2O for 1–7 d

! CAUTION The glass chamber should be placed in a fume hood and covered with plastic wrap and aluminum foil to avoid evaporation of the solution and light exposure. EtOH, MeOH and DCM are highly volatile liquids, especially under the fume hood. The chamber should be carefully sealed with several layers of plastic wrap and tape to prevent evaporation. Replenish the desired solutions if needed to ensure the whole sample is covered during the perfusion. As DCM could erode some types of tubing (e.g., polystyrene), the recommended tubing is PTFE or polypropylene (PP). Replace the reference tubing every 2 d.

? TROUBLESHOOTING

ECM loosening ● Timing 2–15 d

10 Perform the following incubations at room temperature, under the fume hood. If perfusion is applicable, continue using the same pump perfusion system; if not, continue with passive incubation on the shaker.

- Collagen hydrolysis with acetic acid solution for 1–7 d
- DiH_2O wash twice for 6 h each time
- Glycoprotein extraction with guanidine solution for 1–7 d

! CAUTION The glass chamber should be covered with plastic wrap and aluminum foil to avoid evaporation and light exposure.

? TROUBLESHOOTING

(Optional) Labeling ● Timing 7–15 d

▲ CRITICAL If perfusion is applicable, continue using the same pump perfusion system. If it is not applicable, continue with passive incubation on the shaker. The whole organ can be stained with a cell nuclei dye, for example using a PI or TO-PRO-3 solution in PBS (1 µg/ml and 1 µM final concentration, respectively) at room temperature for 2–7 d. The solution should cover the whole organ.

▲CRITICAL If antibody staining is needed, the antibody should be tested in the organ of interest in sections first (a list of validated antibodies is available in Table 2, and a list of antibodies found to be noncompatible with SHANEL is available in Supplementary Table 1).

! CAUTION Antibodies are macromolecules, and their large size may limit their ability to penetrate and stain thick organs. Thus, if perfusion is not available, big organs should be dissected into sections no more than 1.5 cm thick to reach full antibody penetration. Actively pumped antibody solutions to stain intact human organ have not yet been tested, while nanobodies have been proven to stain intact pig organs in active pumping set up.

11 Sample preparation for antibody/dye/nanobody screening: slice parts of the targeted tissue to 40-µm-thin sections on glass slides using a cryostat following standard protocols or cut into 0.3–1 mm floating slices by vibratome following standard protocols. Use the sections on glass if storing samples for several months in a −80 °C freezer and floating slices for quick antibody screening performed within 1 week.

12 SHANEL pretreatment for antibody screening: at room temperature, treat the floating slices with CHAPS/NMDEA solution two times for 12 h each. Wash three times with PBS for 20 min each. Gradually dehydrate in 50%, 70% and 100% EtOH/H_2O, 2 h per step. Change to DCM/MeOH (2:1, v/v) solution overnight. Rehydrate in 100%, 70%, 50% EtOH/H_2O and diH_2O, 2 h per step. Treat with acetic acid solution overnight, wash twice for 20 min in diH_2O, treat with guanidine solution for 6 h and wash twice for 20 min in diH_2O.

13 Block the floating slices with blocking buffer at 37 °C overnight, then incubate with antibodies in antibody incubation buffer at 37 °C for 2 d.

14 The concentration of antibody tested should be according to the manufacturer's suggestions. If needed, incubate the tissue with appropriate secondary antibody at 37 °C for 2 d. Wash the samples with washing buffer three times for 1 h at room temperature.

15 Gradually dehydrate in 50%, 70% and 100% EtOH/H_2O, 2 h per step. Change to DCM for 1 h, then change to BABB until the slices become transparent.

16 Lastly, examine the results with a confocal microscope to find the best conditions for strong and specific antibody staining.

▲CRITICAL STEP We strongly suggest using Alexa or Atto dye as the fluorophores conjugated to antibodies, because these dyes are stable and bright in clearing solution.

17 After obtaining good-quality staining results from antibody screening, dissect the region of interest from the human organ and treat the tissue slice or block following the timing guidelines in Table 3.

▲CRITICAL STEP Autofluoresecnt lipofusin accumulates in aged human samples. Incubate the slice with $CuSO_4$ solution for 1–7 d before clearing to eliminate tissue autofluorescence.

? TROUBLESHOOTING

Clearing ● Timing 7–40 d

18 If perfusion is applicable, continue using the same pump perfusion system at room temperature, under the fume hood for the following incubations. If not applicable, continue with passive incubation on the shaker.

- PBS wash twice for 6 h each time
- Dehydrate with 50% EtOH/H_2O solution for 1–7 d
- Dehydrate with 70% EtOH/H_2O solution for 1–7 d
- Dehydrate with 100% EtOH solution for 1–7 d
- Dehydrate with 100% EtOH solution for 1–7 d, until the organ does not shrink anymore
- Delipidate with DCM solution for 1–7 d, until the sample sinks to the bottom of the container
- Perform RI matching with BABB solution for 1–30 d until the organ becomes completely transparent

! CAUTION The glass chamber should be covered with plastic wrap and aluminum foil to avoid evaporation and light exposure. EtOH and DCM are highly volatile liquids, especially under the fume hood. The chamber should be carefully sealed with several layers of plastic wrap and tape to prevent the volatility of solutions. Replenish the desired solutions to cover the whole sample if needed during the circulation. DCM can erode some types of tubing (e.g., polystyrene), therefore, the recommended tubing is from PTFE or PP. Replace the reference tubing every 2 d (Supplementary Video 1).

■PAUSE POINT The cleared human organs in BABB solution can be stored covered with aluminum foil at room temperature for months to years before imaging.

? TROUBLESHOOTING

Table 3 | Timing guidelines for treatment of various human organs

Sample type	Human kidney	Human pancreas	Human spleen	Human heart/lung	Human pulvinar	Human brain	Human skull	Tissue slice/block
PBS wash	1 d	1 d	1 d	1 d	1 d	2 d	1 d	1 d
Vessel labeling	1 d	1 d	1 d	1 d	–	–	–	–
EDTA	–	–	–	–	7–10 d	–	14–20 d	–
CHAPS/NMDEA	10–14 d	5–7 d	5–7 d	10–14 d	5–7 d	20 d	5 d	3 d
PBS	1 d	1 d	1 d	2 d	1 d	3 d	1 d	1 d
50% EtOH	1 d	1 d	1 d	2 d	1 d	5 d	1 d	1 d
70% EtOH	2 d	1 d	1 d	2 d	1 d	7 d	1 d	1 d
100% EtOH	2 d	1 d	1 d	3 d	1 d	7 d	1 d	1 d
100% EtOH	2 d + 2 d	1 d	1 d	3 d	1 d	7 d	1 d	1 d
DCM/MeOH	3 d	2 d	2 d	3 d	2 d	7 d	2 d	2 d
100% EtOH	1 d	1 d	1 d	2 d	1 d	4 d	1 d	1 d
70% EtOH	2 d	1 d	1 d	2 d	1 d	5 d	1 d	1 d
50% EtOH	2 d	1 d	1 d	2 d	1 d	5 d	1 d	1 d
DiH_2O	1 d	1 d	1 d	2 d	1 d	3 d	8 h	8 h
Acetic acid	2 d	1 d	1 d	2 d	1 d	7 d	1 d	1 d
DiH_2O	8 h	8 h	8 h	2 d	8 h	3 d	8 h	8 h
Guanidine HCl	1 d	1 d	1 d	2 d	1 d	7 d	1 d	1 d
PBS	8 h	8 h	8 h	2 d	8 h	3 d	8 h	1 d
Cell nuclei dye	7 d	7 d	7 d	7 d	7 d	–	2 d	–
Antibody labeling	–	–	–	–	–	–	–	7–14 d
PBS	2 d	1 d	1 d	2 d	1 d	–	1 d	1 d
50% EtOH	1 d	1 d	1 d	2 d	1 d	5 d	1 d	1 d
70% EtOH	2 d	1 d	1 d	2 d	1 d	7 d	1 d	1 d
100% EtOH	2 d	1 d	1 d	2 d	1 d	7 d	1 d	1 d
100% EtOH	2 d	1 d	1 d	3 d	1 d	7 d	1 d	1 d
DCM	3 d	1 d	1 d	3 d	1 d	7 d	1 d	1 d
BABB	3 d	2 d	2 d	5 d	2 d	7 d	2 d	1 d
Total processing time for each organ	~54–60 d	~36–38 d	~36–38 d	~69–73 d	~43–48 d	~135 d	~43–49 d	~32–39 d

Imaging with light-sheet fluorescent microscopy ● Timing 1–8 d

▲**CRITICAL** Here we use the prototype light-sheet microscope from Miltenyi Biotec to image the human pancreas (Fig. 3). The commercialized UltraMicroscope Blaze can also be applied for high-resolution imaging of large human organs. Both microscopes are controlled by the same software named 'Imspector'.

19 Check if there are bubbles inside the organ in BABB solution. If yes, carefully suck out the bubbles using a 1 ml syringe (Supplementary Video 2).

20 Use one piece of tissue paper soaked with 80% EtOH/H_2O solution to clean the sample holder, and wait for the sample holder to dry.

21 Cut three pieces of tape, and stick them on the top, middle and bottom parts of the sample holder.

22 Add glue on each piece of tape on the sample holder. To stick the sample durably, the glue should cover the full area of the tape.

! CAUTION If the glue is not sufficient, the sample will not be stable on the holder and may shift or fall down during the 2–3 d of scanning.

23 Use tissue paper to absorb BABB solution from one side of sample several times.

24 The glue would contact the dry side of the sample. Carefully put the sample on the sample holder, and try to keep the center of sample aligning with the holder. One end of sample should be close to one end of the moving range of holder (e.g., top to top).

25 Wait for 30–60 s until the glue solidifies.

26 Put the sample holder back into the light-sheet microscope, and fix it.

27 Check again if there are bubbles inside of organs in BABB solution. If yes, carefully suck out the bubbles using 1 ml syringe.

! CAUTION Gently touch the sample when sucking out bubbles; otherwise, the glue bonding would be destroyed mechanically and the sample would shift or fall down.

28 To set imaging parameters in Imspector software (Extended Data Fig. 3) go to 'Settings' → 'Hardware' → 'Ultra3 Settings' → 'Objective' to choose the right objective, for example 'LVBT 1x'.

29 Start the View settings of the software with the following settings:

Measurement mode	Multicolor mosaic acquisition
Devices 1	Ultra3 filter
Devices 2	*xyz*-Table Z
Devices 3	*xyz*-Table X
Devices 4	*xyz*-Table Y
AS (autosave)	'abled' in green
Split	'abled for Devices 1'
Channel setup	Click the targeted scanning channels according to the labeling, Excitation 561, Emission 595/40 and Excitation 785, Emission empty here
Lightsheet properties	Set 'Sheet NA' to '0.035', and 'Thickness' to '21 µm'
Sheet width	100%
Zoom	1.0×
Measurement → Liquid	BABB
Measurement → Mount	None
Exposure time	90.000–100.000 ms
Gain	16-bit low noise
Step (the step size in µm between each two images in *Z* axis)	8.00 (for human pancreas)

▲**CRITICAL STEP** The smaller the step size, the more images will be acquired, and the longer scanning will take, but the resolution in *XZ* and *YZ* direction will increase.

30 Set 'LightSheet Selection' to be only 'left' or only 'right' when checking the signal and position of the sample.

31 Select the top surface of the sample for the focus by adjusting the sample stage in the *Z* direction (Supplementary Video 3).

! CAUTION When adjusting the focus, be careful to avoid collision of the moving objective with the sample. The sample should only be illuminated on the surface in the starting position step.

32 Mount the 1.1× objective, and then click the ‘Focus → down’ button in the software until the lens gets immersed in the BABB solution inside the chamber holding the sample, then adjust the movement of the objective to get a clear and bright signal. Then lower the sample holder until the sample is just lower than the light-sheet illumination region, click ‘Current Position → Set as Zero’ and ‘Scan Range → Start’ to ‘0.000’.

? TROUBLESHOOTING

33 Next lift the sample holder. The signal gets blurry when the imaging plane gets deeper in the sample. When this occurs, click ‘Scan Range → End’. Since with light-sheet microscopy using a 1.1× objective, the working distance is ~17 mm in *z* direction, the maximum imaging depth would be −14 mm.

34 Adjust ‘Mosaic → Set Parameters’ to find the proper ‘X Axis, Y Axis’ and ‘Overlap’ to cover the scanning volume of the samples from all edges. In general, for a 1.1× objective, ‘3×8’ with 30% overlap or ‘4×7’ with 33% overlap would cover the human pancreas or human kidney. For a 12× objective, ‘10×10’ with 30–40% overlap is possible.

! CAUTION The following image stitching will be less accurate if the overlap value is set too small. When setting the scanning volume, do not modify the travelling limitations of the stage in *X*, *Y* and *Z* direction. Otherwise, the software would report an error and fail.

35 Choose ‘Autosave Settings’ to fill in the ‘path’ and ‘name’ for saving, for example ‘humanpancreas_1x_4×7_33o_90ex_8um_56130_78540_forwardup’.

36 Stop the live ‘View’, and click the ‘Lightsheet Selection’ to be ‘both’.

37 Start the scanning, and keep the room in the dark for ~2–3 d.

38 When the scanning has finished, take the sample holder out and cut the tape to remove the sample from the holder. Put the sample in BABB solution and peel off the glue and tape at the same time. Wash the sample holder with 100% EtOH, and clean with tissue paper.

39 Repeat Steps 19–38 for scanning different parts of the sample, changing the position of the sample, or flipping the sample in Step 31 to make sure the scanning covers both ends and both sides of the sample. For example, the human pancreas took four rounds of scanning to image the whole organ covering the forward-up, forward-down, backward-up and backward-down orientations.

Data stitching, renaming and compression ● Timing 1–2 d

40 Scanning with the light-sheet microscope generates a series of grid images in the auto save folder. Inside the auto save folder, prepare new folders named C00, C01, etc. corresponding to the channels used for imaging.

41 Begin by stitching a preview image. Start Fiji, and go to the plugin ‘Stitch Sequence of Grids of Images’.

42 In the ‘Stitch Sequence of Grids of Images’ dialog, set the following parameters as specified (Extended Data Fig. 4a) and keep the rest as default:

‘Grid size in X’ as the number of tiles per row.
‘Grid size in Y’ as the number of tiles per column.
‘Grid size in Z’ as 1.
‘overlap’ as the overlap defined when scanning.
‘Input directory’ as the folder path containing the grid images.
‘file names’: copy one of the file names of the grid images from the auto save folder, and replace the specific numbers of Ultra3[00 ×00] to be the variable numbers Ultra3[{yy} x {xx}]; Z0000 should be changed to Z{zzzz}.
‘Output directory’ as the folder where the resulting stitched images will be saved.
‘Start x’ and ‘start y’ as ‘0’.
‘Start z’ as any number roughly in the middle of the *z*-stack
‘Start i’ as ‘1’.

43 Click ‘OK’, and wait for the preview image to be stitched.

44 Open the preview stitched image in the output folder using Fiji, and check if the image aligned properly without any mismatched images. When the preview stitching is completed, a file called ‘TileConfiguration.text.registered’ will be generated in ‘Input folder’. This file contains the grid image layout parameters.

▲CRITICAL STEP It is possible to use other alternative algorithms for stitching, for example, TeraStitcher (https://abria.github.io/TeraStitcher/).

? TROUBLESHOOTING

45 Copy the 'TileConfiguration.text.registered' file into the different channels folder (C00, C01, etc.), and change the file format to.txt.

46 In one channel, open the 'TileConfiguration.txt' file and change the *Z* panel number back to 0000 in all tiles using the replace function, for example, 'Zxxxx' to 'Z0000'.

47 If there is more than one channel, copy this 'TileConfiguration.txt' file to the other channel folders, and replace the channel number to the corresponding channel number, for example, 'C00' to 'C01' in folder 'C01'.

48 Open the plugin file 'Stitching.py' with Fiji.

49 Run the 'TileConfiguration.txt' file, and enter the total number of sections in one round of scanning.

50 Repeat Steps 48–49 for each 'TileConfiguration.txt' file in the other channel folders to stitch the rest of the images. All stitched images will be separately saved in corresponding channel folders, 'C00', 'C01', etc.

51 The stitched images will have the same name in the different channel folders 'Manual_StitchedZxxxx'. Use 'Total Commander' software to rename the images. Open the software, find the corresponding channel folder (e.g., C00) and select all of the images in the folder. Then click 'Files' → 'Multi-Rename Tool', and fill the information as follows:
'file name' set as 'C00_Z'. Then click '[C] Counter'.
Define the counter number as 'Start at 0', 'Step by 1' and 'Digits 4'.

52 Repeat Step 51 for all other channel folders.

53 Combine all stitched images from different channel folders into one folder so that they can be compressed.

54 Open the 'LZW compression' of 'ImageMagick'. Input the file path of the folder with all the stitched images and output to the same path. Press 'Enter' to compress all the stitched images, and wait for Arivis volumetric fusion.

Arivis fusion ● Timing 1–6 d

▲CRITICAL Whole organ scanning, covering different parts of the organ, will be completed after multiple rounds of light-sheet microscopy scaning. Following organ stitching by Fiji, use 'Arivis Vision 4D' to fuse the 3D organ volumes.

55 Arivis Vision 4D software requires a .sis file format to visualize and analyze the image. To convert the image into a .sis file, open 'Arivis SIS Converter' and select 'Add Files' to load the stitched images composed of all channels from one folder, for example, 'C00' folder. If the dialog 'Assume same structure for all files?' appears, click 'Yes'.
▲CRITICAL STEP All stitched images from different channels must be transferred to the same folder in advance.

56 In the 'Arivis SIS Converter' tab, select 'Custom import' as file import style and define the name of .sis Arivis file in the export folder (e.g., 'Human pancreas_forward up.sis').

57 To define the imported image pixel size, select 'more options' and select the right image pixel type, then click 'OK'.

58 A new window 'Manual import mapper' will appear; click 'Selection', and choose 'Pattern matching'.

59 Click 'Start' to begin the conversion.
! CAUTION The .sis Arivis file could be several terabytes after fusion; for example, human pancreas Arivis file is 2.5 TB. It is recommended to check the drive capacity before starting the conversion.

60 Repeat Steps 56–59 to convert volumetric scans of the different parts of the organ to.sis files. For example, four rounds of scanning were performed on the human pancreas to cover different parts of the organ, and the results should be converted into four individual .sis Arivis files, corresponding to the forward-up, forward-down, backward-up and backward-down scans.

61 After all different parts of the organ image set are converted to Arivis file (.sis), open the first .sis file in Arivis Vision 4D. Correct the parameters of pixel size in *X*, *Y* and *Z* coordinates by clicking 'Data' → 'Pixel Size'.

62 To fuse the second part of the organ with the first part, load the second .sis file as a new image set: click 'File' → 'Import' to choose the second .sis file, then click 'Import Files' → 'more options' → 'Import as New Image set' and set 'Target Pixel Type' to '16 Bit integer'.
▲CRITICAL STEP The pixel type should be matched for all loaded volumetric image sets.

63 If the two volumetric scans are from different orientations, correct the second image set to the same orientation as the first image set by clicking 'Flipping' and click 'OK' to run the transformation (Extended Data Fig. 5a).

64 After transformation, a new image set called 'flipped' will appear in the 'Image Set'. Click the 'Vertical Split' on the menu. Then click 'Navigator' → 'Vertical Split' to load two volumetric scans side by side (one is the first image set, the other is the flipped second image set) (Extended Data Fig. 5b). Check the loaded image set quality by scrolling the 2D images to zoom in and out, and adjust the color bar of each channel for brightness and contrast.

65 If satisfied with the image quality of these two volumetric scans, prepare the matching landmarks for volume fusion in the Arivis Vision 4D software. Find at least three landmarks in both overlapping volumes from the two image sets (Extended Data Fig. 5c,d).

▲ **CRITICAL STEP** The landmarks should distribute in the overlapping volume as much as possible. The landmarks could be the same cell, the same vessel structure or the same junctions.

66 To label the landmarks in both image sets, click the icon 'Place New Object' → 'Marker' to label the target landmark region.

67 Click 'Show Objects Table' to view the marker information.

68 After collecting enough landmarks from the two image sets, volume fusion can be initiated. Click 'Data' → 'Volume Fusion' → 'Image Sets' to choose one image set as 'Base Image Set' and the other image set as 'Moving Image Set'. Before running the full function of volume fusion, add all landmarks in the 'Transformation' → 'Landmark Registration' → 'Base Image Set' → 'Add All Objects as Landmarks' by right clicking the set icon. Do the same for 'Moving Image Set'. Then select the 'Scale' to be '10%' for generating a new preview image set (Extended Data Fig. 5e).

▲ **CRITICAL STEP** The sequence of landmarks should be the same in both image sets. The highlighted locations of landmarks will be displayed in the right window.

69 If not satisfied with the fusion in the new preview image set, for example, if the new preview image set shows mismatching or gaps after the volume fusion, try different landmarks to get the best fusion quality in both 2D and 3D view.

70 If the preview fusion doesn't show mismatching or gaps, change the 'Scale' to '100%' in Step 68 and run the final fusion to generate the new .sis file. Repeat Steps 62–69 to fuse each of the other parts of the volumetric scan into the new fused .sis file. For example, repeat the process three times to generate the final 3D fusion .sis file for the human pancreas, which contains four Arivis Vision4D image sets.

71 After finishing the whole organ fusion (Extended Data Fig. 5f), export a series of .tiff files by clicking 'File' → 'Export' → 'TIFF Exporter' and defining the file name in a new folder.

72 As the Arivis Vision4D exports all the .tiff files with different channels into the same folder, run 'Total Commander' software to rename each image and separate the channels. Click the 'Multiple rename tool' in the Total Commander, and repeat Step 51.

73 After all the images are renamed, run 'LZW TIFF 16bit' to compress all fused images in the saved folder.

? TROUBLESHOOTING

Imaris 3D visualization ● Timing ~0.5–2 d

▲ **CRITICAL** We describe below the essential steps to perform visualization with Imaris 3D. For a more detailed overview, please check the user guide on the Imaris website.

74 Convert the image set .tiff files to the .ims file format. To perform the file conversion, open the 'Imaris File Converter', and click 'Add Files' to load all .tiff images from the saved folder (Extended Data Fig. 6a).

75 When the .tiff files contain different channels, save the channel information during the conversion process by using the 'Settings' window. Select 'File name with delimiter', confirm the format as C"C"_Z"Z".tif, and click 'Start All' (Extended Data Fig. 6b).

76 Double click to open the converted .ims file, and proceed to adjust the voxel size by performing the following steps: 'Edit' → 'Image Properties' → 'Geomertry' → 'Voxel Size'; $X = 6.5$/objective, $Y = 6.5$/objective and $Z =$ 'z', where 'z' is the step size from the imaging microscopy setting.

Example: When choosing the 1× objective with a z step of 8 μm, the voxel size would be $X = 6.5$ μm, $Y = 6.5$ μm, $Z = 8$ μm; when choosing the 12× objective with a z step of 6 μm, the voxel size would be $X = 0.542$ μm, $Y = 0.542$ μm, $Z = 6$ μm (Extended Data Fig. 6c).

77 Once the voxel size is adjusted, proceed to change the channel colors and adjust the contrast: click 'Edit' → 'Show Display Adjustment' (Extended Data Fig. 6c).

78 Before rendering the 3D view, click 'Imaging Processing' → 'Camera Function' → 'Set The Angle Of The Camera'.

79 Select the region of interest, and capture an image in the 'Snapshot' menu. Click 'Snapshot' → 'Preferences' to set the size with DPI of 300 and save as Type (TIFF images) in the Image Output Directory.

Timing

Steps 1–5, perfusion, fixation and washing of human organs: 1–2 d
Step 6, organ pretreatment according to the experimental needs: 1–14 d
Steps 7–8, permeabilization and decolorization with CHAPS/NMDEA: 3–20 d
Step 9, delipidation: 7–50 d
Step 10, ECM loosening: 2–15 d
Steps 11–17, (optional) labeling: 7–15 d
Steps 18, clearing: 7–40 d
Steps 19–39, imaging with light-sheet fluorescent microscopy: 1–8 d
Steps 40–54, data stitching, renaming and compression: 1–2 d
Steps 55–73, Arivis fusion: 1–6 d
Steps 74–79, Imaris 3D visualization: ~0.5–2 d
See Table 3 for timing guidelines for treatment of various human organs.

Troubleshooting

Troubleshooting advice can be found in Table 4.

Table 4 | Troubleshooting table

Step	Problem	Possible reason	Solution
3	Undissolved deposits in dextran blood vessel labeling solution	Insufficient volume of dextran working solution	Prepare stock solutions and final dextran working solution mixture step by step
	Difficult to distinguish blood vessels from similar structures	Some organs have tubular structures that appear similar to blood vessels. For example, the urinary tract in kidney and the trachea in lung	Confirm the main arteries using an anatomy textbook as a reference, or ask experts for help
	Organ does not turn red after dextran injection	Blockages in blood vessels	Use higher pressure or a 50 ml syringe to inject dextran solution
4, 6, 7, 14	Solution leakage during active pumping	Disconnection or breakage of tubing	Replace tubing and continue pumping
15	Poor organ shrinkage after clearing	Insufficient incubation with ethanol	Increase incubation time with ethanol
17	The samples are not transparent enough and appear blurry under a microscope	The samples are not dehydrated enough	Make sure the organs are sufficiently dehydrated; organs are sufficiently dehydrated when they are no longer shrinking
		Insufficient incubation in BABB	Keep the sample in BABB until it becomes transparent
	Shade inside the sample	Insufficient light-sheet width	Ensure sufficient light-sheet width
		Light absorption by a high-cell-density region on surface of the organ	Try staining with a lower concentration of dye
	Blood vessel labeling only in some regions of the organs	The blood vessels of the organ are not intact	Collect the organs carefully, and try not to damage them
		Residual blood clot in the sample	Perfuse sample with sufficient amount of PBS and heparin before organ harvest
	Signal cannot be detected in the deeper tissue layer	Short-wavelength light cannot penetrate the tissue due to scattering	Use chemical probes or secondary antibodies coupled to fluorophores with near-infrared or longer-wavelength-emission spectra

Table continued

Table 4 (continued)

Step	Problem	Possible reason	Solution
	Staining worked only on the sample surface	Incubation times were too short, or antibody incubation buffer volumes were too small	Repeat staining starting from Step 9, gradually rehydrating samples. Also, increase incubation times and/or antibody incubation buffer volume
	Sample is not visible during the imaging	Sample is out of focus	Move the stage to find bright halos under objective, and adjust the contrast on the computer screen
	No positive signal, although the antibody works in immunofluorescent staining on tissue sections	Incompatibility with SHANEL protocol	Check antibody lists (Table 2 and Supplementary Table 1) or prototype with sections pretreated with SHANEL protocol
	Weak or nondetectable antibody signals	Insufficient antibody labeling or antibody incompatible with SHANEL protocol	Select an antibody from our verified antibody list or optimize the antibody staining conditions
	High autofluorescence	PFA fixation time is too long	Reduce PFA fixation time. Fix the sample in PFA less than 4 weeks. Change to PBS with sodium azide for long-term storage
18	Stitching failed with the tiling scans	Sample has movement during imaging	Use enough BABB-resistant glue to fix the sample or use a custom-made holder to fix the sample
	Shade inside the sample	Obstruction, such as bubbles	Remove obstruction, for example by using a syringe to withdraw bubbles
	Datasets are too large to analyze	Unnecessarily high *z*-resolution	Optimize the *Z* steps based on the maximum possible *z*-resolution of the lens
		Unnecessarily high overlapping percentage of mosaic	Optimize overlapping percentage
19	Misalignment of the stitched image	Sample moved during scanning	Perform manual stitching or make sure the sample is well fixed in the holder, and repeat imaging

Anticipated results

We described SHANEL in this protocol as a scalable tissue labeling and clearing method for a variety of human organs (Supplementary Video 4), including pancreas (Figs. 3–5) and kidney, and show additional vessel labeling of spleen, heart and lung (Fig. 5). Compared with our original publication[20], we also extended the original method to be compatible with hard human tissue with bone (Fig. 7). SHANEL allows imaging of intact human organs at cellular resolution, which paves the way for human organ mapping, and potentially extends our knowledge in human organ anatomy. The technique can be used to study vascular morphology and pathology, as the fine details of capillaries can be visualized throughout whole organ (Fig. 5).

We previously used SHANEL to label and quantify the pancreas islets in *INS*-EGFP transgenic pig[20], demonstrating the scalability of this method to study large-scale biological samples. SHANEL is also applicable to antibody staining in human tissue or biopsies (Fig. 6), increasing its adaptability in biomedical research.

After using the recently developed LSFM to image transparent human organs or tissues and to therefore acquire spatial information of vessels and fluorescent protein signal (Fig. 3, Extended Data Fig. 3), the whole dataset can be efficiently stitched with an easily operated software (Extended Data Fig. 4). Here we show an example of how raw images were processed and visualization of the entire 3D field and cellular states information was rapidly achieved (Extended Data Figs. 5, 6). Note that, owing to the size of human organs, terabytes of the image data will be generated. Consequently, we recommend combining our methodology with deep learning approaches to achieve accuracy and speed in quantification and further analysis. We summarize a workflow (Extended Data Fig. 7) that will be useful for researchers to understand the main steps of this protocol.

Data availability

The main data supporting the findings in this protocol are available within the paper and its Supplementary Information. The raw image files used to obtain Figs. 1–7, Extended Data Figs. 1–7 and Supplementary Videos 1–4 are available from the corresponding author on reasonable request.

References

1. Snyder, M. P. et al. The human body at cellular resolution: the NIH Human Biomolecular Atlas Program. *Nature* **574**, 187–192 (2019).
2. Rood, J. E. et al. Toward a common coordinate framework for the human body. *Cell* **179**, 1455–1467 (2019).
3. Rozenblatt-Rosen, O., Stubbington, M. J. T., Regev, A. & Teichmann, S. A. The Human Cell Atlas: from vision to reality. *Nature* **550**, 451–453 (2017).
4. Srivastava, S., Ghosh, S., Kagan, J. & Mazurchuk, R. The PreCancer Atlas (PCA). *Trends Cancer* **4**, 513–514 (2018).
5. Ardini-Poleske, M. E. et al. LungMAP: The Molecular Atlas of Lung Development Program. *Am. J. Physiol. Lung Cell Mol. Physiol.* **313**, L733–L740 (2017).
6. Amunts, K. et al. BigBrain: an ultrahigh-resolution 3D human brain model. *Science* **340**, 1472–1475 (2013).
7. Deverman, B. E. et al. Cre-dependent selection yields AAV variants for widespread gene transfer to the adult brain. *Nat. Biotechnol.* **34**, 204–209 (2016).
8. Erturk, A. et al. Three-dimensional imaging of solvent-cleared organs using 3DISCO. *Nat. Protoc.* **7**, 1983–1995 (2012).
9. Cai, R. et al. Panoptic imaging of transparent mice reveals whole-body neuronal projections and skull–meninges connections. *Nat. Neurosci.* **22**, 317–327 (2019).
10. Pan, C. et al. Shrinkage-mediated imaging of entire organs and organisms using uDISCO. *Nat. Methods* **13**, 859–867 (2016).
11. Park, Y.-G. et al. Protection of tissue physicochemical properties using polyfunctional crosslinkers. *Nat. Biotechnol.* **37**, 73–83 (2019).
12. Renier, N. et al. Mapping of brain activity by automated volume analysis of immediate early genes. *Cell* **165**, 1789–1802 (2016).
13. Belle, M. et al. Tridimensional visualization and analysis of early human development. *Cell* **169**, 161–173 e112 (2017).
14. Pan, C. et al. Deep learning reveals cancer metastasis and therapeutic antibody targeting in the entire body. *Cell* **179**, 1661–1676.e19 (2019).
15. Kubota, S. I. et al. Whole-body profiling of cancer metastasis with single-cell resolution. *Cell Rep.* **20**, 236–250 (2017).
16. Lai, H. M. et al. Next generation histology methods for three-dimensional imaging of fresh and archival human brain tissues. *Nat. Commun.* **9**, 1066 (2018).
17. Morawski, M. et al. Developing 3D microscopy with CLARITY on human brain tissue: Towards a tool for informing and validating MRI-based histology. *Neuroimage* **182**, 417–428 (2018).
18. Hildebrand, S., Schueth, A., Herrler, A., Galuske, R. & Roebroeck, A. Scalable labeling for cytoarchitectonic characterization of large optically cleared human neocortex samples. *Sci. Rep.* **9**, 10880 (2019).
19. Ku, T. et al. Elasticizing tissues for reversible shape transformation and accelerated molecular labeling. *Nat. Methods* **17**, 609–613 (2020).
20. Zhao, S. et al. Cellular and molecular probing of intact human organs. *Cell* **180**, 796–812 e719 (2020).
21. Murakami, T. C. et al. A three-dimensional single-cell-resolution whole-brain atlas using CUBIC-X expansion microscopy and tissue clearing. *Nat. Neurosci.* **21**, 625–637 (2018).
22. Matsumoto, K. et al. Advanced CUBIC tissue clearing for whole-organ cell profiling. *Nat. Protoc.* **14**, 3506–3537 (2019).
23. Susaki, E. A. et al. Whole-brain imaging with single-cell resolution using chemical cocktails and computational analysis. *Cell* **157**, 726–739 (2014).
24. Tainaka, K. et al. Whole-body imaging with single-cell resolution by tissue decolorization. *Cell* **159**, 911–924 (2014).
25. Chung, K. et al. Structural and molecular interrogation of intact biological systems. *Nature* **497**, 332–337 (2013).
26. Ku, T. et al. Multiplexed and scalable super-resolution imaging of three-dimensional protein localization in size-adjustable tissues. *Nat. Biotechnol.* **34**, 973–981 (2016).
27. Treweek, J. B. et al. Whole-body tissue stabilization and selective extractions via tissue-hydrogel hybrids for high-resolution intact circuit mapping and phenotyping. *Nat. Protoc.* **10**, 1860–1896 (2015).
28. Tainaka, K. et al. Chemical landscape for tissue clearing based on hydrophilic reagents. *Cell Rep.* **24**, 2196–2210 e2199 (2018).
29. Lai, H. M., Ng, W. L., Gentleman, S. M. & Wu, W. Chemical probes for visualizing intact animal and human brain tissue. *Cell Chem. Biol.* **24**, 659–672 (2017).
30. Cequier-Sánchez, E., Rodríguez, C., Ravelo, A. G. & Zárate, R. Dichloromethane as a solvent for lipid extraction and assessment of lipid classes and fatty acids from samples of different natures. *J. Agric. Food Chem.* **56**, 4297–4303 (2008).
31. Schmidt, M. M. et al. Collagen extraction process. *Int. Food Res. J.* **23**, 913–922 (2016).
32. Yanagishita, M., Podyma-Inoue, K. A. & Yokoyama, M. Extraction and separation of proteoglycans. *Glycoconj. J.* **26**, 953–959 (2009).
33. Todorov, M. I. et al. Machine learning analysis of whole mouse brain vasculature. *Nat. Methods* **17**, 442–449 (2020).

34. Ugryumova, N., Matcher, S. J. & Attenburrow, D. P. Measurement of bone mineral density via light scattering. *Phys. Med. Biol.* **49**, 469–483 (2004).
35. Greenbaum, A. et al. Bone CLARITY: clearing, imaging, and computational analysis of osteoprogenitors within intact bone marrow. *Sci. Transl. Med.* https://doi.org/10.1126/scitranslmed.aah6518 (2017).
36. Grüneboom, A. et al. A network of trans-cortical capillaries as mainstay for blood circulation in long bones. *Nat. Metab.* **1**, 236–250 (2019).
37. Gonzalez-Chavez, S. A., Pacheco-Tena, C., Macias-Vazquez, C. E. & Luevano-Flores, E. Assessment of different decalcifying protocols on osteopontin and osteocalcin immunostaining in whole bone specimens of arthritis rat model by confocal immunofluorescence. *Int. J. Clin. Exp. Pathol.* **6**, 1972–1983 (2013).
38. Savi, F. M., Brierly, G. I., Baldwin, J., Theodoropoulos, C. & Woodruff, M. A. Comparison of different decalcification methods using rat mandibles as a model. *J. Histochem. Cytochem.* **65**, 705–722 (2017).
39. Liu, A. K. et al. Bringing CLARITY to the human brain: visualization of Lewy pathology in three dimensions. *Neuropathol. Appl. Neurobiol.* **42**, 573–587 (2016).
40. Murray, E. et al. Simple, scalable proteomic imaging for high-dimensional profiling of intact systems. *Cell* **163**, 1500–1514 (2015).
41. Perbellini, F. et al. Free-of-Acrylamide SDS-based Tissue Clearing (FASTClear) for three dimensional visualization of myocardial tissue. *Sci. Rep.* **7**, 5188 (2017).
42. Nojima, S. et al. CUBIC pathology: three-dimensional imaging for pathological diagnosis. *Sci. Rep.* **7**, 9269 (2017).
43. Jensen, K. H. & Berg, R. W. CLARITY-compatible lipophilic dyes for electrode marking and neuronal tracing. *Sci. Rep.* **6**, 32674 (2016).
44. Mann, D. M., Yates, P. O. & Stamp, J. E. The relationship between lipofuscin pigment and ageing in the human nervous system. *J. Neurol. Sci.* **37**, 83–93 (1978).
45. Schnell, S. A., Staines, W. A. & Wessendorf, M. W. Reduction of lipofuscin-like autofluorescence in fluorescently labeled tissue. *J. Histochem. Cytochem.* **47**, 719–730 (1999).
46. Neumann, M. & Gabel, D. Simple method for reduction of autofluorescence in fluorescence microscopy. *J. Histochem. Cytochem.* **50**, 437–439 (2002).
47. Yang, J. et al. Quenching autofluorescence in tissue immunofluorescence [version 1; peer review: 2 approved with reservations, 1 not approved]. *Wellcome Open Res.* https://doi.org/10.12688/wellcomeopenres.12251.1 (2017).
48. Helsby, M. A. et al. CiteAb: a searchable antibody database that ranks antibodies by the number of times they have been cited. *BMC Cell Biol.* **15**, 6 (2014).
49. Voigt, F. F. et al. The mesoSPIM initiative: open-source light-sheet microscopes for imaging cleared tissue. *Nat. Methods* **16**, 1105–1108 (2019).
50. Preibisch, S., Saalfeld, S. & Tomancak, P. Globally optimal stitching of tiled 3D microscopic image acquisitions. *Bioinformatics* **25**, 1463–1465 (2009).

Acknowledgements

We thank A. Ghasemi Mag for developing the Python script ‘Stitching.py’ to stitch sequences of images. We thank I. Horvath, K. Joseph, K. Biniossek and E. Süheda for revising the manuscript. We thank Miltenyi Biotec for providing the PE-conjugated antibodies. A schematic of the SHANEL pipeline (Fig. 1) was created with BioRender.com. This work was supported by the Vascular Dementia Research Foundation, Deutsche Forschungsgemeinschaft (DFG, German Research Foundation) under Germany’s Excellence Strategy within the framework of the Munich Cluster for Systems Neurology (EXC 2145 SyNergy, ID 390857198) and DFG (SFB 1052, project A9; TR 296 project 03), H.M. and Z.R. would like to thank the China Scholarship Council (CSC) for the financial support (no. 201806780034 and no. 201806310110).

Author contributions

A.E. conceived and led the project. S.Z. developed the original SHANEL protocol. H.M., Z.R. and S.Z. performed the experiments and wrote the manuscript. R.C. performed the antibody screening. H.S. and I.B. dissected and provided the human organs. All authors commented on the manuscript text.

Competing interests

A.E. and S.Z. have filed a patent on the SHANEL technology described in this protocol.

Additional information

Extended data is available for this paper at https://doi.org/10.1038/s41596-022-00712-8.

Supplementary information The online version contains supplementary material available at https://doi.org/10.1038/s41596-022-00712-8.

Correspondence and requests for materials should be addressed to Ali Ertürk.

Peer review information *Nature Protocols* thanks Etsuo A. Susaki and the other, anonymous, reviewer(s) for their contribution to the peer review of this work.

Received: 6 April 2021; Accepted: 5 April 2022;

Related links

Key reference using this protocol

Zhao, S. et al. *Cell* **180**, 796–812 (2020): https://doi.org/10.1016/j.cell.2020.01.030

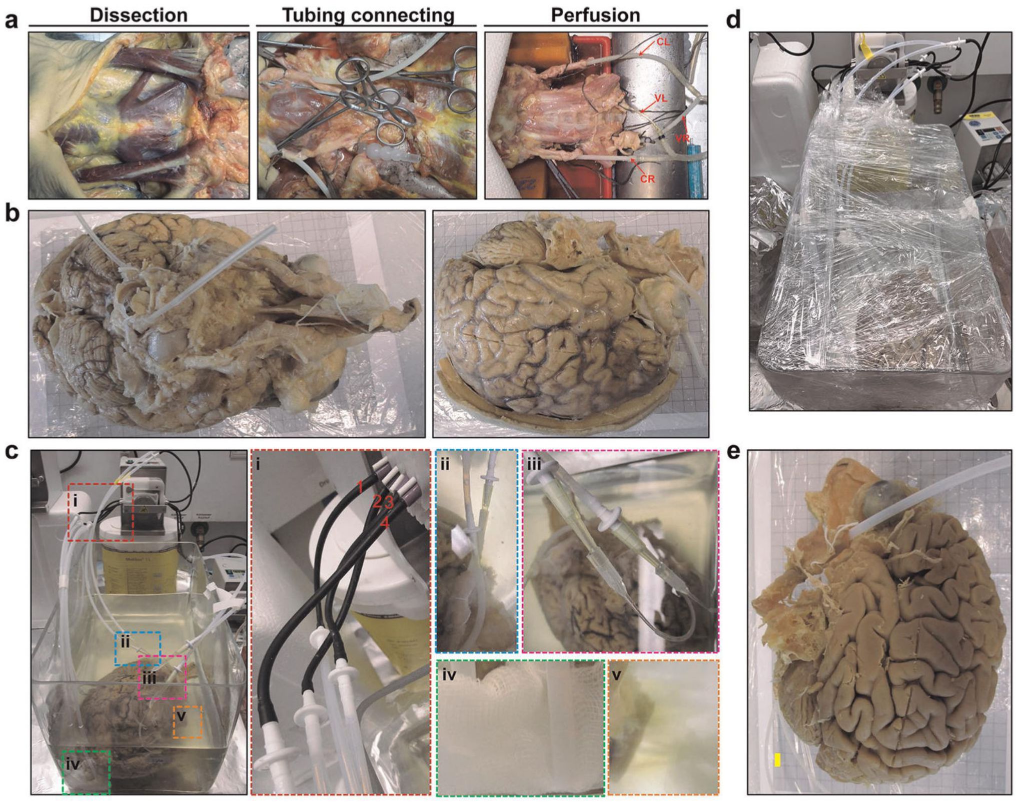

Extended Data Fig. 1 | Human brain clearing by perfusion system. a, The dissection of human brain with CL and CR (left and right carotids, respectively), VL and VR (left and right vertebral arteries, respectively). **b**, The human brain after dissection and fixation. **c**, The setup to clear a human brain by perfusion system under the fume hood. The human brain was put in a glass container and connected with input and output tubing controlled by a peristaltic pump. There are four channels controlling the four connecting tubes as indicated in **c** (i). Two output tubes are connected to the carotid arteries as shown in **c** (ii), and two output tubes are connected to the vertebral arteries as shown in **c** (iii). The input tubes are protected with gauze to avoid solid impurities entering and blocking the tubing (see **c** (iv)). **c** (v) shows the decolorization effects of CHAPS/NMDEA that manifest as the blooming of dark-green color from the organ. **d**, The glass container was sealed with several layers of plastic wrap to prevent evaporation of the running solutions, especially EtOH, DCM and MeOH. **e**, Photo of human brain after SHANEL pretreatment and before clearing. Remaining blood in the vessels (**b**) was decolorized.

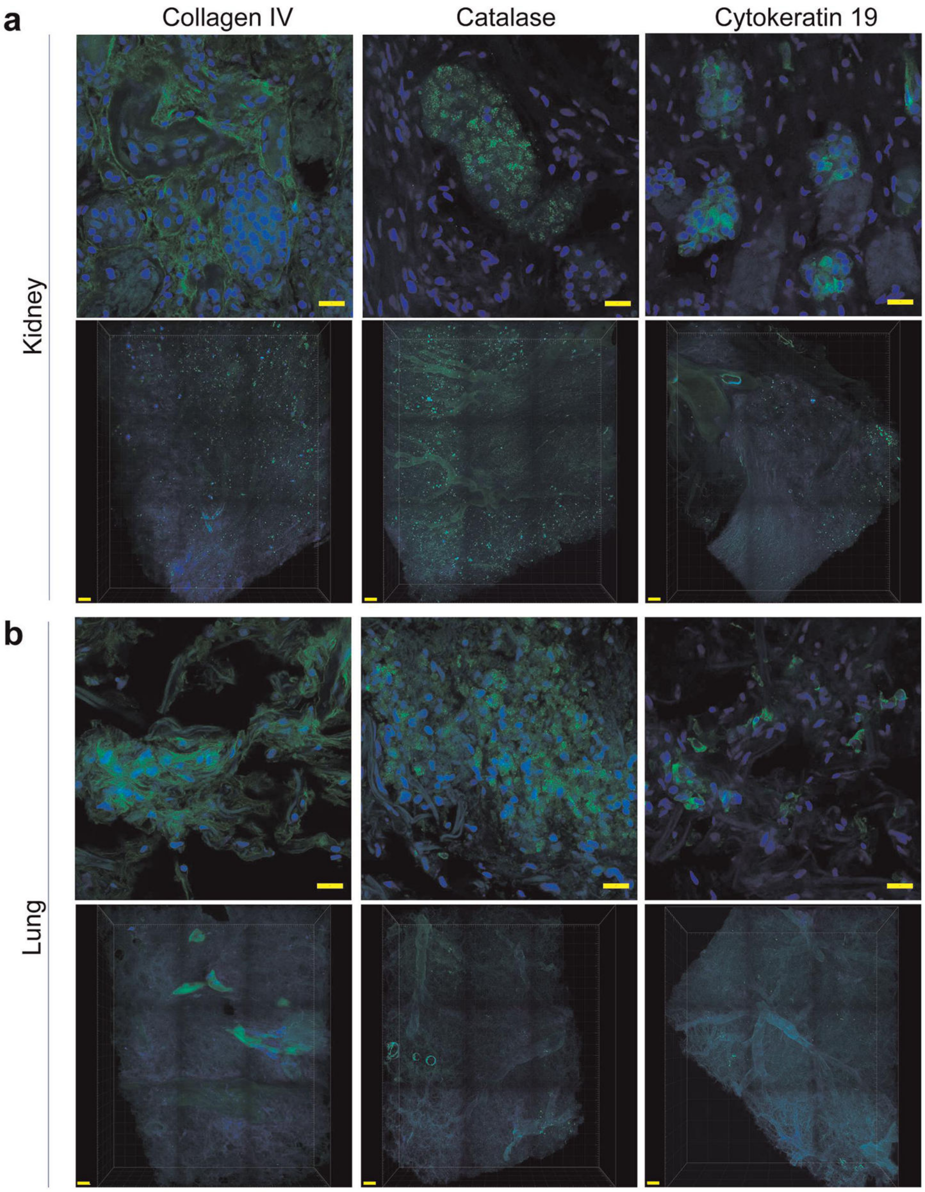

Extended Data Fig. 2 | Passively stained conjugated antibody in centimeter-size human kidney and lung tissue. a,**b**, Collagen IV, catalase and cytokeratin 19 antibody staining (green) in human kidney (**a**) and lung (**b**). Top panel in **a** and **b** shows immunofluorescent staining images obtained by confocal microscopy to verify antibody compatibility with SHANEL. Bottom panel shows 3D reconstruction of tissue with antibody labeling in Imaris. Scale bars, 20 µm and 500 µm, respectively.

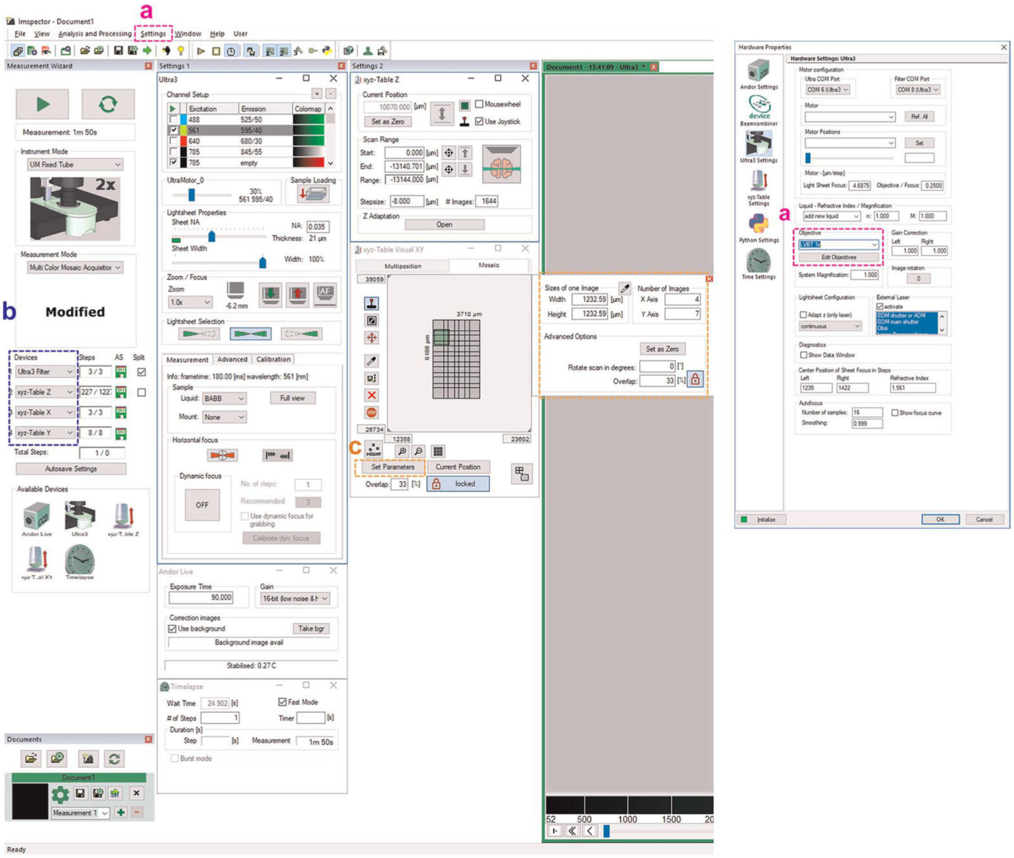

Extended Data Fig. 3 | Imaging software settings. The user interface of LaVision Imspector software. **a**, Settings of the objective lens and magnification. **b**, Names of the devices should be listed in the correct order. **c**, One example for settings of the tiling scan with 4 × 7 tiles and 33% overlap.

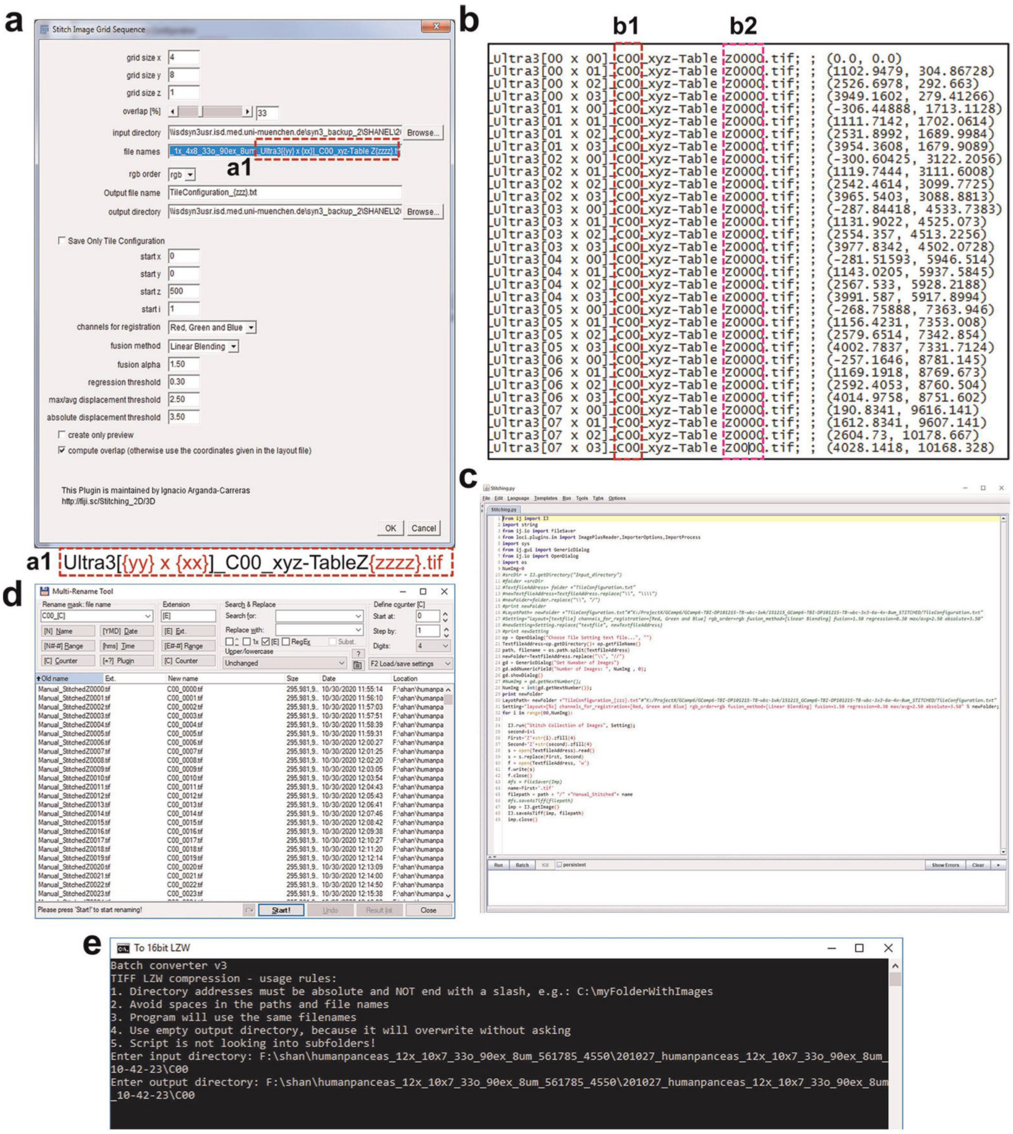

Stitch Image Grid Sequence

grid size x: 4
grid size y: 8
grid size z: 1
overlap [%]: 33
input directory: \\isdsyn3usr.isd.med.uni-muenchen.de\syn3_backup_2\SHANEL\2
file names: _1x_4x8_33o_90ex_8um_Ultra3[{yy} x {xx}]_C00_xyz-Table Z{zzzz}.t
rgb order: rgb
Output file name: TileConfiguration_{zzz}.txt
output directory: \\isdsyn3usr.isd.med.uni-muenchen.de\syn3_backup_2\SHANEL\2

☐ Save Only Tile Configuration

start x: 0
start y: 0
start z: 500
start i: 1
channels for registration: Red, Green and Blue
fusion method: Linear Blending
fusion alpha: 1.50
regression threshold: 0.30
max/avg displacement threshold: 2.50
absolute displacement threshold: 3.50

☐ create only preview

☑ compute overlap (otherwise use the coordinates given in the layout file)

This Plugin is maintained by Ignacio Arganda-Carreras
http://fiji.sc/Stitching_2D/3D

OK Cancel

a1 Ultra3[{yy} x {xx}]_C00_xyz-TableZ{zzzz}.tif

```
_Ultra3[00 x 00]_C00_xyz-Table Z0000.tif; ; (0.0, 0.0)
_Ultra3[00 x 01]_C00_xyz-Table Z0000.tif; ; (1102.9479, 304.86728)
_Ultra3[00 x 02]_C00_xyz-Table Z0000.tif; ; (2526.6978, 292.663)
_Ultra3[00 x 03]_C00_xyz-Table Z0000.tif; ; (3949.1602, 279.41266)
_Ultra3[01 x 00]_C00_xyz-Table Z0000.tif; ; (-306.44888, 1713.1128)
_Ultra3[01 x 01]_C00_xyz-Table Z0000.tif; ; (1111.7142, 1702.0614)
_Ultra3[01 x 02]_C00_xyz-Table Z0000.tif; ; (2531.8992, 1689.9984)
_Ultra3[01 x 03]_C00_xyz-Table Z0000.tif; ; (3954.3608, 1679.9089)
_Ultra3[02 x 00]_C00_xyz-Table Z0000.tif; ; (-300.60425, 3122.2056)
_Ultra3[02 x 01]_C00_xyz-Table Z0000.tif; ; (1119.7444, 3111.6008)
_Ultra3[02 x 02]_C00_xyz-Table Z0000.tif; ; (2542.4614, 3099.7725)
_Ultra3[02 x 03]_C00_xyz-Table Z0000.tif; ; (3965.5403, 3088.8813)
_Ultra3[03 x 00]_C00_xyz-Table Z0000.tif; ; (-287.84418, 4533.7383)
_Ultra3[03 x 01]_C00_xyz-Table Z0000.tif; ; (1131.9022, 4525.073)
_Ultra3[03 x 02]_C00_xyz-Table Z0000.tif; ; (2554.357, 4513.2256)
_Ultra3[03 x 03]_C00_xyz-Table Z0000.tif; ; (3977.8342, 4502.0728)
_Ultra3[04 x 00]_C00_xyz-Table Z0000.tif; ; (-281.51593, 5946.514)
_Ultra3[04 x 01]_C00_xyz-Table Z0000.tif; ; (1143.0205, 5937.5845)
_Ultra3[04 x 02]_C00_xyz-Table Z0000.tif; ; (2567.533, 5928.2188)
_Ultra3[04 x 03]_C00_xyz-Table Z0000.tif; ; (3991.587, 5917.8994)
_Ultra3[05 x 00]_C00_xyz-Table Z0000.tif; ; (-268.75888, 7363.946)
_Ultra3[05 x 01]_C00_xyz-Table Z0000.tif; ; (1156.4231, 7353.008)
_Ultra3[05 x 02]_C00_xyz-Table Z0000.tif; ; (2579.6514, 7342.854)
_Ultra3[05 x 03]_C00_xyz-Table Z0000.tif; ; (4002.7837, 7331.7124)
_Ultra3[06 x 00]_C00_xyz-Table Z0000.tif; ; (-257.1646, 8781.145)
_Ultra3[06 x 01]_C00_xyz-Table Z0000.tif; ; (1169.1918, 8769.673)
_Ultra3[06 x 02]_C00_xyz-Table Z0000.tif; ; (2592.4053, 8760.504)
_Ultra3[06 x 03]_C00_xyz-Table Z0000.tif; ; (4014.9758, 8751.602)
_Ultra3[07 x 00]_C00_xyz-Table Z0000.tif; ; (190.8341, 9616.141)
_Ultra3[07 x 01]_C00_xyz-Table Z0000.tif; ; (1612.8341, 9607.141)
_Ultra3[07 x 02]_C00_xyz-Table Z0000.tif; ; (2604.73, 10178.667)
_Ultra3[07 x 03]_C00_xyz-Table Z0000.tif; ; (4028.1418, 10168.328)
```

```
from ij import IJ
import string
from ij.io import FileSaver
from loci.plugins.in import ImagePlusReader,ImporterOptions,ImportProcess
import sys
from ij.gui import GenericDialog
from ij.io import OpenDialog
import os
NumImg=0
#srcDir = IJ.getDirectory("Input_directory")
#folder =srcDir
#TextfileAddress= folder +"TileConfiguration.txt"
#newTextfileAddress=TextfileAddress.replace("\\", "\\\\")
#newFolder=folder.replace("\\", "/")
#print newFolder
#LayotPath= newFolder +"TileConfiguration.txt"#"K:/ProjectX/GCamp6/GCamp6-TBI-DP101215-TB-wbc-1wk/151215_GCamp6-TBI-DP101215-TB-wbc-3x3-6o-4x-8um_STITCHED/TileConfiguration.txt"
#Setting="layout=[textfile] channels_for_registration=[Red, Green and Blue] rgb_order=rgb fusion_method=[Linear Blending] fusion=1.50 regression=0.30 max/avg=2.50 absolute=3.50"
#newSetting=Setting.replace("textfile", newTextfileAddress)
#print newSetting
op = OpenDialog("Choose Tile Setting text file...", "")
TextfileAddress=op.getDirectory()+ op.getFileName()
path, filename = os.path.split(TextfileAddress)
newFolder=TextfileAddress.replace("\\", "//")
gd = GenericDialog("Get Numaber of Images")
gd.addNumericField("Number of Images: ", NumImg , 0);
gd.showDialog()
#NumImg = gd.getNextNumber();
NumImg = int(gd.getNextNumber());
print newFolder
LayotPath= newFolder +"TileConfiguration_{zzz}.txt"#"K:/ProjectX/GCamp6/GCamp6-TBI-DP101215-TB-wbc-1wk/151215_GCamp6-TBI-DP101215-TB-wbc-3x3-6o-4x-8um_STITCHED/TileConfiguration.txt"
Setting="layout=[%s] channels_for_registration=[Red, Green and Blue] rgb_order=rgb fusion_method=[Linear Blending] fusion=1.50 regression=0.30 max/avg=2.50 absolute=3.50" % newFolder;
for i in range(00,NumImg):

  IJ.run("Stitch Collection of Images", Setting);
  second=i+1
  First='Z'+str(i).zfill(4)
  Second='Z'+str(second).zfill(4)
  s = open(TextfileAddress).read()
  s = s.replace(First, Second)
  f = open(TextfileAddress, 'w')
  f.write(s)
  f.close()
  #fs = FileSaver(Imp)
  name=First+'.tif'
  filepath = path + "/" +"Manual_Stitched"+ name
  #fs.saveAsTiff(filepath)
  imp = IJ.getImage()
  IJ.saveAsTiff(imp, filepath)
  imp.close()
```

Multi-Rename Tool

Rename mask: file name: C00_[C]
Extension: [E]
Search for:
Replace with:
☐ ^ ☐ 1x ☑ [E] ☐ RegEx ☐ Subst.
Upper/lowercase: Unchanged
Define counter [C]
Start at: 0
Step by: 1
Digits: 4

[N] Name [YMD] Date [E] Ext. [N#-#] Range [hms] Time [E#-#] Range [C] Counter [=?] Plugin [C] Counter ? F2 Load/save settings

Old name	Ext.	New name	Size	Date	Location
Manual_StitchedZ0000.tif		C00_0000.tif	295,981,9...	10/30/2020 11:55:14	F:\shan\humanpa
Manual_StitchedZ0001.tif		C00_0001.tif	295,981,9...	10/30/2020 11:56:10	F:\shan\humanpa
Manual_StitchedZ0002.tif		C00_0002.tif	295,981,9...	10/30/2020 11:57:03	F:\shan\humanpa
Manual_StitchedZ0003.tif		C00_0003.tif	295,981,9...	10/30/2020 11:57:51	F:\shan\humanpa
Manual_StitchedZ0004.tif		C00_0004.tif	295,981,9...	10/30/2020 11:58:39	F:\shan\humanpa
Manual_StitchedZ0005.tif		C00_0005.tif	295,981,9...	10/30/2020 11:59:31	F:\shan\humanpa
Manual_StitchedZ0006.tif		C00_0006.tif	295,981,9...	10/30/2020 12:00:27	F:\shan\humanpa
Manual_StitchedZ0007.tif		C00_0007.tif	295,981,9...	10/30/2020 12:01:25	F:\shan\humanpa
Manual_StitchedZ0008.tif		C00_0008.tif	295,981,9...	10/30/2020 12:02:20	F:\shan\humanpa
Manual_StitchedZ0009.tif		C00_0009.tif	295,981,9...	10/30/2020 12:03:05	F:\shan\humanpa
Manual_StitchedZ0010.tif		C00_0010.tif	295,981,9...	10/30/2020 12:03:54	F:\shan\humanpa
Manual_StitchedZ0011.tif		C00_0011.tif	295,981,9...	10/30/2020 12:04:43	F:\shan\humanpa
Manual_StitchedZ0012.tif		C00_0012.tif	295,981,9...	10/30/2020 12:05:43	F:\shan\humanpa
Manual_StitchedZ0013.tif		C00_0013.tif	295,981,9...	10/30/2020 12:06:41	F:\shan\humanpa
Manual_StitchedZ0014.tif		C00_0014.tif	295,981,9...	10/30/2020 12:07:46	F:\shan\humanpa
Manual_StitchedZ0015.tif		C00_0015.tif	295,981,9...	10/30/2020 12:08:42	F:\shan\humanpa
Manual_StitchedZ0016.tif		C00_0016.tif	295,981,9...	10/30/2020 12:09:38	F:\shan\humanpa
Manual_StitchedZ0017.tif		C00_0017.tif	295,981,9...	10/30/2020 12:10:27	F:\shan\humanpa
Manual_StitchedZ0018.tif		C00_0018.tif	295,981,9...	10/30/2020 12:11:20	F:\shan\humanpa
Manual_StitchedZ0019.tif		C00_0019.tif	295,981,9...	10/30/2020 12:12:14	F:\shan\humanpa
Manual_StitchedZ0020.tif		C00_0020.tif	295,981,9...	10/30/2020 12:13:09	F:\shan\humanpa
Manual_StitchedZ0021.tif		C00_0021.tif	295,981,9...	10/30/2020 12:14:00	F:\shan\humanpa
Manual_StitchedZ0022.tif		C00_0022.tif	295,981,9...	10/30/2020 12:14:50	F:\shan\humanpa
Manual_StitchedZ0023.tif		C00_0023.tif	295,981,9...	10/30/2020 12:15:38	F:\shan\humanpa

Please press 'Start!' to start renaming!

Start! Undo Result list Close

To 16bit LZW

```
Batch converter v3
TIFF LZW compression - usage rules:
1. Directory addresses must be absolute and NOT end with a slash, e.g.: C:\myFolderWithImages
2. Avoid spaces in the paths and file names
3. Program will use the same filenames
4. Use empty output directory, because it will overwrite without asking
5. Script is not looking into subfolders!
Enter input directory: F:\shan\humanpanceas_12x_10x7_33o_90ex_8um_561785_4550\201027_humanpanceas_12x_10x7_33o_90ex_8um_
10-42-23\C00
Enter output directory: F:\shan\humanpanceas_12x_10x7_33o_90ex_8um_561785_4550\201027_humanpanceas_12x_10x7_33o_90ex_8um
_10-42-23\C00
```

Extended Data Fig. 4 | Key steps for data stitching, renaming and compression. a, One example for correcting information in 'Stitching Image Grid Sequence'; a1 highlights the replacement of red letters in Step 42 about 'file names'. **b**, The key information of 'TileConfiguration' txt file; b1 highlights the responding channel number that should be corrected and saved in the respective separate folder, and b2 highlights that the starting *Z* number should be '0000' for all 'TileConfiguration' files. **c**, The information of 'Stitching.py'. **d**, One example for settings of 'Multi-Rename Tool. **e**, One example of compressing tiff files with 'LZW TIFF'. Panel **a** produced with software from ref. [50], Oxford University Press.

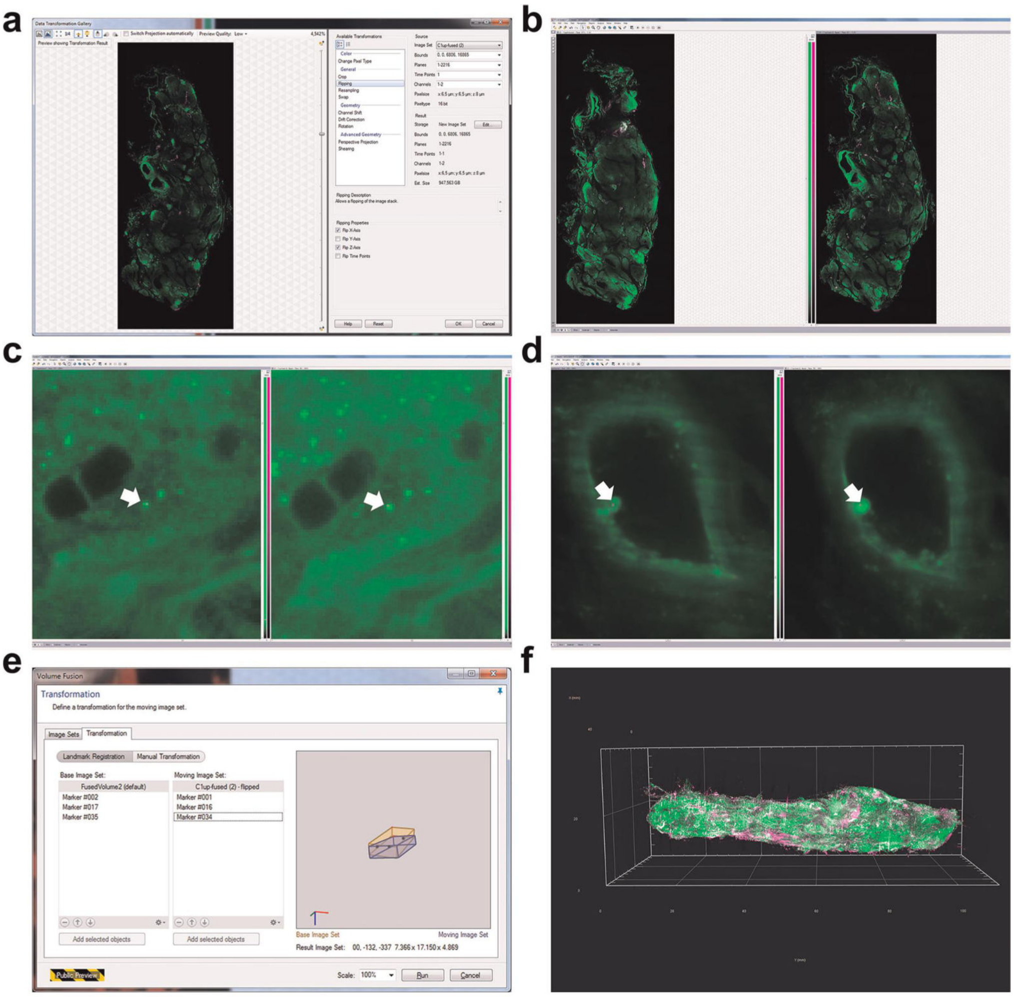

Source
Image Set: C1up-fused (2)
Bounds: 0, 0, 6806, 16865
Planes: 1-2216
Time Points: 1
Channels: 1-2
Pixelsize: x:6.5 µm; y:6.5 µm; z:8 µm
Pixeltype: 16 bit

Result
Storage: New Image Set
Bounds: 0, 0, 6806, 16865
Planes: 1-2216
Time Points: 1-1
Channels: 1-2
Pixelsize: x:6.5 µm; y:6.5 µm; z:8 µm
Est. Size: 947,563 GB

Flipping Description
Allows a flipping of the image stack.

Flipping Properties
☑ Flip X-Axis
☐ Flip Y-Axis
☑ Flip Z-Axis
☐ Flip Time Points

Transformation
Define a transformation for the moving image set.

Base Image Set: FusedVolume2 (default)
Marker #002
Marker #017
Marker #035

Moving Image Set: C1up-fused (2) - flipped
Marker #001
Marker #016
Marker #034

Result Image Set: 00, -132, -337 7.366 x 17.150 x 4.869
Scale: 100%

Extended Data Fig. 5 | Key steps for Arivis fusion of 3D images. a, An example of flipping one set of volumetric dataset in *X*, *Y* or *Z* direction to match with another volumetric dataset. **b**, Overview of two volumetric datasets oriented in the same *XYZ* direction after flipping. **c**,**d**, Examples of identical structural markers from two volumetric datasets for fusion. **e**, Loading of three key markers for optimal fusion. **f**, 3D fused image of pancreas from two volumetric datasets.

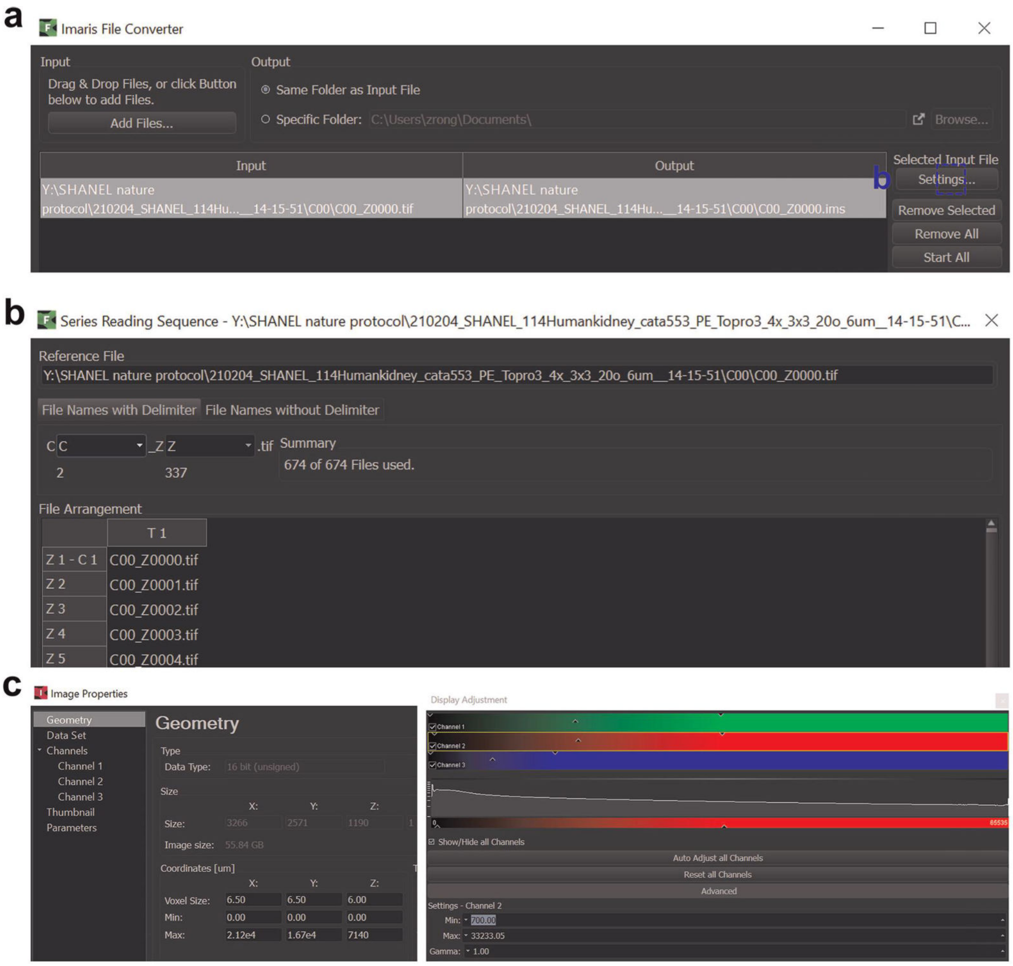

a

Output: ● Same Folder as Input File

○ Specific Folder: C:\Users\zrong\Documents\

Input	Output
Y:\SHANEL nature protocol\210204_SHANEL_114Hu...__14-15-51\C00\C00_Z0000.tif	Y:\SHANEL nature protocol\210204_SHANEL_114Hu...__14-15-51\C00\C00_Z0000.ims

b

Reference File

Y:\SHANEL nature protocol\210204_SHANEL_114Humankidney_cata553_PE_Topro3_4x_3x3_20o_6um__14-15-51\C00\C00_Z0000.tif

C C _Z Z .tif

2 337

Summary

674 of 674 Files used.

File Arrangement

	T 1
Z 1 - C 1	C00_Z0000.tif
Z 2	C00_Z0001.tif
Z 3	C00_Z0002.tif
Z 4	C00_Z0003.tif
Z 5	C00_Z0004.tif

c

Geometry

Type

Data Type: 16 bit (unsigned)

Size

	X:	Y:	Z:
Size:	3266	2571	1190

Image size: 55.84 GB

Coordinates [um]

	X:	Y:	Z:
Voxel Size:	6.50	6.50	6.00
Min:	0.00	0.00	0.00
Max:	2.12e4	1.67e4	7140

☑ Show/Hide all Channels

Settings - Channel 2

Min: 700.00

Max: 33233.05

Gamma: 1.00

Extended Data Fig. 6 | Key steps for Imaris data loading and visualization. a, An example of converting a stitched image sequence data to the .ims format using Imaris File Converter. **b**, The settings for file names with a delimiter should be changed to 'C _ Z.tif'. **c**, 3D image properties including *XYZ* voxel size and channel color can be set in Imaris for analysis.

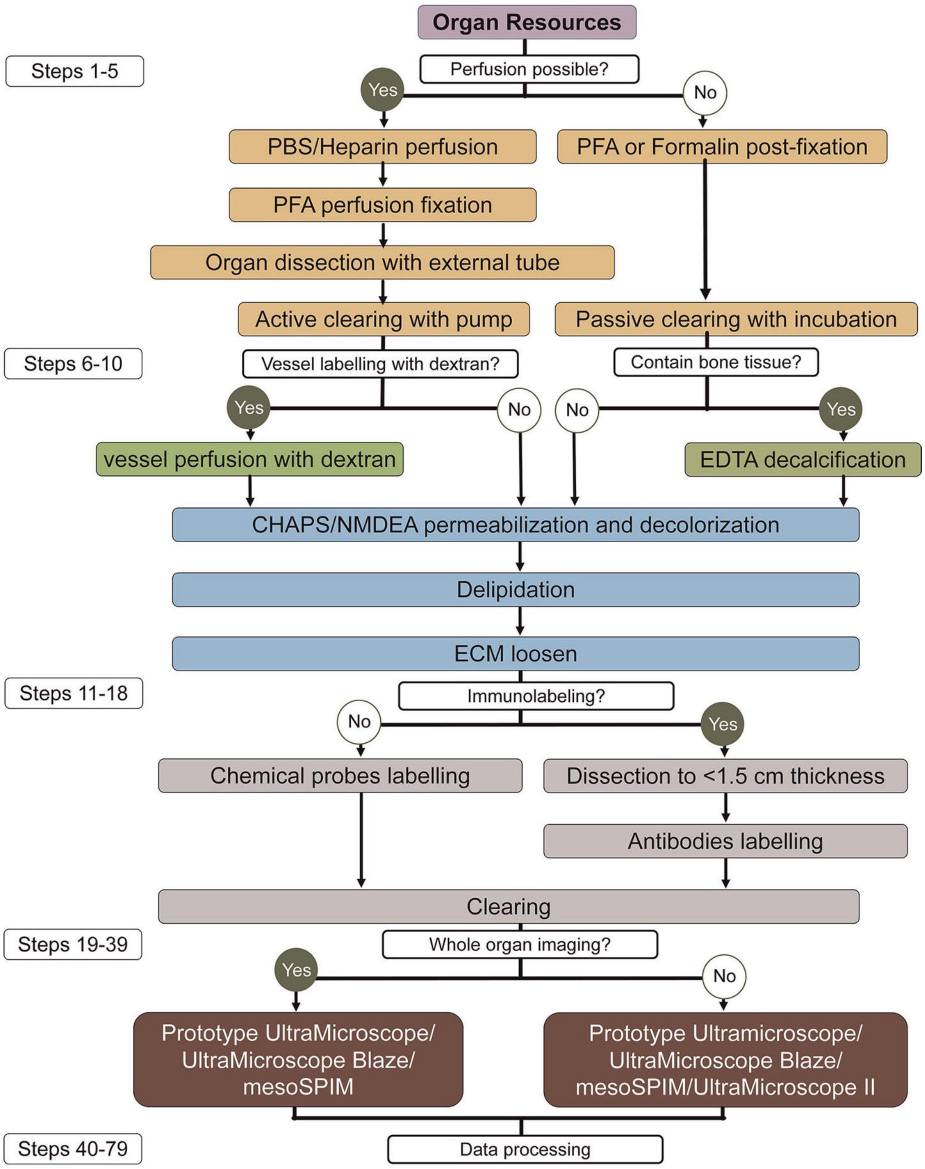

Extended Data Fig. 7 | Overview of SHANEL workflow. This workflow summarizes the main steps after organ collection: experimental setup (Steps 1–5), pretreatments (Steps 6–10), labeling and clearing (Steps 11–18), imaging (Steps 19–39) and data processing (Steps 40–79). We describe two ways of handling samples: active perfusion with a pump, if the blood vessels can be connected with external tubes, and passive incubation on a shaker. We also outline the differences in the procedure that are dependent on the organ components, organ size, targeted labeling and imaging equipment.

5. Paper II

Resource

Cell

Cellular and Molecular Probing of Intact Human Organs

Graphical Abstract

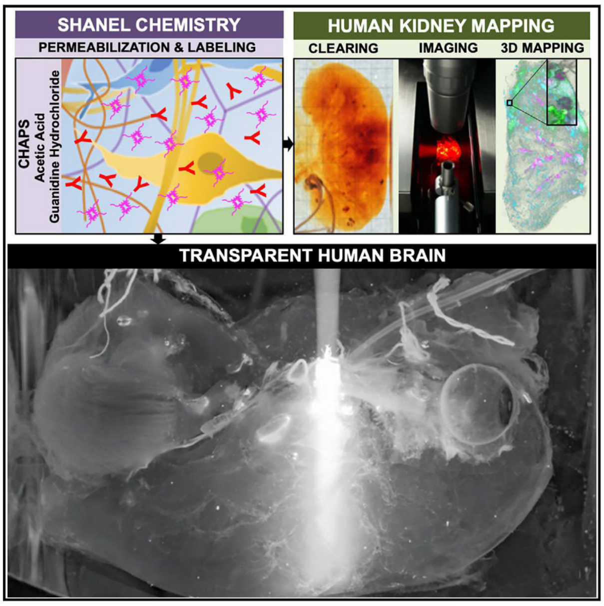

Highlights

- CHAPS forms smaller micelles allowing full permeabilization of aged human organs
- SHANEL enables centimeters deep molecular labeling and clearing of whole human organs
- SHANEL renders intact adult human brain and kidney transparent
- Deep learning and light-sheet microscopy with SHANEL allows human organ mapping

Authors

Shan Zhao, Mihail Ivilinov Todorov,
Ruiyao Cai, ..., Eckhard Wolf,
Ingo Bechmann, Ali Ertürk

Correspondence

erturk@helmholtz-muenchen.de

In Brief

Zhao et al. present an approach for intact human organ mapping that uses a new tissue permeabilization method to clear and deeply label whole organs followed by light-sheet microscopy imaging and a deep learning-based pipeline for 3D reconstruction and data analysis.

Zhao et al., 2020, Cell *180*, 796–812
February 20, 2020 © 2020 Elsevier Inc.
https://doi.org/10.1016/j.cell.2020.01.030

CellPress

Cell

Resource

Cellular and Molecular Probing of Intact Human Organs

Shan Zhao,[1,2,3] Mihail Ivilinov Todorov,[1,2,4] Ruiyao Cai,[1,2] Rami Al -Maskari,[2,5,6,7] Hanno Steinke,[8] Elisabeth Kemter,[9,10,11] Hongcheng Mai,[1,2] Zhouyi Rong,[1,2] Martin Warmer,[12] Karen Stanic,[1] Oliver Schoppe,[5,6] Johannes Christian Paetzold,[5,6,7] Benno Gesierich,[2] Milagros N. Wong,[13] Tobias B. Huber,[13] Marco Duering,[2,14] Oliver Thomas Bruns,[12] Bjoern Menze,[5,6,7] Jan Lipfert,[15] Victor G. Puelles,[13,16] Eckhard Wolf,[9,10,11] Ingo Bechmann,[8] and Ali Ertürk[1,2,14,17,*]

[1] Insititute for Tissue Engineering and Regenerative Medicine (iTERM), Helmholtz Zentrum München, 85764 Neuherberg, Germany
[2] Institute for Stroke and Dementia Research (ISD), University Hospital, Ludwig Maximilian University of Munich (LMU), 81377 Munich, Germany
[3] Munich Medical Research School (MMRS), 80336 Munich, Germany
[4] Graduate School of Neuroscience (GSN), 82152 Munich, Germany
[5] Department of Computer Science, Technical University of Munich (TUM), 81675 Munich, Germany
[6] Center for Translational Cancer Research (TranslaTUM) of the TUM, 80798 Munich, Germany
[7] Graduate School of Bioengineering, Technical University of Munich (TUM), 85748 Munich, Germany
[8] Institute of Anatomy, University of Leipzig, 04109 Leipzig, Germany
[9] Institute of Molecular Animal Breeding and Biotechnology, Gene Center, Ludwig Maximilian University of Munich (LMU), 81377 Munich, Germany
[10] Center for Innovative Medical Models (CiMM), 85764 Oberschleißheim, Germany
[11] German Center for Diabetes Research (DZD), 85764 Neuherberg, Germany
[12] Helmholtz Pioneer Campus, Helmholtz Zentrum München, 85764 Neuherberg, Germany
[13] III. Department of Medicine, University Medical Center Hamburg-Eppendorf, 20246 Hamburg, Germany
[14] Munich Cluster for Systems Neurology (SyNergy), 81377 Munich, Germany
[15] Department of Physics and Center for Nanoscience, Ludwig Maximilian University of Munich (LMU), 80799 Munich, Germany
[16] Department of Nephrology, Monash Health, and Center for Inflammatory Diseases, Monash University, Melbourne VIC 3168, Australia
[17] Lead Contact
*Correspondence: erturk@helmholtz-muenchen.de

https://doi.org/10.1016/j.cell.2020.01.030

SUMMARY

Optical tissue transparency permits scalable cellular and molecular investigation of complex tissues in 3D. Adult human organs are particularly challenging to render transparent because of the accumulation of dense and sturdy molecules in decades-aged tissues. To overcome these challenges, we developed SHANEL, a method based on a new tissue permeabilization approach to clear and label stiff human organs. We used SHANEL to render the intact adult human brain and kidney transparent and perform 3D histology with antibodies and dyes in centimeters-depth. Thereby, we revealed structural details of the intact human eye, human thyroid, human kidney, and transgenic pig pancreas at the cellular resolution. Furthermore, we developed a deep learning pipeline to analyze millions of cells in cleared human brain tissues within hours with standard lab computers. Overall, SHANEL is a robust and unbiased technology to chart the cellular and molecular architecture of large intact mammalian organs.

INTRODUCTION

Structural and functional mapping of human organs is of a great interest for diverse biomedical studies. For example, mapping the human brain has been a major target of research as many countries have initiated their own ‘‘human brain mapping’’ projects (Reardon, 2016). Furthermore, tissue engineering efforts demand cellular maps of human organs to replicate large-scale human tissues and organs by emerging technologies including 3D-bioprinting (Kang et al., 2016; Murphy and Atala, 2014). Yet, the progress in mapping intact human organs has been limited, especially in deciphering the anatomical complexity, mainly due to a lack of scalable technologies to image human organs at the cellular level. Although magnetic resonance imaging (MRI) can provide longitudinal imaging for human organs including the brain and kidney, it lacks cellular resolution (Despotović et al., 2015; Heusch et al., 2014; Sijens et al., 2010). Therefore, tissue histology has been the major approach to study the molecular and cellular complexity of the human organs. Although routine standard histology is limited to small pieces of the human brain (typically a tissue section is ~1/10,000,000 of the whole brain volume), there have been efforts to perform histology for whole human brain mapping (Amunts et al., 2013; Ding et al., 2016). However, slicing and imaging thousands of thin sections from a whole human brain alone could require years of labor, and subsequent reconstruction of the whole brain in 3D could be very complicated or impossible because of the numerous tissue distortions introduced by mechanical sectioning. Thus, a scalable and routine technology to enable cellular and molecular interrogation of centimeters-sized human organs could substantially reduce sectioning artifacts and also overcome complications in registering large-scale imaging data in 3D.

In the last decade, emerging optical tissue clearing methods have enabled fast 3D histology on transparent specimens avoiding major pitfalls of standard histology, especially tissue sectioning (Garvalov and Ertürk, 2017; Richardson and Lichtman, 2015). Furthermore, new deep tissue labeling methods were developed in combination with clearing methods to better phenotype whole rodent organs and human embryos (Belle et al., 2014, 2017; Cai et al., 2019; Deverman et al., 2016; Murray et al., 2015; Renier et al., 2014, 2016). Progress in optical tissue clearing first allowed the clearing of increasingly larger rodent samples (up to whole adult rodent bodies) (Jing et al., 2018; Pan et al., 2016; Tainaka et al., 2014; Yang et al., 2014). Then, the adaptation of light-sheet microscopy systems allowed the imaging of whole transparent rodent bodies (Cai et al., 2019; Kubota et al., 2017; Pan et al., 2016). However, clearing of human organs has been notoriously challenging so far, in particular for adult human brain tissue. Recent efforts with chemical screening of thousands of compounds (Tainaka et al., 2018) and application of electrical field forces (Chung et al., 2013) could achieve clearing of only small pieces of human organs. For example, it took 10 months to clear an 8 mm-thick human brain specimen (Morawski et al., 2018) and 3.5 months to clear a 5 mm-thick human striatum sample (Lai et al., 2018). Furthermore, deep-tissue antibody labeling methods developed on rodent tissues also encounter hurdles to label adult human tissue thicker than 1 mm (Park et al., 2018). We reasoned that highly myelinated content, lipidome complexity (Bozek et al., 2015), and age-related accumulation of diverse opaque and dense molecules such as lipofuscin and non-soluble collagen (Monnier et al., 1984; Moreno-García et al., 2018) impede penetration of chemicals deep into human organs, thereby blocking both clearing and labeling of centimeters-sized specimens.

Here, we introduce SHANEL (small-micelle-mediated human organ efficient clearing and labeling), a new method that is driven by detergent permeabilization chemistry allowing the penetration of labeling and clearing agents into centimeters-thick mammalian organs. Our approach enables histology using dyes and antibodies in human samples ranging from 1.5 cm thickness to whole adult human organs. We also show that the technology works on other large mammalian organs such as pig brain and pancreas, which can readily be labeled transgenically. Furthermore, we outline a deep learning-based pipeline to start accurate analysis of the large 3D dataset coming from the cleared human organs using standard lab computers. Thus, the SHANEL histology pipeline presented here can pave the way for cellular and molecular mapping of whole adult human organs for diverse applications.

RESULTS

Development of New Detergent Permeabilization Chemistry

We hypothesized that both labeling and clearing of large and sturdy human organs require a new permeabilization chemistry allowing deep tissue penetration of molecules. Ionic SDS (sodium dodecyl sulfate) and nonionic Triton X-100 are commonly used detergents for tissue clearing, and they are characterized as containing typical ‘‘head-to-tail’’ amphipathic regions. Their structural features lead to the formation of relatively large micelles suggesting that they can get stuck at tissue surfaces, and therefore exhibit low tissue permeabilization capacity and limit the penetration of molecules (Figures 1A–1C). We anticipated that detergents forming smaller micelles would be better candidates for deep tissue permeabilization as they could penetrate more rapidly and deeply into the tissue. We identified the zwitterionic detergent CHAPS (3-[(3-cholamidopropyl)dimethylammonio]-1-propanesulfonate), containing a rigid steroidal structure with a hydrophobic convex side, a hydrophilic concave side (bearing three hydroxyl groups), and a sulfobetaine-type polar group. CHAPS possesses atypical “facial” amphiphilicity (Lee et al., 2013). With this peculiar structure of hydrophobic and hydrophilic faces, it has higher critical micelle concentration (CMC), smaller aggregation number, and forms much smaller micelles compared to SDS and Triton X-100, which could enable its rapid permeabilization of large and sturdy tissues (Figures 1A–1C and S1A–S1C; Table S1). Indeed, CHAPS permeabilization allowed full and rapid penetration of methylene blue dye into centimeters-sized pig pancreas while SDS and Triton X-100 allowed only a limited penetration (Figures 1D–1F). Furthermore, once the micelles travel into the tissue and interact with the bilayer of lipids, the facial hydrophobic side of CHAPS reclines on the bilayer surface with a larger area rather than being embedded into the lipid as head-to-tail detergents. These different interaction behaviors of the detergents suggest that detectable fragments of SDS and Triton X-100 exist after washing while no residual of CHAPS would be left inside of the tissue (Rodi et al., 2014; White et al., 2017; Zhang et al., 2011). Thus, CHAPS could function as an efficient tissue permeabilization reagent by traveling throughout sturdy tissue and disrupting densely packed extracellular matrix ultrastructure meshes, without leaving behind residual detergent fragments after washing out.

Human organs carry residual blood clots due to several hours to days of delay until organ harvest after death. Heme in the blood causes strong autofluorescence at visible wavelengths (400–700 nm) and reduces the intensity of traveling light within the tissue, thereby impeding the full transparency of cleared organs (Tainaka et al., 2014). PFA-fixed blood was washed by detergent solutions, resulting in colorless supernatant and red pellet, indicating detergent alone was unable to remove the heme (Figure S1D). To overcome this issue, we first screened CHAPS compatible chemicals to elute the heme. In particular, we focused on effective, colorless, and cheap chemicals to facilitate scalability to large human organs (Figures 1G–1I, S1E, and S1F). Our screen showed that NMDEA (N-methyldiethanolamine) was an efficient candidate when combined

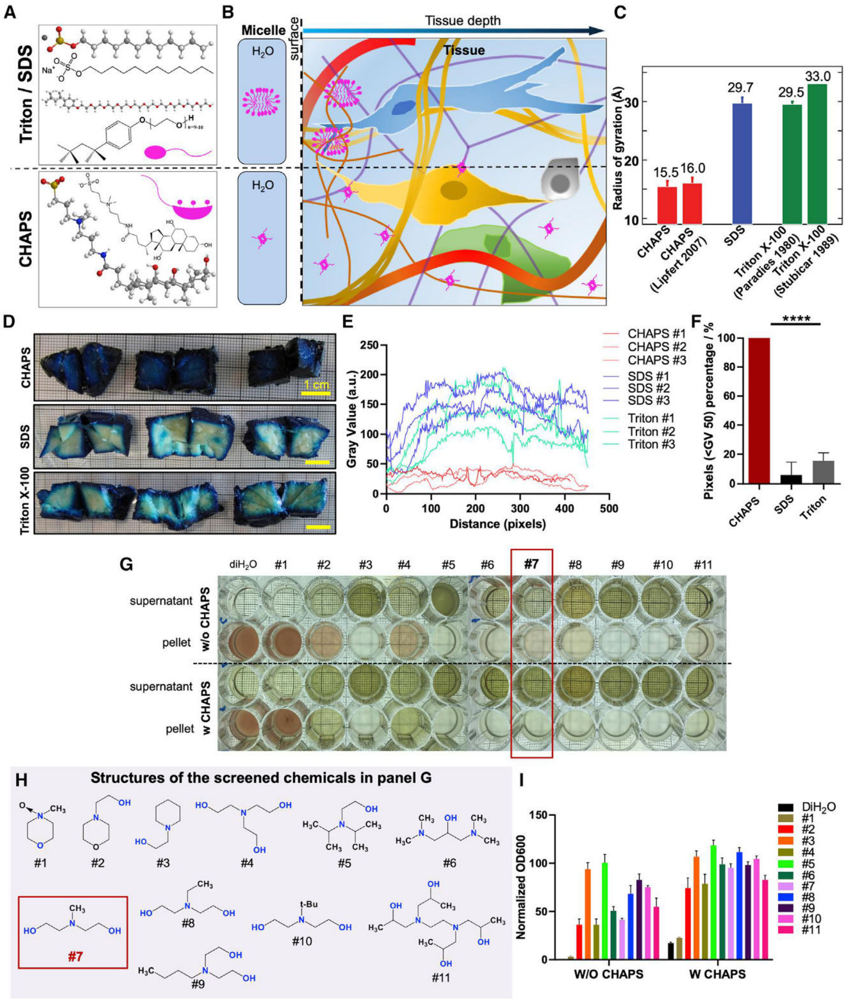

Figure 1. CHAPS-Mediated Deep Tissue Permeabilization and Blood Decolorization by Forming Small Micelle

(A) 3D molecular and structural features of SDS and Triton X-100 exhibiting typical head-to-tail amphiphilicity, whereas, CHAPS exhibiting peculiar facial amphiphilicity.

(B) Schematic diagram showing facial CHAPS could more efficiently and deeply permeabilize tissue compared to standard detergents (SDS and Triton X-100) owing to the formation of smaller micelle.

(C) Radii of gyration determined for CHAPS and SDS with their literature values (full references are in Table S1) for R_g (the size of micelle is characterized by the squared radius of gyration of the micellar core, R_g^2). Values for CHAPS and SDS represent mean and standard error from at least three independent repeats.

(D) Methylene blue dye staining of pig pancreas samples (1–1.5 cm cubes) after detergents permeabilization, showing CHAPS greatly enhanced deep tissue permeabilization for dye traveling comparing with SDS or Triton X-100.

(E) Profile plot along each sample dimension in (D).

(F) Quantification of the pixel numbers in (E) under selected threshold (gray value [GV] < 50) (n = 3). p values were calculated with a one-way ANOVA test; error bars show standard deviations.

(G and H) Screening of 11 chemicals in (H) without or with CHAPS admixtures for blood decolorization (see Table S2 for the name and CAS number of the chemicals). Good candidates show green supernatant and colorless pellet. CHAPS improves the decolorization efficiency with most tested chemicals. The structures of screened chemicals in (G) are presented in (H).

(I) Normalized OD600 of the supernatant corresponded well with the photocamera pictures in (G) (n = 3).

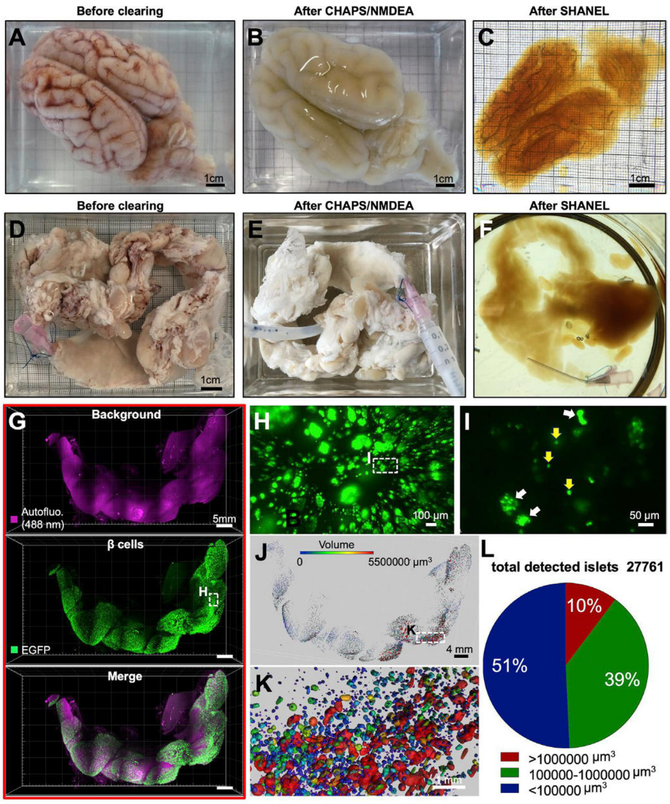

Figure 2. SHANEL Clearing of Brain and Pancreas from Adult Pigs

(A) PFA-fixed adult pig brain with retained blood.

(B) Permeabilized and decolorized pig brain by CHAPS/NMDEA.

(C) Fully transparent adult pig brain after SHANEL clearing.

(D) PFA-fixed, dissected (*INS*-EGFP transgenic pig) pancreas with retained blood.

(E) After CHAPS/NMDEA treatment, the pancreas is completely decolorized.

(F) Transparent pig pancreas after SHANEL clearing.

(G) 3D distribution of β-cell islets imaged by light-sheet microscopy after anti-EGFP nanobody boosting.

(H) High-magnification view of the region marked in (G) (middle panel).

(I) High-magnification view of the region marked in H showing β-cell islets of single cells (yellow arrows) or multiple cells (white arrows). The majority of larger islet shapes appear circular or oval. See also Video S1.

(J and K) Segmented 3D distribution of β-cells based on their volume in the islets of Langerhans. The heterogeneity of islet sizes is evident. The marked region in (J) is shown at high magnification in (K).

(L) Quantification of the total number of detected islets and categorization according to their volume.

with CHAPS, resulting in a completely colorless pellet from PFA-fixed blood (chemical 7 in Figures S1G and S1H and Table S2). In addition, NMDEA was the cheapest among the screened chemicals, reducing the cost when used in large amounts for intact human organs (Table S2). Compared to Triton X-100 and SDS that were used in prior clearing methods as detergents, CHAPS was faster and more successful in decolorizing mouse kidney, liver, heart, spleen, and brain, suggesting a better performance for large human organs (Figure S1I). Moreover, protein loss assay indicated the superior retention of endogenous biomolecules with CHAPS, assuring a more reliable molecular investigation of intact organs (Figure S1J). Thus, we anticipated that CHAPS, by forming small micelles, could completely diffuse through intact large mammalian organs and ameliorate tissue meshes, leaving behind a fully permeabilized biological tissue for cellular and molecular phenotyping.

Development of SHANEL Tissue Clearing

Next, we tested the accessibility of CHAPS permeabilized large mammalian organs using tissue clearing reagents. We chose to work with organic solvent-based clearing methods because they are fast and robust in addition to inducing tissue shrinkage (Pan et al., 2016), which helps to image larger organs with the limited sample holding capacity of light-sheet microscopy. First, we cleared the intact brain of a 2-year-old adult pig by passive immersion using standard organic solvent clearing reagents (Dodt et al., 2007; Ertürk et al., 2012). We found that a combination of ethanol for dehydration, DCM (dichloromethane) for delipidation, and BABB (benzyl alcohol + benzyl benzoate) for RI (refractive index) matching was highly effective in rendering the centimeters-thick pig brain transparent after CHAPS/NMDEA permeabilization and decolorization (all together represents the SHANEL clearing) (Figures 2A–2C; Table S3). SHANEL clearing provided rapid transparency of the ~12.0 × 7.3 × 5.0 cm size pig brain including heavily myelinated white matter, thalamus, and brainstem within 1.5 months (Figure 2C). The dimensions of the pig brain after clearing became 7.5 × 5.0 × 3.3 cm, with a shrinkage ratio of ~30% in volume. With the pretreatments of CHAPS/NMDEA, SHANEL clearing showed prominent capacity to render centimeters-sized mammal organs transparent compared with other clearing methods (Figures S2A and S2B).

Recent developments in gene editing with CRISPR/Cas9 technology have enabled the generation of large transgenic reporter mammals, expressing fluorescent proteins in the tissues of interest (Hsu et al., 2014; Kurome et al., 2017). Therefore, we applied SHANEL clearing to *INS*-EGFP transgenic pig pancreas exhibiting porcine insulin gene (*INS*) promotor driven beta-cell-specific EGFP expression in the islets of Langerhans (Kemter et al., 2017) (Figures 2D–2F). To enhance and stabilize the EGFP signal in centimeters-sized tissue, we used anti-GFP nanobodies conjugated with bright Atto dyes (Cai et al., 2019) (Figure S2C). We demonstrated that the 3D distribution of pancreatic beta cells as single cell or groups of cells within the islets of Langerhans could be readily assessed by our new approach enabling quantification of islet volume and demonstration of islet size heterogeneity (Figures 2G–2L; Video S1).

Generation of Intact Transparent Human Brain by SHANEL Clearing

Labeling and clearing of the intact human brain would be a major step forward toward mapping its cellular content in the near future. As the human brain vascular system is an established network reaching all parts of the brain, we used it to deliver the chemical cocktails deep into the brain tissue (Figure S3A). We used the two main pairs of large arteries, the CR and CL (right and left internal carotids, respectively) and the VR and VL (right and left vertebral arteries, respectively) to circulate solutions. First, we used PBS/heparin solution to wash out the liquid blood, followed by 4% PFA/PBS solution to fix the brain. Subsequently, we carefully isolated the whole human brain with these major vessels and connected eyes (with a volume of $\sim$1,344 cm^3 and dimensions of $\sim$15.0 × 10.4 × 14.4 cm) from the skull. Then, we set up a pressure-driven pumping system to circulate all clearing reagents and cell nucleus labeling dye (TO-PRO-3) through the four arteries to accelerate the process (Figure 3A). By doing so, we rendered the whole adult human brain transparent for the first time. To demonstrate the full transparency, we performed the following experiments. First, we used SWIR (short-wave infrared) imaging light at 1,450 nm wavelength and visualized the text through the intact cleared human brain (Figures 3B and S3B) (Bruns et al., 2017; Carr et al., 2018). Second, we used a condensed white light from epifluorescence microscopy to illuminate the whole brain and observed that the light traveled end-to-end (Figure 3C). Third, we used MRI to visualize and quantify the proton density of uncleared and cleared human brain tissue, comparing the results to well-cleared mouse brain (Baek et al., 2019). The results showed that SHANEL clearing generated homogeneous tissue water replacements in both whole human brain and human brain slice, with the brain slice showing similar proton density values as the whole brain (Figure S3C). The difference in proton density between cleared and uncleared human samples was similar to the mouse samples (Figure S3C). The intact transparent human brain represents a 2–3 order of magnitude increase in the volume of sample that could be rendered transparent compared to prior methods (Hildebrand et al., 2018). The whole process including labeling and clearing takes $\sim$4 months and costs $\sim$3,200 € for one adult human brain (Table S2). The final volume of the shrunken brain was 56% of the initial volume. Next, we used light-sheet microscopy to acquire mosaic images of the intact cleared human eye with a diameter of $\sim$3 cm. We imaged TO-PRO-3 and autofluorescence signals of the intact cleared eye and reconstructed the details of its anatomical structures including sclera, iris, and suspensory ligament in 3D (Figures 3D and 3E; Video S2). Thus, our approach provides the basis for 3D histological assessment of the whole human brain in the near future.

SHANEL Histology of Centimeters-Sized Human Organs

Because *in vivo* genetic labeling and fluorescent dye tracing are not applicable to study post-mortem human tissue, cellular and molecular interrogation of human organs requires post-mortem staining using dyes and antibodies. However, state-of-the-art antibody labeling techniques of decades-aged human samples are limited to $\leq$50 μm thickness in standard histology, and to a maximum of $\sim$1 mm thickness in prior clearing methods, mainly due to the weak permeabilization of the tissue and slow diffusion of the standard antibodies ($\sim$150 kDa) (Lai et al., 2018; Murray et al., 2015; Park et al., 2018). In addition, age-related accumulation of highly autofluorescent molecules increases the background substantially in thicker tissues (Davis et al., 2014). To overcome these limitations and achieve staining of centimeters-sized human brain, we set out to develop a deep-tissue antibody labeling method. Toward this goal, we perfused an intact human brain from a 92-year-old female body donor using CHAPS/NMDEA to permeabilize and decolorize. This treatment softened the sturdy human brain and allowed its easy sectioning into 12 coronal slices (each 1.5 cm thick) using a brain slicer (Figures S3D–S3F). The permeabilized human brain slice was further slackened by delipidation using DCM/MeOH (methanol). Next, we identified acetic acid and guanidine hydrochloride as powerful reagents for loosening the ECM (extracellular matrix) for the diffusion of large molecules such as antibodies (all together represents the SHANEL histology) (Figures 4A and 4B).

We first used Methoxy-X04 (Jung et al., 2015; Klunk et al., 2002) and TO-PRO-3, which were affordable dyes in large quantities, to label Abeta plaques and cell nuclei, respectively, in an intact 16.5 × 16.5 × 1.5 cm human brain slice. After clearing, we scanned a 7.5 × 5 × 0.4 cm brain slice in $\sim$2 days by using MAVIG upright confocal microscope that is designed to scan large slices of tissue. We detected Abeta plaque accumulation in several brain regions including CG (cingulate gyrus), PCun (precuneus), STG (superior temporal gyrus), and MTG (middle temporal gyrus) (Figures S4A–S4D; Table S3; Video S2). We also used epifluorescence microscopy to quickly screen the 1.5 cm thick half human brain slice and again readily located the regions with Methoxy-X04-labeled Abeta accumulation for subsequent high-resolution laser-scanning microscopy (Figures S4E–S4H).

Antibody labeling of tissues has been widely used to interrogate the specific cellular architecture and underlying molecular mechanisms of biological processes. Therefore, we next applied SHANEL to assess the possibility of antibody-based histology of centimeters-sized human tissues. Toward this goal, we first used Iba1 (ionized calcium binding adaptor molecule 1) antibody to immunolabel microglia (Figures 4C–4J) and PI (propidium iodide) to label cell nucleus. Iba1$^+$ microglia were identifiable throughout the 2.0 × 1.8 × 1.5 cm size human brain slice (Video S3). We also observed morphological differences: microglia cells in gray matter were mostly larger and more ramified compared to white matter (Figures 4G–4J). Next, we used

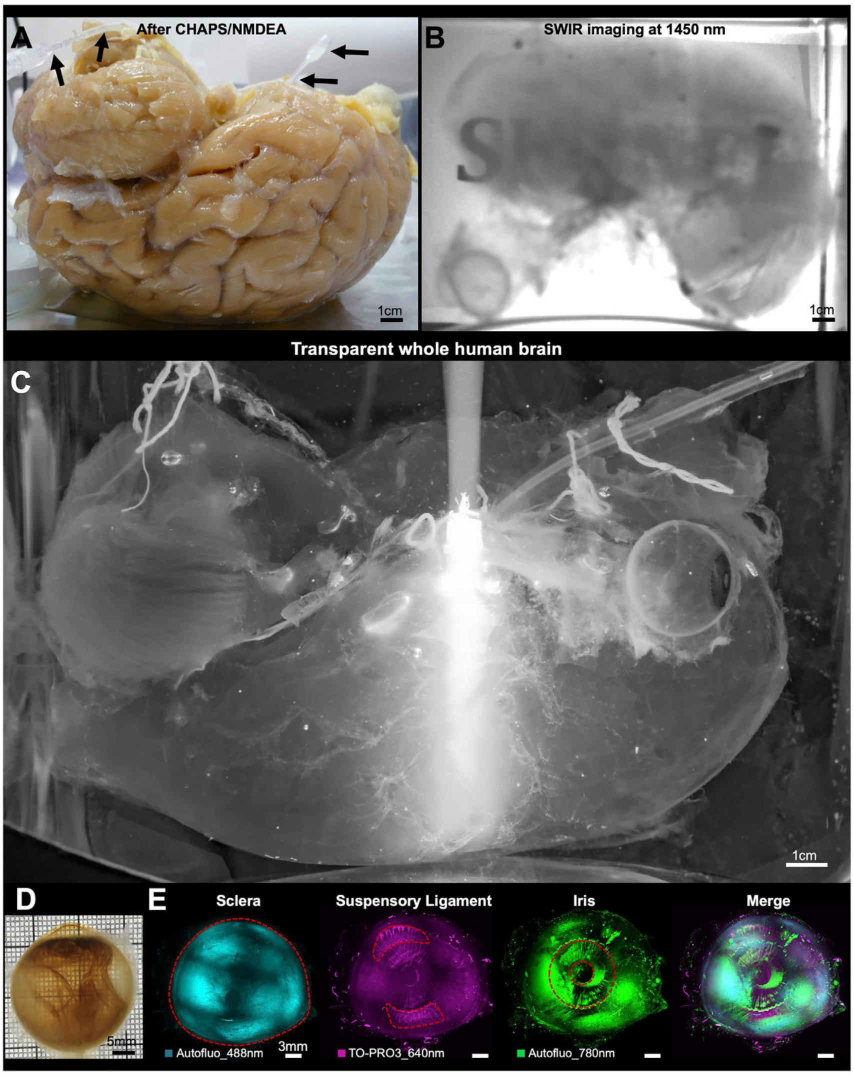

Figure 3. SHANEL Clearing of Intact Adult Human Brain

(A) A sample of permeabilized and decolorized intact adult human brain by CHAPS/NMDEA via active pumping setup (black arrows).

(B) SHANEL letters are visible, through the transparent whole human brain illuminated with 1,450 nm short-wave infrared (SWIR) light.

(C) Light of an epifluorescent microscope can travel in the brain end-to-end, demonstrating the full transparency of intact human brain, which has volume of ~1,344 cm^3 and dimensions of ~15.0 × 10.4 × 14.4 cm.

(D) Camera picture of an eye, dissected from the intact transparent human brain.

(E) 3D reconstruction from light-sheet microscopy scans of the eye showing the sclera, suspensory ligament, and iris structures.

See also Video S2.

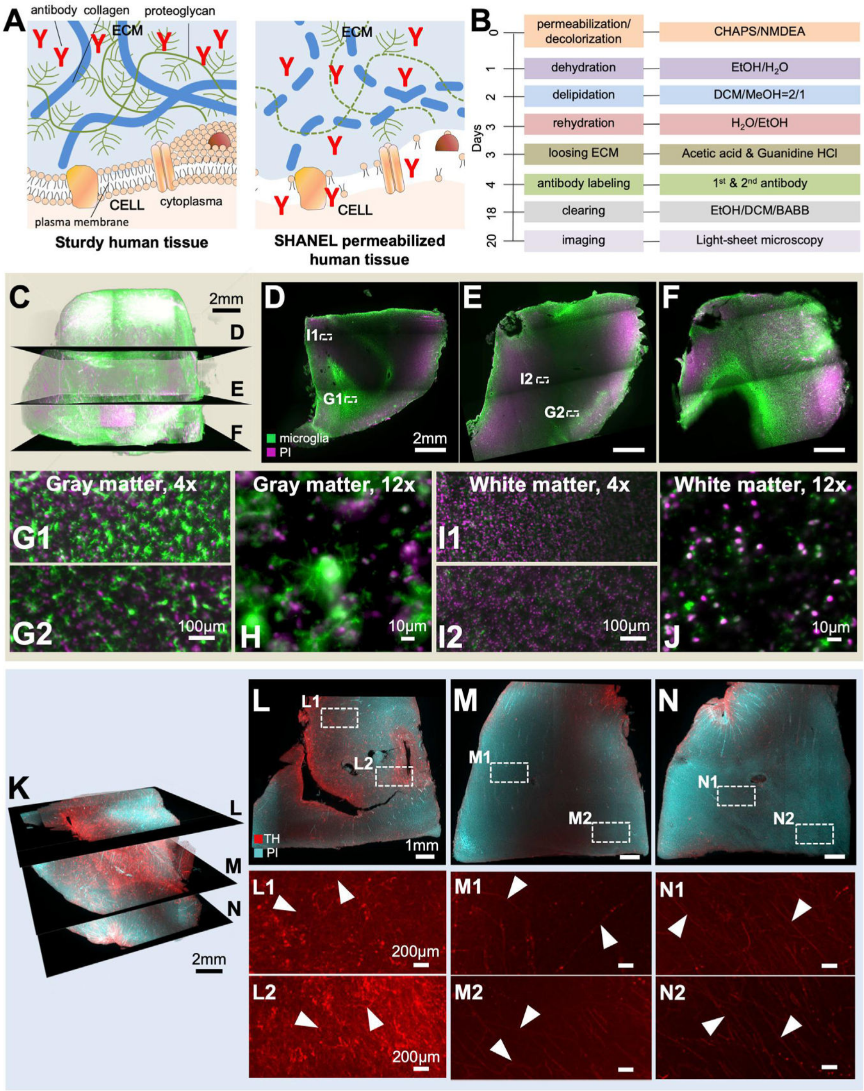

Figure 4. SHANEL Histology on Centimeters-Thick Human Tissues Imaged by Light-Sheet Microscopy

(A) SHANEL histology is further characterized by loosening extracellular matrix (ECM) and extracting lipids, which enable antibody-size molecules to fully penetrate into centimeter-thick sturdy human tissues.

(B) The step by step SHANEL histology pipeline (with durations) for deep tissue antibody labeling.

(C–F) Iba1 microglia (green) and propidium iodide (PI) (magenta) labeling of post-mortem human brain tissue with an original size of 2.0 × 1.8 × 1.5 cm (1.3 × 1.2 × 1.0 cm after shrinkage). The differences in microglia density and morphology are evident throughout the gray matter (G and H) and white matter (I and J).

(legend continued on next page)

TH (tyrosine hydroxylase) antibody to immunolabel neuronal structures along with PI labeling of the cell nucleus (Figures 4K–4N). We were able to observe specifically labeled axonal extensions throughout the 1.8 × 1.8 × 1.5 cm human brain slice (Figures 4K–4N; Video S3). These results demonstrate that SHANEL histology can successfully permeabilize the entire 1.5 cm thick sturdy human brain slices for deep tissue antibody labeling using diverse antibodies (Figure S5A). This represents a 1–2 order of magnitude enhancement in the thickness of adult human tissue that could be processed for histology compared with prior methods (Hildebrand et al., 2018). We also found that the signal was stable for several months after SHANEL histology (Figure S5B). Studying vasculature has been a valuable method to explore diverse developmental and pathological phenomena in biological tissues. Again, histological assessment of the vasculature in human tissue has been limited by the penetration of specific vascular dyes and antibodies. Here, we used Lectin dye to effectively label a human brain sample with a size of 3.0 × 1.9 × 1.5 cm (Figure S5C). In addition to specific vascular structures (Figures S5D–S5F), we could identify vasculature-related tissue abnormalities as swollen structures of vascular morphology (Figure S5F), which could be aneurysms, a prevalent vascular disorder affecting 25% of the population (Duan et al., 2018). 50% of intracranial aneurysms are <5 mm in diameter (Morita et al., 2012), which is in line with our observations. Thus, SHANEL histology allows the labeling of specific molecules, cells, and vasculature in centimeters-sized human brain samples presenting a viable tool to scale up the investigation of brain pathologies.

Next, we tested our SHANEL technology on entire human kidneys using small molecular dyes. There is a huge shortage of organ donors for hundreds of thousands of people, with a large portion (~55%) waiting for kidney transplantation (Chung et al., 2014). Overall the waiting time for donation might be several years, and the cost of transplantation can reach half a million dollars (Chung et al., 2014). Understanding the 3D structure of the human kidney would be very valuable for tissue engineering efforts aiming to generate artificial kidneys using 3D-bioprinting technologies (Murphy and Atala, 2014), which require detailed cellular and molecular knowledge on intact human kidney to be replicated. Kidneys are the major organs for blood filtration through glomeruli, whose density, size, and cellular integrity are critical for healthy organ function (Puelles and Bertram, 2015). Toward understanding the 3D cellular structures of the human kidney, we used SHANEL histology with active perfusion of TRITC-dextran and TO-PRO-3 dyes through the renal artery to label the vessels and dense cellular structure of the glomeruli in the entire kidney with a size of 11.5 × 8.2 × 3.0 cm. After labeling, we also actively pumped the clearing reagents through the kidney to overcome the age- and size-related challenges (Table S3). We achieved full transparency, revealing the primary renal artery, secondary branches of segmental arteries, and interlobar arteries (Figures 5A–5C). Using standard light-sheet microscopy, we could visualize the 3D distribution of vessels and glomeruli in the kidney cortex over large volumes (1.2 × 1.2 × 0.45 cm) and trace individual afferent arterioles and their corresponding glomeruli (Figures 5D–5F; Video S4). Through cortex profile counting, we found that the width of the cortex zone was around 2,742 ± 665 μm (mean ± SD), the diameter of glomerular caliper was 221 ± 37 μm, and afferent arteriole diameter was 71 ± 28 μm (Figure 5G).

Next, we examined whether SHANEL histology leads to tissue alterations by assessing macro- and micro-structures. The ratiometric enlargement of shrunken tissues after SHANEL histology overlaid well with their pre-cleared images suggesting an isotropic tissue shrinkage (Figure S6A). Assessing the cellular details before and after SHANEL histology, we also did not observe a notable deformation (Figure S6B). Moreover, we also rehydrated the SHANEL-treated tissues, and performed histological assessments using H&E, Nissl, and PAS (periodic acid Schiff) stainings (Puelles et al., 2019), further confirming the integrity of cellular structures upon SHANEL (Figure S6C).

3D Reconstruction of Intact Human Organs and Analysis of Big Data Using Deep Learning

To enable the imaging of intact human organs, we used a prototype light-sheet microscope with extended stage movements and a large sample accommodation chamber (size of 25 × 9 × 7 cm) (Figures 6A–6E). Using this new system, we scanned and reconstructed an intact human thyroid (7 × 5 × 3 cm) in 3D revealing the vessels and lymph nodes (Figures S7A–S7D; Table S3). We scanned an intact human kidney (11 × 6.5 × 5 cm) from a 93-year-old donor end-to-end (Figures 6F–6I). We confirmed the transparency and imaging quality by observing the perfusion/labeling-free autofluorescence signal at 780 nm channel, which was clearly visible throughout the entire scan (Video S4). Interestingly, we observed that a large segment of the kidney cortex had significantly reduced vascular structures appearing in 780 nm channel (Figures 6J and 6K; Video S4), which was also evident in dextran channel (Figure 6H). We also dissected exemplarily pieces and performed PAS staining to analyze the structural details. These experiments showed that the glomeruli structures were similar for both sides (Figure 6L). Overall, our data suggests a vascular pathology affecting a large segment of the kidney, which is typical of hypertensive related changes in older individuals that could potentially be preceding glomeruli pathology (Denic et al., 2017; Hughson et al., 2016). Thus, SHANEL technology can be a new tool to study pathologies of intact human organs at a gross scale proving valuable information to understand organ functions in health and disease.

Analyzing the large data coming from cleared tissues has remained a major obstacle. The state-of-the-art methods for

(K) Tyrosine hydroxylase (TH) (red) and propidium iodide (PI) (cyan) labeling of post-mortem human brain tissue with an original size of 1.8 × 1.8 × 1.5 cm (1.2 × 1.2 × 0.91 cm after shrinkage).

(L–N) TH+ axonal extensions in gray matter (white arrowheads in L1–L2) and white matter (white arrowheads in M1–N2) throughout the entire depth of tissue are evident. Note that cyan channel is not shown in (L1)–(N2) to emphasize the TH labeling.

See also Video S3.

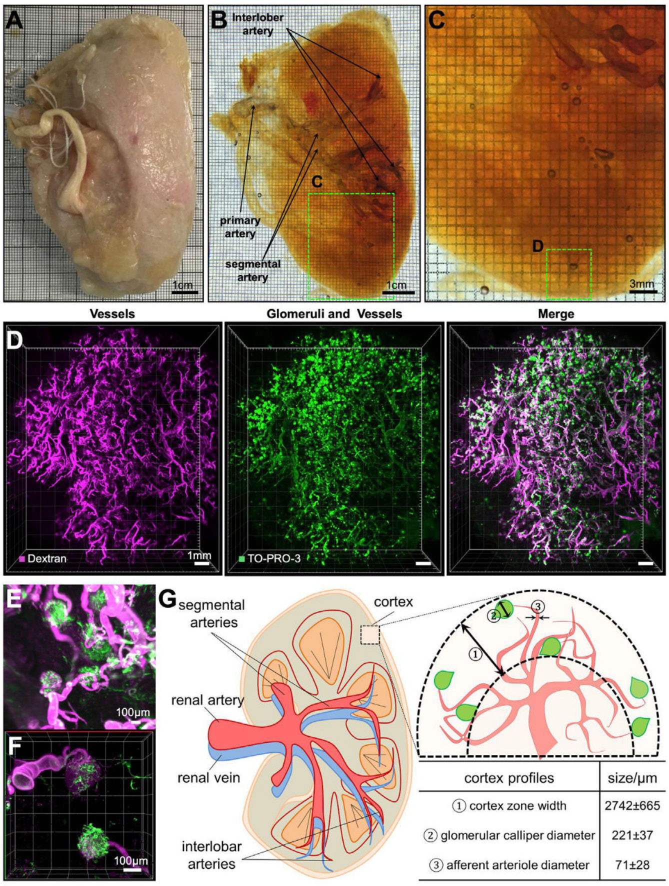

Figure 5. Cellular Investigation of Human Kidney

(A–C) A PFA-fixed adult human kidney (A) was rendered totally transparent after SHANEL clearing, revealing visible arteries (B and C). The marked region in (B) is shown at high magnification in (C).

(D) 3D reconstruction of vessels and glomeruli of the kidney cortex region marked in (C) by light-sheet microscopy.

(E and F) TRITC-dextran labels mostly the vessels (magenta), while TO-PRO-3 labels glomeruli more prominently (green). High-magnification light-sheet microscopy (E) and confocal microscopy (F) images show the structural details of afferent arteriole (magenta) and glomeruli (green).

(G) Human kidney anatomy and cortex profiles from the 3D reconstruction.

See also Video S4.

object and cell detection, for example the "3D Object Counter" tool (Bolte and Cordelières, 2006) in the Fiji software package (Schindelin et al., 2012) and Imaris software (Bitplane, 2019) rely on filter-based approaches such as brightness thresholding or watershed algorithms that cannot readily be scaled to analyzing terabytes of data. Recent deep learning approaches have proven to be superior for the analysis of large imaging data compared to prior methods both in terms of segmentation accuracy and computational power requirements (Belthangady and Royer, 2019; Kermany et al., 2018; Moen et al., 2019; Wainberg et al., 2018). To analyze large-scale data from the cleared human tissue in a scalable and unbiased manner, we adopted a deep learning approach based on CNNs (convolutional neural networks) (Tetteh et al., 2018; Todorov et al., 2019) (Figure 7A). To generalize the efforts, we chose to focus on reliable detection, segmentation, and counting millions of cells in cleared human brain tissues. Our deep learning approach consists of a CNN-based segmentation of the cells and a connected component analysis for detecting and counting of the cells. Our CNN was ~10× faster compared to the Imaris Surface Detection Tool while they had similar accuracies on the test data patches (Figures 7B and 7C). The CNN was 20× faster compared to the Fiji 3D Object Counter, which had a substantially lower performance (Figures 7B and 7C). We also tested an implementation of 3D U-Net (Çiçek et al., 2016), a common state-of-the-art CNN architecture for medical image segmentation, which performed very similar to our CNN in terms of cell detection accuracy, albeit slightly slower in processing speed (Figure 7C). Next, we applied our algorithms to 4 different large brain regions (size of ~60–145 mm^3). We could readily detect, segment, and map the 10–22 million cells in each brain region within a few hours (Figures 7D–7G), a task that is impossible to complete with the same speed and accuracy without a deep learning approach. We designed our pipeline to be able to work on any size of scan using a standard lab workstation (e.g., with Titan T1080i GPUs [graphics processing units]). Our code is freely available at Google Colab (see Data and Code Availability), where the model can be tested and applied to scientists' proprietary data in their browsers without installing any software.

DISCUSSION

Histological studies of human tissues suffer from a lack of scalable methods to label and image large human specimens. Here, we present the SHANEL method, which is derived from a new chemistry achieving thorough permeabilization of fixed

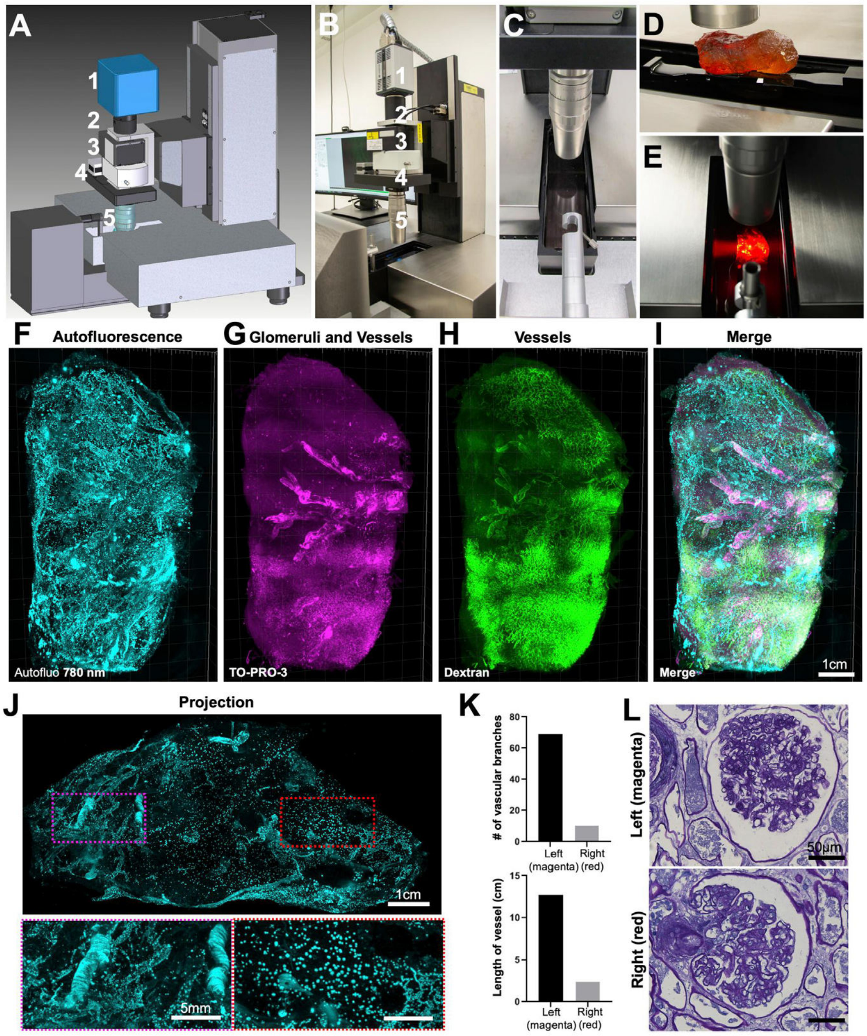

Figure 6. Whole Kidney Imaging Using Ultramicroscope Blaze with Extended Sample Holding Capacity

(A and B) Plan (A) and picture (B) of the prototype LaVision (Miltenyi) Biotec light-sheet Ultramicroscope Blaze for large samples, featuring (1) Andor sCMOS camera, (2) tube, (3) LaVision autofocusing unit for automatic focus correction at different wavelengths, (4) zoom body, and (5) 1.1× MI PLAN objective.

(C) Imaging chamber.

(D) A whole adult human kidney was mounted on the holder (note that the sample does not look transparent if not immersed in RI matching solution [BABB] as shown in the image).

(E) View of cleared whole human kidney placed in the imaging chamber with the light-sheet from the left crossing through the sample.

(F–I) 3D reconstruction of whole adult human kidney (original size of 11 × 6.5 × 5 cm) imaged by the prototype light-sheet microscope. Shown are the auto-fluorescence signal at 780 nm (F, cyan), the glomeruli and vessels from TO-PRO-3 labeling (G, magenta), the vessels from the dextran labeling (H, green), and the merged view of (F)–(H) in (I).

(legend continued on next page)

post-mortem human tissues. It allows full penetration of labeling molecules and clearing chemicals into centimeters-sized decades-aged human tissues such as post-mortem human brain and kidney specimens. Our method can also readily be applied to many organs in parallel, because it does not require lengthy handwork other than setting up the perfusion system and exchanging of the solutions (Table S3). Thus, this scalable method could vastly accelerate the 3D structural and molecular mapping of cells in intact human organs including the human brain.

Early efforts of adult human organ clearing started a century ago with slow progress in transparency and labeling options (Steinke and Wolff, 2001). A particular difficulty has been the age-dependent accumulation of intracellular and extracellular molecules such as lipofuscin and neuromelanin pigments. Lipofuscin is a mixture of highly oxidized cross-linked macromolecules including proteins, lipids, and sugars from different cellular metabolic processes (Moreno-García et al., 2018). Age-related accumulation of lipofuscin in the human body, in particular in the brain, correlates with senescence and sturdiness of human tissues (Moreno-García et al., 2018). Similarly, insolubility of the collagen also increases in the human body with aging, leading to hardening, browning, and autofluorescence of the tissues (Monnier et al., 1984). Due to age-related accumulation of such insoluble macromolecules in human tissues over several decades, histological examination relying on the penetration of large molecules such as antibodies deep into tissues has been very challenging. Recently developed tissue clearing methods have proven to be a promising way to achieve histological assessment of intact specimen. Although diverse clearing methods have been quite successful in rodents with the age of a few months, they have not been as effective on decades-aged human tissues. We solved this problem by developing a new method to permeabilize the sturdy human tissues, which is the prerequisite step for any tissue labeling and clearing method.

Here, we hypothesize that the micellar structures of detergents would be critical to penetrate the dense meshes of sturdy human tissues. Toward this goal, we identified CHAPS, a zwitterionic detergent having rigid steroidal structure with hydrophobic and hydrophilic faces. The “facial” amphiphilicity of CHAPS is responsible for the aggregation behavior and surface configuration of molecules at interface. First, CHAPS aggregates into much smaller micelles compared to standard “head-to-tail” detergents such as SDS and Triton X-100, facilitating its rapid penetration deep into dense human tissues. In aggregate formation, the hydrophobic faces (β-plane of steroid) are considered to contact each other, whereas the hydrophilic ones (three hydroxyl groups) remain exposed to the aqueous environment. Second, in terms of interfacial interaction, the facial amphiphiles bind to the bilayer in a unique mode that allows coverage of a larger hydrophobic area instead of being embedded into the bilayer. In this way, less facial amphiphile CHAPS is needed, and no residual CHAPS is left behind in the tissue after the treatment. Moreover, as a mild zwitterionic detergent, CHAPS exhibits better preservation of tissue endogenous biomolecules compared to SDS and Triton X-100 for cellular and molecular interrogation. Starting from this new permeabilization chemistry, we further developed our technology by loosening ECM using acetic acid and guanidine hydrochloride (Rajan et al., 2006; Yanagishita et al., 2009).

The resulting SHANEL histology method enabled diffusion of molecules as large as conventional IgG antibodies for straightforward 3D histology of centimeters-sized human organs. Thus, our approach can also tremendously help scaling up the efforts on Human Protein Atlas (HPA) by reducing the time to label and annotate across large human tissues (Sullivan et al., 2018; Vogt, 2018). Yet, SHANEL alone does not fully eliminate the tissue autofluorescence, in particular those coming from the lipofuscin in the brain tissue, without additional chemical treatments (Figures S7E–S7H). Thus, additional background signal might be observed in some of the antibody stainings. However, this autofluorescence can be used to extract more information on senescence of cells throughout different tissue layers in addition to imaging of specific dye/antibody signals in other channels. Similar to prior clearing methods using SDS and Triton, CHAPS-based SHANEL does also not preserve the lipid-base tracers such as DiI.

The SHANEL technology is also applicable to other large mammal organs. As pig is a much better model system for the human islets research compared to rodents, study of transgenic *INS*-EGFP pig pancreas in combination with SHANEL clearing can also accelerate research in metabolic disorders. We demonstrate that the 3D distribution of pancreatic beta cells as single cell or groups of cells within the islet of Langerhans can be readily imaged and quantified by our new approach demonstrating the islet size heterogeneity. Regional differences of islet size and distribution (head versus tail) in human pancreas are well known, and alterations in beta cell mass occur in diverse metabolic disorders (Chen et al., 2017). For instance, in disease conditions like type 2 diabetes, regional changes of islet distribution leading to preferentially large islets in the head region occur (Wang et al., 2013). Another interesting application would be to assess the quantity and distribution of porcine islets after intraportal xenotransplantation into the liver of non-human primate models (Kemter and Wolf, 2018; Wang et al., 2013).

The development of imaging systems with extended stages and imaging capacities would tremendously accelerate studies on phenotyping of the cellular and molecular architecture of the whole human organs. To start addressing this major need, we introduced a prototype light-sheet microscope with extended stage movement and sample holding capacity, which, in principle, could accommodate and image more than ∼80% of the human organs including kidney, bladder, ovaries, testes,

(J) An orthogonal 1 mm projection of the kidney showing that vascular structures are significantly reduced at the right side (red-dashed region) compared to left side of the kidney (magenta-dashed region). See also Video S4.

(K) Quantification of vascular features between the left (magenta) and right (red) regions of the kidney.

(L) Periodic acid Schiff (PAS) images of rehydrated samples dissected from the left (magenta) and right (red) regions showing similar glomeruli structures for both sides.

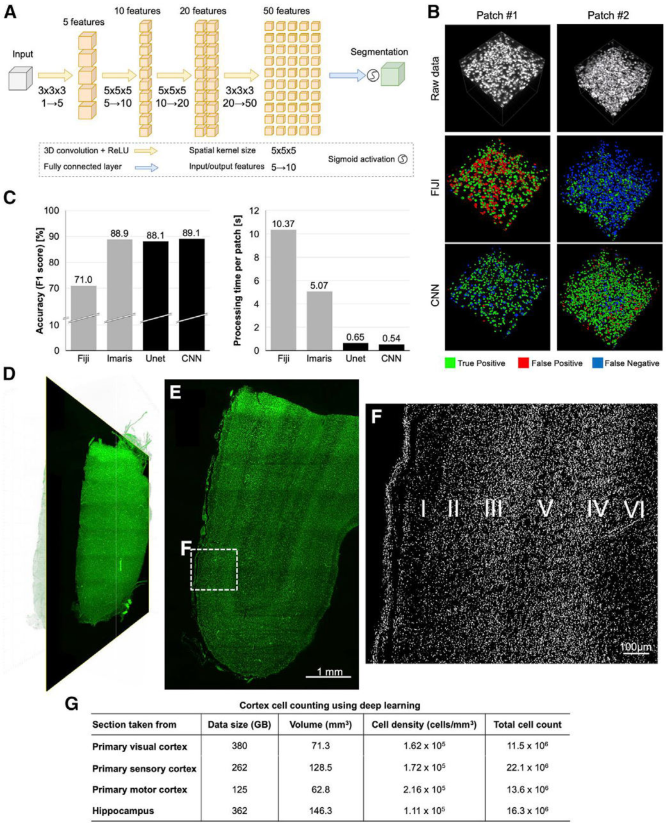

Cortex cell counting using deep learning

Section taken from	Data size (GB)	Volume (mm^3)	Cell density (cells/mm^3)	Total cell count
Primary visual cortex	380	71.3	1.62×10^5	11.5×10^6
Primary sensory cortex	262	128.5	1.72×10^5	22.1×10^6
Primary motor cortex	125	62.8	2.16×10^5	13.6×10^6
Hippocampus	362	146.3	1.11×10^5	16.3×10^6

Figure 7. Deep Learning-Based Quantification of Cleared Human Brain Tissues

(A) The architecture of our convolutional neural network (CNN).

(B) Visual comparisons of deep learning segmentation performance to alternative automated methods on two test patches, color-coded.

(C) Comparisons of deep learning (black columns) and alternative automated methods (gray columns) for cell counting accuracy (left) and processing time (right). The cell counting accuracy is quantified as the F1 score, which represents the harmonic mean of recall (cell detection rate) and precision (false positive rate). Reported processing times were measured for the task of detecting and segmenting all cells of a 3D patch (291 μm^3) on a normal workstation (32 cores, 2 GPUs).

(D) 3D reconstruction of primary visual cortex area having ~11.5 million cells.

(E) Raw orthogonal image from the middle of (D).

(F) CNN segmented image from the region marked in (E). Six layers of primary visual cortex can readily be identified in CNN segmented images (100 µm projection).

(G) The summary of cell properties from different brain regions taken from cortex and hippocampus area analyzed using our CNN.

throat, heart, thyroid, pancreas, and tongue. Imaging the entire transparent human brain on the other hand is still beyond the capacity of current microscope systems. Leading toward this possibility, Voigt et al. (2019) recently proposed the mesoSPIM (mesoscale selective plane illumination microscopy), an open-hardware microscopy platform for imaging cleared tissues several centimeters in size, which could potentially be further modified to accommodate and image the whole cleared human brain. In addition, SHANEL-induced shrinkage (e.g., 44% reduction in volume for adult human brain) and usage of light-sheet microscopes with double-sided illumination could further facilitate imaging of the large, cleared human samples. To test more imaging options, we sliced the intact adult human brain into twelve 1.5 cm-thick sections using standard slicer equipment and imaged with a mosaic upright confocal fluorescent microscopy. Still, such thick slices are much easier to handle compared to micrometer- or even millimeter-thick sections, because there is no need to embed or collect them on glass slides. Moreover, SHANEL histology allowed a thorough labeling of these 1.5 cm-thick brain slices. This allows the usage of high NA (numerical aperture) objectives such as 4× Olympus objective (NA: 0.28 and WD [working distance]: 10 mm) and 20× Zeiss clarity objective (NA: 1, WD: 5.6 mm) on defined regions of interest to reconstruct the entire 1.2–2 cm thick human tissue by scanning from both sides in such laser scanning systems. While the usage of high NA and high WD objectives enables ~1–2 µm resolution, this will also lead to large data in the order of at least hundreds of terabytes. It is noteworthy to mention that imaging samples as large as human brain will also benefit from imaging at near-infrared and SWIR wavelength having much better tissue penetration capabilities compared to the visible spectra used in the current light-sheet microscopes. In addition, imaging at longer wavelengths can provide further advantages in both reducing the tissue autofluorescence at the visible spectrum and multi-color imaging for which new probes are being developed (Cosco et al., 2017; Schnermann, 2017). Indeed, a near-infrared light-sheet microscopy has recently been presented (Wang et al., 2019). Imaging whole adult human kidney, we observed a large segment of the kidney lacked vascular structures at 780 nm autofluorescence channel. Our observations of the signal around the vessels, and at the fibrous capsule (outer membrane of the kidney) suggests that this autofluorescence signal could be coming from the collagen (Genovese et al., 2014; Jain et al., 2016; Manon-Jensen et al., 2016). Currently, we do not know the origin of this observed vascular change. Another advantage of our approach is that, after SHANEL histology, the specimens become hard, enabling easy handling of complete organs and slices. Finally, owing to the complete dehydration and incubation in organic solvents, the tissues are preserved by SHANEL histology, allowing long-term storage for the future studies by the same investigators or in other labs.

The rapid progresses in tissue clearing methods and applications have introduced datasets of previously unseen sizes in mesoscale imaging. Even more limiting has been the lack of reliable methods to analyze these large datasets with conventional computational resources in moderately equipped biology labs. Here, we developed a deep learning-based framework using a CNN for the segmentation of millions of cells in cleared human brain tissue, which could not be completed without a deep learning approach at the same accuracy and speed. Here, we used our pipeline to detect and segment cells in diverse brain regions. Deep learning approaches could be expanded to classify the cells and analyze new structures such as vessels, nerves, and muscles—tasks that cannot be achieved easily with traditional software packages. Thanks to the adaptability of deep learning approaches, new algorithms can be trained with a small amount of training data to perform previously unknown segmentation tasks at high accuracy and speed (Belthangady and Royer, 2019; Moen et al., 2019; Todorov et al., 2019). Deep learning methods can also be parallelized on multiple GPUs (such as using cloud computing) to quickly scale up the processing speed for data size of hundreds of terabytes.

In conclusion, this work presents a new technology to permeabilize centimeters-sized aged human tissues for molecular and cellular phenotyping. This method allows deep tissue labeling and clearing of human specimens as large as the intact human kidney and brain. Thus, in combination with light-sheet microscopy systems having extended sample scanning capacity and deep learning-based algorithms, SHANEL histology can be a key technology to map intact human organs in the near future, which would accelerate our understanding of physiological and pathological conditions governing human life.

STAR★METHODS

Detailed methods are provided in the online version of this paper and include the following:

- KEY RESOURCES TABLE
- LEAD CONTACT AND MATERIALS AVAILABILITY
- EXPERIMENTAL MODEL AND SUBJECT DETAILS
    - Mouse samples
    - Pig samples
    - Human samples
- METHOD DETAILS
    - Small-angle X-ray scattering measurements
    - Small-angle X-ray scattering data analysis
    - Comparison of permeabilization capacity of different detergents on pig pancreas using methylene blue dye staining
    - Screening of affordable and scalable chemicals for blood decolorization
    - Permeabilization and decolorization of mouse organs containing remaining blood
    - Protein loss assay
    - Pig brain clearing with passive SHANEL
    - Active SHANEL clearing of pig pancreas
    - Other clearing methods
    - Active SHANEL clearing of intact human brain
    - 1.5 cm-thick human brain slices preparation
    - Passive histology of a 1.5 cm-thick intact human brain slice
    - Passive SHANEL antibody histology of 1.5 cm-thick human brain samples
    - Copper sulfate treatment in SHANEL to eliminate tissue autofluorescence
    - Passive SHANEL histology of intact human thyroid
    - Active SHANEL histology study of intact human kidney
    - Safety recommendations of handling chemicals
    - SWIR imaging
    - Proton density MRI imaging
    - Light-sheet microscopy imaging
    - Laser-scanning confocal microscopy imaging
    - Epifluorescence stereomicroscopy imaging
- QUANTIFICATION AND STATISTICAL ANALYSIS
    - Image processing
    - Tissue deformation analysis using RMSE calculation
    - 3D volume and iso-surface rendering and quantification of pig pancreas islets
    - Cell detection and image analysis
    - Non-deep learning approaches to cell counting
    - Deep learning model 1: Our CNN
    - Deep learning model 2: 3D UNet
    - Performance comparison of models
- DATA AND CODE AVAILABILITY

SUPPLEMENTAL INFORMATION

Supplemental Information can be found online at https://doi.org/10.1016/j.cell.2020.01.030.

ACKNOWLEDGMENTS

We thank Oliver Thorn-Seshold for the critical comments on the manuscript and David Eliezer and Sebastian Doniach for support in the initial stages of this project. We thank Lavision BioTec for producing the protoype Utramicrscope light-sheet microscope. We thank Alireza Ghasemigharagoz for RMSE analysis and Melanie Shaper for technical assistance. We thank Doris Kaltenecker for discussion about the name of the technology. The authors are grateful to the patients and their families, who made brain donation possible. This work was supported by the Vascular Dementia Research Foundation, Deutsche Forschungsgemeinschaft (DFG, German Research Foundation) under Germany's Excellence Strategy within the framework of the Munich Cluster for Systems Neurology (EXC 2145 SyNergy, ID 390857198), ERA-Net Neuron (01EW1501A to A.E.), Fritz Thyssen Stiftung (10.17.1.019MN to A.E.), DFG (ER 810/2-1 to A.E., BR 5355/2-1 to O.T.B., CRC/1192 to T.B.H. and V.G.P., TRR127 to E.W. and E.K., and SFB 1052 to I.B.), German Center of Diabetes Research (DZD) (82DZD00802 to E.W.), NIH (to A.E.), Helmholtz ICEMED Alliance (to A.E. and I.B.), National Health and Medical Research Council of Australia (NHMRC), the Humboldt Foundation, and BMBF eMed Consortia Fibromap (to V.G.P.), NVDIA GPU grant program, and Software Campus grant (to O.S.). The procurement of the MRI scanners was supported by the DFG within the framework of SyNergy (EXC 2145 SyNergy, ID 390857198) and (DFG, INST 409/193-1 FUGG).

AUTHOR CONTRIBUTIONS

S.Z. developed the protocols and performed organs processing, labeling, clearing, imaging, and data analysis. M.I.T. and R.C. contributed to optimize the protocol, organs processing, imaging, and data analysis. R.A.-M., O.S., J.C.P., and B.M. developed the deep learning architecture and quantitative analyses. H.S. and I.B. perfused and dissected the human organs. E.K. and E.W. generated the *INS*-EGFP transgenic pig line. E.K. perfused and dissected pig pancreas. S.Z., R.C., H.M., and Z.R. annotated the ground truth data. M.W. and O.T.B. designed and performed SWIR images. M.D. and B.G. performed the MRI images and analysis. J.L. performed the SAXS experiment and data analysis. K.S., V.G.P., M.N.W., and T.B.H. contributed to confocal, tissue recycling, and histology analyses. S.Z. and A.E. wrote the manuscript. All authors edited the manuscript. A.E. initiated and led all aspects of the project.

DECLARATION OF INTERESTS

A.E. has filed a patent on SHANEL technologies described in this study.

Received: May 22, 2019
Revised: December 4, 2019
Accepted: January 22, 2020
Published: February 13, 2020

SUPPORTING CITATIONS

The following references appear in the Supplemental Information: Corrin and Harkins (1947); le Maire et al. (2000); Mandal et al. (1988); Paradies (1980); Stubičar and Petres (1981); Stubičar et al. (1989).

REFERENCES

Amunts, K., Lepage, C., Borgeat, L., Mohlberg, H., Dickscheid, T., Rousseau, M.E., Bludau, S., Bazin, P.L., Lewis, L.B., Oros-Peusquens, A.M., et al. (2013). BigBrain: an ultrahigh-resolution 3D human brain model. Science *340*, 1472–1475.

Annunziato, M.E., Patel, U.S., Ranade, M., and Palumbo, P.S. (1993). p-maleimidophenyl isocyanate: a novel heterobifunctional linker for hydroxyl to thiol coupling. Bioconjug. Chem. *4*, 212–218.

Baek, K., Jung, S., Lee, J., Min, E., Jung, W., and Cho, H. (2019). Quantitative assessment of regional variation in tissue clearing efficiency using optical coherence tomography (OCT) and magnetic resonance imaging (MRI): A feasibility study. Sci. Rep. *9*, 2923.

Belle, M., Godefroy, D., Dominici, C., Heitz-Marchaland, C., Zelina, P., Hellal, F., Bradke, F., and Chédotal, A. (2014). A simple method for 3D analysis of immunolabeled axonal tracts in a transparent nervous system. Cell Rep. *9*, 1191–1201.

Belle, M., Godefroy, D., Couly, G., Malone, S.A., Collier, F., Giacobini, P., and Chedotal, A. (2017). Tridimensional Visualization and Analysis of Early Human Development. Cell *169*, 161–173.

Belthangady, C., and Royer, L.A. (2019). Applications, promises, and pitfalls of deep learning for fluorescence image reconstruction. Nat. Methods *16*, 1215–1225.

Bitplane. (2019). Imaris Microscopy Image Analysis (Oxford Instruments Group).

Bolte, S., and Cordelières, F.P. (2006). A guided tour into subcellular colocalization analysis in light microscopy. J. Microsc. *224*, 213–232.

Bozek, K., Wei, Y., Yan, Z., Liu, X., Xiong, J., Sugimoto, M., Tomita, M., Pääbo, S., Sherwood, C.C., Hof, P.R., et al. (2015). Organization and evolution of brain lipidome revealed by large-scale analysis of human, chimpanzee, macaque, and mouse tissues. Neuron *85*, 695–702.

Brett, M., Hanke, M., Cipollini, B., Côté, M.-A., Markiewicz, C., Gerhard, S., Larson, E., Lee, G.R., Halchenko, Y., and Kastman, E. (2016). nibabel: 2.1.0 (Zenodo).

Brett, M., Markiewicz, C.J., Hanke, M., Côté, M.-A., Cipollini, B., McCarthy, P., Cheng, C.P., Halchenko, Y.O., Cottaar, M., Ghosh, S., et al. (2020). nipy/nibabel: 3.0.1 (Zenodo) https://doi.org/10.5281/zenodo.3628482.

Bruns, O.T., Bischof, T.S., Harris, D.K., Franke, D., Shi, Y., Riedemann, L., Bartelt, A., Jaworski, F.B., Carr, J.A., and Rowlands, C.J. (2017). Next-generation in vivo optical imaging with short-wave infrared quantum dots. Nat. Biomed. Eng. *1*, 0056.

Cai, R., Pan, C., Ghasemigharagoz, A., Todorov, M.I., Forstera, B., Zhao, S., Bhatia, H.S., Parra-Damas, A., Mrowka, L., Theodorou, D., et al. (2019). Panoptic imaging of transparent mice reveals whole-body neuronal projections and skull-meninges connections. Nat. Neurosci. *22*, 317–327.

Carr, J.A., Aellen, M., Franke, D., So, P.T.C., Bruns, O.T., and Bawendi, M.G. (2018). Absorption by water increases fluorescence image contrast of biological tissue in the shortwave infrared. Proc. Natl. Acad. Sci. USA *115*, 9080–9085.

Carrim, Z.I., Chohan, A.W., and Devlin, H.C. (2006). Iris damage and acute pigment dispersion following photo-epilation. Eye (Lond.) *20*, 1486–1488.

Chen, C., Cohrs, C.M., Stertmann, J., Bozsak, R., and Speier, S. (2017). Human beta cell mass and function in diabetes: Recent advances in knowledge and technologies to understand disease pathogenesis. Mol. Metab. *6*, 943–957.

Chung, K., Wallace, J., Kim, S.Y., Kalyanasundaram, S., Andalman, A.S., Davidson, T.J., Mirzabekov, J.J., Zalocusky, K.A., Mattis, J., Denisin, A.K., et al. (2013). Structural and molecular interrogation of intact biological systems. Nature *497*, 332–337.

Chung, R., Howard, K., Craig, J.C., Chapman, J.R., Turner, R., and Wong, G. (2014). Economic evaluations in kidney transplantation: frequency, characteristics, and quality-a systematic review. Transplantation *97*, 1027–1033.

Çiçek, Ö., Abdulkadir, A., Lienkamp, S.S., Brox, T., and Ronneberger, O. (2016). 3D U-Net: learning dense volumetric segmentation from sparse annotation. arXiv, arXiv:1606.06650. https://arxiv.org/abs/1606.06650.

Clarke, S. (1981). The hydrophobic effect: Formation of micelles and biological membranes, 2nd edition (Tanford, Charles). J. Chem. Educ. *58*, A246.

Corrin, M.L., and Harkins, W.D. (1947). The effect of salts on the critical concentration for the formation of micelles in colloidal electrolytes. J. Am. Chem. Soc. *69*, 683–688.

Cosco, E.D., Caram, J.R., Bruns, O.T., Franke, D., Day, R.A., Farr, E.P., Bawendi, M.G., and Sletten, E.M. (2017). Flavylium Polymethine Fluorophores for Near- and Shortwave Infrared Imaging. Angew. Chem. Int. Engl. *56*, 13126–13129.

Davis, A.S., Richter, A., Becker, S., Moyer, J.E., Sandouk, A., Skinner, J., and Taubenberger, J.K. (2014). Characterizing and Diminishing Autofluorescence in Formalin-fixed Paraffin-embedded Human Respiratory Tissue. J. Histochem. Cytochem. *62*, 405–423.

De Maria, A., Wilmarth, P.A., David, L.L., and Bassnett, S. (2017). Proteomic Analysis of the Bovine and Human Ciliary Zonule. Invest. Ophthalmol. Vis. Sci. *58*, 573–585.

Denic, A., Mathew, J., Lerman, L.O., Lieske, J.C., Larson, J.J., Alexander, M.P., Poggio, E., Glassock, R.J., and Rule, A.D. (2017). Single-Nephron Glomerular Filtration Rate in Healthy Adults. N. Engl. J. Med. *376*, 2349–2357.

Despotović, I., Goossens, B., and Philips, W. (2015). MRI segmentation of the human brain: challenges, methods, and applications. Comput. Math. Methods Med. *2015*, 450341.

Deverman, B.E., Pravdo, P.L., Simpson, B.P., Kumar, S.R., Chan, K.Y., Banerjee, A., Wu, W.L., Yang, B., Huber, N., Pasca, S.P., and Gradinaru, V. (2016). Cre-dependent selection yields AAV variants for widespread gene transfer to the adult brain. Nat. Biotechnol. *34*, 204–209.

Ding, S.L., Royall, J.J., Sunkin, S.M., Ng, L., Facer, B.A., Lesnar, P., Guillozet-Bongaarts, A., McMurray, B., Szafer, A., Dolbeare, T.A., et al. (2016).

Comprehensive cellular-resolution atlas of the adult human brain. J. Comp. Neurol. *524*, 3127–3481.

Dodt, H.U., Leischner, U., Schierloh, A., Jährling, N., Mauch, C.P., Deininger, K., Deussing, J.M., Eder, M., Zieglgänsberger, W., and Becker, K. (2007). Ultramicroscopy: three-dimensional visualization of neuronal networks in the whole mouse brain. Nat. Methods *4*, 331–336.

Duan, Z., Li, Y., Guan, S., Ma, C., Han, Y., Ren, X., Wei, L., Li, W., Lou, J., and Yang, Z. (2018). Morphological parameters and anatomical locations associated with rupture status of small intracranial aneurysms. Sci. Rep. *8*, 6440.

Ertürk, A., Becker, K., Jährling, N., Mauch, C.P., Hojer, C.D., Egen, J.G., Hellal, F., Bradke, F., Sheng, M., and Dodt, H.U. (2012). Three-dimensional imaging of solvent-cleared organs using 3DISCO. Nat. Protoc. *7*, 1983–1995.

Garvalov, B.K., and Ertürk, A. (2017). Seeing whole-tumour heterogeneity. Nat. Biomed. Eng. *1*, 772–774.

Genovese, F., Manresa, A.A., Leeming, D.J., Karsdal, M.A., and Boor, P. (2014). The extracellular matrix in the kidney: a source of novel non-invasive biomarkers of kidney fibrosis? Fibrogenesis Tissue Repair *7*, 4.

Guinier, A. (1939). La diffraction des rayons X aux très petits angles: application à l'étude de phénomènes ultramicroscopiques. Ann Physiol. *11*, 161–237.

Hammouda, B. (2013). Temperature Effect on the Nanostructure of SDS Micelles in Water. J. Res. Natl. Inst. Stand. Technol. *118*, 151–167.

Heusch, P., Wittsack, H.J., Blondin, D., Ljimani, A., Nguyen-Quang, M., Martirosian, P., Zenginli, H., Bilk, P., Kröpil, P., Heusner, T.A., et al. (2014). Functional evaluation of transplanted kidneys using arterial spin labeling MRI. J. Magn. Reson. Imaging *40*, 84–89.

Hildebrand, S., Schueth, A., Herrler, A., Galuske, R., and Roebroeck, A. (2018). Scalable cytoarchitectonic characterization of large intact human neocortex samples. bioRxiv. https://doi.org/10.1101/274985.

Hsu, P.D., Lander, E.S., and Zhang, F. (2014). Development and applications of CRISPR-Cas9 for genome engineering. Cell *157*, 1262–1278.

Hughson, M.D., Hoy, W.E., Mott, S.A., Puelles, V.G., Bertram, J.F., Winkler, C.L., and Kopp, J.B. (2016). *APOL1* Risk Alleles are Associated with More Severe Arteriosclerosis in Renal Resistance Vessels with Aging and Hypertension. Kidney Int. Rep. *1*, 10–23.

Jain, M., Robinson, B.D., Aggarwal, A., Shevchuk, M.M., Scherr, D.S., and Mukherjee, S. (2016). Multiphoton microscopy for rapid histopathological evaluation of kidney tumours. BJU Int. *118*, 118–126.

Jing, D., Zhang, S., Luo, W., Gao, X., Men, Y., Ma, C., Liu, X., Yi, Y., Bugde, A., Zhou, B.O., et al. (2018). Tissue clearing of both hard and soft tissue organs with the PEGASOS method. Cell Res. *28*, 803–818.

Jung, C.K., Keppler, K., Steinbach, S., Blazquez-Llorca, L., and Herms, J. (2015). Fibrillar amyloid plaque formation precedes microglial activation. PLoS ONE *10*, e0119768.

Kang, H.W., Lee, S.J., Ko, I.K., Kengla, C., Yoo, J.J., and Atala, A. (2016). A 3D bioprinting system to produce human-scale tissue constructs with structural integrity. Nat. Biotechnol. *34*, 312–319.

Kemter, E., and Wolf, E. (2018). Recent progress in porcine islet isolation, culture and engraftment strategies for xenotransplantation. Curr. Opin. Organ Transplant. *23*, 633–641.

Kemter, E., Cohrs, C.M., Schäfer, M., Schuster, M., Steinmeyer, K., Wolf-van Buerck, L., Wolf, A., Wuensch, A., Kurome, M., Kessler, B., et al. (2017). INS-eGFP transgenic pigs: a novel reporter system for studying maturation, growth and vascularisation of neonatal islet-like cell clusters. Diabetologia *60*, 1152–1156.

Kermany, D.S., Goldbaum, M., Cai, W., Valentim, C.C.S., Liang, H., Baxter, S.L., McKeown, A., Yang, G., Wu, X., Yan, F., et al. (2018). Identifying Medical Diagnoses and Treatable Diseases by Image-Based Deep Learning. Cell *172*, 1122–1131.

Kingma, D.P., and Ba, J. (2014). Adam: A method for stochastic optimization. arXiv, arXiv:14126980. https://arxiv.org/abs/1412.6980.

Klunk, W.E., Bacskai, B.J., Mathis, C.A., Kajdasz, S.T., McLellan, M.E., Frosch, M.P., Debnath, M.L., Holt, D.P., Wang, Y., and Hyman, B.T. (2002). Imaging Abeta plaques in living transgenic mice with multiphoton microscopy and methoxy-X04, a systemically administered Congo red derivative. J. Neuropathol. Exp. Neurol. *61*, 797–805.

Kubota, S.I., Takahashi, K., Nishida, J., Morishita, Y., Ehata, S., Tainaka, K., Miyazono, K., and Ueda, H.R. (2017). Whole-Body Profiling of Cancer Metastasis with Single-Cell Resolution. Cell Rep. *20*, 236–250.

Kurome, M., Leuchs, S., Kessler, B., Kemter, E., Jemiller, E.M., Foerster, B., Klymiuk, N., Zakhartchenko, V., and Wolf, E. (2017). Direct introduction of gene constructs into the pronucleus-like structure of cloned embryos: a new strategy for the generation of genetically modified pigs. Transgenic Res. *26*, 309–318.

Lai, H.M., Liu, A.K.L., Ng, H.H.M., Goldfinger, M.H., Chau, T.W., DeFelice, J., Tilley, B.S., Wong, W.M., Wu, W., and Gentleman, S.M. (2018). Next generation histology methods for three-dimensional imaging of fresh and archival human brain tissues. Nat. Commun. *9*, 1066.

le Maire, M., Champeil, P., and Moller, J.V. (2000). Interaction of membrane proteins and lipids with solubilizing detergents. Biochim. Biophys. Acta *1508*, 86–111.

Lee, S.C., Bennett, B.C., Hong, W.X., Fu, Y., Baker, K.A., Marcoux, J., Robinson, C.V., Ward, A.B., Halpert, J.R., Stevens, R.C., et al. (2013). Steroid-based facial amphiphiles for stabilization and crystallization of membrane proteins. Proc. Natl. Acad. Sci. USA *110*, E1203–E1211.

Lipfert, J., and Doniach, S. (2007). Small-angle X-ray scattering from RNA, proteins, and protein complexes. Annu. Rev. Biophys. Biomol. Struct. *36*, 307–327.

Lipfert, J., Millett, I.S., Seifert, S., and Doniach, S. (2006). Sample holder for small-angle x-ray scattering static and flow cell measurements. Rev. Sci. Instrum. *77*, 046108.

Lipfert, J., Columbus, L., Chu, V.B., Lesley, S.A., and Doniach, S. (2007). Size and shape of detergent micelles determined by small-angle X-ray scattering. J. Phys. Chem. B *111*, 12427–12438.

Mandal, A.B., Nair, B.U., and Ramaswamy, D. (1988). Determination of the critical micelle concentration of surfactants and the partition coefficient of an electrochemical probe by using cyclic voltammetry. Langmuir *4*, 736–739.

Manon-Jensen, T., Kjeld, N.G., and Karsdal, M.A. (2016). Collagen-mediated hemostasis. J. Thromb. Haemost. *14*, 438–448.

McCulloch, C. (1954). The zonule of Zinn: its origin, course, and insertion, and its relation to neighboring structures. Trans. Am. Ophthalmol. Soc. *52*, 525–585.

McKinney, W. (2010). Data structures for statistical computing in python. In Proceedings of the 9th Python in Science Conference (SciPy 2010), pp. 51–56.

Moen, E., Bannon, D., Kudo, T., Graf, W., Covert, M., and Van Valen, D. (2019). Deep learning for cellular image analysis. Nat. Methods *16*, 1233–1246.

Monnier, V.M., Kohn, R.R., and Cerami, A. (1984). Accelerated age-related browning of human collagen in diabetes mellitus. Proc. Natl. Acad. Sci. USA *81*, 583–587.

Morawski, M., Kirilina, E., Scherf, N., Jäger, C., Reimann, K., Trampel, R., Gavriilidis, F., Geyer, S., Biedermann, B., Arendt, T., and Weiskopf, N. (2018). Developing 3D microscopy with CLARITY on human brain tissue: Towards a tool for informing and validating MRI-based histology. Neuroimage *182*, 417–428.

Moreno-García, A., Kun, A., Calero, O., Medina, M., and Calero, M. (2018). An Overview of the Role of Lipofuscin in Age-Related Neurodegeneration. Front. Neurosci. *12*, 464.

Morita, A., Kirino, T., Hashi, K., Aoki, N., Fukuhara, S., Hashimoto, N., Nakayama, T., Sakai, M., Teramoto, A., Tominari, S., and Yoshimoto, T.; UCAS Japan Investigators (2012). The natural course of unruptured cerebral aneurysms in a Japanese cohort. N. Engl. J. Med. *366*, 2474–2482.

Moschovakis, A.K., and Highstein, S.M. (1994). The anatomy and physiology of primate neurons that control rapid eye movements. Annu. Rev. Neurosci. *17*, 465–488.

Murphy, S.V., and Atala, A. (2014). 3D bioprinting of tissues and organs. Nat. Biotechnol. *32*, 773–785.

Murray, E., Cho, J.H., Goodwin, D., Ku, T., Swaney, J., Kim, S.Y., Choi, H., Park, Y.G., Park, J.Y., Hubbert, A., et al. (2015). Simple, Scalable Proteomic Imaging for High-Dimensional Profiling of Intact Systems. Cell *163*, 1500–1514.

Oliver, R.C., Lipfert, J., Fox, D.A., Lo, R.H., Doniach, S., and Columbus, L. (2013). Dependence of micelle size and shape on detergent alkyl chain length and head group. PLoS ONE *8*, e62488.

Oliver, R.C., Lipfert, J., Fox, D.A., Lo, R.H., Kim, J.J., Doniach, S., and Columbus, L. (2014). Tuning micelle dimensions and properties with binary surfactant mixtures. Langmuir *30*, 13353–13361.

Pan, C., Cai, R., Quacquarelli, F.P., Ghasemigharagoz, A., Lourbopoulos, A., Matryba, P., Plesnila, N., Dichgans, M., Hellal, F., and Ertürk, A. (2016). Shrinkage-mediated imaging of entire organs and organisms using uDISCO. Nat. Methods *13*, 859–867.

Paradies, H.H. (1980). Shape and size of a nonionic surfactant micelle. Triton X-100 in aqueous solution. J. Phys. Chem. *84*, 599–607.

Park, Y.-G., Sohn, C.H., Chen, R., McCue, M., Yun, D.H., Drummond, G.T., Ku, T., Evans, N.B., Oak, H.C., Trieu, W., et al. (2018). Protection of tissue physicochemical properties using polyfunctional crosslinkers. Nat. Biotechnol. *37*, 73.

Paszke, A., Gross, S., Massa, F., Lerer, A., Bradbury, J., Chanan, G., Killeen, T., Lin, Z., Gimelshein, N., Antiga, L., et al. (2019). PyTorch: An imperative style, high-performance deep learning library. Adv. Neural Inf. Process. Syst., 8024–8035.

Puelles, V.G., and Bertram, J.F. (2015). Counting glomeruli and podocytes: rationale and methodologies. Curr. Opin. Nephrol. Hypertens. *24*, 224–230.

Puelles, V.G., Fleck, D., Ortz, L., Papadouri, S., Strieder, T., Böhner, A.M.C., van der Wolde, J.W., Vogt, M., Saritas, T., Kuppe, C., et al. (2019). Novel 3D analysis using optical tissue clearing documents the evolution of murine rapidly progressive glomerulonephritis. Kidney Int. *96*, 505–516.

Rajan, N., Habermehl, J., Coté, M.F., Doillon, C.J., and Mantovani, D. (2006). Preparation of ready-to-use, storable and reconstituted type I collagen from rat tail tendon for tissue engineering applications. Nat. Protoc. *1*, 2753–2758.

Reardon, S. (2016). Worldwide brain-mapping project sparks excitement - and concern. Nature *537*, 597.

Renier, N., Wu, Z., Simon, D.J., Yang, J., Ariel, P., and Tessier-Lavigne, M. (2014). iDISCO: a simple, rapid method to immunolabel large tissue samples for volume imaging. Cell *159*, 896–910.

Renier, N., Adams, E.L., Kirst, C., Wu, Z., Azevedo, R., Kohl, J., Autry, A.E., Kadiri, L., Umadevi Venkataraju, K., Zhou, Y., et al. (2016). Mapping of Brain Activity by Automated Volume Analysis of Immediate Early Genes. Cell *165*, 1789–1802.

Richardson, D.S., and Lichtman, J.W. (2015). Clarifying Tissue Clearing. Cell *162*, 246–257.

Rodi, P.M., Bocco Gianello, M.D., Corregido, M.C., and Gennaro, A.M. (2014). Comparative study of the interaction of CHAPS and Triton X-100 with the erythrocyte membrane. Biochim. Biophys. Acta *1838*, 859–866.

Ronneberger, O., Fischer, P., and Brox, T. (2015). U-Net: convolutional networks for biomedical image segmentation. In Proceedings of the International Conference on Medical Image Computing and Computer-Assisted Intervention (MICCAI 2015), *9351*, N. Navab, J. Hornegger, W. Wells, and A. Frangi, eds., pp. 234–241, (Springer). https://doi.org/10.1007/978-3-319.

Schindelin, J., Arganda-Carreras, I., Frise, E., Kaynig, V., Longair, M., Pietzsch, T., Preibisch, S., Rueden, C., Saalfeld, S., Schmid, B., et al. (2012). Fiji: an open-source platform for biological-image analysis. Nat. Methods *9*, 676–682.

Schneider, C.A., Rasband, W.S., and Eliceiri, K.W. (2012). NIH Image to ImageJ: 25 years of image analysis. Nat. Methods *9*, 671–675.

Schnermann, M.J. (2017). Chemical biology: Organic dyes for deep bioimaging. Nature *551*, 176–177.

Shen, G., Anand, M.F., and Levicky, R. (2004). X-ray photoelectron spectroscopy and infrared spectroscopy study of maleimide-activated supports for immobilization of oligodeoxyribonucleotides. Nucleic Acids Res. *32*, 5973–5980.

Sijens, P.E., Edens, M.A., Bakker, S.J., and Stolk, R.P. (2010). MRI-determined fat content of human liver, pancreas and kidney. World J. Gastroenterol. *16*, 1993–1998.

Steinke, H., and Wolff, W. (2001). A modified Spalteholz technique with preservation of the histology. Ann. Anat. *183*, 91–95.

Stubičar, N., and Petres, J. (1981). Micelle Formation by Tritons in Aqueous Solutions. Croat. Chem. Acta *54*, 255–266.

Stubičar, N., Matejaš, J., Zipper, P., and Wilfing, R. (1989). Size, shape and internal structure of Triton X-100 micelles determined by light and small-angle X-ray scattering techniques. In Surfactants in Solution (Springer), pp. 181–195.

Sullivan, D.P., Winsnes, C.F., Åkesson, L., Hjelmare, M., Wiking, M., Schutten, R., Campbell, L., Leifsson, H., Rhodes, S., Nordgren, A., et al. (2018). Deep learning is combined with massive-scale citizen science to improve large-scale image classification. Nat. Biotechnol. *36*, 820–828.

Svergun, D.I., and Koch, M.H.J. (2003). Small-angle scattering studies of biological macromolecules in solution. Rep. Prog. Phys. *66*, 1735–1782.

Tainaka, K., Kubota, S.I., Suyama, T.Q., Susaki, E.A., Perrin, D., Ukai-Tadenuma, M., Ukai, H., and Ueda, H.R. (2014). Whole-body imaging with single-cell resolution by tissue decolorization. Cell *159*, 911–924.

Tainaka, K., Murakami, T.C., Susaki, E.A., Shimizu, C., Saito, R., Takahashi, K., Hayashi-Takagi, A., Sekiya, H., Arima, Y., Nojima, S., et al. (2018). Chemical Landscape for Tissue Clearing Based on Hydrophilic Reagents. Cell Rep. *24*, 2196–2210.

Tetteh, G., Efremov, V., Forkert, N.D., Schneider, M., Kirschke, J., Weber, B., Zimmer, C., Piraud, M., and Menze, B.H. (2018). Deepvesselnet: Vessel segmentation, centerline prediction, and bifurcation detection in 3-d angiographic volumes. arXiv, arXiv:180309340.

Todorov, M.I., Paetzold, J.C., Schoppe, O., Tetteh, G., Efremov, V., Voelgyi, K., Duering, M., Dichgans, M., Piraud, M., and Menze, B. (2019). Automated analysis of whole brain vasculature using machine learning. bioRxiv. https://doi.org/10.1101/613257.

Van Der Walt, S., Colbert, S.C., and Varoquaux, G. (2011). The NumPy array: a structure for efficient numerical computation. Comput. Sci. Eng. *13*, 22.

Virtanen, P., Gommers, R., Oliphant, T.E., Haberland, M., Reddy, T., Cournapeau, D., Burovski, E., Peterson, P., Weckesser, W., Bright, J., et al. (2020). SciPy 1.0: fundamental algorithms for scientific computing in Python. Nat. Methods. https://doi.org/10.1038/s41592-019-0686-2.

Vogt, N. (2018). Raising the game in image classification. Nat. Methods *15*, 759.

Voigt, F.F., Kirschenbaum, D., Platonova, E., Pagès, S., Campbell, R.A., Kästli, R., Schaettin, M., Egolf, L., Van Der Bourg, A., Bethge, P., and Haenraets, K. (2019). The mesoSPIM initiative: open-source light-sheet mesoscopes for imaging in cleared tissue. bioRxiv. https://doi.org/10.1101/577122.

Wainberg, M., Merico, D., Delong, A., and Frey, B.J. (2018). Deep learning in biomedicine. Nat. Biotechnol. *36*, 829–838.

Wang, X., Misawa, R., Zielinski, M.C., Cowen, P., Jo, J., Periwal, V., Ricordi, C., Khan, A., Szust, J., Shen, J., et al. (2013). Regional differences in islet distribution in the human pancreas–preferential beta-cell loss in the head region in patients with type 2 diabetes. PLoS ONE *8*, e67454.

Wang, F., Wan, H., Ma, Z., Zhong, Y., Sun, Q., Tian, Y., Qu, L., Du, H., Zhang, M., Li, L., et al. (2019). Light-sheet microscopy in the near-infrared II window. Nat. Methods *16*, 545–552.

White, L.J., Taylor, A.J., Faulk, D.M., Keane, T.J., Saldin, L.T., Reing, J.E., Swinehart, I.T., Turner, N.J., Ratner, B.D., and Badylak, S.F. (2017). The impact of detergents on the tissue decellularization process: A ToF-SIMS study. Acta Biomater. *50*, 207–219.

Yanagishita, M., Podyma-Inoue, K.A., and Yokoyama, M. (2009). Extraction and separation of proteoglycans. Glycoconj. J. *26*, 953–959.

Yang, B., Treweek, J.B., Kulkarni, R.P., Deverman, B.E., Chen, C.K., Lubeck, E., Shah, S., Cai, L., and Gradinaru, V. (2014). Single-cell phenotyping within transparent intact tissue through whole-body clearing. Cell *158*, 945–958.

Yushkevich, P.A., Gao, Y., and Gerig, G. (2016). ITK-SNAP: An interactive tool for semi-automatic segmentation of multi-modality biomedical images. In 38th Annual International Conference of the IEEE Engineering in Medicine and Biology Society (EMBC) (IEEE) Orlando, FL, pp. 3342–3345.

Zhang, Q., Tao, H., and Hong, W.X. (2011). New amphiphiles for membrane protein structural biology. Methods *55*, 318–323.

Zhao, H.L., Zhang, C.P., Zhu, H., Jiang, Y.F., and Fu, X.B. (2017). Autofluorescence of collagen fibres in scar. Skin Res. Technol. *23*, 588–592.

STAR★METHODS

KEY RESOURCES TABLE

REAGENT or RESOURCE	SOURCE	IDENTIFIER
Antibodies		
Rabbit Anti-Iba1	Wako	Cat.# 019-19741; RRID: AB_839504
Rabbit Anti-Tyrosine Hydroxylase	abcam	Cat.# ab112; RRID: AB_297804
Alexa 647-conjugated secondary antibody	Thermo Fisher	Cat.# A-21245; RRID: AB_2535813
Mouse Anti-MBP	Atlas antibodies	Cat.# AMAb91064; RRID: AB_2665784
Rabbit Anti-Laminin	Sigma	Cat.# L9393; RRID: AB_477163
Rabbit Anti-Neuropeptide Y	abcam	Cat.# Ab30914; RRID: AB_1566510
Rabbit Anti-GFAP	Dako	Cat.# Z033401-2; RRID: AB_10013382
Alexa 647 goat anti-rabbit secondary antibody	Life Technology	Cat.# A31852; RRID: AB_162553
Chemicals, Peptides, and Recombinant Proteins		
Phosphate Buffer Saline containing Heparin	Ratiopharm	Cat.# N68542.03
4% paraformaldehyde (PFA)	Morphisto	Cat.# 11762.05000
CHAPS	Roth	Cat.# 1479.4
Triton X-100	PanReac Applichem	Cat.# A4975,1000
SDS	PanReac Applichem	Cat.# A2572,0250
Methylene blue	Sigma	Cat.# M9140
N-Methyldiethanolamine	Sigma	Cat.# 471828
Ethanol	Merck	Cat.# 10098535000
Benzyl benzoate	Sigma	Cat.# W213802
Benzyl alcohol	Sigma	Cat.# 24122
Dichloromethane	Roth	Cat.# KK47.1
Methyl-β –cyclodextrin	Sigma	Cat.# 332615
Trans-1-acetyl-4-hydroxy-l-proline	Sigma	Cat.# 441562
Atto647N-conjugated anti-GFP nanobooster	Chromotek	Cat.# gba647n-100; RRID: AB_2629215; Batch No. 60920001SAT2
TO-PRO-3	Thermo Fisher	Cat.# T3605
Methoxy X-04	Tocris	Cat.# 4920
NaOH	Roth	Cat.# 6771.1
Acetic acid	Roth	Cat.# T179.1
Guanidine hydrochloride	Roth	Cat.# 6069.3
Sodium acetate	Sigma	Cat.# S2889
DMSO	Roth	Cat.# A994.2
Propidium iodide	Thermo Fisher	Cat.# P3566
Gill's hematoxylin	Sigma	Cat.# GHS3
Eosin	Roth	Cat.# 7089.1
Cresyl violet	Sigma	Cat.# C5042
Copper sulfate	Roth	Cat.# CP86.1
Ammonium chloride	Roth	Cat.# P726.1
DyLight 649-lectin	Vector	Cat.# DL-1178
Goat serum	GIBCO	Cat.# 16210072
Bovine Serum Albumin	Sigma	Cat.# A7906
Critical Commercial Assays		
Bio-Rad DC protein assay kit	Bio-Rad	Cat.# 5000116
PAS staining system	Sigma	Cat.# 395B

(*Continued on next page*)

Continued

REAGENT or RESOURCE	SOURCE	IDENTIFIER
Deposited Data		
Raw data and data labels for SHANEL	This paper	http://discotechnologies.org/SHANEL/
Experimental Models: Organisms/Strains		
CD-1 IGS	Charles River	Cat.# 022
Software and Algorithms		
ImageJ	Schneider et al., 2012	https://imagej.nih.gov/ij/
AxioZoom EMS3 software	Carl Zeiss AG	https://www.zeiss.com/microscopy/int/products/stereo-zoom-microscopes/axio-zoom-v16.html#downloads
ImSpector	Aberrior/LaVision	https://www.lavisionbiotec.com/
Photoshop CS6	Adobe	https://www.adobe.com/products/photoshop.html
Imaris	Bitplane	https://imaris.oxinst.com/
Vision4D	Arivis	https://www.arivis.com/de/imaging-science/arivis-vision4d
SciPy package for Python	Virtanen et al., 2020	https://www.scipy.org
Python Anaconda distribution	Anaconda	https://www.anaconda.com/distribution/
PyTorch deep learning framework for Python	Paszke et al., 2019	https://pytorch.org/
Cuda	NVIDIA	https://developer.nvidia.com/cuda-downloads
NiBabel	Brett et al., 2020	https://nipy.org/nibabel
Connected-components-3d	Seung Lab	https://github.com/seung-lab/connected-components-3d
SHANEL algorithm	This paper	https://github.com/erturklab/shanel-network
CuDNN	NVIDIA	https://developer.nvidia.com/cuda-downloads
Other		
Online demonstration of the SHANEL algorithm	This paper	https://colab.research.google.com/drive/1Lpfo6AoHGfpzHvHiD7pnH6DuW9VQxFgq
Resource website for SHANEL	This paper	http://discotechnologies.org/SHANEL/

LEAD CONTACT AND MATERIALS AVAILABILITY

Further information and requests for resources and reagents should be directed to and will be fulfilled by the Lead Contact, Ali Ertürk (erturk@helmholtz-muenchen.de). The clearing protocols as well as cleared samples, algorithms and data on SHANEL are freely available from the Lead contact and shared at http://discotechnologies.org/SHANEL/.

EXPERIMENTAL MODEL AND SUBJECT DETAILS

Mouse samples

CD-1 IGS (Charles River, stain code: 022) mice were used for blood collection, organs screening and protein loss assay. The animals were housed under a 12/12 hours light/dark cycle. The animal experiments were conducted according to institutional guidelines: Klinikum der Universität München / Ludwig Maximilian University of Munich and after approval of the Ethical Review Board of the Government of Upper Bavaria (Regierung von Oberbayern, Munich, Germany) and in accordance with the European directive 2010/63/EU for animal research. All data are reported according to the ARRIVE criteria. Animals were randomly selected related to age and gender. Mice were deeply anesthetized using a combination of medetomidine, midazolam and fentanyl (MMF; 5 mg, 0.5 mg and 0.05 mg per kg body mass for mice; intraperitoneal). As soon as the animals did not show any pedal reflex, the chest of the animal was opened and exposed. The blood was extracted intracardially from the left ventricle. The animals were sacrificed afterward. Then the blood was mixed with 2 times volume of 4% paraformaldehyde (PFA, pH 7.4; Morphisto, 11762.05000) in 0.01 M PBS (pH 7.4; Morphisto, 11762.01000) and incubated for 24 h at 4°C. Animals for protein loss assay were intracardially perfused with heparinized 0.01 M PBS (10 U ml^{-1} of heparin, Ratiopharm; ~110 mmHg pressure using a Leica Perfusion One system) for 5–10 min at room temperature until the blood was washed out, followed by 4% PFA for 10–20 min. The brains were dissected and post-fixed in 4% PFA for 1 d at 4°C and later washed with 0.01 M PBS for 10 min 3 times at room temperature.

Pig samples

An intact pig brain was bought from a local slaughterhouse and selected randomly relate to gender, then fixed for 10 days immersing it in 4% PFA at 4°C. Housing, breeding and animal experiments of *INS*-EGFP transgenic pigs were done at the Institute of Molecular Animal Breeding and Biotechnology at LMU Munich according to the approval of the Ethical Review Board of the Government of Upper Bavaria (Regierung von Oberbayern, Munich, Germany) and in accordance with the European directive 2010/63/EU for animal research. All data are reported according to the ARRIVE criteria. *INS*-EGFP transgenic pigs have a beta-cell specific EGFP reporter gene expression driven by the porcine insulin (*INS*) promoter (Kemter et al., 2017). Pancreas of an exsanguinated 5.5 month-old *INS*-EGFP transgenic male pig of a German landrace background was dissected, its pancreatic ducts were cannulated and 20 mL of ice-cold 4% PFA was slowly injected into the ducts.

Human samples

Intact human brains were taken from different human body donors with no known neuropathological diseases. All donors gave their informed and written consent to explore their cadavers for research and educational purposes, when still alive and well. The signed consents are kept at the Anatomy Institute, University of Leipzig, Germany. Institutional approval was obtained in accordance to the Saxonian Death and Funeral Act of 1994. The signed body donor consents are available on request.

The brains of a 92 years-old female and a 48 years-old male of the body donation program of the Institute of Anatomy, University of Leipzig were fixed *in situ* by whole head perfusion via carotid and vertebral arteries under a pressure of below 1 bar. The head was first perfused with 5 L heparinized 0.01 M PBS (10 U ml^{-1} of heparin, Ratiopharm), followed by 3 L 4% PFA in 0.01 M PBS for 2-3 h. The veins were finally closed to maintain the PFA to the brain. Then the brains were recovered by calvarian dissection and preserved at least 1-2 weeks for post-fixation submersed in the 4% PFA solution. The thyroid was dissected and post-fixed by 200 mL PFA for 3 days. The kidneys of a 93 years-old female donor were dissected from the body. The blood was flushed with 200 mL of heparinized PBS in a PBS bath for 1 hr and perfused with 400 mL of PFA immersed in PFA solution. The kidneys were preserved at least 1-2 weeks for post-fixation submersed in the 4% PFA solution at 4°C.

METHOD DETAILS

Small-angle X-ray scattering measurements

We used small-angle X-ray scattering to determine the size, shape and aggregation number of CHAPS and SDS micelles. Experimental data were collected at beam line 12ID at the Advanced Photon Source (APS) using procedures as previously described (Lipfert et al., 2007; Oliver et al., 2013, 2014). In brief, measurements were carried out with a custom-made sample cell and holder (Lipfert et al., 2006), at a temperature of 25°C and an X-ray energy of 12 keV, with a sample-to-detector distance of 1.8 m. We defined the magnitude of momentum transfer as $q = 4\pi / \lambda \cdot \sin(\theta)$, where 2θ is the total scattering angle and $\lambda = 1$ Å the X-ray wavelength. The useable q-range in our measurements was 0.02 $Å^{-1} < q < 0.275$ $Å^{-1}$. Scattering angles were calibrated using a silver behenate standard sample. Data read out, normalization, and circular averaging were performed using custom routines at beam line 12ID, APS. SDS and CHAPS were measured in PBS buffer for 10 exposures of 0.1 s. Matching buffer profiles were subtracted for background correction. Subsequent exposures were compared to verify the absence of radiation damage. Horse heart cytochrome *c* at 8 mg/ml was used as a molecular mass standard.

Small-angle X-ray scattering data analysis

Radii of gyration R_g and forward scattering intensities $I(0)$ were determined from Guinier analysis (Guinier, 1939; Lipfert and Doniach, 2007; Svergun and Koch, 2003) of the low q region of scattering profiles, i.e., from a fit of the logarithm of the scattering intensity versus q^2 for small q (Figures S1A and S1B). The fitted radii of gyration are in excellent agreement with previously reported values, as far as available (Figure 1C). In addition, the full scattering profiles were fitted with one- and two-component ellipsoid models (Lipfert et al., 2007) (Figure S1C). We found that the CHAPS data were well described by a prolate one-component ellipsoid model with long axis of ≈30 Å and short axis ≈12 Å. In contrast, the SDS data require a two-component ellipsoid model for a convincing fit, similar to other 'head-to-tail' detergents (Lipfert et al., 2007), and were well described by a oblate two-component ellipsoid model with an inner core (representing the region occupied by the hydrophobic tail groups) with small axis ≈15 Å and long axis ≈25 Å (in good agreement with results from neutron scattering) (Hammouda, 2013), surrounded by a shell (representing the head groups) of thickness ≈3.5 Å.

Aggregation numbers for CHAPS and SDS micelles were determined using two independent approaches (Lipfert et al., 2007). One approach was to use the fitted geometric models to compute the volumes of the micelle (in the case of CHAPS) or of the hydrophobic core (in the case of SDS) and to compute the aggregation number by dividing the total volume by the volume of the monomer (for CHAPS, see Table S1) or the hydrophobic core volume by the volume of the alkyl tail (determined from the Tanford formula (Clarke, 1981), 350.2 $Å^3$ for SDS). We note that the approach of using the micelle volume to determine the aggregation number uses the entire scattering profile in the model fit, but is independent of the scale of the scattering intensity, since only the shape of the scattering pattern is fit. An alternative and independent approach to determining the aggregation number is to determine the forward scattering intensity $I(0)$ from Guinier analysis and to compute the aggregation number from the equation (Lipfert et al., 2007):

$$N = I(0)/I_{mon}(0) = I(0)\Big/\left[K \times (C - CMC) \times (r_{det} - r_{sol})^2 \times V_{mon}^2\right]$$

Here K is a proportionality constant that was determined from measurements of horse heart cytochrome c as a scattering standard, C is the detergent concentration, CMC the critical micelle concentration, ρ_{det} the electron density of the detergent, $\rho_{sol} = 0.34$ e/Å^3 the electron density of the solvent, and V_{mon} the detergent monomer volume. Values for CMC, ρ_{det} and V_{mon} are given in Table S1. The approach of using *I(0)* to determine the aggregation number only uses the very low q information in the scattering pattern and is independent of any model assumptions about the size or shape of the micelles. Aggregation numbers determined by the independent approaches are in good agreement.

Comparison of permeabilization capacity of different detergents on pig pancreas using methylene blue dye staining

1-2 cm pig pancreas cubic samples were incubated with the following detergents: 10% w/v CHAPS (Roth, 1479.4), 10% w/v Triton X-100 (PanReac Applichem, A4975,1000) or 200 mM SDS (PanReac Applichem, A2572,0250) for 2 days at 37°C. After PBS wash, the samples were incubated with 50 mL of 0.05% methylene blue dye (Sigma, M9140) in plastic tubes (Falcon) at 37°C overnight. After PBS wash, the samples were cut into half to evaluate the staining efficiency of the inner tissue. The camera pictures of the samples were analyzed by ImageJ for profile plot along the center of the cut samples, and we quantified the pixels under threshold gray value.

Screening of affordable and scalable chemicals for blood decolorization

PFA-fixed mouse blood was thoroughly vortexed with either only 25% w/v screened chemicals (Sigma, for the catalog codes, see Table S2) or only detergents (10% w/v CHAPS, 10% w/v Triton X-100 or 200 mM SDS), or the mixture of detergents and 25% w/v chemicals, and then immediately centrifuged at 15000 rpm for 5 min at room temperature. Supernatants were transferred into multi-well plates (Corning, CLS3527) and pellets were dissolved in diH_2O and also transferred into the paired wells. Camera images were immediately captured. In accordance with our hypothesis that electron-rich nitrogen donor and polarizable hydrogen of chemicals tend to bind with the iron of heme as double-action multidentate ligands, then eluting the heme from the blood, all of the tested chemicals would partly decolorize the red heme. These effects were improved with the addition of detergents. 100 μL supernatant solution from each well was transferred to a 96-well black microplate (Corning, CLS3925) and the visible spectra were recorded using a microplate reader (Fluostar Omega, BMG Labtech). The OD600 values were measured with the Omega analysis software. Considering the practical prices and availability of reagents to process large samples such as the human brain, we optimized the concentration of CHAPS with N-Methyldiethanolamine (chemical 7, Sigma, 471828) for later experiments (Tainaka et al., 2014).

Permeabilization and decolorization of mouse organs containing remaining blood

Mouse organs were dissected and post-fixed with 4% PFA/PBS from deeply anesthetized animals intended to be euthanized. The blood-rich organs were washed with PBS for 3 h x 3 times and put into a multi-well plate and camera pictures images were taken. Then the organs were incubated with the following mixtures: 10% w/v CHAPS and 25% w/v N-Methyldiethanolamine, 10% w/v Triton X-100 and 25% w/v N-Methyldiethanolamine, 200 mM SDS and 25% w/v N-Methyldiethanolamine at 37°C on a shaking rocker (IKA, 2D digital). The solutions were refreshed when the color changed to green until colorless. Then the grouped samples were washed with PBS 3 times for 3 h at room temperature and imaged again with a camera.

Protein loss assay

PFA-fixed adult mouse (3-4 months) brains were cut into 1-mm-thick sections using a vibratome (Leica, VT1200S) (Chung et al., 2013; Murray et al., 2015). All sections were weighted and randomly grouped, then placed in 5 mL solutions as follow: distilled water, 2.5% w/v CHAPS, 5% w/v CHAPS, 10% w/v CHAPS, 200 mM SDS or 10% w/v Triton X-100. The samples were incubated for 2 weeks at 37°C on a shaking rocker. The respective solutions and quantity of protein loss from the tissue which diffused into the solutions were measured using Bio-Rad *DC* protein assay kit (Bio-Rad, 5000116). Total protein in the mouse brain was estimated at 10% (wt). For each group, the standard solution was prepared in the same buffer as the sample.

Pig brain clearing with passive SHANEL

PFA-fixed pig brain samples were washed with PBS at room temperature in a 500 mL glass beaker and incubated with 10% w/v CHAPS and 25% w/v N-Methyldiethanolamine solution at 37°C on a shaking rocker. The incubation time for a single whole brain was 10 days, with the solution refreshed once at day 5. After the PBS washing performed at room temperature, the samples were shaken with a series of Ethanol (Merck, 10098535000)/DiH_2O solutions (50%, 70%, 100%, 100% v/v) at room temperature, followed by a DCM (Roth, KK47.1) incubation and in the end they were immersed into the BABB (benzyl benzoate:benzyl alcohol = 2:1, Sigma, W213802, 24122) solution until complete transparency. The incubation time depended on the sample size: for whole brains, 4 days for each step were needed.

Active SHANEL clearing of pig pancreas

Pancreas from a 5.5-months old *INS*-EGFP transgenic pig was dissected without the tail part, a G 20 venous catheter was inserted into the pancreatic duct and sewed on. 4% PFA was injected to fix the tissue, followed by post-fixation for 3 days at 4°C. Then the sample was placed into the active pumping system consisting of a peristaltic pump (ISMATEC, REGLO Digital MS-4/8 ISM 834), chemical-resistant PTFE tubing (VWR, 228-0735) and a glass chamber (Omnilab, 5163279). After PBS washing, 200 mL solution of 5% w/v CHAPS and 12.5% w/v N-Methyldiethanolamine was circulated through the pancreas for 8 days in total, refreshing the solution with fresh one every 2 days. After 2 times of PBS washing for 3 hours, the sample was pretreated with 200 mL of permeabilization solution containing 1.5% goat serum (GIBCO, 16210072), 0.5% Triton X-100, 0.5 mM of methyl-β –cyclodextrin (Sigma, 332615), 0.2% trans-1-acetyl-4-hydroxy-l-proline (Sigma, 441562) and 0.05% sodium azide (Sigma, 71290) in PBS for half day at room temperature. Subsequently, the perfusion proceeded further, through connection of a 0.20 μm syringe filter (Sartorius, 16532) to the intake-ending of the tube to prevent accumulation of dye aggregates in the sample. At the same time, an infrared lamp (Beuer, IL21) was used to heat up the solution to 26–28°C. With this setting, the pancreas was perfused for 13 days with 250 mL of the same permeabilization solution containing 30 μL of Atto647N-conjugated anti-GFP nanobooster (Chromotek, gba647n-100, 60920001SAT2). After that, the pancreas was washed out by perfusing with a washing solution (1.5% goat serum, 0.5% Triton X-100, 0.05% of sodium azide in PBS) for 6 h 3 times at room temperature and PBS for 3 h at room temperature. The clearing was started with a series of 250 mL of Ethanol(EtOH)/DiH$_2$O solutions (50%, 70%, 100%, 100% v/v) pumping for 6 hours at each step. Then the pancreas was passively incubated with DCM for 1 day, proceeded by incubation into BABB solution until complete transparency in around 2 weeks.

Other clearing methods

Centimeters-sized pig pancreas, human brain and human kidney samples were cleared by 1) SHANEL without CHAPS/NMEDA pretreatment, 2) 3DISCO, 3) uDISCO, 4) vDISCO, 5) iDISCO+, 6) PACT (Passive CLARITY) and 7) MASH (RIMS = WGO/CA) protocols. 1) Samples were incubated in 50%, 70%, 100%, 100% v/v Ethanol/DiH$_2$O solutions at room temperature for 4h each step, followed by overnight DCM and then BABB incubation. 2) Samples were incubated in 50%, 70%, 80%, 100%, 100% v/v THF(Roth, CP82.1)/DiH$_2$O solutions at room temperature for 4h each step, followed by overnight DCM and then dibenzyl ether (DBE, Sigma, 33630) incubation. 3) Samples were incubated in 30%, 50%, 70%, 80%, 90%, 96%, 100% v/v tert-butanol(Roth, AE16.3)/DiH$_2$O solutions at room temperature for 4h each step, following DCM overnight and in the end BABB. 4) Samples were incubated in permeabilization solution (1.5% goat serum, 0.5% Triton X-100, 0.5 mM methyl-β -cyclodextrin, 0.2% trans-1-acetyl-4-hydroxy-l-proline and 0.05% sodium azide in PBS) at 37°C for 1 day, then washed with washing solution (1.5% goat serum, 0.5% Triton X-100, 0.05% sodium azide in PBS) and PBS for 4 hours each. Next, the samples were treated with 50%, 70%, 80%, 100%, 100% v/v THF/DiH$_2$O solutions at room temperature for 4 hours each step, followed by overnight DCM and then BABB incubation. 5) We were following the latest protocol updates from https://idisco.info. Samples were incubated in 20%, 40%, 60%, 80%, 100%, 100% v/v methanol (Roth, 4627.6)/DiH$_2$O solutions at room temperature for 4h each step and, after chilling at 4°C, the samples were shaken in 66%DCM/33%methanol. Then, after two washing in 100% methanol, the samples were chilled at 4°C and bleached with 5% H_2O_2 in methanol overnight. Next, samples were rehydrated with methanol/DiH$_2$O 80%, 60%, 40%, 20%, PBS at room temperature for 4 hours each step. Then, the samples were permeabilized with 20% DMSO and 2.3% w/v glycine solution overnight at room temperature. Last, the samples were cleared with 20%, 40%, 60%, 80%, 100%, 100% v/v methanol/DiH$_2$O solution for 4 hours each step, 66% DCM/33% methanol overnight, DCM 4h and DBE. 6) The samples were incubated at 4°C for 2 days in the hydrogel monomer solution of 4% acrylamide in PBS supplemented with 0.25% photoinitiator 2,2′-Azobis[2-(2-imidazolin-2-yl)propane]dihydrochloride (a.k.a VA-044, Wako Chemicals, 011-19365). Samples were degassed and incubated at 37°C for 6 hours to initiate the tissue-hydrogel hybridization. After removing the excess of hydrogel on the surface, the matrices were delipidated with 8% SDS in PBS for 5 days with shaking. Last, the samples were transferred to the RIMS media (Forty grams of Sigma D2158 (Histodenz) in 30 mL of 0.02 M PBS with 0.1% tween-20 and 0.01% sodium azide, pH to 7.5 with NaOH—which results in a final concentration of 88% Histodenz w/v). 7) MASH protocol was modified iDISCO+ protocol with another RIMS solution (WGO/CA: 72% methyl salicylate also known as wintergreen oil (WGO, Sigma-Aldrich, 84332) and 28% trans-Cinnamaldehyde (CA, Sigma-Aldrich, C80687).

0.5 cm thick *INS*-EGFP transgenic pig pancreas slices were incubated with 10% w/v CHAPS and 25% w/v N-Methyldiethanolamine solution at 37°C overnight. Half of the samples were dehydrated with EtOH/DiH$_2$O solutions: 50%, 70%, 100%, 100% v/v for 2 hours at each step and delipidated with DCM, then immersed into BABB solution until transparency. The other half of the samples were incubated with the permeabilization solution (1.5% goat serum, 0.5% Triton X-100, 0.5 mM methyl-β -cyclodextrin, 0.2% trans-1-acetyl-4-hydroxy-l-proline and 0.05% sodium azide in PBS) at 37°C for 5 hours, then with 10 mL of the same permeabilization solution containing 20 μL of Atto647N-conjugated anti-GFP nanobooster (Chromotek, gba647n-100) for 4 days. After that, the pancreas samples were washed with the washing solution (1.5% goat serum, 0.5% Triton X-100, 0.05% of sodium azide in PBS) for 1 hour 3 times at room temperature and then with PBS for 1 hour at room temperature. The clearing was started with a series of incubation in EtOH/DiH$_2$O solutions (50%, 70%, 100%, 100% v/v) for 2 hours for each step. Then, the samples were passively incubated with DCM for 1 hour, and finally treated with the BABB solution until complete transparency. The fluorescent signal was imaged with epifluorescence microscopy at designed time point.

Active SHANEL clearing of intact human brain

The four main arteries of the PFA-fixed intact human brain were connected to the ISMATEC peristaltic pump through a chemical-resistant PTFE tubing in a glass chamber. 5 L of 10% w/v CHAPS and 25% w/v N-Methyldiethanolamine solution was pumped continuously into arteries keeping the pressure at 180-230 mmHg (50-60 rpm). One channel from the pump, made by a single reference tube, was set for circulation of the solution through the artery into the brain vasculature system: one ending of the tube was connected to the tip which inserted into the artery tubing, and the other ending was immersed in the solution chamber where the brain was placed. The perfusion tip pumped appropriate solution into the artery, and the other ending collected the solution inside of the glass chamber to recirculate the solution, pumping it back into the brain. At the same time, the solution was also stirred using a blender (IKA, RCT B S000) and heated to 37-39°C. With this setting, the human brain was perfused for one month with the solution refreshed once at day 15. Then the solution was changed to PBS for washing for 2 days. Using the same setting without heating, the human brain was labeled with TO-PRO-3 (Thermo Fisher, T3605) in 2 L PBS (1:2000 dilution) for 1 month at room temperature. After labeling the clearing was performed by perfusing with 5 L of the following series of EtOH/DiH$_2$O solutions: 50%, 70%, 100%, 100% v/v for one week for each step, followed by perfusion of 5 L of DCM for another week to delipidate, in the end the sample was perfused with 5 L of BABB solution until complete transparency. When the brain was getting transparent, the BABB was refreshed and the brain was stored in this solution at room temperature without further circulation or stirring.

After transparency of intact human brain, we dissected one of the eyes for 3D reconstruction using light-sheet microscopy. According to the specific signals from different channels, we identified following structures of the eye. Sclera, also known as the white of the eye, is the opaque, fibrous outer layer of the human eye containing mainly collagen and elastic fibers. Collagen and elastic fibers normally have strong autofluorescence at a wide spectra- more strongly at 488 nm and emission 540nm (Zhao et al., 2017). Iris is a thin, circular structure in the eye. Eye color is defined by the iris. The iris consists of two layers: pigmented fibrovascular layer and pigmented epithelial layer, which were visible at 640 nm and 780 nm. The 780 nm autofluorescence could come from the collagen and/or pigments as suggested (Carrim et al., 2006; Moschovakis and Highstein, 1994). Suspensory ligaments of the lens also refer to the zonule of zinn, which is mainly a collection of zonular fibers (De Maria et al., 2017; McCulloch, 1954). This eye was from a donor with blue eyes, therefore the amount of melanin present was already low. Overall, we don't have any evidence that SHANEL removes the melanin/neuromelanin pigments.

1.5 cm-thick human brain slices preparation

PFA-fixed intact human brain was actively pumped with 5 L 10% w/v CHAPS and 25% w/v N- Methyldiethanolamine solution for one month with solution refreshed once at day 15. Then the solution was changed to PBS for active washing for 2 days. The intact human brain was cooled in PBS at 4°C overnight, then directly cut into 1.5 cm-thick slices in coronal plane using a Rotation Cutting Slicer (Rotation Schneidemaschine, Biodur, Heidelberg, Germany). The total 12 slices were serially labeled and stored in 70% EtOH at 4°C.

Passive histology of a 1.5 cm-thick intact human brain slice

A 1.5 cm-thick intact human brain slice (Number 7, see Figure S3) was randomly chosen and passively incubated with 400 mL TO-PRO-3 (1:2000 dilution) in PBS at room temperature for 1 week. Then the solution was changed to 400 mL with 100 μM of Methoxy X-04 (Tocris, 4920) in 40% EtOH (pH = 10 adjusted by NaOH (Roth, 6771.1)) and the sample was incubated for another week. After labeling, the slice was washed with PBS for 1 day. The clearing started with dehydration using a series of 1 L of EtOH/DiH$_2$O solutions (50%, 70%, 100%, 100% v/v) and followed by delipidation using 1 L DCM. Each step lasted 1 day. Then the samples were incubated in 1 L BABB solution at room temperature until completely transparency in around 2 weeks.

Passive SHANEL antibody histology of 1.5 cm-thick human brain samples

1.5 cm-thick human brain slices (Number 4 and 6, see Figure S3) were randomly chosen and dehydrated with a series of 1 L EtOH/DiH$_2$O (50%, 70%, 100%, 100% v/v), then delipidated with 2 L DCM/MeOH (2:1 v/v), then rehydrated with a series of 1 L EtOH/DiH$_2$O (100%, 70%, 50%, 0% v/v) at room temperature. After incubating with 1 L 0.5 M acetic acid (Roth, T179.1) in DiH$_2$O, this solution was changed to a mixture of 4 M guanidine hydrochloride (Roth, 6069.3), 0.05 M sodium acetate (Sigma, S2889) and 2% Triton X-100 in PBS, pH = 6.0, at room temperature to loosen the extra cellular matrix. The incubation time for each of all above mentioned solutions was 1 day. Next, the slices were shortly incubated with 10% w/v CHAPS and 25% w/v N-Methyldiethanolamine solution for 4 hours and washed with PBS for 1 day. The intact slices were stored in the blocking buffer (0.2% Triton X-100/10% DMSO (Roth, A994.2)/10% goat serum/PBS) at 4°C. Regions of interest (including hippocampus, primary motor cortex, primary sensory cortex, and primary visual cortex, 2-4 cm x 2-4 cm x 1.5 cm) were cut and incubated with the same blocking buffer at 37°C for 1 day. Then the samples were incubated with rabbit antibody anti-Iba1 (1:1000, Wako, 019-19741) or rabbit antibody anti-TH (1:250, abcam, ab112) in the antibody incubation buffer (3% goat serum/3% DMSO/0.2% Tween-20/10mg$\cdot$L^{-1}Heparin/PBS) for 1 week at 37°C. After the primary antibody incubation, samples were washed with the washing buffer (0.2%Tween-20/10mg$\cdot$L^{-1}Heparin/PBS) for 1 day refreshing 3 times and then incubated with Alexa 647-conjugated secondary antibodies (1:500, Thermo Fisher, A-21245) in the antibody incubation buffer for 1 week at 37°C. Other samples were incubated with DyLight 649-lectin (1:500, Vector, DL-1178) in the antibody incubation buffer for 1 week at 37°C. After washing with PBS, propidium iodide (1:100, Thermo Fisher, P3566) or TO-PRO-3 dye was added in PBS for 3 days at 37°C for cell nuclei staining. After labeling, the samples were dehydrated with a series of solutions of EtOH/DiH$_2$O (50%, 70%, 100%, 100% v/v) and delipidated with the DCM solution for 4 hours each solution followed by BABB incubation at room temperature until the sample transparency was reached in 2-3 days.

To test other SHANEL-compatible antibodies, we cut 1 mm thick brain slices pretreated with SHANEL histology using the vibratome, and we stained them with the following primary antibodies: mouse antibody anti-MBP (myelin basic protein) (1:250, atlas antibodies, AMAb91064), rabbit antibody anti-Laminin (1:100, Sigma, L9393), rabbit antibody anti-Neuropeptide Y (1:300, abcam, ab30914), then the incubation was performed with the respective secondary antibodies (1:500, Thermo Fisher, A-21245) for overnight. After washing with PBS, propidium iodide (1:100) was added in PBS for cell nuclei staining for 1 hour. The samples were dehydrated with a series of solutions of EtOH/DiH$_2$O (50%, 70%, 100%, 100% v/v) and delipidated with DCM solution for 1 hour each solution. BABB solution replaced the DCM solution and the samples were incubated in BABB at room temperature until complete transparency.

To evaluate the macroscopic and microscopic deformation after SHANEL clearing, we used 1 mm thick human brain slices. The gross shape of the samples was imaged by the Zeiss AxioZoom EMS3/SyCoP3 epifluorescence stereomicroscope before and after SHANEL clearing. For the evaluation of the deformation at the microscopic level, samples were labeled to highlight cellular structures: in particular microglia and astrocytes in the samples were stained using the primary rabbit antibody anti-Iba1 (1:1000, Wako, 019-19741), and the primary rabbit antibody anti-GFAP (1:1000, Dako, Z033401-2) respectively, followed by the secondary antibody Alexa 647 goat anti-rabbit (1:500, Life Technology, A31852) using the SHANEL histology protocol (see previous sections). Subsequently, same regions before and after clearing of the labeled slices were imaged with the Zeiss confocal microscope LSM 880 coupled with a 25x water-immersion long working distance objective (Leica, 0.95 NA, WD = 2.5 mm) mounted on a custom mounting thread. The mounting of the slices for the imaging session was done by putting the individual samples on the glass surface of 35 mm glass-bottom Petri dishes (MatTek, P35G-0-14-C) for both epifluorescence and confocal microscopy. Closing or sealing of the Petri dish was not needed. These confocal scans were later used for the calculation of the root mean square error (see next section).

A second experiment to demonstrate the preservation of cellular and tissue morphology after SHANEL was performed as follows: SHANEL histology cleared human brain and kidney pieces were rehydrated with DCM, EtOH/diH$_2$O (100%, 70%, 50%) and PBS. These rehydrated samples together with PFA-fixed samples were cut into 20 μm thin slices using a cryostat (Cryostar NX70, Thermo Fisher) for standard hematoxylin and eosin (H&E), Nissl, Periodic Acid Schiff (PAS) staining to qualitatively assess the cellular and extracellular matrix structures with and without SHANEL histology clearing. Hematoxylin-eosin staining was carried out as follows: cryosections were passed through 2 diH2O steps before incubating in Gill's hematoxylin solution (Sigma-Aldrich, GHS3) for 90 s followed by washing under running tap water. Subsequently, cryosections were passed through a battery of increasing concentration of ethanol (50%, 70%, 80% v/v, 2 min each) and then incubated in eosin solution 1% (Roth, 7089.1) for 3 min, followed by 3 quick washes in 96% ethanol and dehydration for 2 times 5 min each in absolute ethanol and Roti-Histol 100% (Roth, 6640.2). Cryosections were then mounted in hydrophobic mounting medium (Sigma-Aldrich, Eukitt 03989) and let dry until imaging. For Nissl staining, cryosections were incubated for 2 min in 70% ethanol prior to incubation in cresyl violet solution 0.5% (Sigma-Aldrich, C5042) for 15 minutes. Following that, slides were quickly washed in distillated water twice and then passed quickly through increasing concentrations of ethanol (70%, 96%, 100% v/v), followed by incubation for 2 min in 100% isopropanol and final dehydration in 100% Roti-Histol twice for 5 minutes. Slides were mounted as described previously. Periodic acid shift staining was performed using PAS staining system (Sigma-Aldrich, 395B) according to manufacturer's instructions. In brief, hydrated cryosections were incubated for 5 minutes in periodic acid solution and then rinsed several times in diH$_2$O, followed by incubation in Schiff's reagent for 15 min. After washing under running tap water, slides were counterstained in Gill's Hematoxylin for 90 s and subsequently dehydrated and mounted as stated earlier. Image acquisition was performed with an AXIO Imager.M2 microscope (Zeiss) couple with AXIOCam MRc camera (Zeiss) and a EC Pan-NEOFLUAR 40x/0,75(NA) M27 WD:0.71 mm dry objective (Zeiss, 420360-9900).

Copper sulfate treatment in SHANEL to eliminate tissue autofluorescence

1 mm thick human brain slices were cut using the vibratome after SHANEL histology pretreatment. Slices were cleared and imaged with light-sheet microscopy in different wavelengths for autofluorescence. Then, the slices were rehydrated with a series of solutions: 5 mL EtOH/DiH$_2$O (100%, 70%, 50%, 0% v/v) into water, 1 hour each step, and incubated with 10 mM copper sulfate ($CuSO_4$, Roth, CP86.1) and 50 mM ammonium chloride (Roth, P726.1) pH = 5.0 solution for 1 hour at room temperature. After washing with PBS, the slices were cleared again and imaged with light-sheet microscopy at the same wavelengths used before to check the grade of autofluorescence elimination after the copper sulfate treatment. The images were then analyzed by ImageJ for profile plots and signal intensity. We also processed slices labeled with DyLight 649-lectin and propidium iodide with the same autofluorescence-elimination procedure to check that copper sulfate treatment did not affect the fluorescence signal from the staining while eliminating the autofluorescence from the tissue.

Passive SHANEL histology of intact human thyroid

A thyroid from an 80 years-old female donor was dissected and post-fixed with PFA for 3 days. After PBS wash for 4 hours at room temperature, the thyroid was incubated at 37°C in 200 mL of a 10% w/v CHAPS and 25% w/v N-Methyldiethanolamine solution for 5 days refreshing once at day 3. Then the dehydration of the sample was done with a series of solutions: 200 mL EtOH/DiH$_2$O (50%, 70%, 100%, 100% v/v), half day each solution, followed by delipidation with 200 mL DCM/MeOH (2:1 v/v) for 2 days in a sealed glass container, and rehydrating with a series of solutions: 200 mL EtOH/DiH$_2$O (100%, 70%, 50%, 0% v/v) half day each solution.

The ECM was loosened with 0.5 M acetic acid in PBS for 1 day and a mixture of 4 M guanidine hydrochloride, 0.05 M sodium acetate and 2% Triton X-100 in PBS, pH = 6.0, for 1 day. After PBS wash, 100 mL of TO-PRO-3 dye (1:1000) was used to label the sample for 10 days. The clearing was started incubating the sample in a series solutions consisting of 200 mL of EtOH/DiH$_2$O solutions (50%, 70%, 100%, 100% v/v), shaking for half day each step, followed by 200 mL of DCM for 5 hours, then proceeded with 200 mL BABB solution until complete transparency reached in 3-5 days.

Active SHANEL histology study of intact human kidney

The PFA-fixed intact kidneys were pumped through primary artery with 36 mL of the mixture of 25 mg/ml tetramethylrhodamine isothiocyabate-dextran, 2 mM *p*-maleimidophenyl isocyanate (PMPI) and 5 mM DL-dithiothreitol (DTT) in PBS (Annunziato et al., 1993; Shen et al., 2004). Then the kidneys were sealed inside a plastic bag and incubated in 37°C overnight. After dextran labeling, we set up the perfusion system with an ismatec peristaltic pump and PTFE tubing at room temperature as the human brain. The first step consisted of the washing with 2 L PBS for one day twice. The second step was the decolorization and permeabilization steps performed with 2 L of the 10% w/v CHAPS and 25% w/v N-Methyldiethanolamine solution for one week. The third step was the dehydration step with a series of solutions: 2 L of EtOH/DiH$_2$O (50%, 70%, 100% v/v), 4 days with each solution. The fourth step was the delipidation step with 4 L DCM/MeOH (2:1 v/v) for 4 days, by sealing the glass container. The fifth step was the rehydration with a series of solutions: 2 L EtOH/DiH$_2$O (100%, 70%, 50%, 0% v/v), 4 days with each solution. The sixth step consisted of the loosening of the ECM with 0.5 M acetic acid for 4 days and mixture of 4 M guanidine hydrochloride, 0.05 M sodium acetate and 2% Triton X-100 in PBS pH = 6.0, for 4 days. The seventh step was again PBS washing for one day twice. Next, 1 L of TO-PRO-3 dye (1:2000) in PBS was continuously pumped for 2 weeks, then washed with PBS for one day twice. The clearing was started with a series solutions consisting of 2 L of EtOH/DiH$_2$O solutions (50%, 70%, 100%, 100% v/v) pumping for 2 days for each solution, followed by 2 L of DCM for 3 days, then proceeded with 2 L BABB solution until complete transparency.

To examine the whole kidney pathology, we used tissue recycling reported in details in Puelles et al. (2019). Briefly, the concept is based on reversing the main clearing steps. Thus, after SHANEL, BABB-immersed tissues were gently placed in sequential washes of 100% ethanol, 30 minutes each, 3-5 times (depending on tissue size). Next, sequential washes in PBS were performed, 30 minutes each, 5 times to get rid of residual BABB. Then, conventional paraffin embedding and slicing (5 μm thick) was carried out, thereby allowing subsequent PAS staining as previously described.

To quantify the vessel structures in normal and reduced areas, 8 mm projection (200-1200 slices) of 780nm autofluorescence signal of whole kidney was evaluated by counting the vessel branches and length in same size areas using ImageJ.

Safety recommendations of handling chemicals

According to the open chemistry database from National Institute of Health (NIH) through PubMed, we summarized the safety recommendations of handling SHANEL chemicals. CHAPS is not a hazard substance. It will cause skin and eye irritation and may cause respiratory irritation. NMDEA will cause eye irritation. EtOH is highly flammable liquid. DCM will cause skin, eye and nose irritation, and in case of inhalation, it could cause anesthetic effects, nausea and drunkenness. Benzyl benzoate is harmful if swallowed, and cause skin and eye irritation. Benzyl alcohol is harmful is swallowed and inhaled. However, it meets Safer Choice Criteria for its functional ingredient-class. According to the American Food and Drug Administration (FDA), both benzyl alcohol and benzyl benzoate can be used in minimum quantity as food additive or cosmetic ingredient for human use and consumption. Storing SHANEL chemicals must follow dispositions for hazardous, inflammable, explosive and toxic substances. In particular, handling must be performed in fume hoods, while wearing safety goggles, nitrile gloves (preferably double layer) and lab coats.

SWIR imaging

The cleared human brain was placed in a rectangular glass jar filled with BABB. The jar was positioned between a 1450nm LED light source (Thorlabs, M1450L3) and a cooled InGaAs camera (Allied Vision, G-032 cool TEC2) equipped with a 35mm objective lens (Navitar, SWIR-35). Homogeneous illumination of the sample was established with the help of an engineered diffuser (Thorlabs, ED1-S50) after the collimated LED and plastic diffuser foils at the illuminated side of the glass jar. Two aligned laser printed transparencies with the "SHANEL" lettering were placed between the diffuser foils and the glass wall. Images were taken at 40ms exposure time in high gain mode (gain 1).

An overhead projector (A+K lux) with a 250W halogen light bulb was used for transmissive illumination of the cleared and uncleared 1.5 cm thick human brain slices. Samples were imaged in glass dishes containing BABB and DCM for the cleared and uncleared samples, respectively. SWIR images where taken with a cooled InGaAs camera (Allied Vision, G-032 cool TEC2) together with a 35mm objective lens (Navitar, SWIR-35) equipped with a 1450/50nm bandpass (Edmund optics 85-901) mounted in front of the objective, 54μs exposure time, gain 0. Visible light images where taken with a silicon industry camera (IDS UI3370CP-NIR) together with a 35mm objective lens (Spacecom VHF 35-MP SWIR), 800μs exposure time.

Proton density MRI imaging

Quantitative MRI experiments were conducted to determine the chemical constitution of uncleared and cleared brain samples as assessed by proton density imaging. Uncleared samples in PBS or cleared samples in BABB were separately encapsulated in Eppendorf tubes (mouse brains) or sealed plastic bags (human brains), which in turn were put in a lager container with 1.5% agarose gel as reference. For all samples, we used a T2-weighted multi-echo spin echo sequence for relaxometry. For animal samples, images were acquired on a Mediso NanoScan 3T (Mediso Medical Imaging Systems, Budapest, Hungary) with repetition time 3850 ms, delta-echo-time 15 ms, 12 echos, field-of-view 16 mm x 16 mm, matrix 96 × 96 and slice thickness 1 mm. For human samples, images were acquired on a Siemens Magnetom Prisma (Siemens Healthineers, Erlangen, Germany) with repetition time 1000 ms, delta-echo-time 15 ms, 15 echos, field-of-view 256 mm x 256 mm, matrix 320 × 320 and slice thickness 1 mm. In order to determine proton density signal (S0), a logarithmic curve was fit to the signal decay measured along the multiple echoes, using MATLAB. S0 was then extrapolated as the fitted T2 signal amplitude at TE = 0 ms. The resulting S0 was normalized to S0 in the 1.5% agarose gel for comparison across the samples.

Light-sheet microscopy imaging

Single plane illuminated (light-sheet) image stacks were acquired using the light-sheet microscopes: Ultramicroscope II featuring the following filter sets: ex 470/40 nm, em 535/50 nm; ex 545/25 nm, em 605/70 nm; ex 580/25 nm, em 625/30 nm; ex 640/40 nm, em 690/50 nm; ex 780 nm, em 845/55 nm; and a prototype Ultramicroscope featuring the following filter sets: ex 470 nm, em 525/50 nm; ex 561 nm, em 595/40 nm; ex 640 nm, em 680/30 nm; ex 785 nm, em 845/55 nm (LaVision BioTec). Samples (detailed information in Table S3) were imaged with a 1x Olympus air objective (Olympus MV PLAPO 1x/0.25 NA [WD = 65mm]) coupled to an Olympus MVX10 zoom body, which provided zoom-out and -in ranging from 0.63x up to 6.3x. Alternatively, the samples were scanned with a dipping 1.1x objective (LaVision BioTec MI PLAN 1.1x/0.1 NA [WD = 17 mm]) coupled with an Olympus revolving zoom body unit (U-TVCAC) on the prototype Ultramicroscope. After low magnification imaging of whole organs, samples were imaged using high magnification objectives (Olympus XLFLUOR 4x corrected/0.28 NA [WD = 10 mm], LaVision BioTec MI PLAN 12x/0.53 NA [WD = 10 mm]) coupled to an Olympus revolving zoom body unit (U-TVCAC) kept at 1x. Tile scans with 20% or 30% overlap along the longitudinal x axis and y axis were obtained using a z-step of 3 μm, 5 μm or 8 μm. Exposure time was 90-120 ms, laser power was adjusted depending on the intensity of the fluorescent signal (in order to avoid saturation of the signal) and the light-sheet width was kept at 80% of maximum. The LaVision light-sheet microscope has ~4 μm lateral and ~6.5 μm axial resolutions (1x objective).

Laser-scanning confocal microscopy imaging

We used different kinds of confocal microscopes: the Zeiss LSM 880 confocal microscope was used for method characterization experiments and the imaging of regions of interest from the samples (1 mm thick, 5-10 mm long) already imaged with light-sheet microscopy. In particular, areas of interest from the human brain and the human kidney, were dissected and imaged with this inverted laser-scanning Zeiss confocal microscope using Zen 2 software (v.10.0.4.910; Carl Zeiss AG). Before imaging, samples were mounted by placing them onto the glass surface of 35 mm MatTek glass-bottom Petri dishes while adding a few drops of BABB to make sure that the imaging region was immersed in BABB (Cai et al., 2019). The imaging was done using a 40x oil-immersion objective (Zeiss, ECPlan-NeoFluar × 40/1.30 oil DIC M27, 1.3 NA [WD = 0.21 mm]) and a 25x objective (Leica, 0.95 NA [WD = 2.5 mm]) mounted on a custom thread.

The second confocal microscope is the upright confocal microscope RSG4 from MAVIG. This microscope was used to image a 7.5 × 5 x 1.5 cm brain section, which was cut from the human slice number 7 previously labeled and cleared. The imaging was performed using Caliber I.D. RS-G4 research software. The working dimensions of the stage of this latter microscope were 46 × 40 × 66 cm. The images were acquired with the UPLFLN 10x objective (OLYMPUS 0.3 NA [WD = 10mm]). Tile scans were obtained along the longitudinal y axis. Laser power was adjusted depending on the intensity of the fluorescent signal (in order to avoid saturation of the signal).

Epifluorescence stereomicroscopy imaging

Epifluorescence stereomicroscope was performed to image a cleared 1.5 cm thick whole human brain slice and 1 mm think small sections of human brain slices. The whole brain slice was put in a glass chamber while the small sections in the MatTek glass bottom dishes. The microscope was a Zeiss AxioZoom EMS3/SyCoP3 fluorescence stereomicroscopy coupled with a 1x long working distance air objective (Plan Z 1x, 0.25 NA, WD = 56 mm). The magnification was set as 32x and for the whole brain slice the imaging areas were selected manually to cover half of the slice. The images were taken with 405 nm filters and files were exported as tiff images.

QUANTIFICATION AND STATISTICAL ANALYSIS

Image processing

Processing, data analysis, 3D rendering and video generation for the imaging data were done on an HP workstation Z840, with 8 core Xeon processor, 196 GB RAM, and Nvidia Quadro k5000 graphics card and HP workstation Z840 dual Xeon 256 GB DDR4 RAM, nVidia Quadro M5000 8GB graphic card. We used Imaris (v.9.1, Bitplane), Arivis, Photoshop (Adobe, CC2018) and Fiji for 3D and 2D image visualization. 16-bit grayscale TIFF images for each channel were separately acquired by the light-sheet microscope software ImSpector (v.5.295, LaVision BioTec). Tile scans were stitched by Fiji's stitching plugin49. Stitched images (Figures 2G–2I, 3D, 3E, 4C–4N, 5D, 5E, 6F–6J, 7D, 7E, S4B–S4H, S5B–S5F, and S7B–S7D) were saved in TIFF format and optionally compressed in LZW format to enable fast processing. To merge the neighboring stacks, alignment was done by manually selecting 3 anatomic landmarks from the overlapping regions. The stitching was performed sequentially with the Scope Fusion module of the Vision4D (v.2.12.6 × 64, Arivis) software. Landmarks were mainly chosen from the cellular structures or vessel structures on the basis of visual inspection of the anatomical features. Please note that the apparent borders (dimmer lines) typically appear at the stitching lines of the mesoscale light-sheet imaging due to overlapping scan of the same region, which can reduce the signal intensity of borders (e.g., Figures S4K–S4N). In addition, some blocks might appear brighter or darker in mesoscale imaging due to 1) long distance travel of light-sheets from left and right, which cannot be equal all the time at different points, 2) a blockage of one of the light-sheets (e.g., Figure 7E) and 3) lack of imaging data at certain positions (e.g., Figure S4E). However, such artifacts does not impede 3D-visualzation. After finishing the 3D reconstructions, the data visualization was done with Imaris in both volumetric and maximum-intensity projection color mapping. Epifluorescence stereomicroscopy images were saved as series TIFF images. The images were stitched manually in Photoshop by overlapping regions from landmarks.

Tissue deformation analysis using RMSE calculation

The grade of the deformation of the tissue caused by SHANEL was assessed visually on the microscopy images and by using the calculation of the Root Mean Square Error (RMSE) that evaluated the morphological deformation of the tissue structures at single-cell level. We applied the same calculation method on 2 different cell types: microglia expressing Iba1 and astrocytes expressing GFAP. To do so, first we imaged the same cells with the Zeiss LSM 880 confocal microscope (see confocal microscopy imaging section) in the samples before and after SHANEL clearing (n = 3 tissue slices per each cell type), then we selected the images (maximum intensity projections) of at least 4 individual cells per each experimental replicate before and after SHANEL clearing, to compare the after-clearing cellular morphology to the corresponding one before the clearing. All the selected images were preprocessed in Fiji using background subtraction (radius 30) and median filtering (radius 2) functions in order to remove artifacts and ease the registration process. Then in the same software, images were scaled up by a factor of 2. Since the clearing process shrinks the samples, we performed a similarity registration to approximately scale the cells from after-clearing samples to match the size of the same cells before-clearing. In this way the RMSE will be calculated on scale-matched images and since the shrinkage effect will not be then considered after the scale matching, the result will be an indication of the grade of the isotropicity of the shrinkage and of the deformation that SHANEL might cause. The similarity transformation was performed using linear stack alignment with SIFT plugin.

Next, we calculated the deformation of the structures of each cell after-clearing over the structures of the same cell before-clearing. To do so, we used a non-rigid Bspline registration, from the Fiji plugin ‘‘bUnwarpJ’’ to align the two cell images with the following parameters: registration mode → accurate, initial deformation → coarse and saving the transformation. To achieve better results, a couple of cellular structures were manually selected as landmarks. We could then visualize this registration as a deformation space or a deformation field, the latter indicated how much each pixel was transformed (how big the error) to match the destination image. The single spot where the deformation field showed minimal value was chosen as center of the cell for the subsequent analysis, therefore its coordinates were taken. To calculate the deformation, we converted the Bspline transformation to raw transformation using ‘‘bUnwarpJ’’: in this step the RMSE was calculated for each pixel. However, in order to calculate this change in morphology (considering RMSE) only for the pixels representing the cells, in Fiji we created a binary image that separated cells from the background by using the ‘‘convert to mask’’ function. Afterward the skeleton image of the cell representing the gross morphology of the cell was created in python using the skeletonize function from the skimage library. We masked the deformation image with the skeleton image giving as output the deformation image of the skeleton. In the end, we calculated the grade of deformation in term of RMSE considering sequential distances away from the previously selected cell center: the radial profile for the deformation was calculated step by step at defined increasing distances from the cell center. We binned the pixels based on their distances from the cell center and calculated the average and the standard deviation of the RMSE of the all pixels falling inside each distance range. These results were then aggregated for the total analysis taking into account all cells considered per each replicate, then the averaged result of the 3 replicates and their standard deviations were displayed together as radial profiles shown in the Figure S6. The analysis procedure from the skeletonization step could be automatized using a scripting language such as Python or MATLAB.

3D volume and iso-surface rendering and quantification of pig pancreas islets

Insulin positive β-cell volumes were quantified by 3D iso-surfacing using the Imaris software. In the software islet volumes were segmented using the ‘absolute threshold’ thresholding option and the intensity threshold was set manually for most of the pancreas with the filter of ‘number of voxels Img = 1’. Statistical data parameters (Overall, Area, Center of Homogeneous Mass, Ellipsoid Axis A, Ellipsoid AxisB, Ellipsoid Axis C, Ellipsoid Axis Length A, Ellipsoid Axis Length B, Ellipsoid Axis Length C, Ellipticity (oblate), Ellipticity (prolate), Number of Voxels, Position, Sphericity and Volume) were exported from Imaris into an Office Excel (14.0.6023.1000, Microsoft, 2010)) spread sheet (*.xls). Statistical analysis of the islet volumes was performed using GraphPad Prism8.

Cell detection and image analysis

General data processing

Data processing after image stitching was performed using Python as well as various libraries such as SciPy (Virtanen et al., 2020), Numpy (Van Der Walt et al., 2011), Pandas (McKinney, 2010) and Nibabel (Brett et al., 2016). Deep learning algorithms were implemented in PyTorch (Paszke et al., 2019). To enable memory efficient and parallel patch-wise processing, the obtained 3D scans were subdivided into neighboring patches of $(100\ \text{px})^3$ (around 4MB file size uncompressed). Patches overlapped 5% in all directions (corresponding to 15% volumetric overlap) to ensure no cell would be divided at a patch boundary. Subsequent re-concatenation rules out double counting of any cells.

Selection of data

In total four different sections of the human brain have been selected for our deep learning pipeline. One section was chosen from the human hippocampus and three sections from the cortex region, namely the areas of the cortex connected to visual, motor and sensory tasks. These scans were acquired with a 12x objective using light-sheet microscope. The x-y-resolution of this scan is 0.54 μm × 0.54 μm and the z-step is 5μm. In total, 278656 patches from the human brain scan were processed.

Data annotation

In order to have a meaningful sample of our complete dataset, representative patches from 12 locations were selected for data annotation. We chose 6 locations from the hippocampus section and 2 locations from each of the three cortex sections. In each location, 8 neighboring patches were sampled for a total of 96 patches. The ground truth annotation was performed by four human experts in this field. These annotations were used for training our deep learning models as well as evaluating and comparing the performance of each method (see below for details). Every cell in a patch has been annotated by marking the core region of the cell in *ITKSnap* (Yushkevich et al., 2016). Afterward, an independent expert reviewed each patch individually to make sure that the annotation was consistent. This revision resulted in the manual refinement of 24 patches until the result was deemed correct.

Non-deep learning approaches to cell counting

Approach 1: FIJI

Fiji is an image processing package for scientific image analysis on the basis of Image-J (Schindelin et al., 2012). To segment and count single cells the function "3D Objects Counter" (Bolte and Cordelières, 2006) was used. This method requires manually setting a threshold for segmentation of a given patch. Automated segmentation for a very large number of patches thus requires of determining one single threshold that will then be used for all patches. For this, we optimized the threshold for all 96 patches individually. The final segmentation mask and cell counting were computed using the average threshold as the threshold value. As the optimal threshold for the entire dataset may differ from the optimal threshold we determined for the 96 patches we annotated for performance assessment, the reported cell counting performance for Fiji may be seen as an upper bound.

Approach 2: Imaris

Imaris is a microscopy image analysis software from Bitplane (2019). All patches have been converted to the Imaris file format. The function "Surfaces" with the following parameters was applied to all patches: "Shortest distance," "Background Subtraction (local contrast)," "Split touching objects" enabled. This function segments the cells of a patch into vector-based surfaces, which are then converted into a pixel-based image of connected components. In contrast to Fiji, this method requires to set two, not one parameter. Again, they were optimized for all 96 patches individually. The final processing was then performed using the average values for each parameter. Just like for Fiji, the reported cell counting performance may be seen as an upper bound. While Imaris also provides an automatic method to determine these parameters, this fully automatic mode failed to yield meaningful results.

Deep learning model 1: Our CNN

Architecture

We designed a 5-layer deep neural network as depicted in Figure 7A. This neural network consists of four convolutional layers with the respective 3D kernel sizes of 3x3x3, 5x5x5, 5x5x5, 3x3x3 and a fully connected layer. Every convolution is followed by a rectifying linear unit (ReLU) and increases the feature channel size from one to a maximum of 50 feature channels. The final fully connected layer reduces the 50 feature channels to one channel. A sigmoid activation function is applied to yield a probability distribution for the presence of a cell in a given voxel. Subsequent threshold at a probability of 50% finally turns the output into a binary mask. This network architecture is similar to the published "Deep Vessel Net" (Tetteh et al., 2018; Todorov et al., 2019)

Hyperparameters

The network is trained for 200 epochs (no data augmentation). The initial learning rate for the training is set to 0.0001. A learning rate scheduler based on the validation performance is used with the patience of 15 epochs and the reduction factor of 0.5. Batch size for training is set to 32. We used the Adam (Kingma and Ba, 2014) optimizer with $\beta_1 = 0.9$, $\beta_2 = 0.999$, $\varepsilon = 1\text{e-}8$.

Training procedure

Each model was trained on 80 of the 96 patches available (the remaining 16 were set aside for testing). Those 80 patches are then further split down into 16 patches for validation of the model and adjusting the learning rate scheduler and 64 patches for training the network. Afterward, the model with the lowest loss of the validation set is chosen for the final prediction on the corresponding test set. The loss function used to calculate the gradients is the Dice loss defined by

$$L_{Dice} = 1 - \frac{\varepsilon + \sum_{n=1} \widehat{y}_n y_n}{\varepsilon + \sum_{n=1} \widehat{y}_n + \sum_{n=1} y_n}$$

with $\widehat{y}$ being the prediction, y the ground truth and $\varepsilon = 1$ to ensure numerical stability.

Postprocessing

In order to distinguish between single cells of the resulting binary mask, a connected component analysis is performed. All connected components smaller than 50% of the median cell size of the dataset (here: ca. 76 voxels) are automatically removed from the prediction. Such cases may occur, for instance, for partially visible cells at the boundary of the patch, and can be safely removed due to the overlap of patches (see General data processing). All remaining connected components which are smaller than two standard deviations of the median cell size are counted as one cell, all bigger connected components are counted as the size of the component divided by the median cell size. This approach was verified by human labeling and analysis of connected components of the ground truth dataset.

Deep learning model 2: 3D UNet

To compare our approach with a more commonly used "standard" model for segmentation of biomedical images, we implemented a 3 layer version of 3D UNet (Çiçek et al., 2016; Ronneberger et al., 2015) with 3 down-sampling and pooling layers and 3 up-sampling layers. We trained it with the almost same hyper parameters and training schedule as for the first deep learning model. The only difference in the hyper parameter set for the initial learning rate is 0.001 and the reduction factor of the learning rate scheduler is set to 0.1.

Performance comparison of models

K-fold cross validation for deep learning models

Model training and evaluation are based on a k-fold cross-validation with k = 6. Our annotated dataset is thus split into two mutually exclusive datasets with 16 of the 96 patches for testing. The exhaustive rotation throughout the dataset leads to a real test performance for our deep learning models on all 96 patches. Importantly, this ensures that the model performance is evaluated based on its prediction on completely unseen data.

Cell counting performance (F1 Score)

To assess the quality of a model's predicted segmentation of individual cells in the scan, we use the F1 score. This is a commonly used metric to assess the quality for any detection task. It quantifies the performance in percent, taking into account the share of detected cells (recall) and the false positive rate (quantified as precision). Here, a detected cell or true positive (TP) is a cell for which the predicted binary mask overlaps with the ground truth. Similarly, a false positive (FP) is a predicted cell which does not exist in the ground truth. Cells in the ground truth which are missed by the model, as in there do not exist overlapping prediction cells, are counted as false negatives (FN). Precision is defined as the fraction of correct detected cells among all detected cells:

$$Precision = \frac{TP}{TP + FP}$$

Recall is defined as the amount of total detected cells of all existing cells:

$$Recall = \frac{TP}{TP + FN}$$

The F1 score is then calculated as following:

$$F1 = 2 * \frac{Precision * Recall}{Precision + Recall}$$

Processing speed

The comparison of processing speed measures the actual prediction speed of all models in a like-for-like setting. All tests were performed on the same hardware with 32 Intel Xeon E5-2620 v4 at 32x 3GHz processors, 252 GB of RAM and two Nvidia Titan V GPUs. To enables a fair and direct comparison, all data was already loaded into the RAM memory of the computer. The speed measurement comprises the segmentation of multiple patches and the connected component analysis for all 4 methods. Final speeds for each method were then averaged over the number of patches. Please note that the patch-wise processing ensures linear scaling of processing times.

DATA AND CODE AVAILABILITY

A fully functional online demo of our CNN segmentation and cell counting is available at Google Colab: https://colab.research.google.com/drive/1Lpfo6AoHGfpzHvHiD7pnH6DuW9VQxFgq. The complete source code for training the network as well as segmenting cells is available online at our github repository: https://github.com/erturklab/shanel-network.

Supplemental Figures

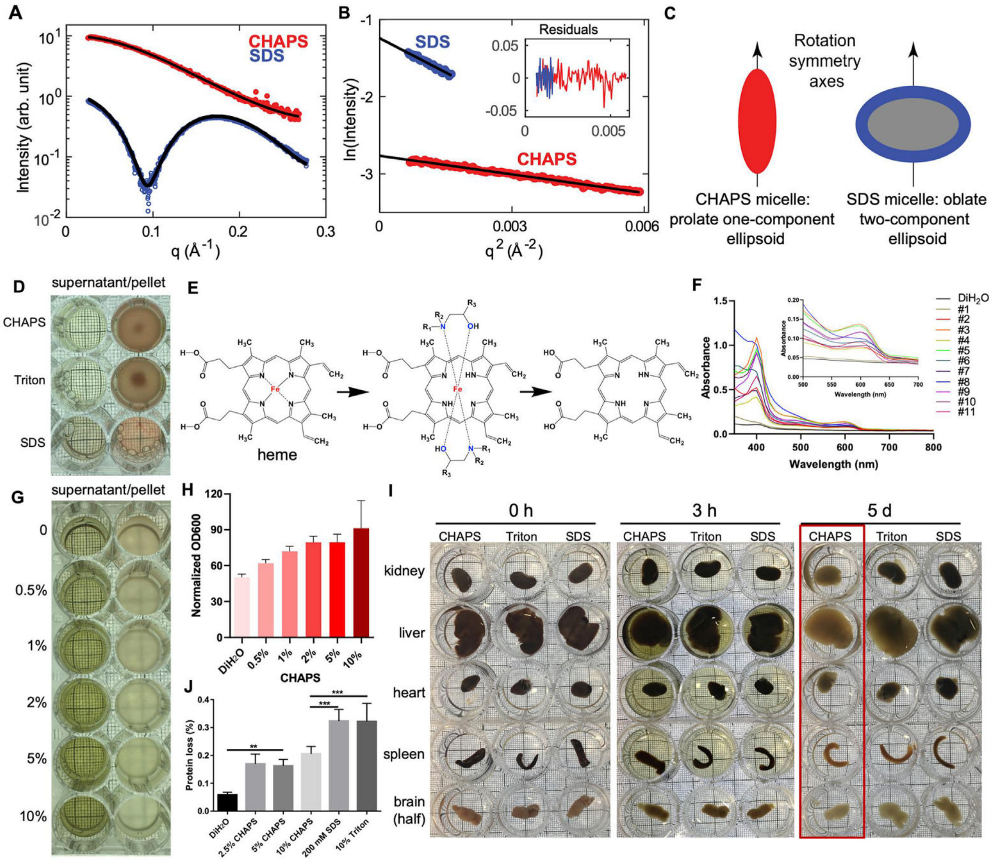

Figure S1. CHAPS Micelle Characterization for Blood Decolorization, Related to Figure 1

(A) Small-angle X-ray scattering profiles of CHAPS (red) and SDS (blue) micelles in PBS buffer. Fits of ellipsoid to the data are shown in black models (see Methods for details).

(B) Guinier analysis of the scattering profiles from panel (A). The black lines indicate linear fits to *ln*(*I*) versus q^2; the steeper slope for SDS corresponds to a larger radius of gyration R_g. The fitting ranges were chosen such that the largest *q*-values included in the fit, q_{max}, satisfy the condition $q_{max} \cdot R_g < 1.2$. The inset shows the residual of the fit, confirming good linearity of the data in the Guinier region.

(C) Schematics of the geometrical models fit the CHAPS and SDS scattering data, shown to relative scale.

(D) Detergents including CHAPS, Triton X-100 and SDS cannot decolorize PFA-fixed blood, showing colorless supernatant and red pellet solution.

(E) Schematic of hypothesized mechanism how chemicals interact with the iron of heme for an efficient decolorization.

(F) Absorbance at visible spectra of the supernatant from 11 screened chemicals. Inset in F: the magnification of the Q-band (500-700 nm) region showing the new peak of 600 nm can be used as quantitative index for the decolorization efficiency.

(G) Optimization of CHAPS concentration combined with 25% w/v N-Methyldiethanolamine (chemical 7) for blood decolorization.

(H) Normalized OD600 quantifications of different CHAPS concentration (n = 3) in G.

(I) After incubation with mixtures of 25% w/v N-Methyldiethanolamine and detergent of 10% w/v CHAPS or 10% w/v Triton X-100 or 200 mM SDS, CHAPS mixture shows superior permeabilization to remove the heme from blood-retaining mouse organs (red rectangle).

(J) Protein loss assay indicating the superior retention of endogenous proteins after CHAPS treatment compared to other detergents (*P values* were calculated using one-way ANOVA test; error bars show standard deviations).

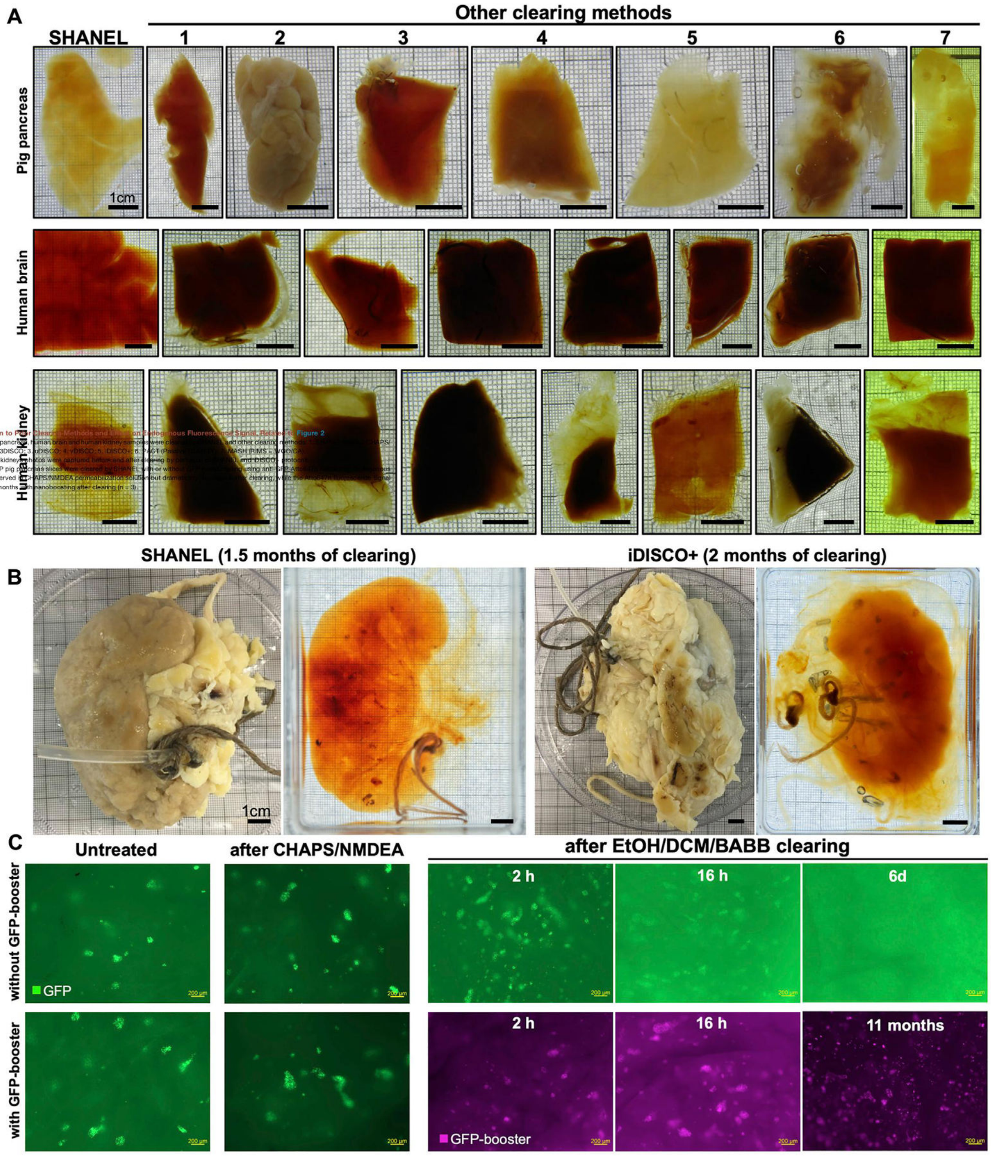

Figure S2. Comparison to Prior Clearing Methods and Effect on Endogenous Fluorescence Signal, Related to Figure 2

(A) Centimeters-sized pig pancreas, human brain and human kidney samples were cleared by SHANEL and other clearing methods: 1. [illegible] CHAPS/NMDEA pretreatment; 2. 3DISCO; 3. uDISCO; 4. vDISCO; 5. iDISCO+; 6. PACT (Passive CLARITY); 7. MASH (RIMS = WGO/CA).

(B) A pair of adult human kidneys photos were captured before and after clearing by performing SHANEL and iDISCO+ protocols.

(C) 0.5 cm thick *INS*-EGFP pig pancreas slices were cleared by SHANEL with or without [illegible] using anti-GFP-Atto647N [illegible] Endogenous GFP signal was well preserved in CHAPS/NMDEA permeabilization solution but dramatically [illegible] after clearing, while the Atto647N fluorescence signal was preserved up to 11 months with nanoboosting after clearing (n = 3).

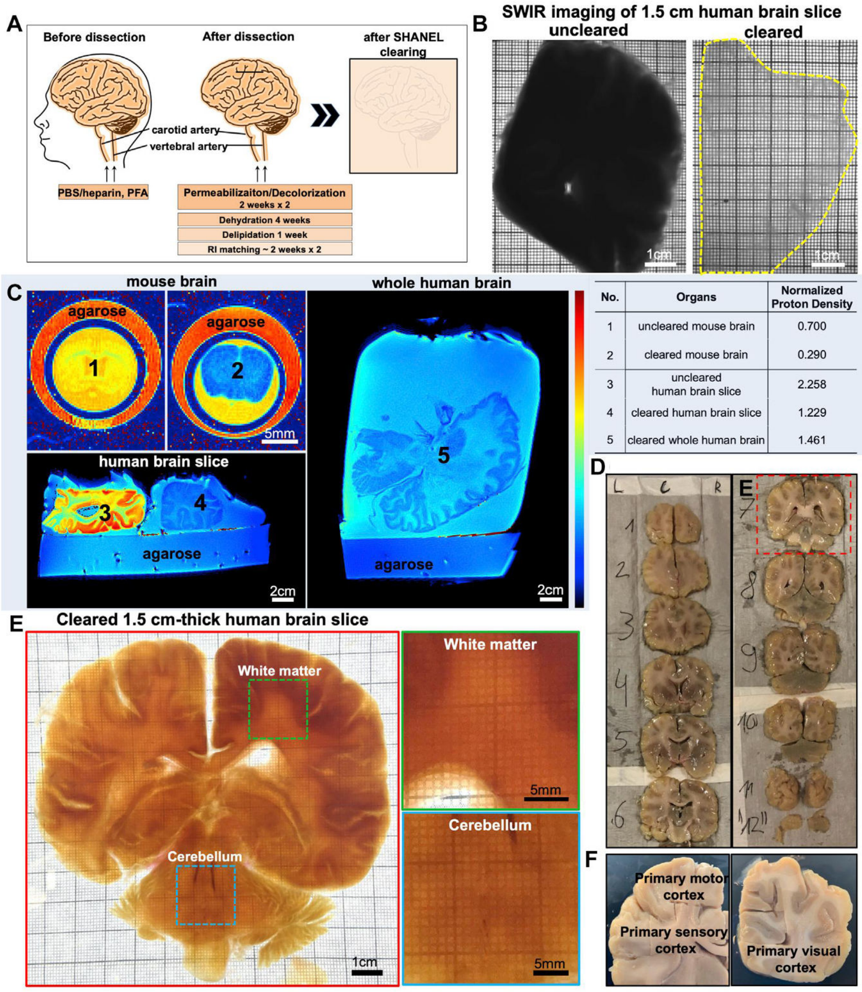

No.	Organs	Normalized Proton Density
1	uncleared mouse brain	0.700
2	cleared mouse brain	0.290
3	uncleared human brain slice	2.258
4	cleared human brain slice	1.229
5	cleared whole human brain	1.461

Figure S3. SHANEL Clearing of Intact Adult Human Brain and Human Brain Slices, Related to Figures 3 and 4

(A) Active perfusion pipeline is used to accelerate whole human brain SHANEL clearing.

(B) Short-wave infrared (SWIR) imaging at 1450 nm of uncleared (left) and cleared (right) 1.5 cm thick human brain slice. The underneath printed grids are visible through the cleared sample.

(C) Color-coded maps of proton density by MRI demonstrated homogeneous replacement of tissue water in the human brain slice and whole human brain similar to in the mouse brain. The difference in normalized proton density (1.5% agarose as reference) between uncleared and cleared samples was comparable for mouse and human samples (see table). Please note that color code and values are not directly comparable between the mouse and human samples because of different measurement setups (e.g., scanner hardware and sequences).

(D) 12 slices with 1.5 cm thickness from an intact adult human brain after CHAPS/NMDEA treatment.

(E) Photo of the slice (#7) after SHANEL clearing showing the full transparency. The colored rectangles from heavily myelinated white matter and cerebellum are shown in higher magnification on the right hand side.

(F) Some cortex areas were cut for further staining as listed in Figure 7G.

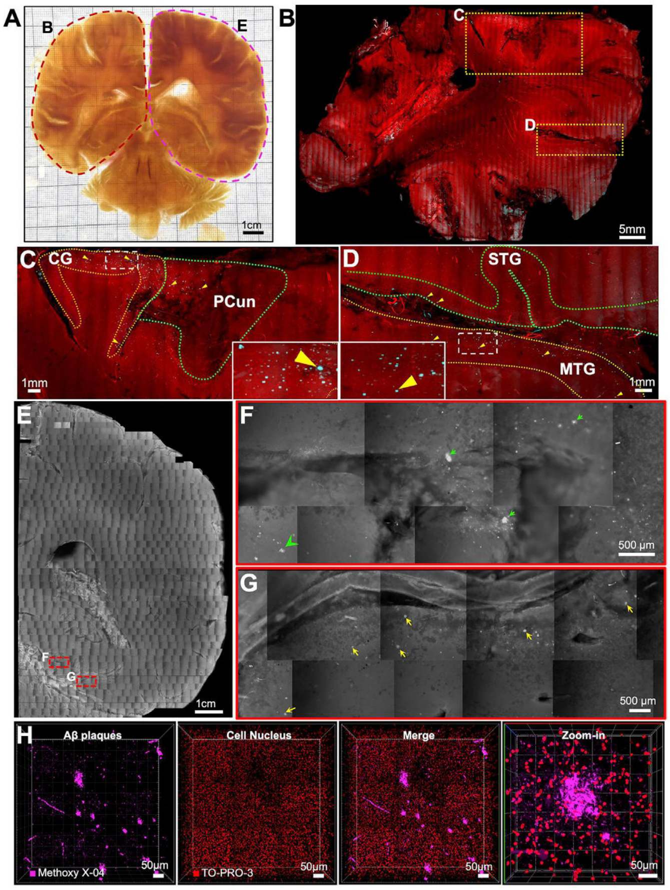

Figure S4. Imaging Centimeters-Sized Human Brain Slice with an Upright Confocal and with an Epifluorescence Microscope, Related to Figures 3 and 4

(A) We imaged large parts of the example slice (#7) using an upright confocal microscope (left side, red dashed region) and with an epifluorescence microscope (right side, purple dashed region).

(B-D) 3D reconstruction of upright confocal images of the left side of the brain slice in (A) showing the TO-PRO-3 labeled cell nuclei (red) and Methoxy-X04 labeled Abeta plaques (cyan). Zoom-in images indicating plaque accumulation regions (arrowheads in C and D) including cingulate gyrus (CG), precuneus (PCun), superior temporal gyrus (STG) and middle temporal gyrus (MTG).

(E-G) Stitched epifluorescent data of the right side of the brain slice in (A) showing Aβ plaques accumulating in the parahippocampal gyrus (PHG, green arrows) and fusiform gyrus (FuG, yellow arrows).

(H) Tiled 3D images from an inverted confocal microscope showing Aβ plaques (magenta) and surrounding cell nuclei (red) from the cortex.

See also Video S2.

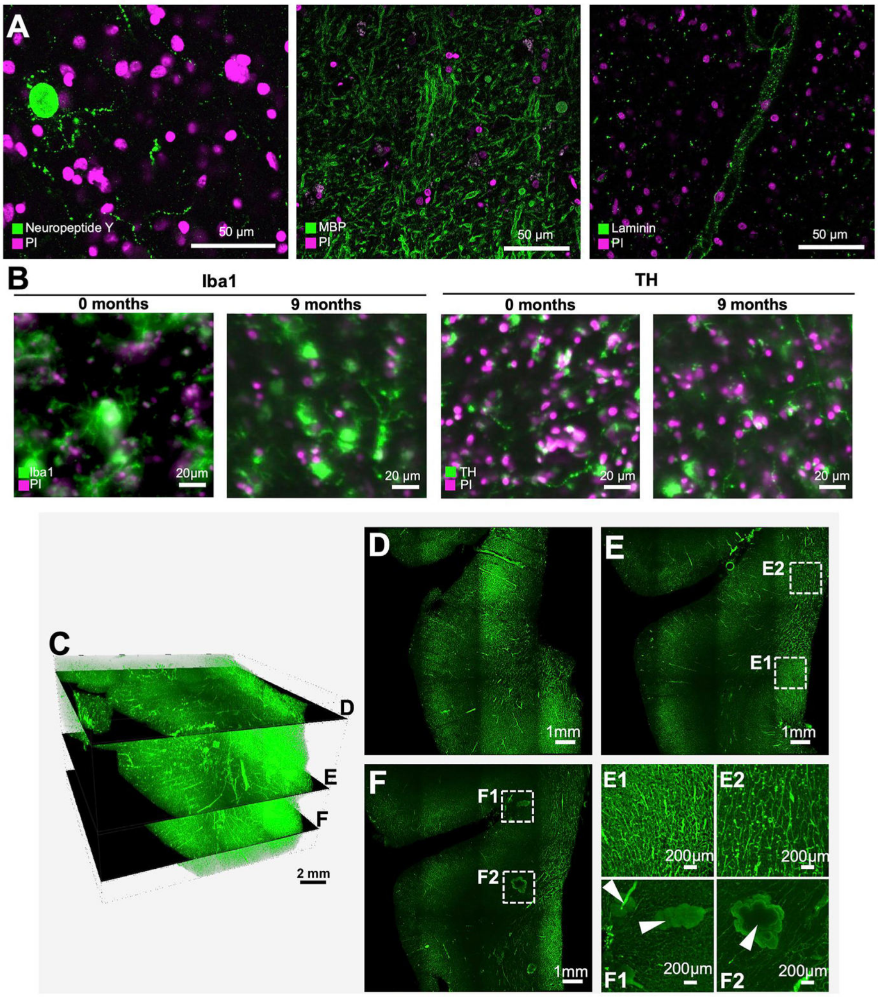

Figure S5. SHANEL Histology of Different Cellular Structures, Related to Figure 4

(A) Human brain slices immunostained with anti-Neuropeptide Y, anti-MBP (myelin basic protein), anti-laminin antibodies and with PI to visualize different cellular structures after SHANEL histology.

(B) Light-sheet images of an antibody-labeled 1.5 cm thick human brain slice showing good preservation of fluorescence signals after 9 months of SHANEL clearing.

(C-F) Lectin labeling of a post-mortem human brain tissue with a size of 3.0 × 1.9 × 1.5 cm. The lectin labeling throughout the entire depth of the centimeters-sized human brain tissue is evident. For example, alteration of regional density of vasculature (compare E1 to E2) and tissue abnormalities (potentially aneurysms) are evident e.g., swollen structures pointed by arrowheads in F1 and F2.

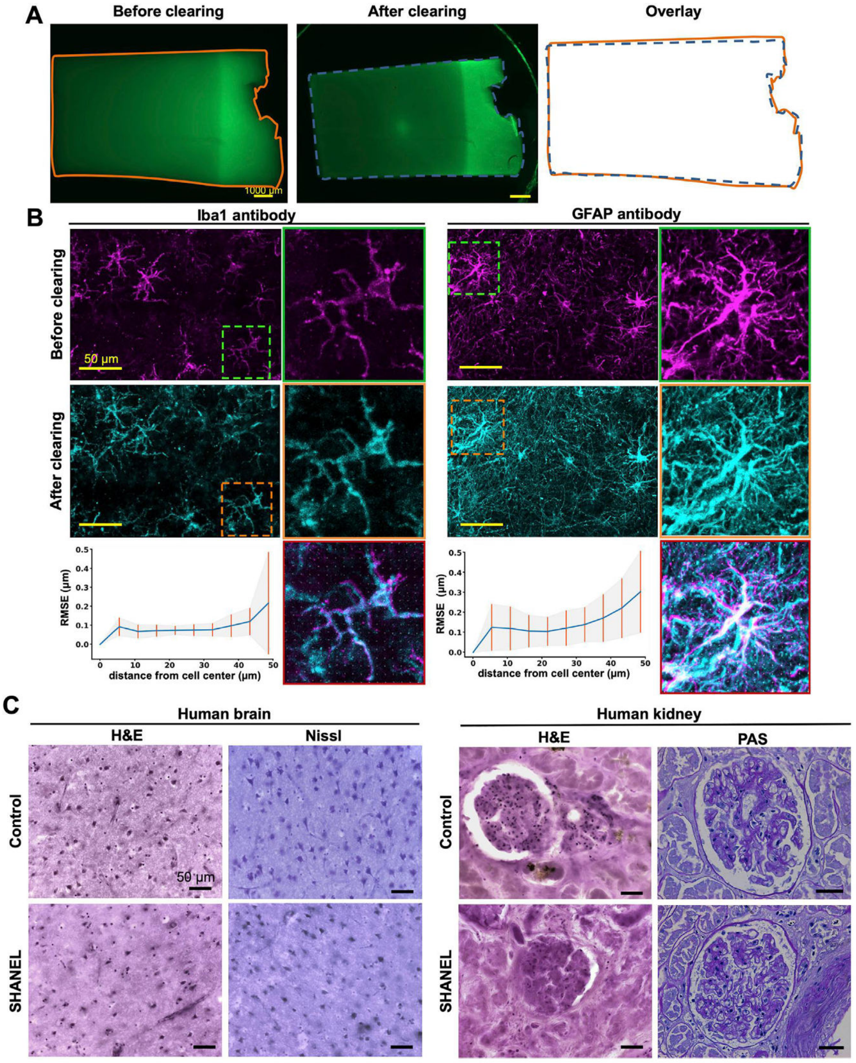

Figure S6. SHANEL Histology Preserves the Morphology of the Tissue and Cellular Structures, Related to Figure 4

(A–B) Macroscopic (A) and microscopic (B) assessments of tissue integrity after SHANEL clearing of 1 mm thick human brain slices immunolabeled for Iba1 and GFAP, then imaged with a stereo-fluorescence microscope (A) and a confocal microscope (B). The preservation of tissue proportions (A) and cellular shape (B) (as calculated by RMSE) after SHANEL treatment (slice n = 3). Please note that there are more cells visible after clearing as expected with the enhanced imaging depth.

(C) Hematoxylin & eosin (H&E), Nissl and Periodic Acid Schiff (PAS) stainings of human brain and kidney without (control) and with SHANEL treatment. Preserved structures after SHANEL histology (similar to controls) are evident.

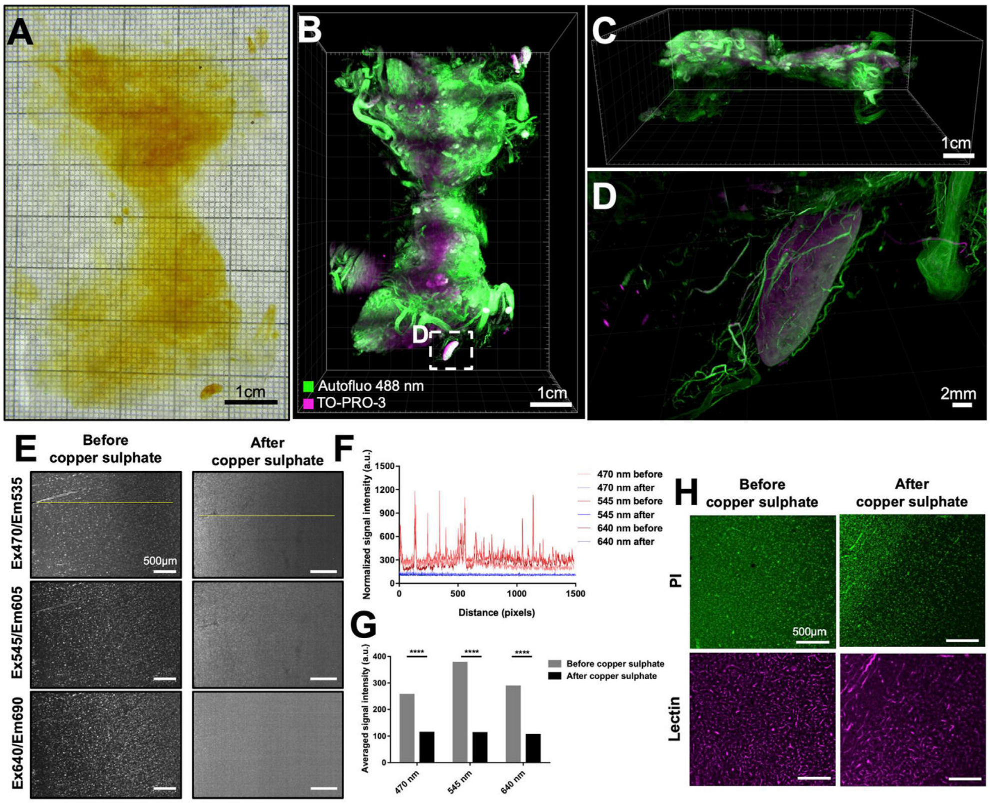

Figure S7. SHANEL on Whole Human Thyroid and Autofluorescence Reduction of SHANEL Samples by Copper Sulfate Treatment, Related to Figure 6

(A) SHANEL cleared intact human thyroid (original size of 7 × 5 x 3 cm) showing full transparency.

(B, C) 3D reconstruction of the thyroid imaged with the new light-sheet system.

(D) Zoomed-in view of lymph node with surrounding vessels.

(E) Autofluorescence of SHANEL cleared human brain sample imaged by light-sheet microscopy before and after copper sulfate ($CuSO_4$) treatment.

(F) Plots of autofluorescence signal intensity profiles along the yellow lines in E.

(G) Averaged autofluorescence signal intensity before and after copper sulfate treatment. P values were calculated using unpaired *t* test; error bars show standard deviations.

(H) Fluorescent dye signals (PI labeled cell nuclei, lectin labeled vessels) are preserved after copper sulfate treatment.

References

ABADIE, S., JARDET, C., COLOMBELLI, J., CHAPUT, B., DAVID, A., GROLLEAU, J. L., BEDOS, P., LOBJOIS, V., DESCARGUES, P. & ROUQUETTE, J. 2018. 3D imaging of cleared human skin biopsies using light-sheet microscopy: A new way to visualize in-depth skin structure. *Skin Res Technol,* 24**,** 294-303.

AMAT, F., HOCKENDORF, B., WAN, Y., LEMON, W. C., MCDOLE, K. & KELLER, P. J. 2015. Efficient processing and analysis of large-scale light-sheet microscopy data. *Nat Protoc,* 10**,** 1679-96.

AOYAGI, Y., KAWAKAMI, R., OSANAI, H., HIBI, T. & NEMOTO, T. 2015. A rapid optical clearing protocol using 2,2'-thiodiethanol for microscopic observation of fixed mouse brain. *PLoS One,* 10**,** e0116280.

ARIEL, P. 2017. A beginner's guide to tissue clearing. *Int J Biochem Cell Biol,* 84**,** 35-39.

BANERJEE, A., LEE, A., CAMPBELL, E. & MACKINNON, R. 2013. Structure of a pore-blocking toxin in complex with a eukaryotic voltage-dependent K(+) channel. *Elife,* 2**,** e00594.

BEISKER, W., DOLBEARE, F. & GRAY, J. W. 1987. An improved immunocytochemical procedure for high-sensitivity detection of incorporated bromodeoxyuridine. *Cytometry,* 8**,** 235-9.

BRENNA, C., SIMIONI, C., VARANO, G., CONTI, I., COSTANZI, E., MELLONI, M. & NERI, L. M. 2022. Optical tissue clearing associated with 3D imaging: application in preclinical and clinical studies. *Histochem Cell Biol,* 157**,** 497-511.

BRIA, A., IANNELLO, G., ONOFRI, L. & PENG, H. 2016. TeraFly: real-time three-dimensional visualization and annotation of terabytes of multidimensional volumetric images. *Nat Methods,* 13**,** 192-4.

BUENROSTRO, J. D., GIRESI, P. G., ZABA, L. C., CHANG, H. Y. & GREENLEAF, W. J. 2013. Transposition of native chromatin for fast and sensitive epigenomic profiling of open chromatin, DNA-binding proteins and nucleosome position. *Nat Methods,* 10**,** 1213-8.

BUTTERWORTH, E., DICKERSON, W., VIJAY, V., WEITZEL, K., COOPER, J., ATKINSON, E. W., COLEMAN, J. E., OTTO, K. J. & CAMPBELL-THOMPSON, M. 2018. High Resolution 3D Imaging of the Human Pancreas Neuro-insular Network. *J Vis Exp*.

CAI, R., PAN, C., GHASEMIGHARAGOZ, A., TODOROV, M. I., FORSTERA, B., ZHAO, S., BHATIA, H. S., PARRA-DAMAS, A., MROWKA, L., THEODOROU, D., REMPFLER, M., XAVIER, A. L. R., KRESS, B. T., BENAKIS, C., STEINKE, H., LIEBSCHER, S., BECHMANN, I., LIESZ, A., MENZE, B., KERSCHENSTEINER, M., NEDERGAARD, M. & ERTURK, A. 2019. Panoptic imaging of transparent mice reveals whole-body neuronal projections and skull-meninges connections. *Nat Neurosci,* 22**,** 317-327.

CALVE, S., READY, A., HUPPENBAUER, C., MAIN, R. & NEU, C. P. 2015. Optical clearing in dense connective tissues to visualize cellular connectivity in situ. *PLoS One,* 10**,** e0116662.

CHAE, P. S., RASMUSSEN, S. G., RANA, R. R., GOTFRYD, K., CHANDRA, R., GOREN, M. A., KRUSE, A. C., NURVA, S., LOLAND, C. J., PIERRE, Y., DREW, D., POPOT, J. L., PICOT, D., FOX, B. G., GUAN, L., GETHER, U., BYRNE, B., KOBILKA, B. & GELLMAN, S. H. 2010. Maltose-neopentyl glycol (MNG) amphiphiles for solubilization, stabilization and crystallization of membrane proteins. *Nat Methods,* 7**,** 1003-8.

CHEN, F., TILLBERG, P. W. & BOYDEN, E. S. 2015. Optical imaging. Expansion microscopy. *Science,* 347**,** 543-8.

CHOI, J., LEE, E., KIM, J. H. & SUN, W. 2019. FxClear, A Free-hydrogel Electrophoretic Tissue Clearing Method for Rapid De-lipidation of Tissues with High Preservation of Immunoreactivity. *Exp Neurobiol,* 28**,** 436-445.

CHUNG, K., WALLACE, J., KIM, S. Y., KALYANASUNDARAM, S., ANDALMAN, A. S., DAVIDSON, T. J., MIRZABEKOV, J. J., ZALOCUSKY, K. A., MATTIS, J., DENISIN, A. K., PAK, S., BERNSTEIN, H., RAMAKRISHNAN, C., GROSENICK, L., GRADINARU, V. & DEISSEROTH, K. 2013. Structural and molecular interrogation of intact biological systems. *Nature,* 497**,** 332-7.

CONRATH, J., ERGINAY, A., GIORGI, R., LECLEIRE-COLLET, A., VICAUT, E., KLEIN, J. C., GAUDRIC, A. & MASSIN, P. 2007. Evaluation of the effect of JPEG and JPEG2000 image compression on the detection of diabetic retinopathy. *Eye (Lond),* 21**,** 487-93.

COSTANTINI, I., CICCHI, R., SILVESTRI, L., VANZI, F. & PAVONE, F. S. 2019. In-vivo and ex-vivo optical clearing methods for biological tissues: review. *Biomed Opt Express,* 10**,** 5251-5267.

CUI, M., ONO, M., KIMURA, H., LIU, B. & SAJI, H. 2011. Synthesis and structure-affinity relationships of novel dibenzylideneacetone derivatives as probes for beta-amyloid plaques. *J Med Chem,* 54**,** 2225-40.

CUI, M., ONO, M., WATANABE, H., KIMURA, H., LIU, B. & SAJI, H. 2014. Smart near-infrared fluorescence probes with donor-acceptor structure for in vivo detection of beta-amyloid deposits. *J Am Chem Soc,* 136**,** 3388-94.

DECROIX, L., VAN MUYLDER, V., DESENDER, L., SAMPAOLESI, M. & THORREZ, L. 2015. Tissue clearing for confocal imaging of native and bio-artificial skeletal muscle. *Biotech Histochem,* 90**,** 424-31.

DENK, W., STRICKLER, J. H. & WEBB, W. W. 1990. Two-photon laser scanning fluorescence microscopy. *Science,* 248**,** 73-6.

DOLENSEK, J., RUPNIK, M. S. & STOZER, A. 2015. Structural similarities and differences between the human and the mouse pancreas. *Islets,* 7**,** e1024405.

ELLENBERG, J., SWEDLOW, J. R., BARLOW, M., COOK, C. E., SARKANS, U., PATWARDHAN, A., BRAZMA, A. & BIRNEY, E. 2018. A call for public archives for biological image data. *Nat Methods,* 15**,** 849-854.

ERBEN, T., OSSIG, R., NAIM, H. Y. & SCHNEKENBURGER, J. 2016. What to do with high autofluorescence background in pancreatic tissues - an efficient Sudan black B quenching method for specific immunofluorescence labelling. *Histopathology,* 69**,** 406-22.

ERTURK, A., BECKER, K., JAHRLING, N., MAUCH, C. P., HOJER, C. D., EGEN, J. G., HELLAL, F., BRADKE, F., SHENG, M. & DODT, H. U. 2012. Three-dimensional imaging of solvent-cleared organs using 3DISCO. *Nat Protoc,* 7**,** 1983-95.

EVERS, D. L., FOWLER, C. B., CUNNINGHAM, B. R., MASON, J. T. & O'LEARY, T. J. 2011. The effect of formaldehyde fixation on RNA: optimization of formaldehyde adduct removal. *J Mol Diagn,* 13**,** 282-8.

FANG, R., XIA, C., CLOSE, J. L., ZHANG, M., HE, J., HUANG, Z., HALPERN, A. R., LONG, B., MILLER, J. A., LEIN, E. S. & ZHUANG, X. 2022. Conservation and divergence of cortical cell organization in human and mouse revealed by MERFISH. *Science,* 377**,** 56-62.

FERNANDEZ, E. & MARULL-TUFEU, S. 2019. 3D imaging of human epidermis micromorphology by combining fluorescent dye, optical clearing and confocal microscopy. *Skin Res Technol,* 25**,** 735-742.

FOWLER, J. L., LEE, S. S., WESNER, Z. C., OLEHNIK, S. K., KRON, S. J. & HARA, M. 2018. Three-Dimensional Analysis of the Human Pancreas. *Endocrinology,* 159**,** 1393-1400.

FU, H., WANG, X., DIAO, K., HUANG, S., LIU, H., GAO, Y., ZHAO, Q., YANG, Z. G. & GUO, Y. K. 2019. CT compared to MRI for functional evaluation of the right ventricle: a systematic review and meta-analysis. *Eur Radiol,* 29**,** 6816-6828.

GIBBS, H. C., MOTA, S. M., HART, N. A., MIN, S. W., VERNINO, A. O., PRITCHARD, A. L., SEN, A., VITHA, S., SARASAMMA, S., MCINTOSH, A. L., YEH, A. T., LEKVEN, A. C., MCCREEDY, D. A., MAITLAND, K. C. & PEREZ, L. M. 2021. Navigating the Light-Sheet Image Analysis Software Landscape: Concepts for Driving Cohesion From Data Acquisition to Analysis. *Front Cell Dev Biol,* 9**,** 739079.

GODDARD, T. D., HUANG, C. C. & FERRIN, T. E. 2005. Software extensions to UCSF chimera for interactive visualization of large molecular assemblies. *Structure,* 13**,** 473-82.

GREENBAUM, A., CHAN, K. Y., DOBREVA, T., BROWN, D., BALANI, D. H., BOYCE, R., KRONENBERG, H. M., MCBRIDE, H. J. & GRADINARU, V. 2017. Bone CLARITY: Clearing, imaging, and computational analysis of osteoprogenitors within intact bone marrow. *Sci Transl Med,* 9.

GREENWOOD, D. J., DOS SANTOS, M. S., HUANG, S., RUSSELL, M. R. G., COLLINSON, L. M., MACRAE, J. I., WEST, A., JIANG, H. & GUTIERREZ, M. G. 2019. Subcellular antibiotic visualization reveals a dynamic drug reservoir in infected macrophages. *Science,* 364**,** 1279-1282.

GUPTA, A. & GOYAL, R. 2016. Amyloid beta plaque: a culprit for neurodegeneration. *Acta Neurol Belg,* 116**,** 445-450.

GURDITA, A., NICKERSON, P. E. B., POKRAJAC, N. T., ORTIN-MARTINEZ, A., SAMUEL TSAI, E. L., COMANITA, L., YAN, N. E., DOLATI, P., TACHIBANA, N., LIU, Z. C., PEARSON, J. D., CHEN, D., BREMNER, R. & WALLACE, V. A. 2021. InVision: An optimized tissue clearing approach for three-dimensional imaging and analysis of intact rodent eyes. *iScience,* 24**,** 102905.

HAMA, H., HIOKI, H., NAMIKI, K., HOSHIDA, T., KUROKAWA, H., ISHIDATE, F., KANEKO, T., AKAGI, T., SAITO, T., SAIDO, T. & MIYAWAKI, A. 2015. ScaleS: an optical clearing palette for biological imaging. *Nat Neurosci,* 18**,** 1518-29.

HAN, E. X., QIAN, H., JIANG, B., FIGETAKIS, M., KOSYAKOVA, N., TELLIDES, G., NIKLASON, L. E. & CHANG, W. G. 2021. A therapeutic vascular conduit to support in vivo cell-secreted therapy. *NPJ Regen Med,* 6**,** 40.

HARRISON, C. H., BUCKLAND, G. R., BROOKS, S. E., JOHNSTON, D. A., CHATELET, D. S., LIU, A. K. L., GENTLEMAN, S. M., BOCHE, D. & NICOLL, J. A. R. 2018. A novel method to visualise the three-dimensional organisation of the human cerebral cortical vasculature. *J Anat,* 232**,** 1025-1030.

HEILINGOETTER, C. L. & JENSEN, M. B. 2016. Histological methods for ex vivo axon tracing: A systematic review. *Neurol Res,* 38**,** 561-9.

HOHBERGER, B., BAUMGART, C. & BERGUA, A. 2017. Optical clearing of the eye using the See Deep Brain technique. *Eye (Lond),* 31**,** 1496-1502.

ISAACSON, D., SHEN, J., MCCREEDY, D., CALVERT, M., MCDEVITT, T., CUNHA, G. & BASKIN, L. 2018a. Lightsheet fluorescence microscopy of branching human fetal kidney. *Kidney Int,* 93**,** 525.

ISAACSON, D., SHEN, J., OVERLAND, M., LI, Y., SINCLAIR, A., CAO, M., MCCREEDY, D., CALVERT, M., MCDEVITT, T., CUNHA, G. R. & BASKIN, L. 2018b. Three-dimensional imaging of the developing human fetal urogenital-genital tract: Indifferent stage to male and female differentiation. *Differentiation,* 103**,** 14-23.

JAHRLING, N., BECKER, K., WEGENAST-BRAUN, B. M., GRATHWOHL, S. A., JUCKER, M. & DODT, H. U. 2015. Cerebral beta-Amyloidosis in Mice Investigated by Ultramicroscopy. *PLoS One,* 10**,** e0125418.

JAKOB-ROETNE, R. & JACOBSEN, H. 2009. Alzheimer's disease: from pathology to therapeutic approaches. *Angew Chem Int Ed Engl,* 48**,** 3030-59.

JONKMAN, J., BROWN, C. M., WRIGHT, G. D., ANDERSON, K. I. & NORTH, A. J. 2020. Tutorial: guidance for quantitative confocal microscopy. *Nat Protoc,* 15**,** 1585-1611.

JUN, Y. W., KIM, H. R., REO, Y. J., DAI, M. & AHN, K. H. 2017. Addressing the autofluorescence issue in deep tissue imaging by two-photon microscopy: the significance of far-red emitting dyes. *Chem Sci,* 8**,** 7696-7704.

KALLER, M. O. & AN, J. 2022. Contrast Agent Toxicity. *StatPearls.* Treasure Island (FL).

KE, M. T., FUJIMOTO, S. & IMAI, T. 2013. SeeDB: a simple and morphology-preserving optical clearing agent for neuronal circuit reconstruction. *Nat Neurosci,* 16**,** 1154-61.

KE, M. T., NAKAI, Y., FUJIMOTO, S., TAKAYAMA, R., YOSHIDA, S., KITAJIMA, T. S., SATO, M. & IMAI, T. 2016. Super-Resolution Mapping of Neuronal Circuitry With an Index-Optimized Clearing Agent. *Cell Rep,* 14**,** 2718-32.

KERMANY, D. S., GOLDBAUM, M., CAI, W., VALENTIM, C. C. S., LIANG, H., BAXTER, S. L., MCKEOWN, A., YANG, G., WU, X., YAN, F., DONG, J., PRASADHA, M. K., PEI, J., TING, M. Y. L., ZHU, J., LI, C., HEWETT, S., DONG, J., ZIYAR, I., SHI, A., ZHANG, R., ZHENG, L., HOU, R., SHI, W., FU, X., DUAN, Y., HUU, V. A. N., WEN, C., ZHANG, E. D., ZHANG, C. L., LI, O., WANG, X., SINGER, M. A., SUN, X., XU, J., TAFRESHI, A., LEWIS, M. A., XIA, H. & ZHANG, K. 2018. Identifying Medical Diagnoses and Treatable Diseases by Image-Based Deep Learning. *Cell,* 172**,** 1122-1131 e9.

KOLESOVA, H., OLEJNICKOVA, V., KVASILOVA, A., GREGOROVICOVA, M. & SEDMERA, D. 2021. Tissue clearing and imaging methods for cardiovascular development. *iScience,* 24**,** 102387.

KONNO, A. & OKAZAKI, S. 2018. Aqueous-based tissue clearing in crustaceans. *Zoological Lett,* 4**,** 13.

KOSTRIKOV, S., JOHNSEN, K. B., BRAUNSTEIN, T. H., GUDBERGSSON, J. M., FLIEDNER, F. P., OBARA, E. A. A., HAMERLIK, P., HANSEN, A. E., KJAER, A., HEMPEL, C. & ANDRESEN, T. L. 2021. Optical tissue clearing and machine learning can precisely characterize extravasation and blood vessel architecture in brain tumors. *Commun Biol,* 4**,** 815.

KU, T., SWANEY, J., PARK, J. Y., ALBANESE, A., MURRAY, E., CHO, J. H., PARK, Y. G., MANGENA, V., CHEN, J. & CHUNG, K. 2016. Multiplexed and scalable super-resolution imaging of three-dimensional protein localization in size-adjustable tissues. *Nat Biotechnol,* 34**,** 973-81.

KUWAJIMA, T., SITKO, A. A., BHANSALI, P., JURGENS, C., GUIDO, W. & MASON, C. 2013. ClearT: a detergent- and solvent-free clearing method for neuronal and non-neuronal tissue. *Development,* 140**,** 1364-8.

LAI, H. M., NG, W. L., GENTLEMAN, S. M. & WU, W. 2017. Chemical Probes for Visualizing Intact Animal and Human Brain Tissue. *Cell Chem Biol,* 24**,** 659-672.

LANCIEGO, J. L. & WOUTERLOOD, F. G. 2011. A half century of experimental neuroanatomical tracing. *J Chem Neuroanat,* 42**,** 157-83.

LERNER, T. N., YE, L. & DEISSEROTH, K. 2016. Communication in Neural Circuits: Tools, Opportunities, and Challenges. *Cell,* 164**,** 1136-1150.

LI, Y., XU, J., WAN, P., YU, T. & ZHU, D. 2018. Optimization of GFP Fluorescence Preservation by a Modified uDISCO Clearing Protocol. *Front Neuroanat,* 12**,** 67.

LIEBMANN, T., RENIER, N., BETTAYEB, K., GREENGARD, P., TESSIER-LAVIGNE, M. & FLAJOLET, M. 2016. Three-Dimensional Study of Alzheimer's Disease Hallmarks Using the iDISCO Clearing Method. *Cell Rep,* 16**,** 1138-1152.

LISCIA, D. S., ALHADI, T. & VONDERHAAR, B. K. 1982. Solubilization of active prolactin receptors by a nondenaturing zwitterionic detergent. *J Biol Chem,* 257**,** 9401-5.

LITVINUKOVA, M., TALAVERA-LOPEZ, C., MAATZ, H., REICHART, D., WORTH, C. L., LINDBERG, E. L., KANDA, M., POLANSKI, K., HEINIG, M., LEE, M., NADELMANN, E. R., ROBERTS, K., TUCK, L., FASOULI, E. S., DELAUGHTER, D. M., MCDONOUGH, B., WAKIMOTO, H., GORHAM, J. M., SAMARI, S., MAHBUBANI, K. T., SAEB-PARSY, K., PATONE, G., BOYLE, J. J., ZHANG, H., ZHANG, H., VIVEIROS, A., OUDIT, G. Y., BAYRAKTAR, O. A., SEIDMAN, J. G., SEIDMAN, C. E., NOSEDA, M., HUBNER, N. & TEICHMANN, S. A. 2020. Cells of the adult human heart. *Nature,* 588**,** 466-472.

LIU, A. K. L., LAI, H. M., CHANG, R. C. & GENTLEMAN, S. M. 2017. Free of acrylamide sodium dodecyl sulphate (SDS)-based tissue clearing (FASTClear): a novel protocol of tissue clearing for three-dimensional visualization of human brain tissues. *Neuropathol Appl Neurobiol,* 43**,** 346-351.

LUCHE, S., SANTONI, V. & RABILLOUD, T. 2003. Evaluation of nonionic and zwitterionic detergents as membrane protein solubilizers in two-dimensional electrophoresis. *Proteomics,* 3**,** 249-53.

MAGLIARO, C., CALLARA, A. L., MATTEI, G., MORCINELLI, M., VIAGGI, C., VAGLINI, F. & AHLUWALIA, A. 2016. Clarifying CLARITY: Quantitative Optimization of the Diffusion Based Delipidation Protocol for Genetically Labeled Tissue. *Front Neurosci,* 10**,** 179.

MARX, V. 2016. Optimizing probes to image cleared tissue. *Nat Methods,* 13**,** 205-9.

MASSELINK, W., REUMANN, D., MURAWALA, P., PASIERBEK, P., TANIGUCHI, Y., BONNAY, F., MEIXNER, K., KNOBLICH, J. A. & TANAKA, E. M. 2019. Broad applicability of a streamlined ethyl cinnamate-based clearing procedure. *Development,* 146.

MATRYBA, P., LUKASIEWICZ, K., PAWLOWSKA, M., TOMCZUK, J. & GOLAB, J. 2021. Can Developments in Tissue Optical Clearing Aid Super-Resolution Microscopy Imaging? *Int J Mol Sci,* 22.

MATSUMOTO, K., MITANI, T. T., HORIGUCHI, S. A., KANESHIRO, J., MURAKAMI, T. C., MANO, T., FUJISHIMA, H., KONNO, A., WATANABE, T. M., HIRAI, H. & UEDA, H. R. 2019. Advanced CUBIC tissue clearing for whole-organ cell profiling. *Nat Protoc,* 14**,** 3506-3537.

MAZZETTI, S., FRIGERIO, S., GELATI, M., SALMAGGI, A. & VITELLARO-ZUCCARELLO, L. 2004. Lycopersicon esculentum lectin: an effective and versatile endothelial marker of normal and tumoral blood vessels in the central nervous system. *Eur J Histochem,* 48**,** 423-8.

MOLBAY, M., KOLABAS, Z. I., TODOROV, M. I., OHN, T. L. & ERTURK, A. 2021. A guidebook for DISCO tissue clearing. *Mol Syst Biol,* 17**,** e9807.

MONNIER, V. M., KOHN, R. R. & CERAMI, A. 1984. Accelerated age-related browning of human collagen in diabetes mellitus. *Proc Natl Acad Sci U S A,* 81**,** 583-7.

MORENO-GARCIA, A., KUN, A., CALERO, O., MEDINA, M. & CALERO, M. 2018. An Overview of the Role of Lipofuscin in Age-Related Neurodegeneration. *Front Neurosci,* 12**,** 464.

NA, M., KIM, K., OH, K., CHOI, H. J., HA, C. & CHANG, S. 2022. Sodium Cholate-Based Active Delipidation for Rapid and Efficient Clearing and Immunostaining of Deep Biological Samples. *Small Methods,* 6**,** e2100943.

NGUYEN, K. A., PEUCHMAUR, M., MAGNARD, S., HAUDECOEUR, R., BOYERE, C., MOUNIEN, S., BENAMMAR, I., ZAMPIERI, V., IGONET, S., CHAPTAL, V., JAWHARI, A., BOUMENDJEL, A. & FALSON, P. 2018. Glycosyl-Substituted Dicarboxylates as Detergents for the Extraction, Overstabilization, and Crystallization of Membrane Proteins. *Angew Chem Int Ed Engl,* 57**,** 2948-2952.

NIKKEN, J. J. & KRESTIN, G. P. 2007. MRI of the kidney-state of the art. *Eur Radiol,* 17**,** 2780-93.

NOE, M., REZAEE, N., ASRANI, K., SKARO, M., GROOT, V. P., WU, P. H., OLSON, M. T., HONG, S. M., KIM, S. J., WEISS, M. J., WOLFGANG, C. L., MAKARY, M. A., HE, J., CAMERON, J. L., WIRTZ, D., ROBERTS, N. J., OFFERHAUS, G. J. A., BROSENS, L. A. A., WOOD, L. D. & HRUBAN, R. H. 2018. Immunolabeling of Cleared Human Pancreata Provides Insights into Three-Dimensional Pancreatic Anatomy and Pathology. *Am J Pathol,* 188**,** 1530-1535.

OUADAH, Y., ROJAS, E. R., RIORDAN, D. P., CAPOSTAGNO, S., KUO, C. S. & KRASNOW, M. A. 2019. Rare Pulmonary Neuroendocrine Cells Are Stem Cells Regulated by Rb, p53, and Notch. *Cell,* 179**,** 403-416 e23.

PAN, C., CAI, R., QUACQUARELLI, F. P., GHASEMIGHARAGOZ, A., LOURBOPOULOS, A., MATRYBA, P., PLESNILA, N., DICHGANS, M., HELLAL, F. & ERTURK, A. 2016. Shrinkage-mediated imaging of entire organs and organisms using uDISCO. *Nat Methods,* 13**,** 859-67.

PARK, Y. G., SOHN, C. H., CHEN, R., MCCUE, M., YUN, D. H., DRUMMOND, G. T., KU, T., EVANS, N. B., OAK, H. C., TRIEU, W., CHOI, H., JIN, X., LILASCHAROEN, V., WANG, J., TRUTTMANN, M. C., QI, H. W., PLOEGH, H. L., GOLUB, T. R., CHEN, S. C., FROSCH, M. P., KULIK, H. J., LIM, B. K. & CHUNG, K. 2018. Protection of tissue physicochemical properties using polyfunctional crosslinkers. *Nat Biotechnol*.

PARRA-DAMAS, A. & SAURA, C. A. 2020. Tissue Clearing and Expansion Methods for Imaging Brain Pathology in Neurodegeneration: From Circuits to Synapses and Beyond. *Front Neurosci,* 14**,** 914.

PENG, H., RUAN, Z., LONG, F., SIMPSON, J. H. & MYERS, E. W. 2010. V3D enables real-time 3D visualization and quantitative analysis of large-scale biological image data sets. *Nat Biotechnol,* 28**,** 348-53.

PERBELLINI, F., LIU, A. K. L., WATSON, S. A., BARDI, I., ROTHERY, S. M. & TERRACCIANO, C. M. 2017. Free-of-Acrylamide SDS-based Tissue Clearing (FASTClear) for three dimensional visualization of myocardial tissue. *Sci Rep,* 7**,** 5188.

PETTERSEN, E. F., GODDARD, T. D., HUANG, C. C., COUCH, G. S., GREENBLATT, D. M., MENG, E. C. & FERRIN, T. E. 2004. UCSF Chimera--a visualization system for exploratory research and analysis. *J Comput Chem,* 25**,** 1605-12.

PIETZSCH, T., SAALFELD, S., PREIBISCH, S. & TOMANCAK, P. 2015. BigDataViewer: visualization and processing for large image data sets. *Nat Methods,* 12**,** 481-3.

PORTER, G. A., PALADE, G. E. & MILICI, A. J. 1990. Differential binding of the lectins Griffonia simplicifolia I and Lycopersicon esculentum to microvascular endothelium: organ-specific localization and partial glycoprotein characterization. *Eur J Cell Biol,* 51**,** 85-95.

POWER, R. M. & HUISKEN, J. 2017. A guide to light-sheet fluorescence microscopy for multiscale imaging. *Nat Methods,* 14**,** 360-373.

PRAHST, C., ASHRAFZADEH, P., MEAD, T., FIGUEIREDO, A., CHANG, K., RICHARDSON, D., VENKARAMAN, L., RICHARDS, M., RUSSO, A. M., HARRINGTON, K., OUARNE, M., PENA, A., CHEN, D. F., CLAESSON-WELSH, L., CHO, K. S., FRANCO, C. A. & BENTLEY, K. 2020. Mouse retinal cell behaviour in space and time using light sheet fluorescence microscopy. *Elife,* 9.

PUELLES, V. G., COMBES, A. N. & BERTRAM, J. F. 2021. Clearly imaging and quantifying the kidney in 3D. *Kidney Int,* 100**,** 780-786.

QI, Y., YU, T., XU, J., WAN, P., MA, Y., ZHU, J., LI, Y., GONG, H., LUO, Q. & ZHU, D. 2019. FDISCO: Advanced solvent-based clearing method for imaging whole organs. *Sci Adv,* 5**,** eaau8355.

QUERFURTH, H. W. & LAFERLA, F. M. 2010. Alzheimer's disease. *N Engl J Med,* 362**,** 329-44.

RABILLOUD, T. 2009. Detergents and chaotropes for protein solubilization before two-dimensional electrophoresis. *Methods Mol Biol,* 528**,** 259-67.

RAGAN, T., KADIRI, L. R., VENKATARAJU, K. U., BAHLMANN, K., SUTIN, J., TARANDA, J., ARGANDA-CARRERAS, I., KIM, Y., SEUNG, H. S. & OSTEN, P. 2012. Serial two-photon tomography for automated ex vivo mouse brain imaging. *Nat Methods,* 9**,** 255-8.

REARDON, S. 2016. Worldwide brain-mapping project sparks excitement - and concern. *Nature,* 537**,** 597.

RENIER, N., WU, Z., SIMON, D. J., YANG, J., ARIEL, P. & TESSIER-LAVIGNE, M. 2014. iDISCO: a simple, rapid method to immunolabel large tissue samples for volume imaging. *Cell,* 159**,** 896-910.

REYNAUD, E. G., KRZIC, U., GREGER, K. & STELZER, E. H. 2008. Light sheet-based fluorescence microscopy: more dimensions, more photons, and less photodamage. *HFSP J,* 2**,** 266-75.

RICHARDSON, D. S., GUAN, W., MATSUMOTO, K., PAN, C., CHUNG, K., ERTURK, A., UEDA, H. R. & LICHTMAN, J. W. 2021. Tissue Clearing. *Nat Rev Methods Primers,* 1.

RICHARDSON, D. S. & LICHTMAN, J. W. 2015. Clarifying Tissue Clearing. *Cell,* 162**,** 246-257.

ROSS, C. A. & POIRIER, M. A. 2004. Protein aggregation and neurodegenerative disease. *Nat Med,* 10 Suppl**,** S10-7.

ROTH, J. 2011. Lectins for histochemical demonstration of glycans. *Histochem Cell Biol,* 136**,** 117-30.

ROYER, L. A., WEIGERT, M., GUNTHER, U., MAGHELLI, N., JUG, F., SBALZARINI, I. F. & MYERS, E. W. 2015. ClearVolume: open-source live 3D visualization for light-sheet microscopy. *Nat Methods,* 12**,** 480-1.

ROZENBLATT-ROSEN, O., SHIN, J. W., ROOD, J. E., HUPALOWSKA, A., HUMAN CELL ATLAS, S., TECHNOLOGY WORKING, G., REGEV, A. & HEYN, H. 2021. Building a high-quality Human Cell Atlas. *Nat Biotechnol,* 39**,** 149-153.

RUSSO, I., OKSMAN, A., VAUPEL, B. & GOLDBERG, D. E. 2009. A calpain unique to alveolates is essential in Plasmodium falciparum and its knockdown reveals an involvement in pre-S-phase development. *Proc Natl Acad Sci U S A,* 106**,** 1554-9.

RZEPKA, Z., BUSZMAN, E., BEBEROK, A. & WRZESNIOK, D. 2016. From tyrosine to melanin: Signaling pathways and factors regulating melanogenesis. *Postepy Hig Med Dosw (Online),* 70**,** 695-708.

SADAF, A., KIM, S., BAE, H. E., WANG, H., NYGAARD, A., UEGAKI, Y., DU, Y., MUNK, C. F., KATSUBE, S., SUNG LEE, H., BAE, J., CHOI, C. W., CHOI, H. J., BYRNE, B., GELLMAN, S. H., GUAN, L., LOLAND, C. J., KOBILKA, B. K., IM, W. & CHAE, P. S. 2021. Conformationally flexible core-bearing detergents with a hydrophobic or hydrophilic pendant: Effect of pendant polarity on detergent conformation and membrane protein stability. *Acta Biomater,* 128**,** 393-407.

SANTI, P. A. 2011. Light sheet fluorescence microscopy: a review. *J Histochem Cytochem,* 59**,** 129-38.

SARITAS, T., PUELLES, V. G., SU, X. T., ELLISON, D. H. & KRAMANN, R. 2019. Optical Clearing and Imaging of Immunolabeled Kidney Tissue. *J Vis Exp*.

SARTORI, M., WEILBAECHER, D., VALDERRAMA, G. L., KUBODERA, S., CHIN, R. C., BERRY, M. J., TITTEL, F. K., SAUERBREY, R. & HENRY, P. D. 1988. Laser-induced autofluorescence of human arteries. *Circ Res,* 63**,** 1053-9.

SCARDIGLI, M., PESCE, L., BRADY, N., MAZZAMUTO, G., GAVRYUSEV, V., SILVESTRI, L., HOF, P. R., DESTRIEUX, C., COSTANTINI, I. & PAVONE, F. S. 2021. Comparison of Different Tissue

Clearing Methods for Three-Dimensional Reconstruction of Human Brain Cellular Anatomy Using Advanced Imaging Techniques. *Front Neuroanat,* 15**,** 752234.

SCHILLER, H. B., MONTORO, D. T., SIMON, L. M., RAWLINS, E. L., MEYER, K. B., STRUNZ, M., VIEIRA BRAGA, F. A., TIMENS, W., KOPPELMAN, G. H., BUDINGER, G. R. S., BURGESS, J. K., WAGHRAY, A., VAN DEN BERGE, M., THEIS, F. J., REGEV, A., KAMINSKI, N., RAJAGOPAL, J., TEICHMANN, S. A., MISHARIN, A. V. & NAWIJN, M. C. 2019. The Human Lung Cell Atlas: A High-Resolution Reference Map of the Human Lung in Health and Disease. *Am J Respir Cell Mol Biol,* 61**,** 31-41.

SCHINDELIN, J., ARGANDA-CARRERAS, I., FRISE, E., KAYNIG, V., LONGAIR, M., PIETZSCH, T., PREIBISCH, S., RUEDEN, C., SAALFELD, S., SCHMID, B., TINEVEZ, J. Y., WHITE, D. J., HARTENSTEIN, V., ELICEIRI, K., TOMANCAK, P. & CARDONA, A. 2012. Fiji: an open-source platform for biological-image analysis. *Nat Methods,* 9**,** 676-82.

SCHMIDT, G., DINTER, D., REISER, M. F. & SCHOENBERG, S. O. 2010. The uses and limitations of whole-body magnetic resonance imaging. *Dtsch Arztebl Int,* 107**,** 383-9.

SCHNELL, S. A., STAINES, W. A. & WESSENDORF, M. W. 1999. Reduction of lipofuscin-like autofluorescence in fluorescently labeled tissue. *J Histochem Cytochem,* 47**,** 719-30.

SHAN, Q. H., QIN, X. Y., ZHOU, N., HUANG, C., WANG, Y., CHEN, P. & ZHOU, J. N. 2022. A method for ultrafast tissue clearing that preserves fluorescence for multimodal and longitudinal brain imaging. *BMC Biol,* 20**,** 77.

SHEN, Z., LU, Z., CHHATBAR, P. Y., O'HERRON, P. & KARA, P. 2012. An artery-specific fluorescent dye for studying neurovascular coupling. *Nat Methods,* 9**,** 273-6.

SHI, W. & MA, H. 2012. Spectroscopic probes with changeable pi-conjugated systems. *Chem Commun (Camb),* 48**,** 8732-44.

SIJENS, P. E., EDENS, M. A., BAKKER, S. J. & STOLK, R. P. 2010. MRI-determined fat content of human liver, pancreas and kidney. *World J Gastroenterol,* 16**,** 1993-8.

SOVENYHAZY, K. M., BORDELON, J. A. & PETTY, J. T. 2003. Spectroscopic studies of the multiple binding modes of a trimethine-bridged cyanine dye with DNA. *Nucleic Acids Res,* 31**,** 2561-9.

SUSAKI, E. A., SHIMIZU, C., KUNO, A., TAINAKA, K., LI, X., NISHI, K., MORISHIMA, K., ONO, H., ODE, K. L., SAEKI, Y., MIYAMICHI, K., ISA, K., YOKOYAMA, C., KITAURA, H., IKEMURA, M., USHIKU, T., SHIMIZU, Y., SAITO, T., SAIDO, T. C., FUKAYAMA, M., ONOE, H., TOUHARA, K., ISA, T., KAKITA, A., SHIBAYAMA, M. & UEDA, H. R. 2020. Versatile whole-organ/body staining and imaging based on electrolyte-gel properties of biological tissues. *Nat Commun,* 11**,** 1982.

SUSAKI, E. A., TAINAKA, K., PERRIN, D., KISHINO, F., TAWARA, T., WATANABE, T. M., YOKOYAMA, C., ONOE, H., EGUCHI, M., YAMAGUCHI, S., ABE, T., KIYONARI, H., SHIMIZU, Y., MIYAWAKI, A., YOKOTA, H. & UEDA, H. R. 2014. Whole-brain imaging with single-cell resolution using chemical cocktails and computational analysis. *Cell,* 157**,** 726-39.

SUSAKI, E. A. & UEDA, H. R. 2016. Whole-body and Whole-Organ Clearing and Imaging Techniques with Single-Cell Resolution: Toward Organism-Level Systems Biology in Mammals. *Cell Chem Biol,* 23**,** 137-157.

TAINAKA, K., KUBOTA, S. I., SUYAMA, T. Q., SUSAKI, E. A., PERRIN, D., UKAI-TADENUMA, M., UKAI, H. & UEDA, H. R. 2014. Whole-body imaging with single-cell resolution by tissue decolorization. *Cell,* 159**,** 911-24.

TAINAKA, K., MURAKAMI, T. C., SUSAKI, E. A., SHIMIZU, C., SAITO, R., TAKAHASHI, K., HAYASHI-TAKAGI, A., SEKIYA, H., ARIMA, Y., NOJIMA, S., IKEMURA, M., USHIKU, T., SHIMIZU, Y., MURAKAMI, M., TANAKA, K. F., IINO, M., KASAI, H., SASAOKA, T., KOBAYASHI, K., MIYAZONO, K., MORII, E., ISA, T., FUKAYAMA, M., KAKITA, A. & UEDA, H. R. 2018. Chemical Landscape for Tissue Clearing Based on Hydrophilic Reagents. *Cell Rep,* 24**,** 2196-2210 e9.

TAO, H., LIU, W., SIMMONS, B. N., HARRIS, H. K., COX, T. C. & MASSIAH, M. A. 2010. Purifying natively folded proteins from inclusion bodies using sarkosyl, Triton X-100, and CHAPS. *Biotechniques,* 48**,** 61-4.

TIAN, T., YANG, Z. & LI, X. 2021. Tissue clearing technique: Recent progress and biomedical applications. *J Anat,* 238**,** 489-507.

TOMER, R., KHAIRY, K. & KELLER, P. J. 2011. Shedding light on the system: studying embryonic development with light sheet microscopy. *Curr Opin Genet Dev,* 21**,** 558-65.

TREWEEK, J. B., CHAN, K. Y., FLYTZANIS, N. C., YANG, B., DEVERMAN, B. E., GREENBAUM, A., LIGNELL, A., XIAO, C., CAI, L., LADINSKY, M. S., BJORKMAN, P. J., FOWLKES, C. C. & GRADINARU, V. 2015. Whole-body tissue stabilization and selective extractions via tissue-hydrogel hybrids for high-resolution intact circuit mapping and phenotyping. *Nat Protoc,* 10**,** 1860-1896.

TUCH, D. S., WEDEEN, V. J., DALE, A. M., GEORGE, J. S. & BELLIVEAU, J. W. 2001. Conductivity tensor mapping of the human brain using diffusion tensor MRI. *Proc Natl Acad Sci U S A,* 98**,** 11697-701.

UEDA, H. R., ERTURK, A., CHUNG, K., GRADINARU, V., CHEDOTAL, A., TOMANCAK, P. & KELLER, P. J. 2020. Tissue clearing and its applications in neuroscience. *Nat Rev Neurosci,* 21**,** 61-79.

UMEZAWA, K., CITTERIO, D. & SUZUKI, K. 2014. New trends in near-infrared fluorophores for bioimaging. *Anal Sci,* 30**,** 327-49.

VERVEER, P. J., SWOGER, J., PAMPALONI, F., GREGER, K., MARCELLO, M. & STELZER, E. H. 2007. High-resolution three-dimensional imaging of large specimens with light sheet-based microscopy. *Nat Methods,* 4**,** 311-3.

VOIE, A. H., BURNS, D. H. & SPELMAN, F. A. 1993. Orthogonal-plane fluorescence optical sectioning: three-dimensional imaging of macroscopic biological specimens. *J Microsc,* 170**,** 229-36.

WALSH, C. L., TAFFOREAU, P., WAGNER, W. L., JAFREE, D. J., BELLIER, A., WERLEIN, C., KUHNEL, M. P., BOLLER, E., WALKER-SAMUEL, S., ROBERTUS, J. L., LONG, D. A., JACOB, J., MARUSSI, S., BROWN, E., HOLROYD, N., JONIGK, D. D., ACKERMANN, M. & LEE, P. D. 2021. Imaging intact human organs with local resolution of cellular structures using hierarchical phase-contrast tomography. *Nat Methods,* 18**,** 1532-1541.

WEISS, K. R., VOIGT, F. F., SHEPHERD, D. P. & HUISKEN, J. 2021. Tutorial: practical considerations for tissue clearing and imaging. *Nat Protoc,* 16**,** 2732-2748.

WILLIAMS, M. P. I., RIGON, M., STRAKA, T., HORNER, S. J., THIEL, M., GRETZ, N., HAFNER, M., REISCHL, M. & RUDOLF, R. 2019. A Novel Optical Tissue Clearing Protocol for Mouse Skeletal Muscle to Visualize Endplates in Their Tissue Context. *Front Cell Neurosci,* 13**,** 49.

XIE, Q., ZENG, N., HUANG, Y., TUCHIN, V. V. & MA, H. 2019. Study on the tissue clearing process using different agents by Mueller matrix microscope. *Biomed Opt Express,* 10**,** 3269-3280.

YANG, B., TREWEEK, J. B., KULKARNI, R. P., DEVERMAN, B. E., CHEN, C. K., LUBECK, E., SHAH, S., CAI, L. & GRADINARU, V. 2014. Single-cell phenotyping within transparent intact tissue through whole-body clearing. *Cell,* 158**,** 945-958.

YANG, J., CHEN, J., DEL CARMEN VITERY, M., OSEI-OWUSU, J., CHU, J., YU, H., SUN, S. & QIU, Z. 2019. PAC, an evolutionarily conserved membrane protein, is a proton-activated chloride channel. *Science,* 364**,** 395-399.

YUAN, L., LIN, W., ZHENG, K., HE, L. & HUANG, W. 2013. Far-red to near infrared analyte-responsive fluorescent probes based on organic fluorophore platforms for fluorescence imaging. *Chem Soc Rev,* 42**,** 622-61.

ZERHOUNI, E. A., PARISH, D. M., ROGERS, W. J., YANG, A. & SHAPIRO, E. P. 1988. Human heart: tagging with MR imaging--a method for noninvasive assessment of myocardial motion. *Radiology,* 169**,** 59-63.

ZHANG, X., TIAN, Y., ZHANG, C., TIAN, X., ROSS, A. W., MOIR, R. D., SUN, H., TANZI, R. E., MOORE, A. & RAN, C. 2015. Near-infrared fluorescence molecular imaging of amyloid beta species and monitoring therapy in animal models of Alzheimer's disease. *Proc Natl Acad Sci U S A,* 112**,** 9734-9.

ZHANG, Y., WANG, Y., CAO, W. W., MA, K. T., JI, W., HAN, Z. W., SI, J. Q. & LI, L. 2018. Spectral Characteristics of Autofluorescence in Renal Tissue and Methods for Reducing Fluorescence Background in Confocal Laser Scanning Microscopy. *J Fluoresc,* 28**,** 561-572.

ZHAO, S., TODOROV, M. I., CAI, R., MASKARI, R. A., STEINKE, H., KEMTER, E., MAI, H., RONG, Z., WARMER, M., STANIC, K., SCHOPPE, O., PAETZOLD, J. C., GESIERICH, B., WONG, M. N., HUBER, T. B., DUERING, M., BRUNS, O. T., MENZE, B., LIPFERT, J., PUELLES, V. G., WOLF, E., BECHMANN, I. & ERTURK, A. 2020. Cellular and Molecular Probing of Intact Human Organs. *Cell,* 180**,** 796-812 e19.

Acknowledgements

I am very happy to write the last section of my dissertation and summarize the fruitful doctoral student life as a time that unites tears and joy in the pandemic of COVID -19. It was not possible to finished the doctoral degree without the help of all the people support. I would like to express my special thanks to Prof.Dr. Ali Ertürk who gave me the unique opportunity to carry out this wonderful project and to be part of the best international team in the world. He gave me continuous support and patience to make progress during my studies. More influence on me has been his spirit of motivation and focus which inspired me to complete my projects. I would also like to express my special thanks to Dr. Farida Hellal. She not only gave me invaluable advice for scientific projects, but also helped me with difficult life problems and philosophizing. Big thanks to you!

I joined the group with my colleague Zhouyi Rong in the same year, and we work on several projects together. The collaboration with Zhouyi has been very influential in designing my experimental methods and critiquing my results. In addition, I would like to thank Dr.Jie Luo, with whom I am also working on some projects. He gives me a lot of pleasure during the project design and has a strong motivation for finalized the scientific project, for which I sincerely thank Zhouyi and Jie. I would also like to thank current and former lab members Dr.Shan Zhao, Dr.Marika Ruiyao Cai, Dr.Mihail Todorov, Dr.Oliver Schoppe, Dr.Benjamin Förstera, Dr.Harsharan S. Bhatia, Marin Bralo, Dr.Chongyue Zhao, Ana Toman, Muege Molbay, Ilgin Kolabas, Dr.Doris Kaltenecker, Xiaoshan Hu, Mayar Ali,Rami Al-Maskari, Karen Biniossek, Dr. Süheda Erener, Basavdatta Pulok Gupta, Luciano Jan Hoeher, Izabela Horvath, Louiza Ignatiou, Karoline Kadletz, Louis Kümmerle, Furkan Ozturk, Johannes Paetzold, Dr.Markus Elsner, Denise Jeridi, Selin Ulukaya, Stefanie Reitinger, Moritz Negwer, Dr.Safiah Olabi, Dr.Jennifer Modamio, Nikolas Galensowske, Tzu-Lun and Dr.Alison Wright for their continuous help and support.

I am also grateful to the members of my thesis advisory committee members, Prof. Dr. Michael Ewers, Prof. Dr. Nikolaus Plesnila, and Prof. Dr. Jochen Herms. They gave me a lot advices on my experiments and career. I really appreciate the fruitful discussions and critical comments during the TAC meetings. I would also like to thank my projects collaboration partners: Prof.Dr. Ingo Bechmann, Prof. Dr. Victor Puelles for their attentive guidance and human research samples support.

My special thanks go to the Institute of Stroke and Dementia and the Institute of Tissue Engineering and Regenerative Medicine for providing me with an open, comfortable, and professional scientific working environment. I would also like to thank the Munich Medical Research School (MMRS) for giving me the fantastic opportunity to conduct my MD research under their great organization. This endeavor would not have been possible without the generous support of the China Scholarship Council scholarship, who financed my research.

A very special gratitude goes out to all friends study together in Munich: Joseph Kroeger, Peng Lun, Lin Yi, Lv Meng, Shen Faqiang, Luo Xianjin, Zhang Fengrong, Teng Binhao.

Above all, I would also like to thank my wife Dr. Lu Dan, without whom this would not have been possible. Words cannot express my gratitude to her. We talk every day via video and she has encouraged me and kept me faithful to finish this doctoral study journey. I would also like to thank my daughter who has supported me emotionally. I also thank my mother-in-law who helps my family. I also appreciate the support I have received from my parents and the rest of my family. Their belief in me has kept me happy and highly motivated throughout this doctoral study process.

Finally, many thanks to you all the I experienced a wonderful and fruitful doctoral study experience.